# MANUFACTURING AND CHARACTERISATION OF A FIBRE OPTIC ACOUSTIC EMISSION SENSOR

by

**FRANCISCO DANIEL NIEVES BOGONEZ**

A thesis submitted to the
University of Birmingham
for the degree of
DOCTOR OF PHILOSPHY

UNIVERSITY OF BIRMINGHAM

School of Metallurgy and Materials
College of Engineering & Physical Sciences
University of Birmingham
April 2017

# Synopsis

Fibre-Reinforced Polymer Composites (FRPCs) are a class of materials which offer significant advantages over conventional metal alloys where weight and/or energy consumption need to be kept to a minimum, as for example in automotive and aerospace applications.

However, FRPCs are complex materials and therefore the damage mechanisms that can affect their structural integrity are also complex. The strongly anisotropic microstructure of FRPCs poses significant challenges for Non-Destructive Techniques (NDT) of the actual structural health of components made from such materials. In modern economy, the profitability of valuable and expensive assets such as airplanes depends highly on the level of 'sweating', which is subsequently a function of the availability of the asset. It is thus highly desirable to minimise inspection requirements to the lowest level possible and at the same time maximise the time between maintenance intervals without compromising safety and reliability.

Acoustic Emission (AE) is a passive Remote Condition Monitoring (RCM) technique which is based on the detection of elastic stress waves emitted when damage evolves in a structure. It allows the on-line assessment of structures and enables the coverage of extensive areas by the addition of an array of sensors. Conventional piezoelectric transducers traditionally used to perform AE are relatively bulky in size and need to be surface mounted. Fibre Optic Acoustic Emission Sensors (FOAES) offer a distinct advantage since they are light weight, have small size and can be effectively embedded in FRPC laminates. In addition, they can be multiplexed with the entire structure being monitored more effectively.

In this study, the fabrication a novel FOAES based in an optical coupler was studied in depth, and the different manufacturing parameters identified and defined. A novel methodology for

embedding the FOAES in glass capillaries in a repeatable, consistent and reliable manner was designed, commissioned and tested. The geometrical characteristics of the produced FOAES were investigated. It was found that the sensors were not symmetrical, and that there were notable differences between FOAES produced by the same manufacturing configuration. The surface characterisation of the FOAES showed differences in the frequency response for sensors with identical manufacturing parameters. In the other hand, all sensors exhibited excellent fidelity. This can be related to different geometrical characteristics from sensor-to-sensor introduced by the applied manufacturing process, and to the double cantilever configuration of the sensor. While the sensor vibrates with identical frequency to the perturbation and therefore will replicate them very accurately, the amplitude of the oscillation will depend on the resonance frequencies of the sensor. Such resonance frequencies will have a strong dependency of the geometry of the sensor.

A comparison between capillary packaged FOAES before and after embedding was performed. A general increase of the response including a higher bandwidth was obtained. On the other hand, bonded FOAES experienced the same increase in the response but not improvements in the bandwidth. It was speculated that the applied adhesive was partly damping the highest frequencies, so potentially this could be resolved with a stiffer adhesive.

The directionality of the embedded sensors was assessed by simultaneous comparison with commercial piezoelectric PZT sensors R30α and R50α (both below 1.5 dB). Both the FOAES and commercial piezoelectric PZT exhibited similar directionality. The FOAES also exhibited a linear response.

Simultaneous tensile tests were performed using embedded FOAES and the same commercial PZT AE sensors. The events collected from the FOAES showed a very rich frequency

spectrum, aligned with the ones acquired simultaneously by the PZT AE sensors. The trend in cumulative hits and energy showed correlation between the FOAES and piezoelectric PZT AE sensors.

The FOAES required much more time than the PZT sensors to return to the relaxed state after picking up a signal. This damping behaviour was an undesired issue. This phenomenon could be reduced by the use of a very soft adhesive in one of the extremes of the capillary. Unfortunately, it was not possible to include this investigation in this research work. Finally, the embedded FOAES was found to be sensitive to the strain. The AE signals were shorter and with less counts according the strain was increased. In addition, correlation between manufacturing draw length and minimum strain at failure was found.

*To my beloved wife Mariana, for all your support and understanding*

# Acknowledgments

I would first like to give thanks to the European Commission for sponsoring this research through the OPTIMUS and MOSAIC FP7 project grants.

I would like to thank Dr Mayorkinos Papaelias for giving me the opportunity to undertake this research investigation under his direction and guidance as well as for his continuous encouragement and moral support. I am grateful to Professor Gerard Fernando for his valuable assistance, advice, guidance and providing access to the required equipment and facilities in order to carry out my experimental work.

I am also indebted to Mr. Frank Biddlestone and Mr. Mark Paget for their assistance and training during different stages of my experimental work. I gratefully acknowledge the provision of facilities and equipment by the School of Metallurgy and Materials of the University of Birmingham necessary to complete this research study.

Special thanks go to my family for your continuous moral support and encouragement.

Finally, the greatest appreciation is given towards my wife Mariana. It has been a long way, and you have always been there to support me.

# Table of Contents

# List of Figures

# List of tables

# Glossary

| | |
|---|---|
| **AE** | Acoustic Emission |
| **AlN** | Aluminium Nitride |
| **CT** | Computer Tomography |
| **CFRP** | Carbon Fibre Reinforced Polymer |
| **DAS** | Data Acquisition System |
| **DWDM** | Dense Wavelength Division Multiplexer |
| **FBG** | Fibre Bragg Grating |
| **FBT** | Fused Bi-conical Taper |
| **FFT** | Fast Fourier Transform |
| **FOAES** | Fibre Optic Acoustic Emission Sensor |
| **FOS** | Fibre Optic Sensors |
| **FRPC** | Fibre Reinforced Polymer Composite |
| **HDT** | Hit Definition Time |
| **HLT** | Hit Lockout Time |
| **KSOM** | Kohonen's Self Organising Map |
| **NDT** | Non Destructive Technique |
| **NR** | Neutron Radiography |
| **OSA** | Optical Spectrum Analyser |
| **PCB** | Printed Circuit Board |
| **PD** | Photo Detector |
| **PDT** | Peak Definition Time |
| **PS-FBG** | Phase Shifted Fibre Bragg Grating |
| **PMN-PT** | Magnesium Niobate-Lead Titanate |
| **PZT** | Lead Zirconate Titanate |
| **RCM** | Remote Condition Monitoring |
| **SD-FBG** | Small Diameter Fibre Bragg Grating |

**SHM** Structural Health Monitoring

**SNR** Signal to Noise Ratio

**SOM** Self-Organising Map

**TLS** Tunable Laser Source

**UV** Ultraviolet

# CHAPTER 1

## Introduction

# 1 Introduction

In recent decades there has been a continuous expansion in the development and use of Fibre-Reinforced Polymer Composite materials (FRPCs). The key applications of FRPC materials are predominantly related to the aerospace, wind energy generation, marine and automotive industries. One of the main reasons for using FRPCs as alternative structural materials to metal alloys is their high specific properties (ratio of the property of interest, mostly strength, and density). Hence, FRPCs are desired materials in applications where weight and energy consumption need to be kept as low as possible, whilst high levels of strength and impact resistance are maintained.

However, in-service performance uncertainty highlights the importance of modelling and the requirement for effectively predicting the structural health and long-term behaviour of these materials in relation with the gradual degradation and service conditions they are exposed to [1, 2]. To address these concerns various Non-Destructive Testing (NDT) techniques are employed [1, 3, 4] for quality control during manufacturing, inspection during maintenance (e.g. ultrasonic inspection, thermography, shearography and radiography) and in-service monitoring (e.g. acoustic emission, acousto-ultrasonics and vibration) [5-8].

Acoustic Emission (AE) testing is a passive NDT and Structural Health Monitoring (SHM) technique, which can be applied for the global evaluation of large structures and components. The application of AE testing can save considerable amounts of time in downtime and can actually be applied during in-service conditions. In this way, it is possible to reduce the amount of time required for maintenance and manual inspection activities, hence maximising availability and profitability of certain assets such as bridges, aircraft, pressure vessels, etc.

Currently, AE testing is carried out using transducers whose operation is based on the direct piezoelectric effect caused by the repositioning of the charge centres in the ferroelectric element when it is deformed elastically. This type of sensors makes use of piezoelectric crystals, which are commonly manufactured of Lead Zirconate Titanate (PZT).

PZT is a typical ceramic material exhibiting strong ferroelectric behaviour. PZT crystals in AE sensors are packaged into a stainless steel protective casing and attached either to an alumina or stainless steel wear plate. The high stiffness of the wear plate material allows the stress waves emitted by propagating cracks or other sources of AE activity to propagate with minimal damping effect to the crystal causing it to deform. The ultrasonic frequency of the stress waves means that the deformation of the crystal occurs very rapidly during the detection of an AE event, causing polarisation changes that give rise to an electric signal. The electric signal is transmitted to the rest of the circuits through electrodes which are attached on the crystal. In this way, AE energy is converted into electric signals which can be further manipulated and analysed in order to extrapolate the type of defect that have given rise to these signals in the first place, the mode of propagation and potentially their severity [4, 9, 10].

Obviously, the piezoelectric effect in a single PZT crystal produces electric signals which are very weak. For this reason, the acquired AE signals need to be subsequently amplified before being digitised and logged by the data acquisition card employed in AE systems. Therefore, prior to digitisation and logging, AE signals are amplified, filtered, and conditioned [4, 11]. There are also other types of piezoelectric materials such as langasite ($La_3Ga_5SiO_{14}$), Lead Magnesium Niobate-Lead Titanate (PMN-PT), Alumium Nitride (AlN), and others, which can be used instead, but due to the very good and reliable performance of PZT crystals, other

materials are normally considered only when temperature or operational conditions necessitate this.

Despite the wide variety of available piezoelectric crystals and performances, these sensors have several fundamental disadvantages. For example, they are bulky in size and although this is not a major problem for surface mounting deployment, the embedment into composite materials is either not straightforward or is impossible altogether since they will cause the introduction of a severe defect into the structure. In addition, piezoelectric crystals are generally sensitive to electromagnetic noise, which renders them less useful in operational environments where strong electromagnetic noise is present.

The low energy electric signals generated by piezoelectric AE sensors naturally attenuate as they propagate through the cabling of the system from the sensor to the data acquisition card. Hence the distance from the piezoelectric element to the first amplification point known as the pre-amplification stage needs to be relatively short and normally no further away than 1.5 metres. Although there are also sensors with integrated (built-in) pre-amplifiers, these sensors tend to be even bulkier. Moreover, the quality of the signals produced tends to be relatively poorer when compared with conventional setups where the AE sensor is separate from the pre-amplification unit. Conventional piezoelectric AE sensors tend to be relatively large (the larger the surface of the crystal the higher its sensitivity) and heavy especially in comparison with Fibre Optic Sensors (FOS). Finally, special design considerations need to be taken into account when intrinsically safe operation is necessary, i.e. in explosive environments such as oil refineries.

While some of the aforementioned problems and drawbacks of conventional AE sensors can be overcome by the application of highly specialised and far more expensive designs, the

application of FOS in SHM as an alternative sensor type to conventional piezoelectric ones has received extensive attention in recent years [12-14]. These optical sensors have been demonstrated to address satisfactorily a number of the previously discussed disadvantages. Therefore, they can be considered as a potential complete replacement or complement to conventional sensing technology. The use of FOS allows several additional capabilities including inertness to the effect of external electromagnetic fields. Furthermore, FOS are much smaller in size (particularly in terms of their diameter) when compared with standard piezoelectric AE sensors and therefore more suitable for embedment in FRPCs and other materials. FOS also suffer from lower attenuation of the detected signals with increasing distance from the data acquisition unit. For example, typical attenuation is less than 0.18dB/km in single mode fibres operating at a 1550 nm wavelength and 15 dB/km in single mode fibres operating at 630 nm wavelength. Furthermore, FOS are intrinsically safe by nature. Hence, their application in potentially explosive hazardous operational environments, such as oil refineries and chemical plants, does not require any additional precautions or design considerations to be taken. This is due to the fact that the signals are based on the transmission of light rather than electricity.

## 1.1 Aims and objectives of the research

The present study investigated in depth the manufacturing procedure and full characterisation of a novel type of AE sensor based on optical fibres. The objectives of this study in detail where the following:

**(i) FOAES manufacturing and comparison versus standard piezoelectric transducers**

In the initial stages of the present study the fibre optic AE sensors developed were assessed in terms of their performance and compared with standard piezoelectric transducers. The effort

was then focused on identifying the factors that influence the consistency of the production of the FOAES. The various effects of these factors were analysed since by modifying the production process variables it becomes possible to manufacture sensors with different resonances. Also the sensitivity and directionality of the FOAES in comparison with standard commercial piezoelectric transducers were assessed. The survival rate of the FOAES during handling was evaluated by carrying out relevant experiments.

The developed fibre optic AE sensors were tested initially by surface-mounting them on a glass piece with rectangular shape. To suppress the uncertainty introduced in the acquired signals by commercial AE systems from filtering and re-sampling, customised software and hardware was developed and commissioned for collecting, storing and analysing the signals generated by the FOAES sensors manufactured.

**(ii) FOAES packaging and embedding into composite materials: influence in response and characterisation**

A novel process for inserting the FOAES into a glass capillary was investigated and developed. The impact of the packaging process and variables on the response of the sensors were assessed.

The packaged sensors were characterised by mounting them on the surface of a test piece prior to subsequently embedding them into different configurations of glass-epoxy composite laminates. The sensors were then re-characterised to understand the overall effect of the embedding process on the response of the sensors.

Again, custom-built software and hardware was developed and commissioned for the collection, storage and analysis of the response of the sensors.

**(iii) Direct comparison between embedded FOAES and conventional piezoelectric AE sensors during strain tests.**

An appropriate testing configuration was designed and implemented in order to establish a direct comparison between two surface-mounted piezoelectric AE sensors with embedded FOAES during tensile testing of epoxy-glass fibre laminates. Commercial, off-the-self, Mistras Group Inc. hardware and AEWIN® software were employed for the acquisition and storage of the AE signals produced by both sensor technologies. During these tests the ultimate tensile strain that the FOAES could endure prior to failure was evaluated.

## 1.2 Thesis structure

The thesis is divided in seven different chapters, as follows:

**Chapter One:** *Introduction*

In this chapter a general introduction about the project is given, followed by the description of the aims and objectives of the research. The structure of the thesis and the contributions of the author to the scientific literature are described.

**Chapter Two:** *Literature Review*

A review of the state of the art of the SHM in general and about the AE in particular is given. Particular attention is given to the results reported by other studies on manufacturing and characterisation of FOS.

**Chapter Three:** *Materials and Methods*

This chapter describes the experimental methods and procedures adopted in order to carry forward the research objectives of the present study. A special in-depth explanation is given to the developed and commissioned software and hardware.

**Chapter Four:** *Sensors Manufacturing and Packaging*

The effect of the different manufacturing parameters on the overall performance of the FOAES is discussed and analysed. The response of different sensor configurations is evaluated on an aluminium standard test piece where FOAES were surface-mounted. The FOAES were tested un-packaged and secured on a rectangular piece of thin-glass by applying two drops of UV adhesive.

In addition, this chapter describes the development of a novel packaging process, embedding the FOAES in a silica glass capillary.

**Chapter Five:** *FOAES embedding and characterisation*

In chapter five, a number of packaged FOAES are surface-mounted on a composite plate prior to being embedded in different configurations of epoxy-glass fibre composite laminates and tested in terms of their response to AE signal sources. The responses are then compared in order to understand the impact of the embedding process on the different aspects of the sensors' performance. The directionality effect is also considered and analysed, and subsequently compared with the benchmarking of conventional piezoelectric AE sensors. Finally, the linearity and fidelity factors are assessed.

**Chapter Six:** *Comparison of embedded FOAES with surface-mounted piezo-electric AE sensors*

A direct comparison of AE activity captured by an embedded FOAES and surface mounted conventional AE sensors are established following tensile testing under an appropriate experimental configuration. To enable this comparison, the laminates with the embedded FOAES were machined and instrumented with a conventional AE sensors and strain gauges. The laminates were then strained via a universal testing machine whilst the AE activity was recorded. A comparison is carried out between the performance of the different FOAES and the benchmarked AE sensors.

**Chapter Seven:** *Conclusions and Suggestions for Future Work*

The conclusions arising from the results of the present study and their comparison with other works previous reported are summarised in Chapter 7. Also suggestions for future work are presented in detail.

## 1.3 Publications

The following publications containing findings from research carried out by the author have been produced:

1. Irfan, M.S., Machavaram, V.R., Murray, R.C., Bogonez, F.N., Wait, C.F., Pandita, S.D., Paget, M.A., Hudson, M. and Fernando, G.F. (2014) *The design and optimisation of a rig to enable the lateral spreading of fibre bundles*. **Journal of Composite Materials**, Jun;48(15):1813-31.

2. Machavaram, V.R., Wang, L., Pandita, S.D., Hellmann, S., Bogonez, F.N. and Fernando, G.F. (2014) *Multi-point monitoring of cross-linking reactions*. **Journal of Applied Polymer Science**, Nov 15;131(22).

3. Irfan, M.S., Shotton-Gale, N., Paget, M.A., Machavaram, V.R., Leek, C., Wootton, S., Hudson, M., Helsmans, S., Bogonez, F.N., Pandita, S.D. and Fernando, G.F. (2017) *A modified pultrusion process*. **Journal of Composite Materials**, Jun;51(13):1925-41.

The following journal paper is under preparation:

4. Bogonez, F.N., King, D., Machavaram, V.R., Billaud, C., Mills, P., Ghosh, N. and Fernando, G.F. (2017) *Simultaneous acquisition of refractive index and thermal properties from within a differential scanning calorimeter using a fibre-optic refractive index sensor.*

# CHAPTER 2

## Literature Review

# 2 Literature Review

## 2.1 Introduction

It is clear that there is a continuous expansion in the development and use of FRPCs in recent years. The key applications of FRPC materials are predominantly related to the aerospace, wind energy generation, marine and automotive industries. One of the main reasons for using FRPCs as alternative structural type of materials to metal alloys is their much higher strength to weight ratio. Hence, FRPCs are desired materials in applications where weight and potentially energy consumption need to be minimised to the lowest level possible. However, apart from their high strength to weight ratio FRPCs also exhibit superior resistance to corrosion which is very important in several applications, particularly when downtime needs to be kept as low as possible and availability needs to be increased to the highest possible level [1]. FRPC are routinely inspected using various conventional NDT techniques in order to ascertain manufacturing quality or the structural degradation level while in service [1, 3, 15-18]. Techniques used for the evaluation of FRPC structures include ultrasonic inspection, thermography, shearography, radiography, AE, acousto-ultrasonics and vibration [5-8].

FRPCs consist of two materials which are completely different at molecular level and can be mechanically separated [19]. These two materials are classified as the matrix and the reinforcement of the FRPC. The matrix binds the fibres together transferring the load to the reinforcing fibres, giving to the composite material some level of ductility. It also provides protection to the reinforcing fibres against chemical or mechanical damage. The reinforcing fibres carry the load, providing increased tensile strength and stiffness properties. Consequently, degradation of the matrix-fibre interface [20] or the cumulative damage

experienced by the reinforcing fibres or the matrix [21-23] will result in different failure modes (e.g. delamination, cracks or tensile failure).

The damage in FRPCs is normally difficult to detect using visual inspection alone [22]. Also the mechanical behaviour of the material prior to final failure does not change significantly either. Hence, these are two of the key reasons of why evaluation of FRPC structures and components using NDT techniques play a major role in the successful widespread application of these materials [1, 3, 15-17].

Conventional X-ray radiography, Neutron Radiography (NR) and Computed Tomography Scan (CT scan) [3, 24-28] can be used for detecting certain types of defects such as delamination, voids or cracks. NR has been proven to perform well in the inspection of bonding lines or material in proximity to metals. Some important disadvantages of radiographic inspection techniques include the high dependency of sensitivity on the defect orientation, the resolution of the detectors (which is normally not sensitive enough for finding small defects at filamentary scale) and the difficulties in their deployment when accessibility from both sides of the component concerned is not straightforward. However, recent advances in backscattered radiography have partially addressed the latter issue although at the expense of inspection resolution. In addition, the health and safety concerns involved in radiographic inspection can render sometimes the in-situ application of radiography impossible or prohibitively expensive. Hence, the component disassembly and inspection in radiation leak-proof chambers may become necessary. The CT scanning equipment has space limitations, and the time required for extracting a 3D image from the samples increases dramatically with increased resolution. The CT resolution is a function of the X-ray images taken per each degree of angle.

Ultrasonic inspection methods, including ultrasonic immersion C-Scan testing [3, 29, 30], are commonly used for online and off-line (ultrasonic immersion C-Scan only off-line) inspection of FRPCs. These techniques allow mapping of the presence of defects in FRPC materials which may be buried or surface-breaking. Again, there are limitations related to the attenuation of the ultrasonic signal due to the high anisotropic nature of FRPCs causing scattering and multiple reflections of the interrogating ultrasonic waves. The geometry of curved or complex-shaped specimens is an additional hurdle that needs to be overcome as well as the defect orientation with respect to the propagation angle of the interrogating ultrasonic beam. The use of ultrasonic phased arrays [31-33] allows the overcoming of some of these problems focusing the ultrasonic beam energy in smaller areas of interest. In addition, phased arrays enable the better adaptation of inspection procedure to variable geometries by changing the focal distance (depth) and/or the angle of the ultrasonic beam accordingly.

Optical or acoustic holography, and thermography [3, 34, 35] are alternative methods of inspection of FRPCs. However, they require the use of very sensitive equipment, which is highly dependent on the test conditions (vibrations, temperature). Therefore, their use is normally limited to laboratories. Advanced pulsed thermographic equipment however, can be deployed in the field. Nonetheless, such equipment is very bulky and expensive and attention needs to be paid in the environmental conditions prior to the inspection.

Finally, vibration and AE are methods which can be employed for successfully detecting structural damage, friction, discontinuities or changes within in-service components [1, 36-44]. The principles of AE testing are discussed in detail in the following section.

## 2.2 Acoustic emission

### 2.2.1 Introduction

AE is defined as the mechanical energy released in the form of elastic waves within a material due to dynamic microstructural changes which are taking place internally [45, 46]. The acquisition and subsequent analysis of AE signals permits continuous in-service monitoring of the structural health of materials with few restrictions [6, 47]. AE can be used for the geometrical location of active damage evolution using a network of two or more sensors with known locations and distance between them [48, 49].

The effective use of AE requires the separation of the damage-related events from unwanted mechanical noise [47]. This can be done through the characterisation of the AE hits/events using several parameters such as threshold level, counts, counts to peak, rise time (known as RT, is the time to the maximum of the hit since the threshold is crossed), and duration. It is important to set the key AE acquisition parameters correctly before any data is acquired. The parameters which need to be determined according to the need of the measurement are the time that the signal requires to reach its peak after the threshold has been exceeded for the first time (known as Peak Definition Time or PDT), the time that the hit remains open after the signal passed the threshold for the last time also known as the Hit Definition Time (HDT), and the hit lock-out time (HLT) during which the sensors do not record any further signals after a hit has been logged [41, 50]. The relevance of these parameters to the AE waveform captured are shown in Figure 1.

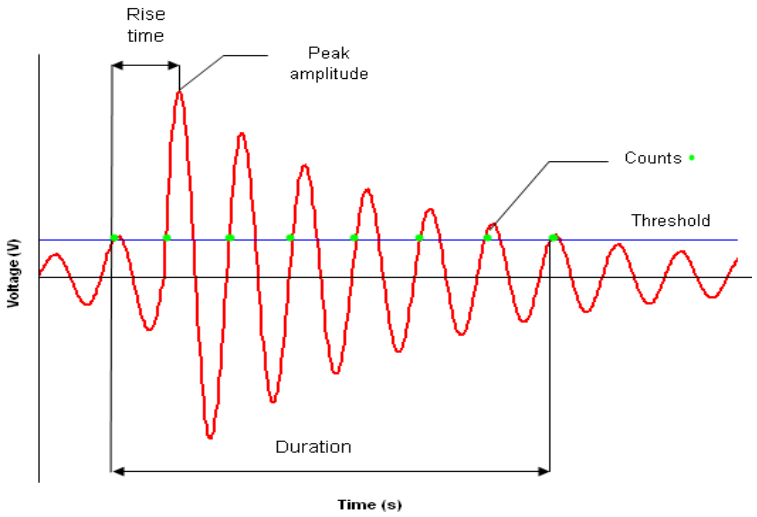


**Figure 1 Typical AE signal with some of the most important parameters (source: http://www.muravin.com).**

In addition, frequency-based filtering should be used for eliminating signals with lower frequency (typically lower than 50-100 kHz, associated with ambient noise). The bandwidth where the AE events happen is normally within the range of 20 kHz to 1 MHz. Most structural defects when they grow will emit stress waves at frequencies within the range of 100-350 kHz. The upper limit of AE testing is rarely increased up to 2-3 MHz [38, 47] for event classification purposes [7, 8]. However, this requires much higher sampling rates in order to avoid aliasing [51, 52]. At the same time more data storage and computing power is required.

AE sensors can be distinguished into two main types: a) the commonly used surface-mounted piezoelectric sensors and b) surface-mounted or embedded optical sensors. A typical piezoelectric sensor consists of a piezoelectric crystal placed in a metallic housing normally made of stainless steel. The sensor is coupled with an appropriate ultrasonic couplant (such as ultrasonic gel, grease or Vaseline) on the sensing face. Consistent contact with the test piece being monitored is ensured by the application of force pressing the sensor against the test surface either through the use of magnetic hold-downs or duct-tape. Alternatively, superglue

or Araldite® adhesive can be employed, particularly when small or non-magnetic test pieces need to be monitored. The piezoelectric crystal (normally PZT ceramic) converts the mechanical energy of the incident elastic waves in an electric signal through the direct piezoelectric effect. The resonance frequencies of the crystal influence the response in the frequency domain. The crystal size and coupling quality influence the sensor's overall sensitivity in detecting stress waves propagating through the monitored structure. A typical AE piezoelectric sensor and its frequency response are shown in Figure 2. It should also be noted that the effectiveness of the AE sensor in detecting damage propagation in a structure with increasing distance from the source will depend on the level of attenuation of the stress waves as they propagate through the microstructure.

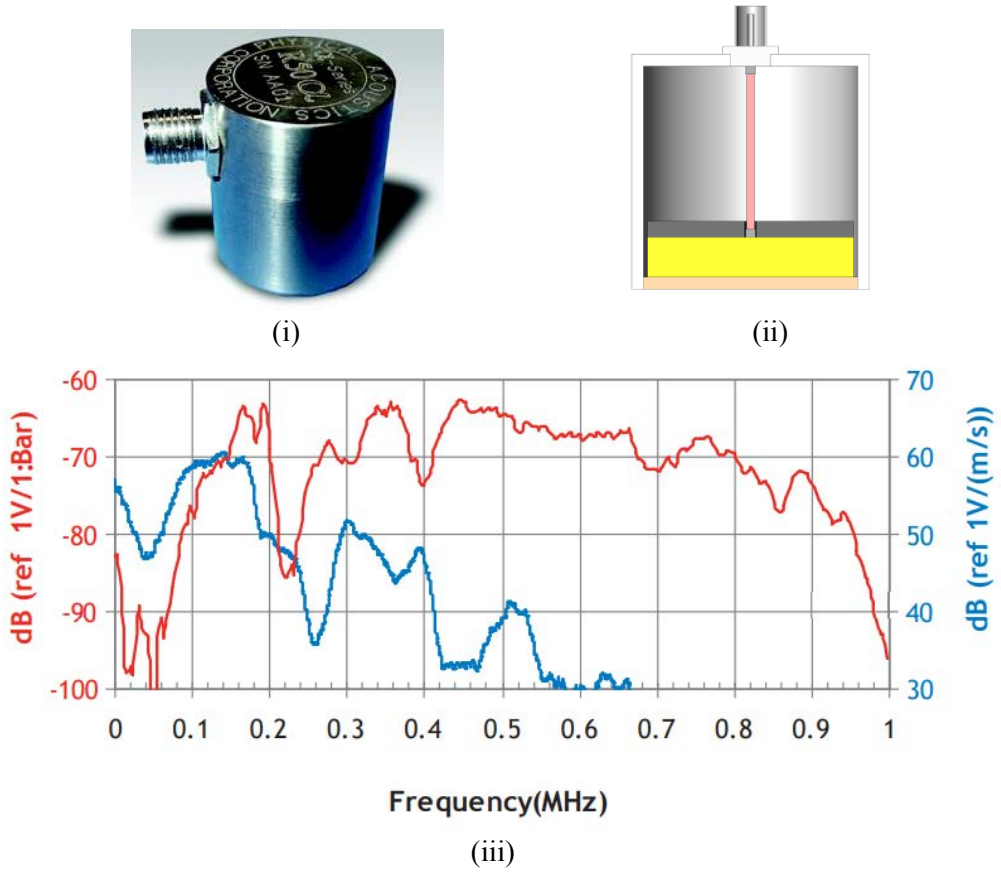


**Figure 2 Piezoelectric sensors; (i) picture of PAC 50α, (ii) typical structure of a piezoelectric sensor, and (iii) response in frequency of a sensor PAC 50α.**

Optical sensors are much different in nature and the sensing principles are based on other fundamentals in comparison with traditional piezoelectric sensors as it will be discussed next.

### 2.2.2 Damage detection using Acoustic Emission

A broad range of AE applications have been reported in the literature [9]. In the rail industry, AE has been employed for monitoring the crack growth in steel alloys used for the track infrastructure [53, 54]. AE has also been evaluated in terms of its capability in detecting damage in wheels and axle bearings [55] of railway rolling stock. Moreover, AE has been employed for SHM of bridge structures and other masonry [2, 11]. Damage can be qualitatively or semi-quantitatively evaluated based on AE signal processing using appropriate statistical analysis and historical data trending. Furthermore, AE has been very successfully applied in monitoring leaks in pipes [56] and pressure vessels [57]. Ozevin and Harding [58] proposed an array of AE sensors to monitor leaks in pressurised pipelines. The leaks created turbulent flow which made particles and bubbles to collide against the material. These collisions caused stress waves to arise that propagated along the pipe, eventually being detected by an AE sensor.

AE can also be applied for corrosion monitoring [59], detection of partial discharges in power electric machines [60, 61], or damage detection and classification in composite structures. Rabiei and Modarres [62] considered an approach of predicting crack propagation based on the analysis of AE data using the risk measure for a crack to change from the stable to rapid growth regime using a statistical model, calculation of crack growth rate and Bayesian estimation technique. The AE activity was collected during standard fatigue crack growth testing using a metallic notched specimen and cycling loading conditions. Kim et al. [63] analysed the damage induced by low energy impact using AE data acquired from two

different types of transducers. Wavelet and short-time Fourier transforms (STFT) were applied for the signal analysis, being able to identify when damage evolution occurred. The analysis was validated by ultrasonic C-scan and microscopic examination of the samples tested.

AE has been extensively reported in the literature as a very powerful technique for detecting and classifying damage in FRPC materials. Scholey et al. [64] described the application of an array of AE sensors in monitoring the structural health of large specimens as a means of minimise the effect of reflections. The evolution of various defects, such as matrix cracking and delamination under quasi-static loading conditions were successfully detected. The signals were classified based on the dominating wave guided mode. While matrix cracking was mainly described by the $S_0$ mode (periodical movement parallel to the neutral axis of the plate as represented in Figure 3), the delamination was predominately dominated by the $A_0$ mode (periodical movement perpendicular to the neutral axis of the plane, as shown in Figure 3). In addition and in contrast to the $A_0$ mode, the $S_0$ mode or matrix cracking transmission mode was found to be highly dependent on the angle.

(i)

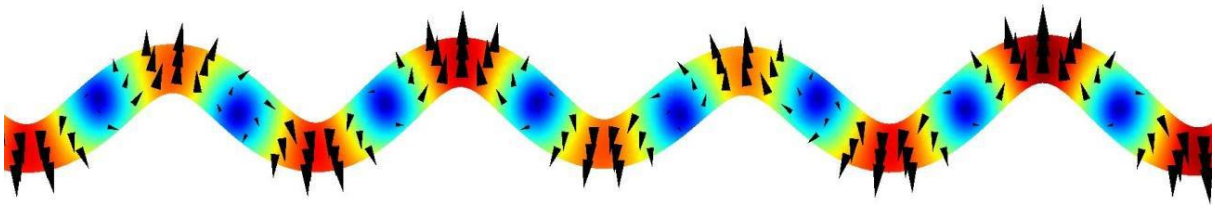

(ii)

**Figure 3 Numerical simulation of the propagation of the fundamental Lamb symmetrical and anti-symmetrical modes in a thin plate [65]. Figure 3 (i) shows the symmetric or movement parallel to the neutral axis, while Figure 3 (ii) represents the antisymmetric or movement perpendicular to the neutral axis. Warmer colours represent higher displacements.**

Quispicuta et al. [66] investigated damage evolution of fatigue test of composite sandwich panels by employing amplitude-clustering of the collected AE signals. The samples consisted of skins of bidirectional carbon fibre bonded on a honeycomb core (polyurethane filled craft paper). The test revealed the core failure as the main contributor, followed by interfacial failure. Laksimi et al. [67] explored damage evolution using AE in tensile tested polypropylene glass fibre composites. A parameter-based identification algorithm was developed which was able to distinguish between matrix cracking, reinforcement-matrix interface damage, delamination and fibre fracture from non-relevant signals such as friction or noise. The signals were classified based on their amplitude.

Weber*s* et al. [46] investigated AE for monitoring fatigue damage in carbon fibre-reinforced epoxy composites (CFRP), curing of concrete and corrosion of carbon and stainless steel. The suitability of AE for monitoring all three of these very different phenomena was confirmed. It was possible to distinguish matrix cracking, delamination and fibre fracture in the AE data collected during the fatigue testing of the composite material considered in this study. The temperature variation and micro-cracking of the concrete was linked to the AE overall activity and counts. Finally, pitting, stress-corrosion-cracking, uniform corrosion and time without corrosion were identified and clustered. An average error on the classification of 2% was obtained. Stepanova et al. [68] proposed a methodology for AE processing based on the amplitude distribution dynamics. The methodology was applied on organic composites enabling the fracture detection and crack growth events occurring in the material. The front velocity of the generated elastic waves was found to change several times in magnitude from the early stages to the full development of the cracks. The author stated the importance of the velocity of the wave front to enhance the location of the defects, with lower speeds leading to inaccuracies. Awerbach et al. [69] brought the analysis typically carried out at laboratory-

level to the identification of types of damage in full-scale composite fuselage structures. Several types of sensors and configurations were investigated. However, the decoupling of the signals arising from different damage mechanisms was found to be unfeasible. The superposition of unwanted signals both in the frequency and time domain, together with a dramatic increment in the number of AE events when close to the ultimate load (superimposing signals) were found to be among the main reasons of failure to distinguish different damage mechanisms in the AE data collected.

Godin et al. [70] investigated the change of AE signal signatures emitted by the same material after different levels of water aging had been sustained. It was found that as the mechanical properties degraded with increasing water content, the AE signals captured decreased in amplitude and activity. A Kohonen's Self-Organising Map (KSOM) was applied to classify the different failure modes in as-received samples with no aging effect. The same approach was then used on aged samples. The AE waves were found to be similar for analogous damage modes in both aged and as-received samples.

AE testing has been extensively used for the investigation of the properties of the matrix-reinforcement interface based on tests carried out on samples with a single or a limited number of fibres as reinforcement. Narisawa and Oba [6] used AE to study the shear fracture strength of the boundary of four matrix system and bundles of 90 filaments of glass fibre, or single carbon fibre filament. The results showed correlation between the shear strength and the proportion of hardener. Haselbach and Lauke [38] proposed the use of a laminate with a single fibre as reinforcement to distinguish between de-bonding in the interface fibre-matrix, fibre fracture and friction during tensile test. The geometry of the samples was optimised by modelling the transverse stress of the fibre-matrix interface. The methodology enabled the calculation of the adhesion strength by monitoring the initiation of the de-bonding.

AE has been demonstrated to be able to successfully characterise and detect failure of fibres bundles under tension. Hamstad and Moore [71] studied the tensile failure of a single filament of Kevlar 49 before proceeding to test dry and lubricated bundles. They investigated the influence of shorter fibre length in causing premature failure in strong fibres and thus identified the importance of simultaneous AE monitoring. Chi et al. [72] reported the possibility of combining AE with two-parameter Weibull distribution to characterise the survivability and behaviour of a bundle of glass fibres. Bundles of 4000 fibres were tested, classifying the bundle in two different clusters based on intrinsic flaw sizes. This could enable the assessment of the effect of manufacturing parameters in the mechanical properties of the fibres. Jihan et al. [73] provided further evidence of the bimodal flaw population in glass bundles, when testing bundles with a population of 4000 filaments. Two clusters of fibres were identified based on the severity of the intrinsic flaws of the individual filaments. The higher frequency AE events were found to be linked with fibre fracture, so the presented methodology was able to fit the data to a two-parameter Weibull distribution representing the survivability of the fibres. The importance of the effect of different factors during bundle manufacturing on the mechanical properties was investigated. Mili et al. and Hall and Okoroafor [39, 41, 74] used AE for defining the parameters of a Weibull distribution describing the surviving probability of glass-fibre bundle tensile test. The role played by inter-filamentary friction, and its contribution to the AE activity were investigated.

### 2.2.3 Signal processing in Acoustic Emission

The frequency analysis of the collected AE has been reported as being a very effective way to process AE signals. Thus, AE can be used for investigating and correlating different damage modes. One of its biggest advantages lies in the relative high sensitivity with respect to the distance of the sensor from the source [75]. However, the high attenuation level arising from

the anisotropic microstructure of composite materials and fibres acting as waveguides renders amplitude-based classification challenging [5, 66, 67]. Different combinations of resin systems, reinforcements and specimen geometry or configuration have been used to classify AE data where phenomena such as matrix cracking, de-bonding, interface related damage (fibre pull-off or matrix-fibre de-bonding) and fibre fracture events (from lower to higher frequencies respectively) [75-78] are contained. These events will shift in frequency and change in range when different resin systems or reinforcements are used. De Groot et al. [76] tested pure resin and unidirectional specimens with the reinforcement aligned at 0°, 10° and 90° of the pulling direction. The different alignments of the reinforcement enabled the possibility of identifying the matrix cracking (pure resin and 90°) from interface failure signals and fibre pull-out (10°) or fibre breakage (0°). Ramirez- Jimenez et al. [77] proposed the use of glass fibres with a polypropylene matrix due to the low AE source potential of the latter material in comparison with glass. Specimens of different orientations were prepared. A relationship between the predominant frequencies of each AE event with micro-mechanical events was reported. The authors discussed the possibility of using the relationship between the first and second frequency harmonics to differentiate combined effects.

Giordano et al. [79] proposed a frequency-based analysis based on fractals. The technique was developed to describe patters whose irregularities made them unsuitable to be described by conventional Euclidean dimensions. Dog-boned shaped samples made of single filament composites consisting of carbon fibre and three different resin systems were tested in tension. The developed algorithm was able to find shape similarities in the spectra describing different failure modes, and thus able to identify the frequency ranges when fibre failure occurred. Bohse [78] used single and multi-fibre glass fibre-epoxy laminates for classifying the different damage mechanism. The applied classification approach was based on the total

spectral power contained in defined frequency intervals. The experiments performed included different types of initial induced damage (notching) with tensile or double cantilever tests. Ni and Iwamoto [75] used single filament carbon fibre-epoxy composites to classify damage by applying FFT and wavelets for spectral analysis. After a first calibration stage, it was found that while the amplitude decayed dramatically with distance, the spectrum envelope shape remained nearly unchanged. The micro-fracture of the single filament composite was successfully classified by frequency analysis. Since the FFT provides spectral information of the different damage mechanisms but lacks time-domain resolution, the authors proposed the addition of complementary wavelet analysis as means of time-frequency analysis tool. This approach provided a much clearer understanding of each failure mode and their interaction.

Clustering signals is defined as the automated analysis that enables the classification of AE events, grouping them in such a way that the elements of a cluster share more similarities with other member of the same cluster than with any member out of the cluster. This is of particular interest when signals generated by similar damage modes can be grouped and identified automatically. KSOM [80] and k-means [81, 82] are among the most popular techniques for data clustering. These techniques are very powerful tools when appropriately applied to AE data analysis, enabling the automatic classification and identification of signals with similar patterns. Godin et al. [7, 8, 70] was able to cluster the AE activity by training unsupervised classification with clusters obtained by k-means. The data was validated by testing different composite materials adding progressively more complex architecture, from neat resin and single fibre to cross-ply laminates. These enable the creation of a library of well identified damage modes able to validate the automatic classification. Kostopoulos, Loutas and Dassios [83] applied successfully the unsupervised pattern recognition to cluster the signals from different failure modes in SiC/MAS-L composites, during quasi-static tensile

tests. Crivelly et al. [84] applied KSOM to the failure classification of pultruded products. The generated map was trained by the data of one specimen, and classified in clusters using the k-means algorithm. The resultant neural network was successfully used with different material layouts. Using this approach it was also possible to detect the anomalies of notched specimens.

Gutkin et al. [85] analysed the suitability of three different clustering techniques to classify the AE activity of laminates with different configurations under tension, double cantilever, four-point bending, compact tension and compact compression. The combination of self-organising map (SOM) with k-means provided the best results with lower computational requirements. The clustering achieved was consistent with the peak frequency distribution, with fibre breakage and pull-out at the higher frequencies and matrix cracking at the lowest. A map of frequencies was presented for the different tests and laminates, where the different failures were assigned to the correspondent frequency bands.

A different approach which is getting more habitual with the increase of computational power is the wavelet transform analysis. Qi et al. [86, 87] used the Wavelet Transform to decompose the signals in several wavelet levels. Each wavelet level corresponded to certain frequency bands. Therefore, the methodology acted as bandpass filter enabling a more simple analysis of the signals, separated in frequency bands assigned to different defects. This approach allowed the multi-level analysis of the energy as well. This information together with the overall energy can be used to assess the severity of the defects. Marec et al. [88] reported the use of wavelet transform analysis to enhance the conventional temporal descriptor-based clustering method. New timescale descriptors were then generated which differentiated much better the various damage mechanisms, improving the overall damage identification capability.

Finally, the AE can locate the origin of the events [49, 89-91]. This is a very powerful capability apart from damage identification, because alternative NDT techniques can be applied to verify the extent of damage and take appropriate measurements if required when severity cannot be ascertained already. The location of AE damage sources is achieved through the deployment of an array of two or more sensors monitoring the area or volume of interest. The basic location of a defect can be carried out using linear location. Where three or more AE sensors are used, location can be carried out using triangulation based on the different times of flight of the signal and the distances between the AE sensors [49].

Eaton et al. [91] applied an improved methodology. Instead of simply using the time of flight they employed an alternative technique, which has been named Delta T Mapping. This approach led to reductions of the RMS of the error up to 30 mm. Surgeon and Wevers [89] proposed the use of a single sensor to perform linear location. The technique was reliant on precise modal speed in the laminate being monitored. The authors presented several experiments with different laminate configuration to demonstrate this principle. Aljets et al. [90] investigated the use of three very closely place sensors to locate AE sources in large plate-shape specimens. The signal analysis relied in the modal analysis and separation of $S_0$ and $A_0$, together with the time of flight of the signals. Advantages of this technique were the much larger area covered in comparison with the other commonly applied location techniques and lower relative distance from sensor to sensor. In addition, the small distance from sensor to sensor enabled the detection of the same signal without noticeable decay in amplitude and with the same modal separation, contrary to the commonly used technique. A reported disadvantage was the necessity of collecting both symmetric and asymmetric Lamb modes. The first one has normally much lower amplitude and thus, can go undetected by the sensor when the relative distance source-sensor increases. Jinping et al. [92] applied a similar

concept of monitoring one frequency component in one mode through the use of the wavelet transform. The arrival times of the modes were clearly distinguished by locating the peak times, enabling the triangulation of the source location.

## 2.3 Optical sensors for Acoustic Emission

There are different ways of using optical fibres for AE testing including interferometric methods, Fibre Bragg Gratings (FBG) or intensity-based sensors [18, 93-96]. The main advantages over the piezoelectric sensors are the very low weight and size of the optical sensors [14, 97], immunity to electromagnetic fields [60, 61] and suitability for application in explosive environments due to their inherent intrinsically safe nature. Furthermore, because all wiring is based on optical fibres too, they allow the interrogation of the structure or component from longer distances with an excellent ratio of weight versus length. The sensors can be mounted on the surface of the component or embedded into the material in the case of FRPCs [97, 98].

Interferometric sensors for AE monitoring can be mainly grouped as Mach-Zehnder, Michelson, Fabry-Perot or Sagnac interferometers [14, 40, 42, 97, 99-102]. They are based on the splitting and further recombination of laser sources. A disadvantage of this type of sensors lies in the more expensive and complex setup required for their interrogation. In addition, they exhibit extraordinary sensitivity to changes in temperature or unwanted mechanical perturbations. However, a significant advantage is the fact that they can be easily multiplexed [103].

FBGs [103, 104] are based on the modification of the refraction index across the fibre length to create a periodic perturbation by printing gratings on the optical fibre. The main advantage of these sensors is the low bandwidth required for their interrogation which enables

multiplexing. The relative robustness of their setup is also very important. The modulation of the laser power within optical fibres can be used as a sensing characteristic for monitoring AE activity with optical sensors [14]. These sensors have the advantage of requiring a much simpler and cheaper setup than the previously described interferometric sensors. Their main disadvantage [65] is that any power fluctuations such as those created by mode hopping in semiconductor lasers, create high levels of background noise resulting in lower signal to noise ratio (SNR) contaminating the AE signals. The intensity-based sensors rely on the modulation of the output power as a sensing parameter [14, 96, 105-108].

## 2.4 Interferometric-based optical sensors

Interferometry is the study of the interaction of waves when they are superimposed [109]. Interferometers are devices which make use of this phenomenon applying it to the measurement or determination of certain parameters. Optical interferometers have been broadly used form monitoring strain, acoustic signals, temperature or angle variation [14, 109-114] among others. They use as a principle the superimposition of a coherent laser source which can be divided and recombined between reference and sensing path. The analysis is based on the evaluation of the phase change. When used to interrogate acoustic phenomena, the interferometers require stabilisation by keeping the interfered signals in quadrature [115]. This enables the cancelling of the quasi-static occurrences which induce a beating or sinusoidal output, such as temperature or external applied strain. Conventional methodologies for interferometeric interrogation are homodyne and heterodyne detection [116-118].

Regarding to the deployment of such sensors in AE applications, three types of configuration are reported in the literature: (i) Mach-Zehnder interferometer; (ii) Michelson interferometer; and (iii) Fabry-Perot interferometer.

### 2.4.1 Mach-Zehnder Interferometer

The Match-Zehnder interferometer consists of a laser beam split in two by a 3 dB coupler, dividing the power equally between two arms. One arm (sensing arm) is exposed to the perturbations while the second arm (reference arm) is completely isolated. Thus, it is kept unaffected by the perturbation. When recombined via a second 3 dB coupler, the dynamic changes in the effective optical path induced by the disturbances create interference in the output due to mutual phase difference [14, 112-114]. The analysis of the interference provides information about the changes in the optical path, and therefore a quantitative measure of the disturbance. A detail of the required setup is shown in Figure 4.

Bucaro et al. [119] were the first in reporting the use of a Mach-Zehnder ultrasonic microphone to detect waves in water from 40 to 400 kHz. This first development was further progressed to construct optical fibre-based hydrophones extensively used in military warships.

Baillie et al. [120] implemented a homodyne feedback technique to stabilise a Mach-Zehnder interferometer monitoring AE activity in carbon fibre composite strips. The sensing arm of the interferometer was stripped and embedded in the centre of the laminate. Polarisation controls at both extremes of the sensing arm enabled the coherence and identical polarisation state of both recombining beams. The system was successfully tested with simulated signals generated by piezoelectric transducers and Hsu-Nielsen emitters. Simultaneous acquisition of the interferometric sensor and a reference piezoelectric AE sensor were carried out during tensile tests, obtaining similar results. Zheng et al. [42] used a similar setup to monitor simulated AE signatures released by piezo-emitters. The reference arm of the interferometer was clamped on the surface by steel blocks, keeping the buffer to improve the compliance and

reducing the resonant oscillation frequency. Similar results with the reference resonant piezoelectric AE sensors were obtained in the frequency range from 0.2 to 1 MHz. The main source of signal noise was identified to be produced by the amplitude drift on the interrogation HeNe laser.

Pierce et al. [121] demonstrated a stabilised homodyne Match-Zehnder interferometer by comparing the response when the sensing arm was embedded or surface-bonded. Different materials were tested such steel, carbon fibre and glass fibre composite material. The sensor which was excited using a 633 nm wavelength laser, achieved up to 20 times higher sensitivity to the propagating Lamb waves when embedded than when surface mounted.

Her et al. [122] developed an inexpensive system for strain sensing under dynamic loading. A conventional setup was applied, but the phase shift demodulation was performed by the symmetric 3x3 coupler methodology reported by Brown et al. [123]. An accurate dynamic response of the system was obtained when compared with the data collected by a strain gauge at low frequencies. The authors stated that the only limitation in applying this methodology to higher frequencies would be a data acquisition card with faster acquisition rate.

Matsuo et al. [100] developed a phase-compensated Mach-Zehnder sensor able to detect the AE activity generated by the attack of molten salt on pipes manufactured from 304 austenitic stainless steel grade. An equally split laser beam was transmitted by the reference and sensing arm, being the reference arm attached to a piezoelectric actuator. The actuator was driven by the low-pass filter feedback signal from the outputs, modifying the effective length of the reference path to keep the system in quadrature. The sensing length consisted of 10 turns of coated optical fibre, wound around a steel rod of 35 mm diameter and 1000 mm length. The system demonstrated temperature resistance up to 673 K, and was able to estimate the

location of the source of the AE events by monitoring the longitudinal and flexural components of the AE events released by the pipe during the salt molten attack.

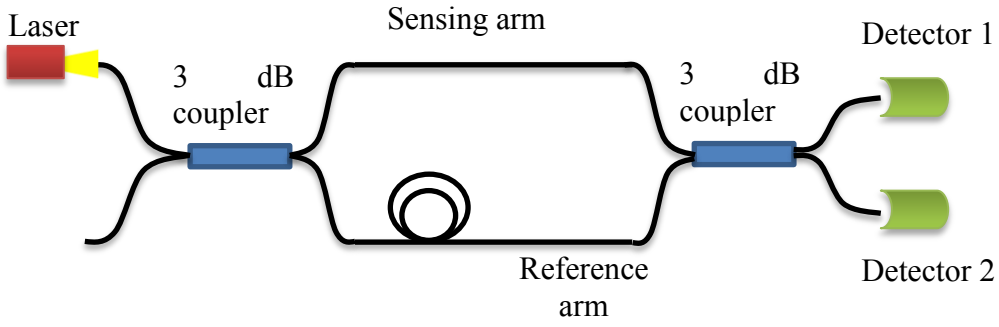


**Figure 4 Simplified setup of the Mach-Zehnder interferometer [97].**

### 2.4.2 Michelson Interferometer

The Michelson Interferometer is fairly similar to the Match-Zehnder interferometer. A beam is split in two by a 3 dB coupler, having again a reference arm and a sensing arm. Both arms, which do not have to be of the same length, are reflected back to the same 3dB coupler where the interference happens before being brought to a detector. As before, the signal can be analysed to understand the changes in the optical path of the sensing arm and thus, have a quantitative monitoring of the perturbation. An illustration of the setup is given as Figure 5.

This type of interferometer was very early reported as being able to detect damage in composites when embedded in composite materials [124], where the direct relationship between gauge length and amplitude of the signals was stated. Liu et al. [99] reported very early the suitability of the use of two lengths of single mode fibre of different dimensions to monitor AE events in a composite laminate by the application of the homodyne demodulation

technique. The system was tested in bi-directional Kevlar-epoxy and graphite-epoxy composite specimens. The peak shifting of the applied HeNe laser and changes in the polarisation state of the fibres were found to create phase noise and random fluctuations. The authors minimised these unwanted factors by securing the fibres and avoiding twists, abrupt bends or vibration.

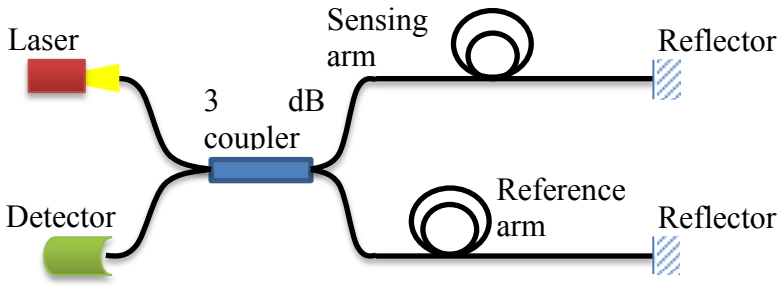


**Figure 5 Simplified setup of a Michelson interferometer [97].**

Changsen et al. [125] investigated the possibility of multiplexing several sensors in series. This overcame one of the limitations of the interferometric sensors when compared with spectrum-based sensors such as the FBGs. Two sensing lengths were fusion spliced in series and their signals recombined with a reference component of the sensor consisting of a Michelson low-coherence interferometer, formed by a 2×4 coupler and three reference arms. The system was able to detect damage in composite rods similarly to conventional methods. But still the temporal resolution and the addition of more sensors or located at a relative shorter distances was found to be problematic.

Zhang et al. [126] reported the utilisation of a Michelson interferometer-based sensor to detect the partial discharges on high-voltage cable system. The sensing arm was winded around a rubber elastomer, using Faraday rotating mirrors to cancel the unwanted effects on the signals created by the fluctuation in the polarisation states of the arms. The results obtained were

found to be similar to those of conventional techniques, obtaining a frequency response up to 150 kHz. Zargari et al. [61] used the same concept to monitor high voltage apparatus such as transformers, by winding the reference arm around the porcelain made insulation material, with typically very poor acoustic transmission properties. It allowed non-invasive monitoring combined with other desirable characteristics such as being chemically inert, non-conductive and immune to electromagnetic interferences. A similar technique based on wrapping the sensing arm of the Michelson interferometer has been successfully demonstrated by Matsuo et al. [127]. The AE signals from a cylindrical pipe protected against corrosion by an adhesive tape were successfully collected when several turns of the sensing arm were winded. Contrarily, the highly attenuative nature of this layer made impossible the detection of the very small out-of-plane displacements by conventional pressure piezoelectric sensors. The authors reported that the oozing of water of unprotected pipes was collected by the same technique. This phenomenon is normally difficult to pick up by conventional piezoelectric AE sensors due to the small velocity of the fluid. The optical sensors were reported to collect signals with amplitudes up to 10 times higher.

Gang T., Hu M. et al. [128] recently reported a sensor based on the Michelson interferometer to detect ultrasounds up to 300 kHz. The sensor consisted of two arms of different length below some centimetres which were coated at the end-faces to increase the reflectivity and etched to decrease the diameter increasing the sensitivity. An inverse relationship of the sensor length with the maximum detectable ultrasound wavelength was reported. This indicated that higher frequencies could be detected by decreasing the sensing region. The sensor was found to be highly directional due to it asymmetric geometry.

### 2.4.3 Fabry-Perot Interferometer

The optical Fabry-Perot interferometer consists of a simpler setup, where the interferometric pattern is created by a single optical fibre. The optical power is reflected or transmitted when differences in the reflection index are introduced, creating an interference pattern. The Fabry-Perot sensors are extrinsic when an air gap is introduced as described in Figure 6 [113, 114, 129]. The ends of the optical fibres at both sides of the cavity act as mirrors due to the different refraction index.

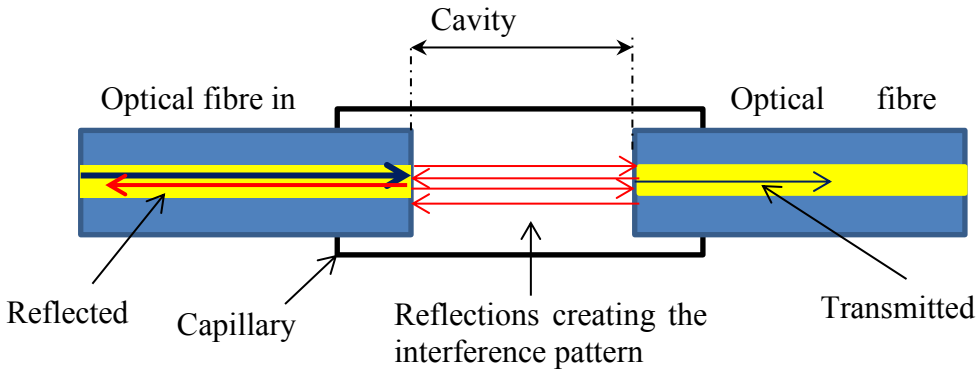


**Figure 6 Schema of a Fabry-Perot interferometric sensor [97].**

The Fabry-Perot is intrinsic when mirrors separated by a continuous segment of single-mode fibre are inserted [113, 114, 129]. The overall effect of the air gap or cavity is to produce an interference pattern which will be correlated to the changes of the cavity's length, acting as a sensing element. A low finesse Fabry–Perot interferometric sensor normally produces a sinusoidal output produced by low frequency changes in the cavity length such as changes in temperature or quasi-static loading conditions [102, 103, 130, 131]. These drifts in the phase should be compensated to keep the output at the highest sensitivity quadrature points as illustrated in Figure 7.

Alcoz et al. [129] reported on an embedded Fabry-Perot sensor to monitor ultrasonic waves, strain or temperature. The sensor was manufactured without cavity by fusion splice $TiO_2$-coated and uncoated optical fibres. The possibility of sensor multiplexing by digital signal analysis and a pulsed laser was pointed out. However, it was not discussed how to separate different stimulus such as temperature variations or strain when these happen simultaneously with ultrasonic waves.

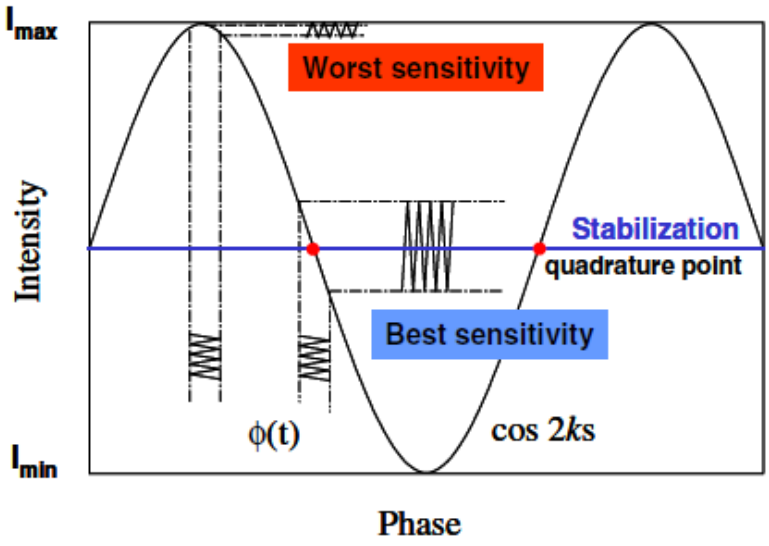


**Figure 7 Detail of the obtained response at different phases extracted from [130]. As it can be seen, fluctuations of the same magnitude give the best sensitivity at the quadrature points.**

Dorighi et al. [132] tracked the low frequency intensity variations to be used as a feedback loop to cancel the drift in the phase introduced by the temperature, and thus, to maintain the quadrature point. The sensor consisted of an intrinsic Fabry-Perot sensor with an internal mirror followed by a short length of fibre performing as sensing element and finished by coating the end face. The system was possible to be kept in quadrature, collecting simulated AE and ultrasonic signals in presence of induced low frequency strains.

Read et al. [40] were able to detect damage related AE signals in carbon fibre composite panels in frequencies close to 150 kHz. The sensors consisted of two single mode fibres with

an air gap in the middle, inserted into a metallic capillary. The second fibre was metallically coated to enhance the reflectivity. Several sensors were distributed on the panel both embedded and surface-mounted. The stabilisation of the output was achieved using the two lasers approach. The lasers had fix wavelengths separated by a quarter of the sensor's free spectral range, being the outputs filtered by matched FBG. The setup ensured modulation of at least one of the outputs. However, the authors located a small number of events with relatively low SNR of the signals. In addition, the sensors presented a directional response, with higher amplitudes with evens parallel to the cavity axis - 0° and 180°.

Dae-Hyun et al. [130] developed a phase-stabilised control system by using a single broadband laser in conjunction with a Fabry-Perot tunable filter. The cavity consisted of two cleaved single mode fibres with the second gold coated to enhance the reflectivity. The interrogation system was able to compensate the quasi-static low frequency cavity length changes by simultaneously shifting the unfiltered frequency through a feedback control actuated by a custom PCB control board. This kept the system at the quadrature point, where the higher SNR was achieved. The system was first demonstrated by monitoring pencil breaks, achieving similar response than a reference commercial piezoelectric sensor. Further tests included the successfully monitoring of the AE activity during a tensile test in a cross-ply composite panel.

Deng et al. [60] reported on an extrinsic Fabry-Perot interferometer able to detect partial discharges in power transformers. The cavity was formed by a single-mode optical fibre inserted in a cylindrical ferrule. The cavity was then sealed by a silica tilted diaphragm which reduced dramatically the second and further reflections enhancing the visibility of the interference fringes. The operation close to the quadrature point was achieved by a very precise bonding process combined with the appropriate design of the diaphragm thickness. By

controlling the cavity length and limiting the maximum deformation of the diaphragm, it was possible to work over the linear range of just half a peak. High frequency signals of 220 kHz belonging to partial discharges were detected. The sensor was of special interest due to low level of electrical conductivity (insulator), immunity to electromagnetic fields and multiplexing capabilities.

Zhao et al. [102] proposed a slightly different approach when stabilising the output. A Fabry-Perot cavity was manufactured by thermally fusing the two single-mode optical fibres to a silica-glass capillary. A double wavelength stabilisation technique named Dense Wavelength Division Multiplexer (DWDM) was successfully applied. The DWDM was able to generate two quadrature phase shifted output signals, which effectively demonstrated the ability to stabilise the response of the sensors. The authors developed a model to calculate the optimum wavelength of both outputs. Signals with frequencies up to 300 kHz were collected by the sensor when excited by a Hsu-Nielsen source used to simulate broadband AE signals.

## 2.5 Fibre Bragg Gratings

FBGs are all-fibre reflective optical devices, which can selectively discriminate certain wavelengths from the transmitted light spectrum propagating through a waveguide [133, 134]. The working principle is based on the creation of discontinuities in the reflexion index of the core which create successive constructive and destructive interference. The constructive and destructive interference results in the discrimination of certain wavelengths of the transmitted spectrum, which are partially reflected back. An illustration of the FBG operational principle is shown in Figure 8. One advantage of the FBG sensors is the narrow optical bandwidth required for their interrogation when just the reflected peaks are tracked. This enables the possibility of serial assembly and thus, multiplexing of the dedicated optical channel.

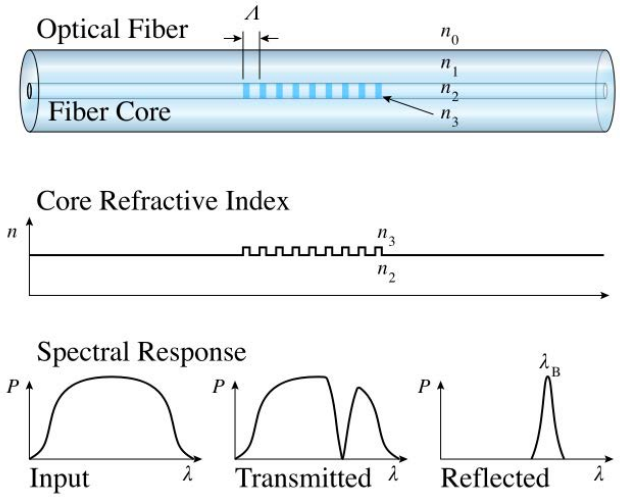


**Figure 8 Description of the construction and working principle of a uniform FBG (extracted from https://en.wikipedia.org/wiki/Fiber Bragg grating).**

The conventional manufacturing of FBG involves the exposure of a germanium-doped silica optical fibre core to ultraviolet (UV) light radiation (with wavelength around 240 nm), leading to a non-reversible change in the refractive index of the radiated region [135].

There are different techniques for the manufacturing of gratings, including their number, geometry and relative distance [136, 137]. FBGs can be classified in various types including conventional, chirped, tilted, phase shifted or long-period among others [134, 138].

The peak wavelength reflected in a conventional FBG depends on the relative distance between gratings, Λ, and thus, the applied strain. Any variation in the magnitude of Λ, will cause the peak wavelength to shift left or right, depending on whether the distance increases or decreases. Nonetheless, variations in other parameters such as temperature or pressure that influence the reflection index can also alter or influence the reading of the sensor [133]. Therefore, the change in temperature has to be compensated or taken into consideration since it introduces changes in the value of Λ, non-related to strain.

In order to quantitatively interrogate FBG sensors, the use of Optical Spectrum Analysers (OSAs) is required. When the nature of the phenomenon being monitored changes at such high frequencies as AE signals in SHM (normally from 50 kHz to 1 MHz) sampling frequencies above 2 MHz (Nyquist frequency) are required to overcome the aliasing or folding back phenomena [52]. This sampling rate is far beyond the capabilities of any commercial OSA, so alternative amplitude-based methodologies have been developed, technically named wavelength-intensity conversions.

Perez et al. [104] demonstrated a system able to interrogate FBG sensors directly through the use of two matched FBGs and a 1300 nm narrowband laser source with spectral width 30 nm. The first FBG was attached onto the testing plate. The reflected signal was split in two through the use of a 3 dB coupler. While one of the split outputs was fed directly to one port of the balanced photo-detector (PD), the second output was filtered by the other matched FBG before arriving to the other port of the PD. A wideband piezoelectric transducer was applied to sweep frequencies from 235 kHz to 2.15 MHz. The sensor was able to detect dynamic micro-strain ($\mu\varepsilon$) of the order of $10^{-2}$ and frequencies up to 1 MHz. However, some directionality was noticed since the sensor response appeared to be more sensitive during transversal excitation. A similar approach was adopted by Tsuda et al. [139] to detect the damage induced on a CFRP caused by an impact of 7.35 J. The system tracked the changes caused by the arriving Lamb waves generated by piezoelectric transducers.

Betz et al. [140, 141] successfully detected ultrasonic Lamb waves by employing a more simple interrogation methodology. The principle of the technique is based on the geometrical shape of the reflected spectrum of FBG gratings as shown in Figure 9. Figure 9 presents a quasi-linear region at both sides of the main peak from the 20% to 80% of the grating's maximum reflectivity.

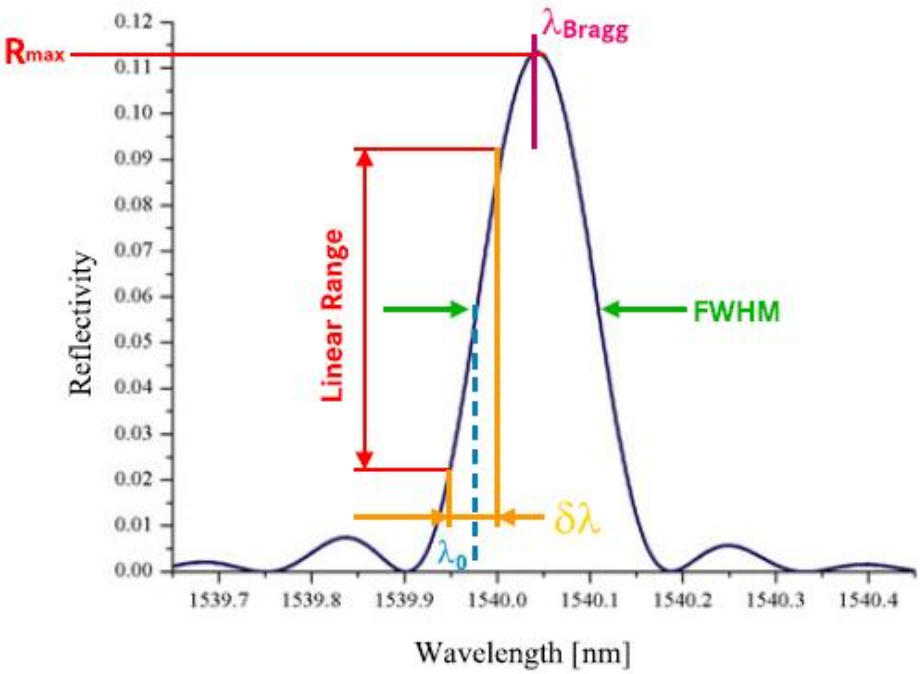


**Figure 9 Detail of the typical reflectivity curve of a FBT [140]. It shows the quasi-linear region, located from approximately 20% to the 80% of the grating's maximum reflectivity.**

Using a narrow-bandwidth laser diode tuned in the centre of one of these linear regions, the strain applied from the Lamb waves in the FBG can be translated directly into optical reflected power. Furthermore, the linear relation between strain and reflectivity was obtained enabling the possibility of converting the reading of a single PD into strain directly. Rosettes of FBGs were used to successfully locate two holes with 12 mm in diameter using this interrogation methodology together with genetic algorithms for damage location [142]. Once more it was found that there is directionality in the sensor's response. The lower steepness of linear region's slope combined with the quantitatively low energy reflected produced signal with low amplitudes, was related to the sensitivity of the system. To overcome this problem, phase-shifted FBG (PS-FBG) sensors have been reported of being able to detect signals, whilst achieving higher sensitivity than conventional FBGs [143, 144].

The major advantage of the PS-FBG sensors is related to the transmitted spectrum, where narrower peaks without the presence of side lobes can be obtained, as shown in Figure 10.

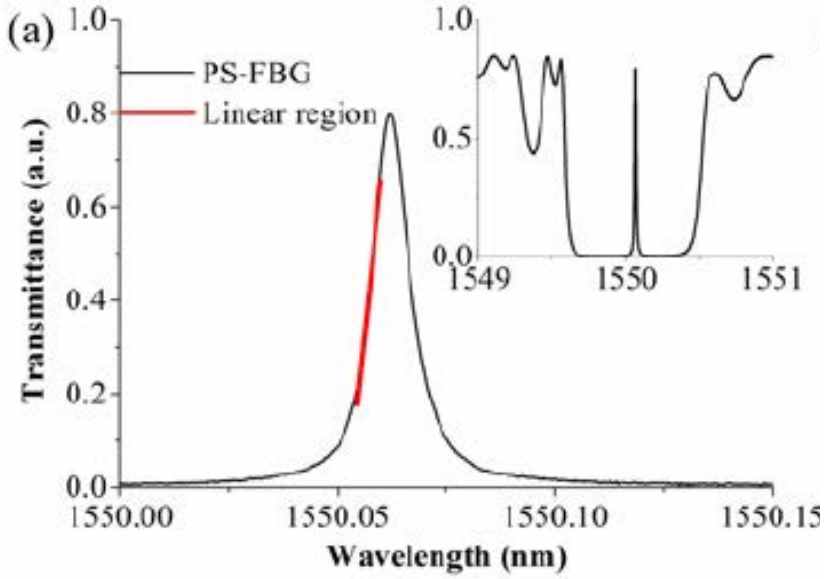


**Figure 10 Typical spectra obtained by sweeping a TLS on a PS-FBG [143], where the left linear region has been marked in red. The transmittance spectrum shows a very narrow peak at around 1550.4 nm. The figure in the top right is a magnification where the absence of side lobes can be clearly appreciated.**

This phenomenon was demonstrated by Wu and Okabe [143] through the use of a tunable laser source (TLS) and a balanced PD to compare the transmittance and reflectivity of a PS-FBG. While the balanced PD removed the DC-component and the common-mode noise doubling the AC component, the steepness of the Bragg-shift enabled signals to be amplified by a factor of about 180 when compared with a conventional FBG. The same authors reported a similar system based on a broadband light source which allowed multiplexing [144]. The broadband light source was "narrowed" by the use of an apodized FBT and a circulator. The interrogation technique consisted of two nearly identical PS-FBGs, one acting as filter and the second one exposed to the acoustic source. This configuration enabled the use of a simple PD in order to detect the AE signals. The setup based on a balanced PD was tested during tensile tests of different configurations of FRCP [145]. The results generated where comparable to

those produced by conventional piezoelectric sensing elements such as PZT. Up to six different types of signals were recorded, with each of them related to different observed types of damage, such as transverse crack in 45°, matrix crack in 90°, transverse crack in 90°, delamination or final fracture.

The FBG sensors have been demonstrated to be applicable for SHM in composite materials, using different techniques than AE. Okabe et al. [146] presented a system able to detect cracks in FRPC produced by quasi-static tensile load. The sensors were embedded in the boundary between the longitudinal and transversal layers in an eight-ply laminate (2 longitudinal - 4 transversal -2 longitudinal). The changes on the spectrum were recorded using an OSA. The sensor showed sensitivity to the induced transverse cracks, and thus, to the non-uniform strain distribution. However, the system was only able to detect the transverse cracks just around the sensor, and hence, was valid just to monitor points were cracks are expected. The same methodology was reported based on the use of a small diameter FBG (SD-FBG) [147, 148]. The main advantage was the reduction of the sensor's diameter from 125 to 40 μm. The smaller diameter decreased the risk of reinforcement distortion, and hence reduced the potential deterioration of the mechanical properties when the sensor is embedded into the composite material. The embedded SD-FBGs were found to be able to detect delamination in a FRCP when the wavelength of the propagating modes was at least seven times longer than the sensor. A new wave mode was detected when delamination occurred, with amplitude linked to the severity of the defect. Okabe et al. [149] demonstrated the application of the SD-FBG for monitoring the de-bonding mechanism in FRPC bonded structures. The received signals were investigated via wavelet transform analysis. It was possible to track the evolution of the de-bonding process as well as to define a damage index.

Finally, the development of a commercial and fully integrated FBG system was presented by Mendoza et al. [150]. The system, with dimensions of 2x2x4 inches, used the two-wave mixing interferometry technique [151] and interrogated up to 4 sensors. The system was demonstrated to be able to monitor signals with frequencies up to 500 kHz.

The FBG sensors have been extensively reported as suitable for embedment in FRPC materials [148, 152-158]. Ling et al. [155] used embedded FBG for monitoring the natural frequencies of a clamped laminate. Guemes and Menendez [152] examined the possibility of using the embedded sensor not just for strain monitoring but to provide information about the residual stresses building up during the composite curing cycle. It was experimentally found and theoretically demonstrated that transverse load on the sensor causes the reflected spectrum to be split in two peaks. The bandwidth between these peaks could be used to analyse the traverse strain. This methodology was applied to monitor the build-up of stress during the curing cycle of a composite material, and then released when a hole was drilled in the vicinity of the embedded sensors. Botsis et al. [153] reported on the same topic, by investigating the feasibility of embedded FBGs as a means of understanding residual and internal strain distribution when external loads are applied or during crack propagation. While the results were promising, the localised nature of the sensor and unwanted effect of the undetectable non-uniform strain were raised as potential issues. Fan and Kahirizi [154] investigated the effects of the embedding on the sensors performance due to radial stress. An orthogonal array of FBGs was embedded in a graphite/epoxy laminate. Further testing demonstrated the survivability of such a sensor when embedded. Positive or negative strain was monitored when the Poisson modulus of the fibre was lower or higher respectively than the one of the laminate. Takeda et al. [148] researched on the applicability of novel small diameter FBG sensors. The application of a custom-built signal interrogation system enabled

the sensor to detect a broad spectrum of acoustic waves. The sensing of Lamb waves made possible the damage monitoring of the host laminates due to delamination and de-bonding. However, the sensor presented a strong directionality, being the amplitude of collected signal function of the wave propagation direction. Lam et al. [157] proposed a similar methodology to monitor delamination in composite materials, by applying embedded FBGs for the detection of Lamb waves. Frieden et al. [158] applied embedded FBGs for high speed strain monitoring up to 100 kHz with a background noise of 2 με, using a custom-built interrogation unit. The system was limited by the maximum acquisition rate of the Digital Acquisition System (DAS) and photodiodes. De Oliveira et al. [156] proposed a hybrid solution consisting of embedded FBG and a low-finesse Fabry-Perot interferometer to sense strain and AE. Damage monitoring was performed using the FBG for measuring dynamic strain. The interferometer was responsible for the evaluation of the transient effects in AE due to the higher sensitivity of this instrument. The collected data required analysis, so unsupervised classification methods such as neural networks could be applied.

## 2.6 Intensity-based optical sensors: the 2x2 optical coupler as Acoustic Emission sensor (FOAES)

This section is dedicated on the discussion of the use of a 2x2 power splitter as AE sensor. The manufacturing methods with special emphasis on the fibre bi-conical tapered (FBT) will be explained A theoretical analysis of the 2x2 optical waveguide and 2x2 fused couplers is going to be discussed. The power transmission mechanism of the 2x2 coupler will be assessed, detailing the parameters used for its characterisation. Finally, the use of the 2x2 coupler as FOAES will be presented in detail.

### 2.6.1 Optical couplers manufacturing

Optical fibre fused couplers are passive devices which are extensively used for power splitting, multiplexing or filtering of optical systems [135, 159-161]. The working principle is based on the propagation of the guide modal field in the fibre far beyond the core-cladding interface [135, 162]. Through the progressive lateral and parallel approach of two or more optical fibres there will be a separation small enough for the fibre cores to overlap their modal fields. The modal field overlap enables mutual interaction and power transmission, which can be used for the manufacturing all-fibre passive components. Figure 11 shows an example of a 2x2 fused directional coupler, where the claddings of two optical fibres have been partially fused along a distance "L".

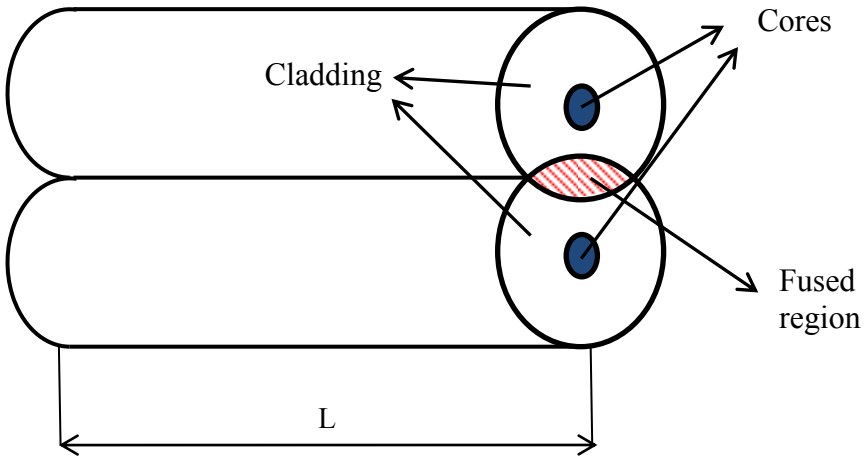


**Figure 11 Schema of a 2x2 fused coupler [163].**

The present study has focused on the use of a 2x2 fused coupler as a directional power splitter. The main manufacturing methods of this component are discussed next with more emphasis on the fibre bi-conical tapered (FBT) technique. In addition, a theoretical analysis of the 2x2 optical waveguide and 2x2 fused couplers is presented. For the latter, the power

transmission mechanism and some models for predicting the behaviour of the component are explained. Finally, descriptions of the parameters used for the fibre couplers characterisation are presented.

The manufacturing of an optical 2x2 coupler involves the progressive reduction of the core-to-core distance, enabling eventually the propagation of the modal fields far beyond the core-cladding boundary. The coupling between these modes traveling through the cladding into the core of the second optical fibre when the distance is small enough creates a coupling effect and allows power to be transferred. By determining the distance between both cores it is possible to evaluate how much power is being transmitted from one fibre to the other. In order to achieve reduction in the core-to-core distance different methodologies have been developed including (i) fibre etching [164, 165]; (ii) fibre polishing [166, 167] and (iii) fibre fusion [168-170].

In the fibre etching technique, two stripped fibres are positioned together and strained while immersed in Hydrofluoric acid solution [164, 165]. A laser is used to emit light in one of the fibres, with both outputs being monitored by using suitable PD sensors. The acid dissolves progressively the cladding decreasing the distance from core to core until eventually power coupling has occurred. The continuous monitoring of the output power of both fibres permits the completion of this process as soon as the desirable coupling ratio has been achieved.

The fibre polishing method is based on the polishing of the cladding of stripped optical fibres, in such a way that allows a flat surface to be obtained as shown in Figure 12 [171, 172]. The polishing process is controlled by emitting light using a suitable laser from one end of the optical fibre and monitoring the fluctuations of the output power at the other end with a PD. The coupling is achieved by bonding or fusing together the flat faces of the two polished

fibres. The power coupling ratio can be adjusted by introducing an offset between the symmetry axes of both optical fibres, as shown in Figure 12.

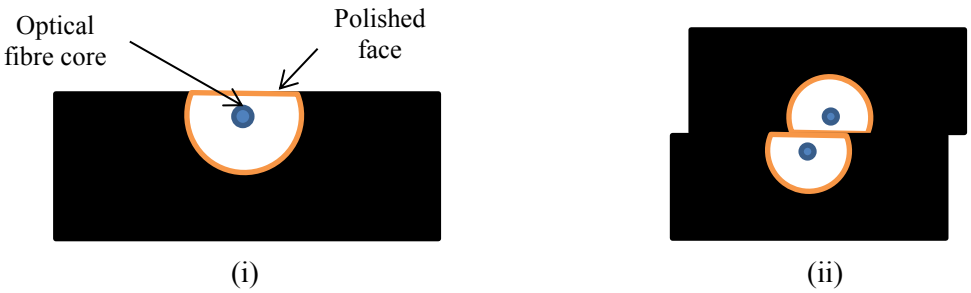


**Figure 12 Detail of the manufacturing and assembly of a polished 2x2 fibre coupler; (i) shows a polished optical fibre ready for being assembled; and Figure 12 (ii) details how the offset introduced during the assembly can modified the power coupling ratio.**

Finally, the fibre fusion or FBT process involves the fusion of stripped and subsequently twisted together optical fibres using gradual straining under appropriate high temperature conditions. The FBT process is by far the most common process for manufacturing couplers. The required temperature conditions are normally achieved using a localised hydrogen flame. The temperature profile of the flame can be adjusted either through (i) the change of the torch-fibre relative height and/or the geometry of the torch; (ii) the modification of the hydrogen flow rate; or (iii) the relative and continuous lateral or brushing movement of the torch along the tapering length of the fibres being fused. The strain is achieved by securing the fibres in two holding positions which are precisely and simultaneously moved in opposite directions using stepper motors. The progressive strain of the fibres is partly converted in lateral force through the introduction of two single twists, each one located at one extreme of the stripped lengths of the fibres. The lateral force enables the fusion of both fibres when required temperature is attained.

The hydrogen torch has two or three degrees of freedom: X-axis or forward-backward movement, Y-axis or brush movement and Z-axis or torch height. The X-axis allows the positioning of the torch above the fibres at the beginning of the process, Z-axis movement enables the adjustment of the distance between the fibres and torch and Y-axis corresponding to the brushing movement allows the manufacturing of a more precise tapered region through better and more uniform distribution of the temperature along the tapered length [173]. While the Z-axis and X-axis movements are common in all the FBT process, the Y-axis or brushing is not available in every machine. The entire FBT process is controlled in real time, emitting light with a suitable laser in one of the optical fibres and monitoring the variations in both outputs using PDs. This permits the stopping of the process when the desired coupling ratio has been achieved.

The FBT process allows the manufacturing of 2x2 optical power couplers with low losses and different power-splitting ratios [174-176]. The quality of the end-product depends on the control and stability of certain key manufacturing parameters, including: (i) quality and cleanliness of the stripped area of the fibres; (ii) knot-to-knot distance and its symmetry with reference to the torch position; (iii) the temperature applied on the tapering length; (iv) pulling speed, or in other words straining rate; (v) pre-heating, pre-tension and post-draw of the tapered length; and (iv) encapsulation/packaging process.

The heat/temperature and the pulling speed in combination with the brushing movement (if it is possible) determine the obtained tapered profile, and subsequently the performance of the coupler. An unbalanced combination of heat/temperature and pulling speed may cause the fibres to slip from the holding positions or to be broken (i.e. the heat generated is not enough for the requested straining rate), or to flow vertically by the effect of gravity (i.e. the heat

generated is much more than the required for the straining rate, so the optical fibres are being melted rather than strained and fused together).

If the temperature profile remains constant, the length of the fibres being melted will be constant too. Hence, the process can be simplified as fixed length of infinitesimal sections of fibre. As the fibres are strained some material will be constantly removed from the fusion area. Since there is a conservation of the mass this is translated in the progressive reduction of the diameters of fibres remaining inside the fusion area. This results in symmetrical geometry with a progressive exponential decay of the diameter and the minimum dimension being at the centre [177, 178]. This can be generally expressed mathematically using Equation (1) [159].

$$r(z) = r_0 \cdot e^{\frac{z}{L_0}} \quad \textbf{(1)}$$

### 2.6.2 2x2 directional coupler: coupling theory mechanism

The directional coupler is one of the most important components in an optical fibre system. Directional couplers effectively work as a power beam splitter. The theory explaining the coupling mechanisms in optical waveguides was firstly developed by Marcuse [179, 180] and Snyder [181] among others working in this field at the beginning of the 1970s. Their theory was refined further after the introduction of the non-orthogonal coupled theory [182].

In the particular case of the 2x2 directional coupler, the coupled system can be analysed as a structure formed by a single waveguide with two cores [135]. This composite structure supports only two modes with different propagation constants [135, 164, 183, 184]: the fundamental symmetric or even mode, and the anti-symmetric or odd mode. When the light

source is coupled in one of the waveguide a combination of these symmetric and anti-symmetric modes - also known as supermodes- is excited as it is seen in Figure 13.

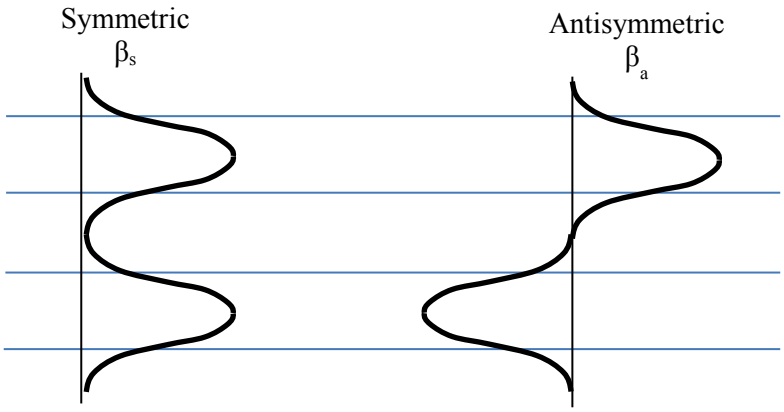


**Figure 13 Detail of the symmetric and anti-symmetric modes excited in a single-mode 2x2 optical coupler , being $\beta_s$ and $\beta_a$ their respective propagation constant [135].**

The difference in the propagation constant will create a phase difference as both modes propagate along the coupled length. This will result in a periodic power transmission or beating between both fibres. When the phase difference is $\pi+2\pi k$ (k=0, 1, …) the superposition of both super-modes will create the cancellation of the signal in the input fibre with all the power transmitted to the parallel fibre. At that point the system is defined as "coupled" and is directly related to the distance needed for the full power transfer occurring at the coupling length "$L_c$". Subsequently, when the phase difference is $2\pi n$ (with n=0, 1, …) and thus the modes have propagated over a distance of $2nL_c$ (with n=0, 1, …), all power will be coupled back into the input fibre and cancelled in the parallel. Additionally, any phase difference between the both described extreme scenarios will split the power between both outputs at different ratios.

In the general case of a composite waveguide composed of two non-identical fibres, the power transfer can be described by the following Equations (2) to (5) [135, 162]:

$$\frac{P_1(z)}{P_1(0)} = 1 - \frac{k^2}{\gamma^2}\sin^2\gamma z \quad \textbf{(2)}$$

$$\frac{P_2(z)}{P_1(0)} = \frac{k^2}{\gamma^2}\sin^2\gamma z \quad \textbf{(3)}$$

$$\gamma^2 = k^2 + \frac{1}{4}(\Delta\beta)^2 \quad \textbf{(4)}$$

$$\Delta\beta = \beta_1 - \beta_2 \quad \textbf{(5)}$$

where $z$ is the coupling length, $P_1(0)$ is the input power inserted into the optical fibre 1 at $z = 0$, $P_1(z)$ and $P_2(z)$ is the output power in optical fibre 1 and 2 respectively at $z$ coupling length, $k$ is the coupling coefficient (measure the effective interaction between both optical fibre in terms of power transmission or in other words, the strength of the coupling), and $\beta_1$ and $\beta_2$ are the propagation constant of both fibres.

In the particular case of identical fibres ($\beta_1 = \beta_2 = \beta$) and assuming no power losses in the coupler, the power coupled in each fibre can be described by Equations (6) and (7). In addition, the relationship between the propagation constant of both symmetric and anti-symmetric modes, the coupling coefficient and the propagation constant of the fibres are shown in Equations (9) and (10) [135, 162].

$$P_1(0) = P_1(z) + P_2(z) \quad \textbf{(6)}$$

$$P_1(z) = P_1(0) \cdot cos^2 kz \quad \textbf{(7)}$$

$$P_2(z) = P_1(0) \cdot sin^2 kz \tag{8}$$

$$k = \left[\frac{\beta_s - \beta_a}{2}\right] \tag{9}$$

$$\beta_{s,a} = \beta \pm k \tag{10}$$

The selection of the parameters "$k$" and "$z$" permits any coupling ratio to be achieved, as shown in Figure 14. The fused length "$z$" depends on the manufacturing process and can be controlled. The parameter $k$ is a function of the fibre, geometry of the volume where the coupling takes place, the applied laser's wavelength and the distance between the cores as it will be explained.

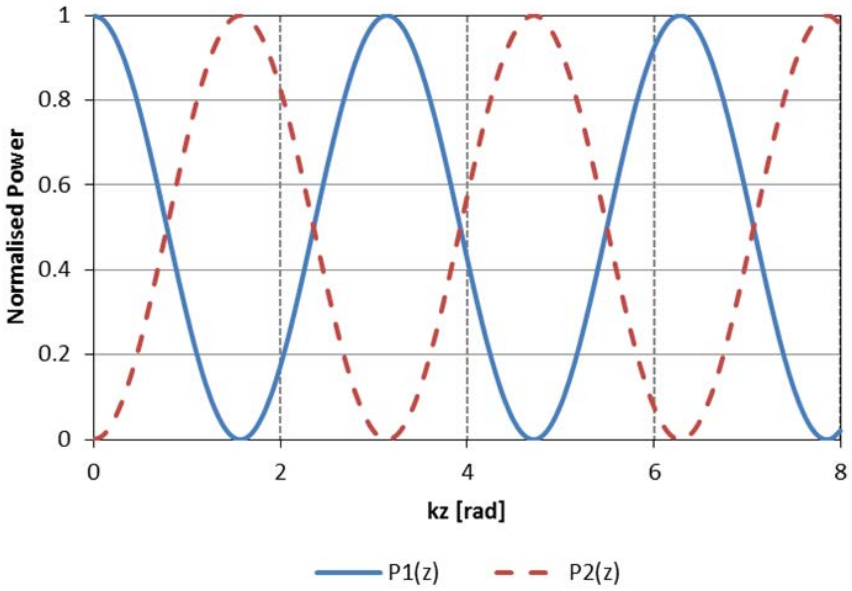


**Figure 14 Ideal normalised power fluctuation along the coupler length z, for a coupler manufactured by two identical fibres, where P1(z) and P2(z) represent the power coupled in each optical fibre which form the composite waveguide [135].**

### 2.6.3 FBT 2x2 coupler

There is a consensus classifying fused couplers into two main categories: the weakly fused and the strongly fused. This classification is based on the level of fusion between the fibres where the power transfer occurs [173, 185, 186]. Thus, according to this criterion, weak fused couplers will comprise of two parallel touching cylinders whilst strong fused couplers will comprise of a nearly rectangular waveguide containing both cores and a single cladding. The theory of power coupling through evanescent fields, although valid for modelling couplers manufactured using the polishing or etching methodologies (they can be considered weakly fused), breaks down when the coupler is manufactured using the FBT process [173, 183, 185, 186]. Since the fibre optic AE sensor requires a reduction in the cross-section of the tapered region to maximise its sensitivity [93], only the basic theory for the strongly fused couplers will be introduced.

The manufacturing of strong fused single-mode couplers creates progressively a notable reduction in the cross-section in the tapered region. This cross-section reduction introduces changes in the angle of incidence in the boundary between the core and cladding as well as a progressive reduction of the core diameter. There is a point, also known as the transition point, at which the transmitted mode leaks from the core and starts being guided by the waveguide cladding-air. After this transition point, the new waveguide will consist of a core comprising of the full tapered section (which will have effectively a higher area than the un-tapered core) with air acting as cladding. This will increase dimensionless parameter know as V-number, which is of special interest when characterising step-index optical fibres as it can be interpreted as a normalised optical frequency. The increase of this will make the tapered region of the optical fibre to behave as a multi-mode, as shown in Figure 15. The calculation of the V-number is given by (13).

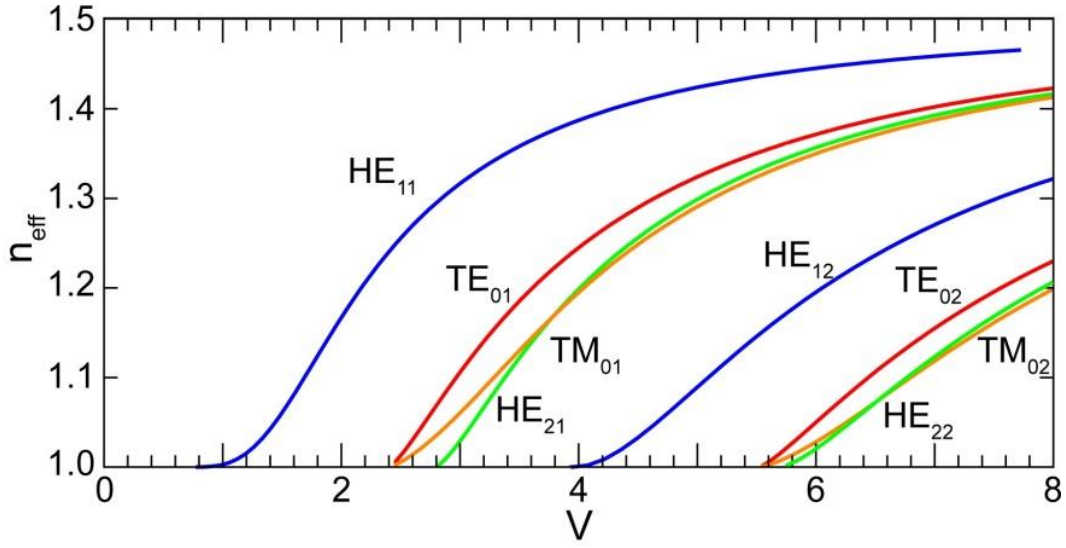


**Figure 15 Graph showing an example of the different modes propagating across a single mode optical fibre [187]. The x-axis shows the V-number and the y-axis show the effective reflexion index, which provide the propagation constant of each mode for a given wave vector (*β/k*).**

Once the transition point has been passed, the section will continue decreasing until the waist or central point of the tapered length is achieved, i.e. where there is an inflexion point in the curvature. After the taper waist the section will start a progressive increase until the geometrical conditions are suitable for having another transition point. In this last transition point is where the power is coupled back into the cores of the fibres, and just the lower order mode is transmitted (and hence, they behave again as single-mode). Ideally and as explained before, the tapered length should be symmetrical with respect to the waist or central point.

The coupling mechanisms taking place in the tapered length can be explained by the beating and overlapping of the different cladding modes [188]. If the tapering angle is small enough and thus it can be ensured that there are no power losses in the fundamental mode along the tapered length, then the tapering process is considered to be adiabatic.

Payne, Hussey and Yataki [183] simplified the fused tapered region to a rectangle of length "2a" and height "a" composed by the cladding of the fibres and thus, neglecting the existence of the cores. This simplification, although it introduced a small error by neglecting the

existence of the cores, created a very straightforward model which enabled the prediction of the power coupled ratio *(P),* coupling coefficient *(c)* and critical angle *($\alpha_c$)* when the $LP_{01}$ mode is detached from the core, as shown in Equations (11) to (14),

$$P = P_0 \cdot sin^2(cL) \tag{11}$$

$$c = \frac{3\pi\lambda}{32 \cdot n_2 \cdot a^2} \cdot \frac{1}{(1 + 1/V)^2} \tag{12}$$

$$\mathrm{V} = \frac{2\pi}{\lambda} \cdot \mathrm{a} \cdot \mathrm{NA} = \frac{2\pi}{\lambda} \cdot \mathrm{a} \cdot \sqrt{\mathrm{n}_{\mathrm{core}}^2 - \mathrm{n}_{\mathrm{cladding}}^2} \tag{13}$$

$$\alpha_c = \frac{\beta^2 - n_2^2 \cdot k^2}{2n_2.(n_1^2 - n_2^2)^{1/2} \cdot c \cdot k^2} \tag{14}$$

where $\lambda$ is the wavelength in μm , $L$ is the tapering length in m, $a$ is the radius of the core in m, $\beta$ is the propagation constant in $m^{-1}$, $k$ is the wave vector in $m^{-1}$, $V$ is the V-number (dimensionless), and $n_1$ and $n_2$ are the reflexion indexes of the core and cladding respectively (dimensionless). However, the influence of the polarisation is not included in this model, and therefore it cannot explain the modulation of the output power introduced by the differences in the beating period for different polarisation states. In addition and with higher importance when the coupler is less strongly fused, neglecting the effect of the cores in the coupling process can introduce important errors. This was investigated by the application of the simple effective-index method [189] simulating the tapered region and cores to rectangular waveguides.

Lacroix, Gonthier and Bures [190] developed a model based in the beating of the super-modes applying a numerical method known as field correction method. The methodology allowed the introduction of corrections to the polarisation modal propagation constants and a realistic geometrical description of the tapering length. While the theoretical results had a very good agreement with the experimental in strongly fused couplers, there were discrepancies matching the results with slightly fused couplers according to the elongation of the tapering length increase.

Chauduri, Pal and Shenoy [177, 178] introduced the effect of the cores, polarisation and geometrical parameters as shape or degree of fusion, and proposed a model using a modification of the perturbation method [191] for rectangular waveguides. They reported a high degree of agreement between the theoretical and experimental data.

### 2.6.4 Characterisation of the FBT 2x2 coupler

The optical characterisation of the 2x2 coupler is based in the efficiency of the power conversion and power splitting ratio between the different ports. The most common parameters given by the manufactures are the exceed loss, the splitting ratio, the directivity and the insertion losses [192]. For the definition of all these parameters, the nomenclature of the ports shown in Figure 16 will be applied.


**Figure 16 Draw and port definition of a 2x2 coupler [192].**

Exceed loss

This parameter measures the ratio of output power to input power. It is normally expressed in dB, for a 2x2 single mode coupler it is calculated as detailed in Equation (15). A typical specification value of this parameter for a 2x2 coupler and 633 nm of wavelength is from -0.6 to -0.7 dB [192].

$$Exceed\ Loss\ (dB) = -10 \cdot log\left(\frac{P_3(mW) + P_4(mW)}{P_1(mW)}\right) \quad \textbf{(15)}$$

Splitting ratio

The splitting ratio characterises how the coupler distribute the power in its output ports. It is normally given in percentage, although it can be calculated in decibels. For a 2x2 coupler it is calculated as detailed in Equation (16) [135].

$$S.R.(\%) = \left(\frac{P_i(mW)}{P_3(mW) + P_4(mW)}\right) \quad ,with\ i = 2\ or\ 3 \quad \textbf{(16)}$$

Directivity

This parameter expresses the fraction of power which is coupled back to an input port instead of being transmitted through the outputs. It is normally expressed in dB and measured by applying the following Equation 17 [135, 192].

$$Directivity\ (dB) = 10 \cdot log\left(\frac{P_1(mW)}{P_2(mW}\right) \quad \textbf{(17)}$$

Insertion losses

This parameter represents in decibels (dB) the power transfer from the input port to any of the output ports. For a 2x2 coupler, two values are calculated as detailed in Equation (18) and (19) [135, 192].

$$I.L._{1\ to\ 3}\,(dB) = 10 \cdot log\left(\frac{P_1(mW)}{P_3\,(mW)}\right) \quad \textbf{(18)}$$

$$I.L._{1\ to\ 4}\,(dB) = 10 \cdot log\left(\frac{P_1(mW)}{P_4\,(mW)}\right) \quad \textbf{(19)}$$

### 2.6.5 Use of the FOAES as Acoustic Emission sensor

The acoustic sensitivity of the 2x2 couplers was discussed during the very early development of the optical technology.

Sheen and Cole [193] constructed a coupler via two etched and mutually twisted fibres which presented fluctuations in the output power were exposed to acoustic fields. Doyle et al. [194] investigated the viability of using both embedding and surface mounted optical couplers as AE transducer. A sixteen layers ±45 degrees glass fibre-epoxy laminate was used as propagation media in conjunction with a piezoelectric pulser to simulate AE signatures. The surface mounted couplers were fixed in a V-groove in a glass rod of 4 mm of diameter and length 50 mm. The embedded sensor was secured into a borosilicate glass capillary of length 50 mm, with internal diameter and wall thickness of 1,000 and 250 μm respectively. The ends of the capillary were sealed with epoxy resin. Experiments were conducted by comparing the response of these sensors with a piezoelectric PZT AE sensor, using two lasers operating at 633 nm and 670 nm. The levels of SNR were assessed together with directionality (response

at angles 0°, 45° and 90°) and attenuation of the signal amplitude with increasing distance from the AE source. It was found that the couplers presented lower SNR and different harmonic structure when compared with the conventional piezoelectric sensor. In addition, they showed longer duration (time required for an acoustic signal to reduce the amplitude below the threshold) than the piezoelectric sensors but similar attenuation ratio when the AE source was moved further from the acquisition area. Finally, some directionality was identified. This directionality was attributed to the anisotropy of the microstructure of the composite material used in the experiments.

The response of the FBT coupler against elastic waves was reported by R Chen et al. [93] to follow the mathematical shown as Equation (20), which identifies the factors in the modulation of the coupling ratio as; (i) the input power "$P_0$"; (ii) the coupling ratio of the coupler or how the input power is divided in the outputs, introduced by the factor "$C$" ; (iii) the amplitude of the strain introduced by the factor "$\varepsilon_0$", so external factors such as the coupling efficiency of the sensor with the media should be considered; (iv) the length of the waist of the sensor introduced by the factor "$l$", where the coupling between both fibres occurs; and (v) the nature of the acoustic wave such as frequency and wavelength introduced by the terms "$f$" and "$\Lambda$".

$$\Delta P(l,t) = 2 \cdot P_0 \cdot \bar{C} \cdot \varepsilon_0 \cdot l \cdot \left[\frac{\sin\left(\frac{\pi l}{\Lambda}\right)}{\left(\frac{\pi l}{\Lambda}\right)}\right] \cdot \cos\left(\frac{\pi l}{\Lambda} - 2\pi f t\right) \qquad \textbf{(20)}$$

The waist of the sensor, when its diameter is reduced substantially in the tapering process, performs as a strain concentrator and thus the response of a FBT coupler would be magnified. This can be potentially exploited with the property of the FBT coupling process [195, 196] of

having near periodical variability in the coupling ratio with the coupling length as it can be seen in Figure 17. This means that the same coupling ratio can be achieved for longer coupling lengths, and consequently with smaller cross-section in the waist of the tapered coupler.

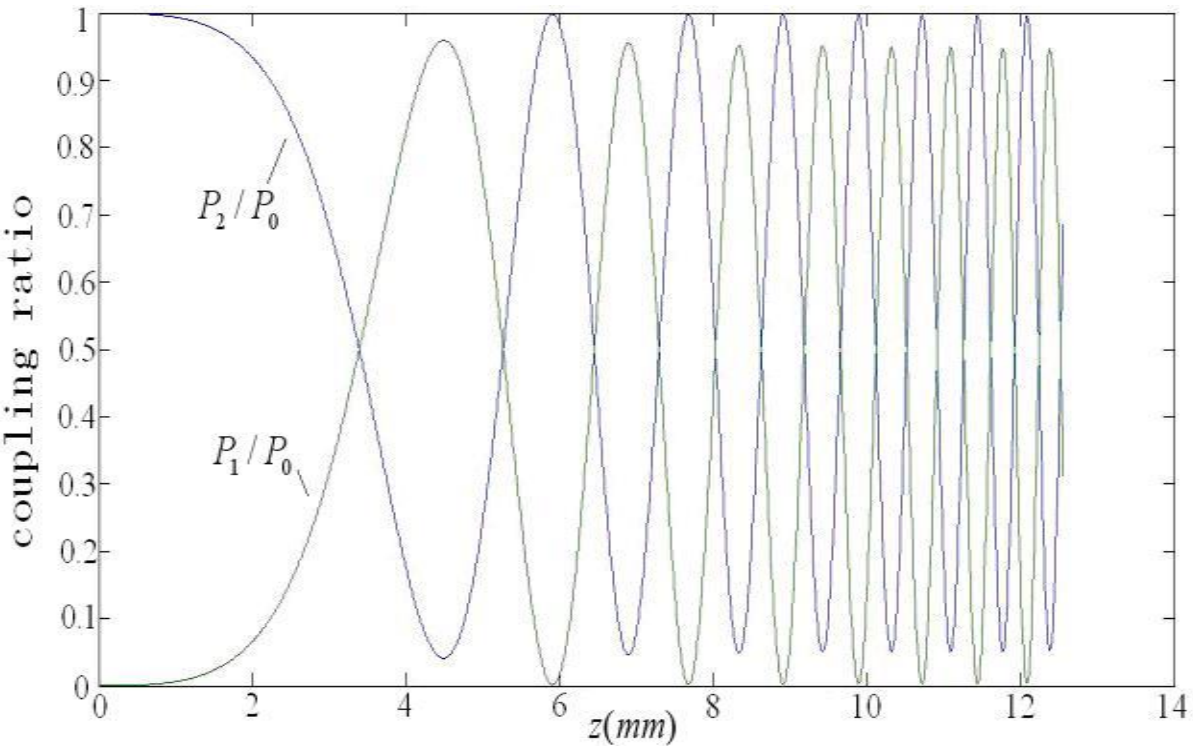


**Figure 17 Periodical change of output power with the coupling length z, where $P_0$ and $P_1/P_2$ are respectively the input and output power (image taken from [195])**

Chen et al. [48] employed two linearly multiplexed FOAES to perform linear location on an aluminium plate. The FOAES where packaged on a silica V-groove of length 20 mm and squared cross-section of 2mm. The sensors were secured by bonding them using UV-Epoxy cured adhesive in one side, and silicone rubber adhesive in the other in such a way than the waist of the sensor was suspended in the air. A pig-tailed laser diode of 635 nm wavelength and power of 5mW was used to interrogate both sensors. The AE source was located within ± 5 mm during the performed experiments.

## 2.7 Summary of Literature Review

The use of FRPC materials in advance application has been increasing over the recent years due to their unique weight to mechanical properties ratio, particularly in transportation and renewable energy related applications. Due to the difficulties in assessing damage in such complex and mechanically anisotropic structures SHM is of paramount important. Thus, the development of suitable NDT techniques which are capable of minimising uncertainty about the structural integrity of these materials has been under constant investigation. Among the NDT techniques considered, AE has been pointed out as one of the most interesting techniques due to: (i) its ability to be used online, hence reducing the down-time and unavailability of assets by increasing the operational periods between maintenance intervals required, (ii) the ability to detect, locate and characterise the severity and type of evolving defects ; (iii) its fast deployment potential and ability to cover broad areas.

AE has been traditionally performed using piezoelectric transducers. These transducers are very well characterised and can be designed to be wideband or resonant at particular frequency bands. Piezoelectric sensors have several disadvantages: (i) their relatively bulky size make them poorly suitable for applications in confined spaces or for being embedded in composite materials; (ii) strong electromagnetic fields will introduce high levels of electric noise in the interrogation system, reducing dramatically the SNR; (iii) they are not inherently intrinsically safe for applications in explosive atmospheres unless special designs are employed; (iv) require several amplification steps, and therefore, the full system including cables and amplifiers can be heavy and bulky. FOS have been thoroughly investigated as alternatives to overcome the described problems. They are very small and light when compared with piezoelectric transducers, intrinsically safe as they use transmitted light for interrogating the structural condition, and can be monitored from far longer distances due to

the very low attenuation of the of the light signals within the optical fibres. In addition, their small diameter of around 250 μm enables their embedment into composite materials.

There are three main categories of FOS performing AE: FBG, interferometers and non-interferometric intensity based sensors. While the first two categories have been extensively reported in the literature, the non-interferometric intensity based sensors have been less developed. In particular, the AE sensor based in the optical coupler has been briefly reported by several groups over the last 15 years, but its manufacturing process and influence of the manufacturing parameters in the sensor's response is still not very well understood. Therefore, the present research study has attempted to increase the knowledge with regards to the manufacturing, packaging, embedding and response of such sensors.

# CHAPTER 3

## Materials and Methods

# 3 Materials and Methods

## 3.1 Introduction

This chapter describes all the materials, tools, software and hardware, and methodologies developed during this research. It is structured in four different parts including: (i) optical fibres and auxiliary equipment; (ii) FOAES manufacturing and packaging; (iii) FOAES characterisation; and (iv) direct comparison between FOAES and conventional AE sensors.

## 3.2 Optical Fibres and auxiliary equipment

Two different types of optical fibres, SM600 and 630HP (Thorlabs, USA), were used for manufacturing and interrogating the FOAES. The criteria for employing these specific two types of optical fibres were as follows: (i) broadly available off-the-shelf optical fibres; (ii) SM600 has been previously used for manufacturing FOAES [97], and has been the optical fibre type used in the majority of optical fibre patches and connections; (iii) they have a step-index reflexion index profile; (iv) they have a single mode with operating frequency containing the desired wavelength of 633 nm; and (v) they employ an acrylate coating for optimised stripping process. The main characteristics of the two optical fibre types considered in the project are summarised in Table 1.

**Table 1 Characteristics of the SM600 and 630HP optical fibres**

| | Core Diameter | Cladding Diameter | Operating Wavelength | Numerical aperture | Core/Clading concentricity | Attenuation (dB/Km)) |
|---|---|---|---|---|---|---|
| **SM600** | 4.3 - 4.6 μm | 125 ± 1.0 μm | 633-780 nm | 0.10 - 0.14 | <1 .0 μm | ≤15 |
| **630HP** | 3.5 μm | 125 ± 1.5 μm | 600-770 nm | 0.13 | <3.5 μm | ≤12 (at 630nm) |

Optical fibres stripping and cleaving

As described in Table 1, both optical fibre types consist of two internal concentric cylinders of glass known as the core and cladding, and an outermost external layer of thermoplastic acrylate coating. The function of acrylate layer is mainly to add mechanical strength and to protect the cladding and core from damage. This coating has to be completely removed from the area where the FOAES is manufactured or the fibres are joined together. The process of removing the acrylate coating is known as fibre stripping. If there are residues of the coating left over after the stripping process, they will burn creating ashes. These ashes will remain as inclusions which will cause perturbations in the transmitted signal and increase losses. In this project the stripping process was performed by using a Miller FO 103-D-250 optical stripper (Rypley, USA). The remaining acrylate was removed through the use of wet and dry lint-free tissue.

Prior to the fusing or joining together process of two optical fibres after stripping has been completed, both ends have to be stripped and then cut perpendicularly to the fibre axis. This operation is called cleaving and enables the fusing process to be carried out. A high performance cleaver CT-30 procured from Fujikura Ltd., Japan was selected for this purpose. The cleaver used was able to cut the ends of the optical fibres at 90° with a typical tolerance of ±0.5°. A schematic of the stripped and cleaved fibre is shown in Figure 18.

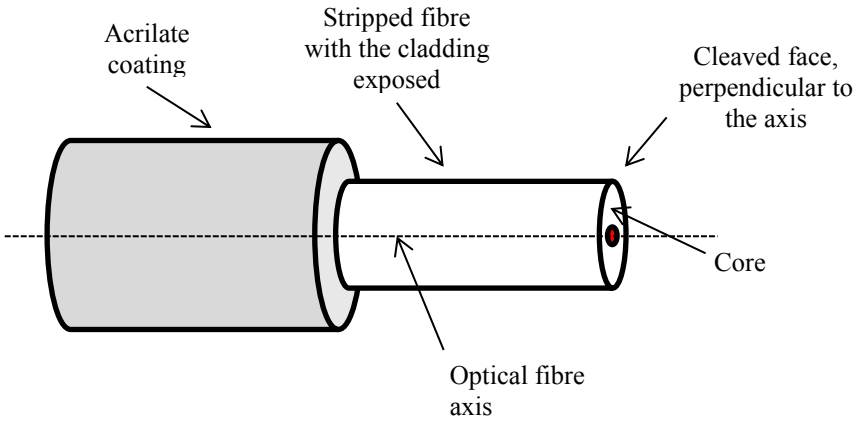


**Figure 18 Stripped and cleaved optical fibre.**

Fusing splicer

A commercial fusion splicer FSM-45F procured from Fujikura Ltd., Japan, was selected for joining the optical fibres. The equipment was able to join two optical fibres previously stripped and cleaved with optical losses in the splice which were typically lower than 0.02 dB.

The equipment was fitted with two translation stages, two cameras for enabling the perfect core-to-core alignment and two electrical electrodes. Once the fibres were clamped, the joining process and a posterior quality assessment were carried out automatically. If the joining process was completed successfully, due to the brittleness of the fused section and lack of the acrylate protective coating, the joined stripped length had to be protected. The protection was achieved by employing a splice protector also procured from Fujikura Ltd., Japan. The splice protector consisted of a sleeve of heat shrinkable material filled with a hot melt fusion tube and reinforced with a longitudinal stainless steel rod. Once the section to be protected is inserted, it is introduced in the built-in heating chamber. The fusion splicer employed was programmed with an appropriate operational temperature in order to allow the

hot melt material to fuse and contract the heat shrinkable tubes, securing everything in a package reinforced by the metallic rod.

Joining fibres was one of the most common processes during the FOAES manufacturing. It enabled the connection of the optical inputs and outputs of the sensor to fibre patches equipped with appropriate connectors, as will be discussed next.

Optical connectors and sensor manufacturing laser

The optical fibres have to be mounted on connectors to enable the optical power to be coupled into the optical fibres from a laser, and to couple the optical power from the optical fibres to optical detectors. Due to the fact that the majority of the existing equipment used in the project was equipped with FC/PC, fibre patches P1-630A-FC-2 procured from Thorlabs, UK were sourced. This fibre patches consisted on lengths of SM600 optical fibre, which is one of the optical fibres used in the project, terminating in an FC-PC connector, and protected by a plastic yellow tube reinforced by an internal Kevlar tow. The photograph of an FP/PC connector is shown in Figure 19.

(i) (ii)

**Figure 19 FC/PC connectors. Figure 19 (i) shows the termination FC/PC of the fibre patches, while Figure 19 (ii) shows the typical female FC/PC connection present in the optical equipment.**

The connectors had to be cleaned periodically to remove any potential debris or dust accumulating. A Cletop S Cassete Cleaner (Cletop.com, USA) and a One-Click Cleaner SC (Fujikura, Japan) were chosen for cleaning the male and female connectors respectively.

Regarding to the laser used during the manufacturing of the sensors, a Fabry-Perot pig-tailed benchtop laser source model S1FC635 procured from Thorlabs was used. The main features of this laser are summarised in Table 2. The typical output spectrum is shown in Figure 20.

**Table 2 Technical characteristics of the laser S1FC635**

| | |
|---|---|
| **Wavelength Minimum** | 625 nm |
| **Wavelength Typical** | 635 nm |
| **Wavelength Maximum** | 640 nm |
| **Minimum Full Output Power** | 2.5 mW |
| **Setpoint Resolution** | 0.01 mW |
| **Laser Class** | 3R |

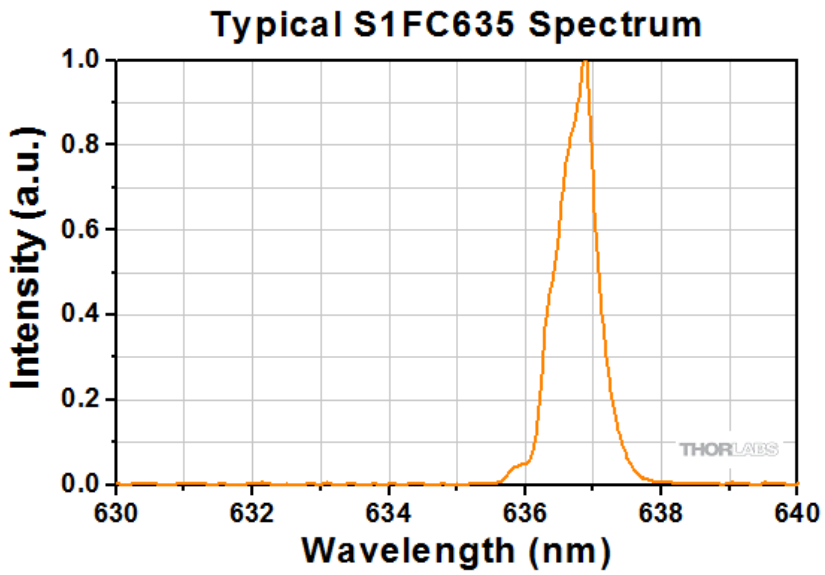


**Figure 20 Typical output spectrum of the S1FC635 (Image extracted from http://www.thorlabs.de/thorproduct.cfm?partnumber=S1FC635)**

## 3.3 FOAES Manufacturing

The production of the FOAES consisted of two distinct stages. Firstly, the coupler manufacturing using a commercial rig, and secondly the packaging of the sensor. In the case of the packaging two different processes were developed for (i) securing the sensor on a rectangular thin glass substrate; (ii) a precision bore capillary to be translated and secured over the sensing region.

### 3.3.1 Production of the FOAES

The FOAESs were manufactured on a custom-modified JW2000A commercial coupler manufacturing rig procured from Joinwit, China. The coupler manufacturing rig consisted of two motorised and synchronised vacuum grip stations travelling in opposite directions, which were able to accommodate two aligned optical fibres as shown in Figure 21. The applied vacuum enabled an even distribution of the force needed to keep the fibres secured while the drawing and melting process was taking place. The heat needed for fusing the optical fibres together was provided by a torch burning Hydrogen ($H_2$) gas. The $H_2$ flame prevented the creation of combustion residues others than water, hence, minimising the risks of adding ashes or inclusions in the fused optical fibre section.

The torch of the JW2000A coupler has movement just in one plane and does not support the brushing movement as illustrated in Figure 21. This movement enabled the repositioning of the torch from the resting position to over the fibres for starting the fusion process, and back to the resting position when the process is completed. The quantity of $H_2$ being burnt was monitored and controlled manually by a knob and a gas flow meter, with a range from 0 to 500 standard $cm^3$/minute. The machine had a set of interchangeable torches with different

exhaust cross sections. The relative distance from the torch to the fibres was adjustable via a micrometre and a translation stage.

The fusion process was monitored by two optical detectors and software capable of measuring in real time the optical power contained in each optical fibre. The hardware configuration programme allowed the customisation of the following parameters: (i) drawing speed or linear speed of the vacuum grips; (ii) linear speed of the torch when moving from or to the resting position; (iii) timers controlling the delay in starting the pulling process since the torch is over the fibres (pre-heating); and (iv) timers controlling the stop of the pulling movement since the torch start travelling to the resting position (post-drawn).

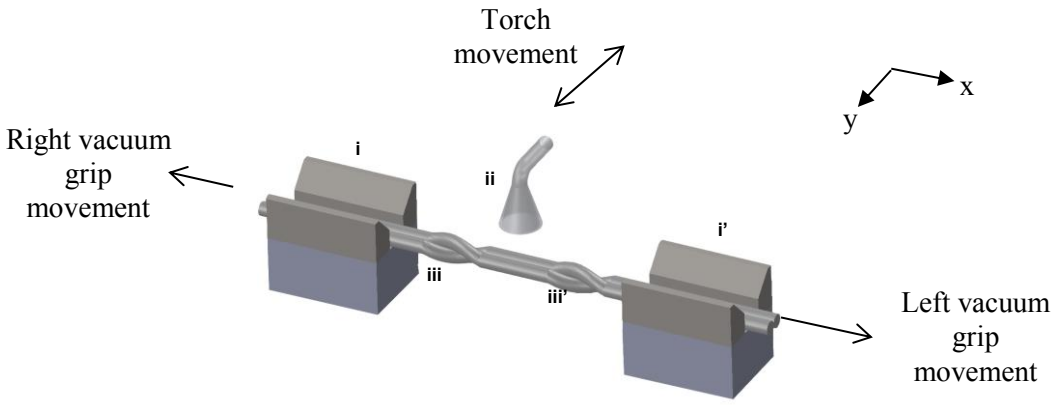


**Figure 21 Schematic illustration of relative positions of a pair of motorised (traversing) the vacuum grips - i and i'; hydrogen torch – ii; and the twisted optical fibres – iii and iii'.**

A pair of optical fibres of length 1000 mm was cut, and a centre section of length 40 mm each was stripped and cleaned two times with acetone and isopropyl alcohol using a lint-free tissue. One fibre was joined via the fusion splicer to patch cables terminating in FC/PC connectors at both ends, while the second fibre was joined just to one patch cable with the FC/PC

connector. The pair of optical fibres were twisted (2 turns) and secured on the vacuum-grips of the coupler rigs. The centre region of the optical fibre was positioned beneath the nozzle of the hydrogen torch as shown in the schematic of Figure 21.

Due to the requirement of inserting the packaging unit which was not standard in the FBT machines, it was necessary to modify the equipment with a custom packaging platform lying on top of the equipment. The machine and the platform were attached on an optical breadboard via optical fittings and custom-machined parts. The packaging platform was designed taking into consideration the accommodation of the retractable enclosure (to avoid fluctuation in the flame due to air currents) and the rotatory UV light. The details of the described elements are shown in Figure 22.

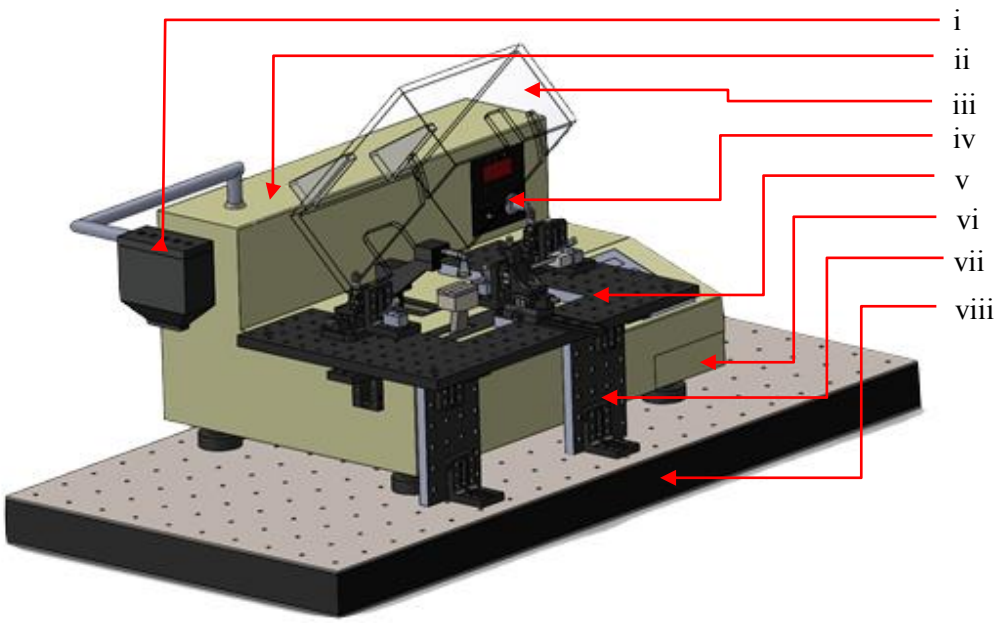


**Figure 22 Modified FBT machine. (i) Rotary UV lamp. (ii) JW2000A. (iii) Retractable cover. (iv) Flow meter and knob for flow control. (v) Packaging platform containing the translation stages for the packaging process. (vi) Optical detectors for process monitoring. (vii) Hardware and custom parts for securing the packaging platform floating and stable over the FBT machine. (viii) Breadboard for securing the machine and the packaging station.**

One of the connectors of the fibre joined with fibre patches at both ends was connected to the laser S1FC635, whilst the second end was connected to one of optical detectors. The optical connector of the other fibre was connected to the second optical detector of the machine. The laser was set at 1 mW and the detectors calibrated prior to starting the manufacturing process. A schematic of the setup for the described process is shown in Figure 23.

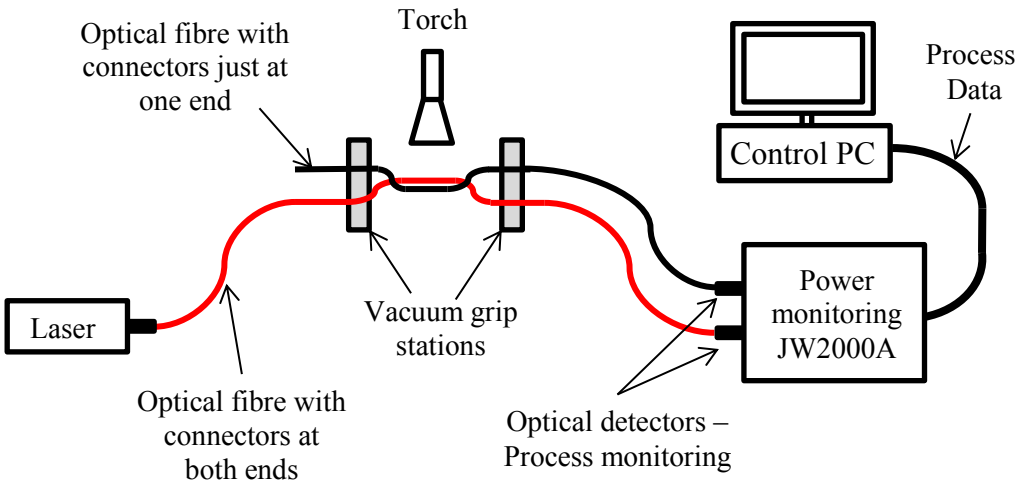


**Figure 23 Schematic of the FOAES manufacturing setup**

After the calibration was completed, the gas valve was opened. The flowing gas was subsequently ignited and the retractable cover deployed. After 40 seconds of temperature stabilisation the process was initiated. The control software allowed the control of the output power in both optical fibres as well as the optical power lost when compared with the power measured before starting the process. When the power ratio was at the desired value, the process was stopped and the gas flow cut. A print-screen of the control software is shown in Figure 24.

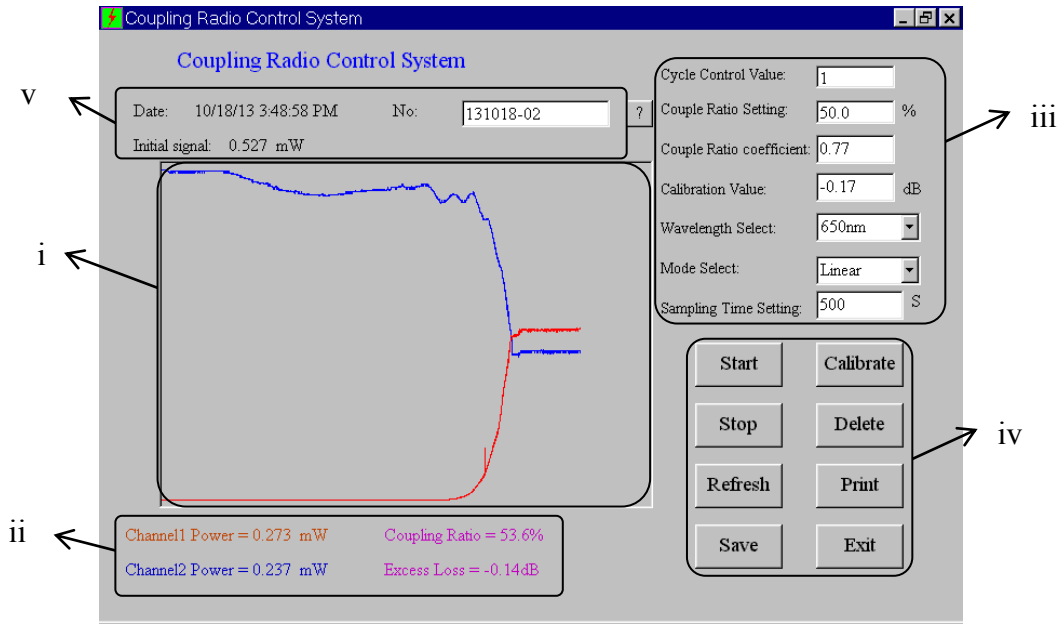


**Figure 24 Detail of the control software. (i) Graphical representation of results; (ii) numerical representation of results; (iii) detectors and graph parameters configuration; (iv) test control buttons; and (v) initial power, date and sensor name.**

### 3.3.2 Sensor packaging process

The FOAES were packaged in two different ways: i) surface mounted in a glass coverslip and ii) inserted in a borosilicate capillary, which will be referred to as Type I and Type II packaging respectively. The schematics of both packaging methodologies are shown in Figure 25.

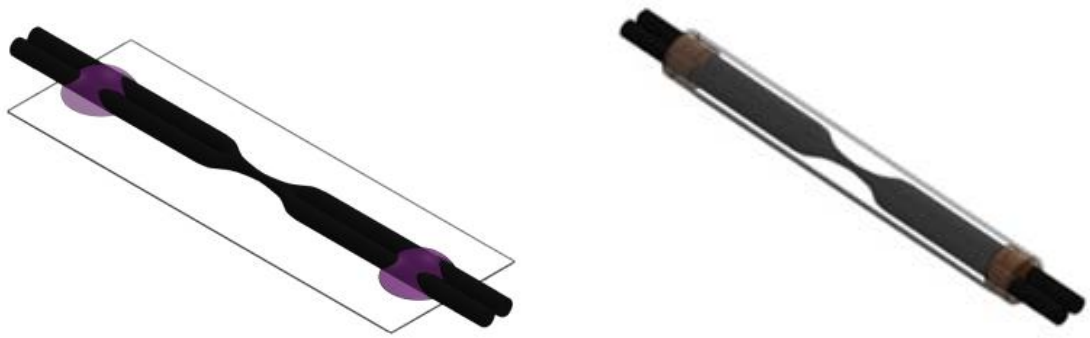

(i) (ii)

**Figure 25 Schematics of the FOAES packaging. (i) Surface mounted or Type-I; and (ii) inserted in a glass capillary or Type II.**

Type-I Packaging

Type-I packaging consisted of a borosilicate glass coverslip of dimensions 50 x 20 x 0.17 mm. Once the sensor was fabricated, the glass coverslip was placed on the horizontal translation stage shown in Figure 26 (vii) and moved to its position just below the sensor. It was ensured that the sensing region of the FOAES was positioned over the centre of the coverslip. The vertical translation fixture (item vi in Figure 26) was used to bring the coverslip into contact with the pair of optical fibres and when in position, secured with two drops of photo-curable adhesive NOA81 or NOA65 procured from Norland Products Inc., USA, at both sides of the tapered region. The volume of the liquid dispensed was approximately 5 µl. Precautions were taken to apply the drops on the stripped region of the optical fibres only and never on the thermoplastic coating. The adhesive was then cured under the machine's built-in UV lamp. A schematic illustration of the bonding points for the coverslip and the capillary tube with the sensors is illustrated in Figure 25 (i). A brief summary of the technical characteristics of the NOA81 is given in Table 3.

**Table 3 Technical characteristics of the adhesive NOA81**

| Parameters | NOA 65 | NOA 81 |
|---|---|---|
| Solids | 100% | 100% |
| Viscosity at 25° C | 1200 cps | 300 cps |
| Refractive Index of Cured Polymer | 1.524 | 1.560 |
| Elongation at Failure | 80% | 25% |
| Modulus of Elasticity (psi) | 20,000 | 200,000 |
| Tensile Strength (psi) | 1,500 | 4,000 |
| Hardness - Shore D | 50 | 90 |

Type-II Packaging

The Type-II package consisted of a borosilicate capillary tube with internal/external diameters 700/870 µm and 100 mm of length, which enabled custom lengths to be cut. A repeatable

process was developed to position, guide and slide the capillary from one side of the vacuum-grip to the required position over the sensing region but without touching the tapered region. This was achieved by the aforementioned custom-made packaging platform which is shown in Figure 22. The packaging platform was equipped with the following optical hardware from Thorlabs Inc., USA: (i) Single-axis translation stages MS1S/M with side-mounted micrometer; (ii) base plates MS10; (iii) angle brackets MS102; (iv) dovetail optical rail and carrier RLA150/M and RC2/M; (v) Fibre clamps for diametre 250 μm T711/M-250; and (vi) an aluminium breadboard for fixing all the components.

The aluminium breadboard was machined for fitting on the machine allowing the rotating cover to deployed during the manufacturing as well as not obstructing the machine controls. The fibre clamps were machined to increase the holding capacity from one to two fibres. An aluminium sliding fixture was custom machined to hold the capillary during the manufacturing process. The different elements are shown in Figure 26. A full description of the process is provided in Chapter 4. After inserting the capillary, it was locked in position by a clamp and then secured by the application of UV adhesive at both sides. The adhesive selected was the NOA81 at either sides, or a combination of NOA81 and NOA65 to reduce the directionality of the sensor. The adhesive was finally cured by the machine's built-in UV light.

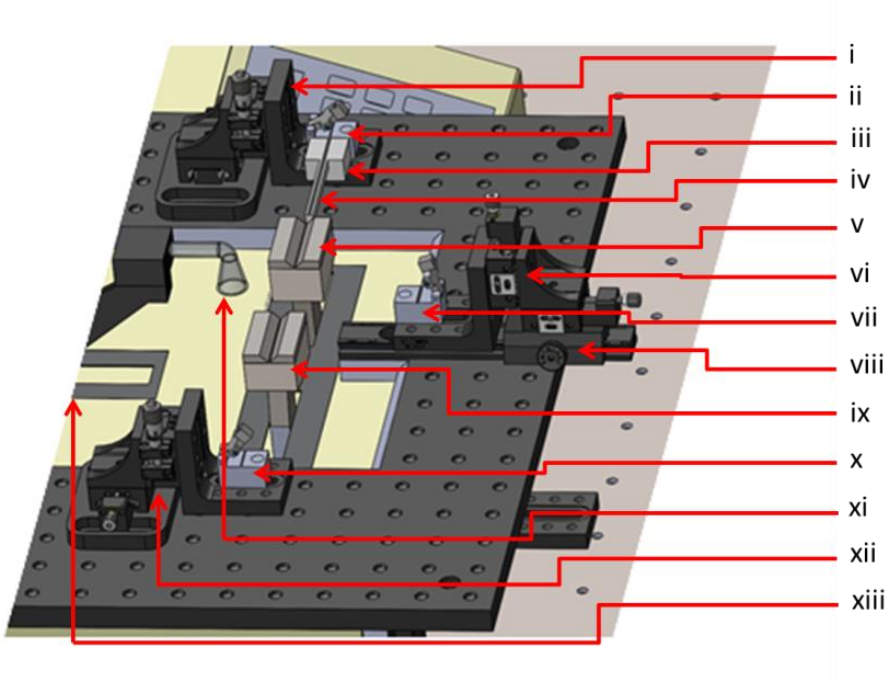


**Figure 26 Schematic illustration of the key components of the custom-modified coupler production rig. (i) 3D translation stage. (ii) Secondary modified clamp for the pair of unstripped optical fibres. (iii) A sliding fixture to translate the precision bore capillary tube. (iv) Precision bore capillary tube. (v) Vacuum grip for securing the stripped optical fibres. (vi) Vertical translation stage. (vii) Fixture for supporting the glass coverslip-based packaging medium. (viii) Coarse translation stage, guided by a dovetail rail and carrier. (ix) Traverse drive for the vacuum grip. (x) Secondary fibre grip. (xi) Hydrogen gas-powered torch. (xii) 3D translation stage. (xiii) Horizontal translation fixture for translating the torch and hydrogen gas supply.**

## 3.4 FOAES Embedding

Unidirectional glass fibre prepegs (VTM264/1062-300, Cytec, UK) were cut to panel dimensions of 300 x 300 mm. Panels of 4 and 8 plies were laminated following different configurations as: (i) all the plies with the reinforcement aligned designed as $(0)_{\text{number of plies}}$; or (ii) when the plies were laminated alternating the angle from perpendicular to parallel designed $(0/90)_{\text{number of plies}}$.

Since the reinforcement should be distributed evenly through the thickness of the panel to avoid internal tensions which could create the panels to deform, the lamination of the different

layers were always symmetrical with a plane crossing through half of the thickness. As an example, if a $(0/90)_8$ panel was manufactured the orientation of the different plies would be: 0-90-0-90-|-90-0-90-0.

The sensors were embedded between plies 2 and 3 when the panel was manufactured with 4 layers. Subsequently for a laminate of 8 plies, the sensors were embedded between plies 4 and 5. In addition and for avoiding shear stress on the cylindrical packaging which could end in brittle fracture, the sensors were orientated in the same direction as the reinforcement. A PTFE tubing of 0.75 and 1.5 mm of internal and external diameters respectively was used at both sensors' exit points from the laminate to protect the optical fibres from: (i) the vacuum/pressure applied during the manufacturing process; and (ii) from accidental bending during the manipulation and cutting of the laminates.

The laminates were laid on a 4 mm thickness carbon fibre flat working surface, sandwiched between release films. Silicone grease procured from RS, UK, was used to seal the protection tubing and the perimeter of the laminate. This sealing process stopped the resin bleeding out from the prepegs and thus, avoided the impregnation of optical fibres with resin. Once the silicon was cured, the standard preparation for autoclaving composites were carried out and the materials cured at 80°C. Figure 27 shows a photograph of a panel with two embedded FOAES, the protective tubing and the silicone seal.

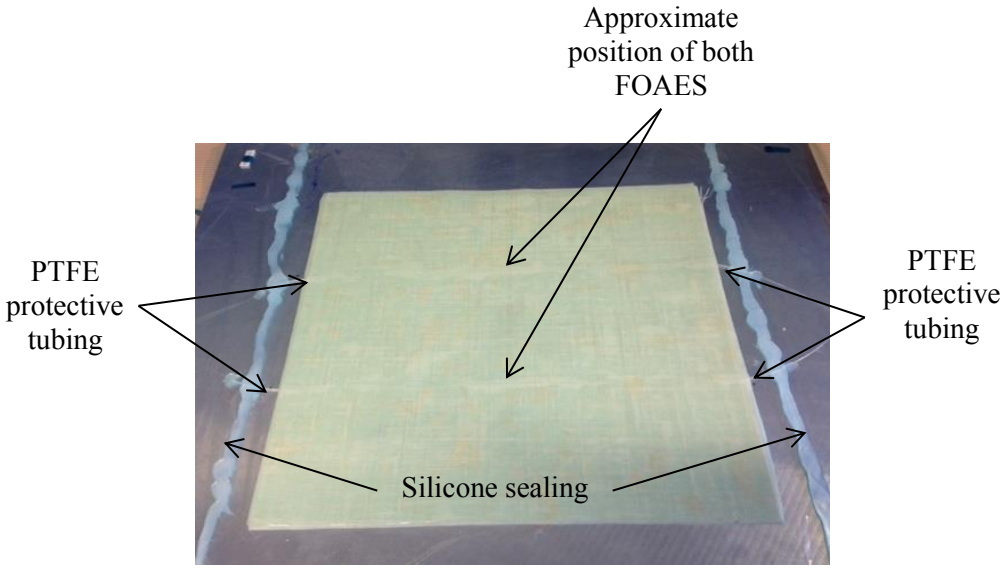


**Figure 27 Image of a panel with two FOAES embedded. The protective tubing at both extremes of each sensor and the silicone sealant is signalled.**

## 3.5 FOAES Characterisation

The FOAES characterisation process consisted of evaluating the response of the sensor, understanding its directionality (i.e. how the sensor responded to the same acoustic signature at different angular positions) and frequency response (i.e. the sensitivity of the sensor at different frequencies).

The Type-I sensors were surface-mounted on the centre of an aluminium plate of dimensions 500 x 500 x 3mm using Vaseline as the coupling agent. The Type-II sensors were surface-mounted on the same aluminium plate and on composite plates $(0)_4$ using Vaseline as coupler too. Some of the surface tested Type-II sensors were then embedded in composite laminates and re-tested using the embedding panel as the test piece.

The sensor characterisation was carried out in four different steps: (i) sensor noise characterisation; (ii) response of the sensor to a Hsu-Nielsen excitation source (mechanical pencil lead tip breaks); (iii) response of the sensor against a burst of sinus generated by two different piezo-emitters; and (iv) response against continuous sinuses at discrete frequencies generated by the same piezo-emitters. For simplification purposes, test (ii) and (iii) will be called discrete characterisation, and test (iv) frequency sweep tests respectively. To understand if directionality existed, the discrete characterisation and the frequency sweep tests were repeated covering a circumference with a radius of 75 mm around the tapering region of the sensor, and every 45 degrees. A schematic illustrating the setup of a surface mounted FOAES indicating the different excitation points is shown in Figure 28. The laser input and output were located at 0° and 180° position respectively.

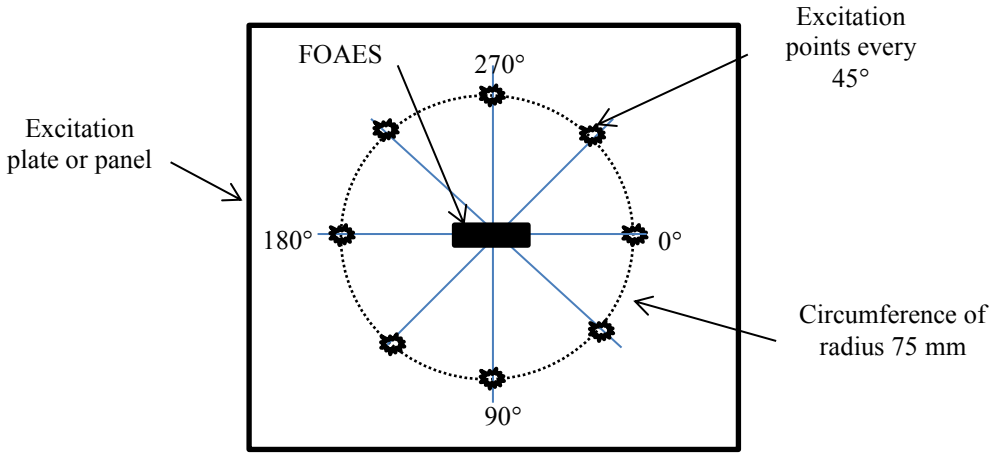


**Figure 28 Detail of the position of the FOAES and excitation points (surface mounted).**

Two commercial piezoelectric AE sensors were used for benchmarking purposes. Hence the response of the manufactured FOAES was compared to the aforementioned commercial piezoelectric AE sensors. The benchmarking sensors were characterised in the same way as the FOAES, using the same coupling agent and testing plates. When the FOAES were

embedded, the characterisation of the FOAES and each benchmarking sensor were carried out simultaneously. In order to achieve this, the piezoelectric sensors used for benchmarking were surface mounted in the flat face (tool-face) of the composite panel by applying a thin layer of the coupling agent. To ensure good and constant contact during the tests carried out, the benchmarking piezoelectric sensors and emitters were secured by placing masses of 200 grams on the top face. An illustration of the setup where the FOAES was embedded is shown in Figure 29.

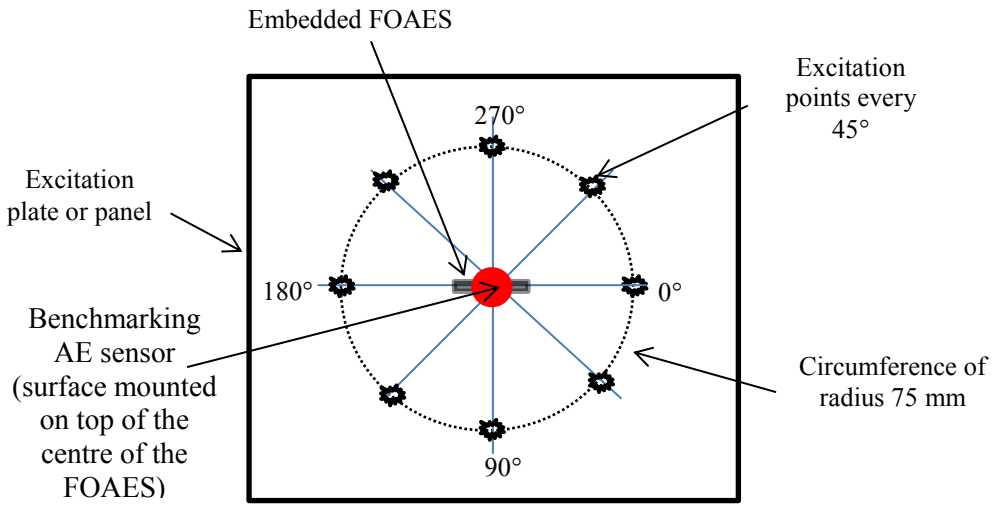


**Figure 29 Detail of the position of the FOAES and excitation points (embedded).**

In the following section a full description of the aforementioned four sub-tests carried out for the FOAES characterisation (including the hardware and software) is going to be given.

### 3.5.1 Photodetectors, lasers, amplifiers and DAQ

The sensors were interrogated by a balanced TA10 trans-impedance differential amplifier PDPAH procured from Theoptics, UK, named for the purpose of this thesis Box A. This equipment was previously designed and constructed with the idea of integrating the detectors and a semiconductor laser as a stand-alone system. The Box A had a selectable low pass filter

set at 100 kHz, and an antialiasing filter of 500 kHz. An image of Box A is shown in Figure 30.

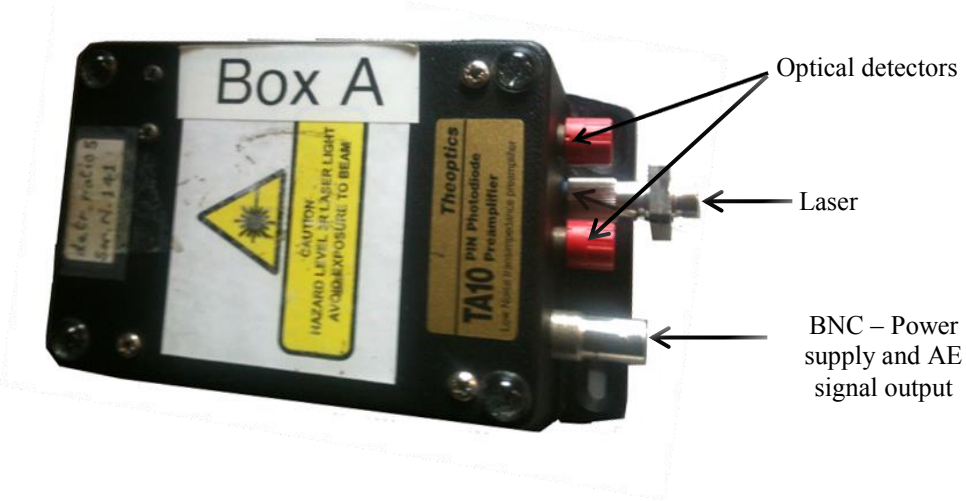


**Figure 30 Image of Box A.**

Box A consisted on two optical detectors and a semi-conductor laser. The box worked using a phantom power supply of $28V_{dc}$ which enabled the use of the same BNC cable for powering the electronic and transmitting the analogical differential voltage output. This powering/interrogation design was the same as the one used by the Mistras AE hardware, so Box A was fully compatible with any of commercially available AE PCI-based systems or amplifiers.

During the characterisation stages, Box A was connected to an AE2A AE amplifier procured from Mistras, USA. The function of this amplifier was as discussed to power the Box A adding adjustable gain from 0 to 61 dB in steps of 3 dB. The output from the amplifier was connected to a 4–channel model L4534A DAS procured from Agilent USA. This data acquisition system has a programmable acquisition rate of up to 20 MHz, a built-in memory of 128 MSamples per channel, resolution of 16 bits and programmable trigger modes. The

acquisition range of the DAS employed was adjustable too, enabling its adjustment to the working voltages for a better resolution.

The sensors were interrogated by two different laser systems: a HeNe (Helium-Neon) gas laser model 1107 procured from JDSU, USA and the built-in semiconductor laser of Box A. The HeNe laser had a very narrow spectrum centred at 632.8 nm, delivering low noise signal with a minimum of 0.8 mW of power. The laser was coupled to the single mode optical fibres via a laser-to-fibre adapter SMJ-A3A,X-633-4/125-3-5 procured from Ozoptics, USA, which reduced the power to around 0.6 mW (related to losses during the coupling process). On the other hand, the semiconductor laser was pig-tailed and delivered a much more powerful output of 1.8 mW but with a broader and less uniform spectrum. The semiconductor laser was additionally more sensitive to changes in the internal temperature which made the power spectrum to drift with time. Details of both spectra are shown in Figure 31.

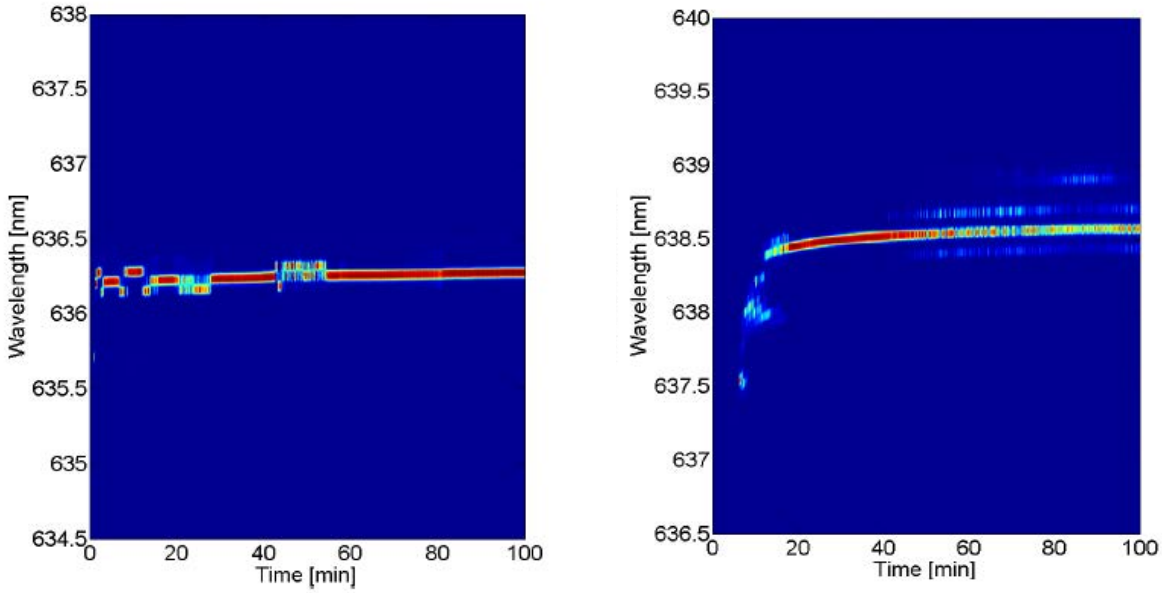


(i) (ii)

**Figure 31 Detail of the evolution of the spectrum of the lasers used during the FOAES characterisation [65].(i) Spectrum of the HeNe laser, which stabilised after nearly 60 minutes; and (ii) semi-conductor laser of Box A, which after the warming up time of nearly 60 minutes showed simultaneous peaks at different wavelengths.**

### 3.5.2 Acoustic Emission excitation sources and benchmarking AE sensors

A Hsu-Nielsen source (mechanical pencil lead tip breaks) and two AE piezoelectric sensors operating as emitters were selected to generate AE signatures as part of the characterisation process of the FOAES. While the pencil breaks consisted of a sudden broadband burst of energy, the piezo-emitters were used to generate pulses of sinuses at discrete frequencies. The selected AE sensors were the general purpose R30α and R50α procured from MISTRAS, USA. The piezo emitters were excited using a 33220A signal generator procured from Agilent, USA. A schematic of the pencil break excitation source and one AE sensor is shown in Figure 32.

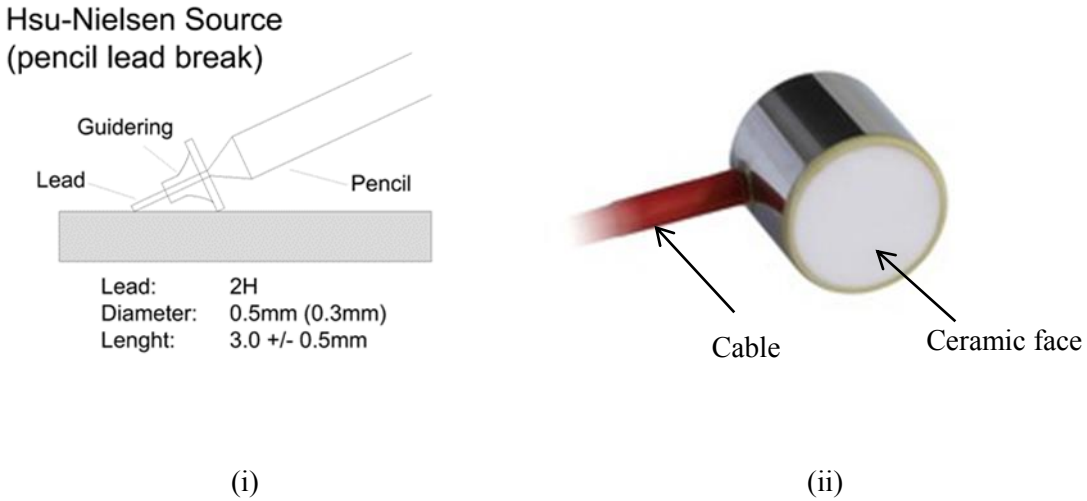


**Figure 32 Schematic of (i) the Hsu-Nielsen excitation source (image extracted from www.ndt.net) and (ii) AE sensor (image extracted form www.physicalacoustics.com/general-purpose/)**

The R30α and R50α piezoelectric transducers consisted of a ceramic wear plate fitted on a stainless steel cylindrical housing of 19 mm of diameter and 22 mm of high, and 30 and 32 grams of weight respectively. The sensors were resonant at 300 KHz (R30α) and 500 kHz

(R50α) respectively. Detailed frequency responses of both R30α and R50α are shown in Figure 33.

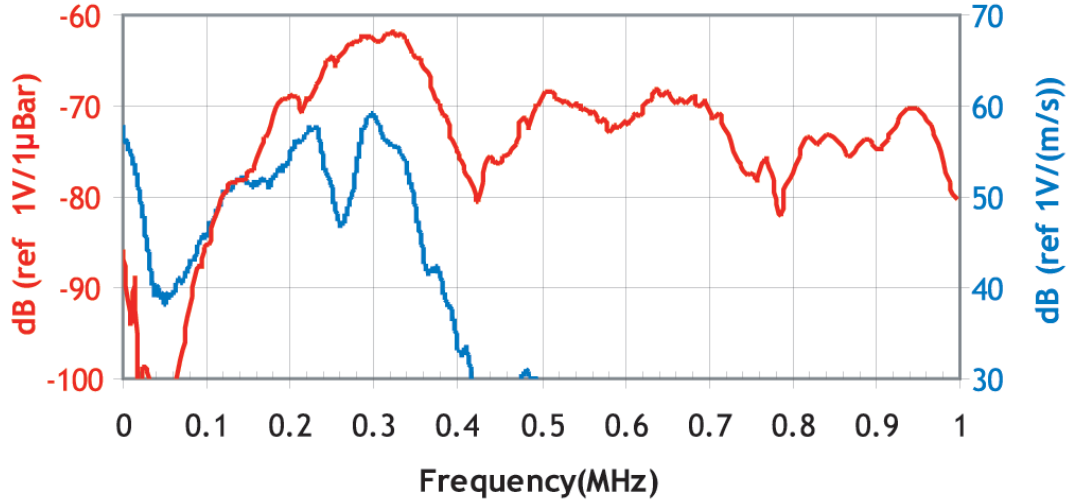


(i)

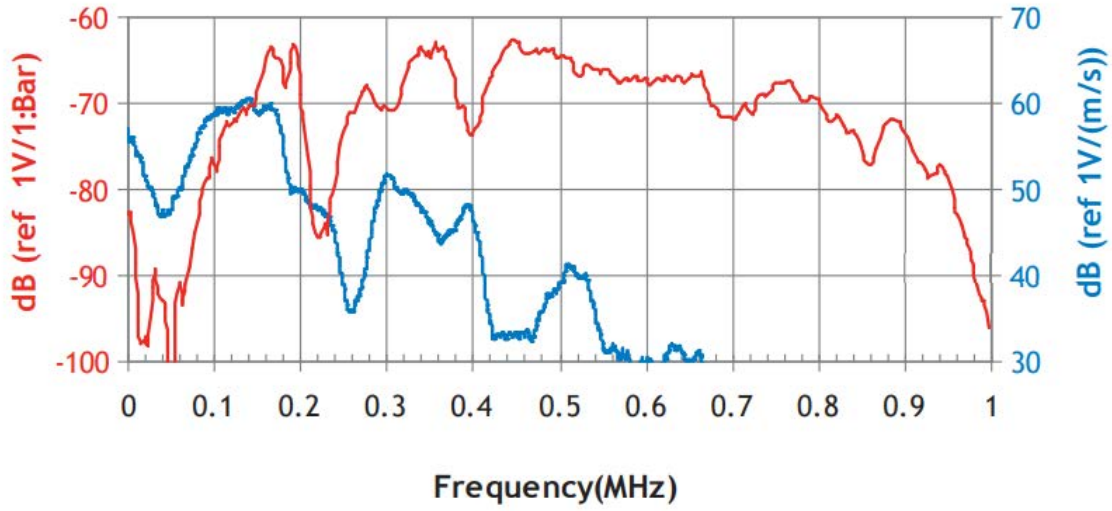


(ii)

**Figure 33 Frequency responses of the AE sensors (i) R30α [197] and (ii) R50α [198]**

The same piezoelectric R30α and R50α transducers were also used as benchmarking references and thus, were compared with each FOAES undergoing characterisation.

### 3.5.3 FOAES noise and discrete characterisation

While the sensor noise characterisation consisted of the experiments designed to record the sensor response in absence of any acoustic excitation, the generation of discrete acoustic signatures were used to understand the frequency response of the FOAES when compared to the two benchmarking piezoelectric AE sensors. For performing these experiments, a custom-written LabVIEW® application was commissioned. This application had all the functionalities required for the data acquisition configuration, acquisition setup, and acquisition triggering and data storage.

Developed software

An application able to control the data acquisition via a control computer was commissioned, as shown in Figure 34. Once connected to the DAS using a Local Area Network (LAN) cable and Visual Instrument Software Architecture (VISA) protocol, the software enabled the insertion of the FOAES identification number (ID), substrate (panel where the test was carried out), coupling agent and laser illuminating the sensor. After this information was inserted, the test file was generated by pressing the "Record Data" virtual button. This opened a pop-up menu to select the file name and location. The selected file structure was the industry standard Technical Data Management System (TDMS) file, which supported the option of creating a customised structure and organisation of the files with a small disc size. In addition, this format allowed high speed streaming and was searchable (i.e. possible to find the information via specific tools, by the use of the tests or sensor properties as filters).

The next step was the selection of the sub-programme. During this project just two of the sub-programmes were of interest: a) "Single Burst Test" for just one sensor characterisation, and b) "Single Burst Test Optical + Piezo" for simultaneous characterisation of the FOAES and a

benchmark sensor. Both sub-programmes allowed the configuration of the DAS with the desired acquisition parameters such as acquisition rate, range, trigger level, acquisition length, pre-trigger length or coupling. The trigger was programme set as channel based, which means that when the system was armed the acquisition started as soon as the DAS read a signal of higher amplitude than the programmed trigger level. In addition, an area with pull-down menus and test boxes were set up for the relevant details of each experiment to be saved with the signals, such as AE source, distance, angle and so on. The user-interfaces of both characterisation sub-applications are shown in Figure 35 and Figure 36.

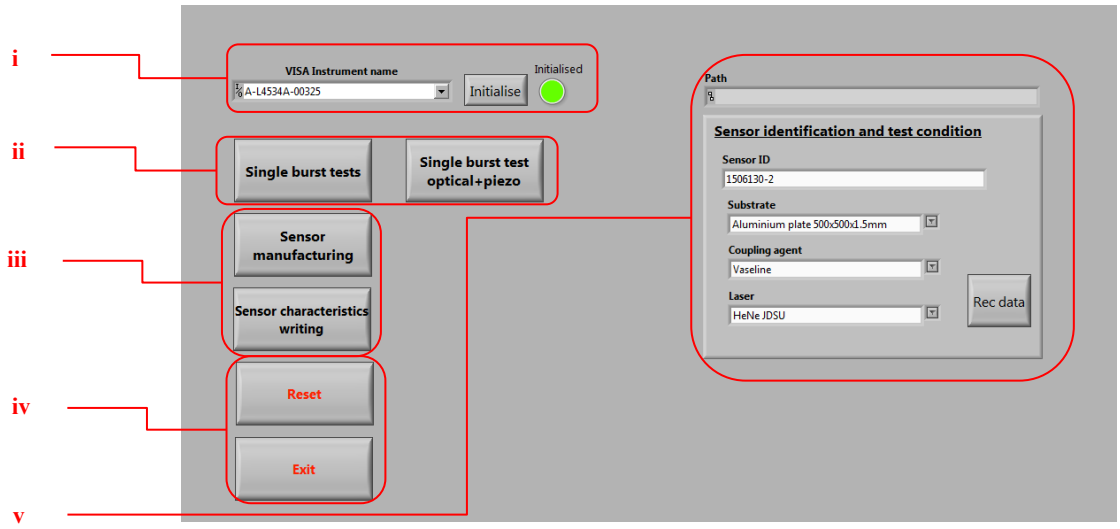


**Figure 34 Main menu of the application. (i) Pull-down menu to look for VISA instruments, LED showing the status of the instrument and the instrument initialise button. (ii) Buttons for starting the characterisation sub-applications. (iii) Other developed sub-application not relevant to this thesis. (iv) DAQ reset and exit botton. (v) Menus for inserting the common information of the test such as coupling agent, laser, testing panel or sensor Id; if a file was created via the "Rec Data" bottom, the path of the file was showed at the top.**

Once a sub-application was selected, the relevant test detail introduced and the DAS configured and armed, the acquisition was triggered by the AE source. The software then converted the obtained signal into frequency domain by performing a FFT with rectangular

window, and plotted both time and frequency domain results graphically. The software offered then the option of saving all the data together with the test details, and further experiments on the same FOAES at different angles or AE excitation sources could be performed. When the measurement was finished, by pressing a button the sub-application was closed and the user returned to the main menu.

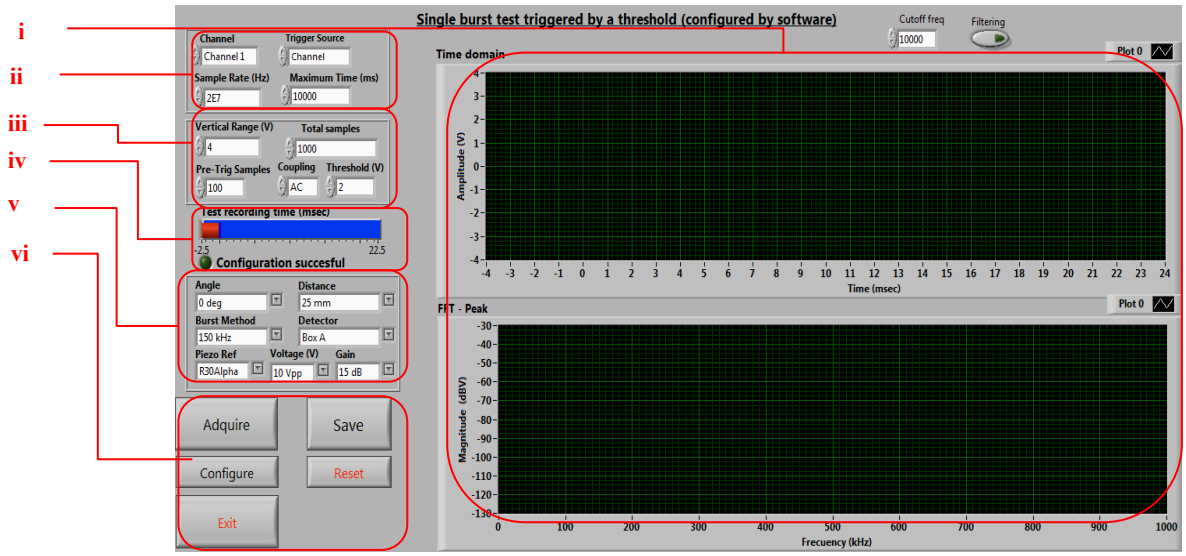


**Figure 35 "Single Burst Test" sub-application. (i) Graphical representation of the results on time and frequency domain. (ii) DAQ channel selection for the signal acquisition, acquisition rate and time-out (time until the software returns error if threshold is not detected). (iii) Voltage levels, coupling, acquisition length and acquisition pre-trigger. (iv) Graphical representation of acquisition and status of the DAQ. (v) Parameters of the acquisition to be stored in the file. (vi) Control buttons.**

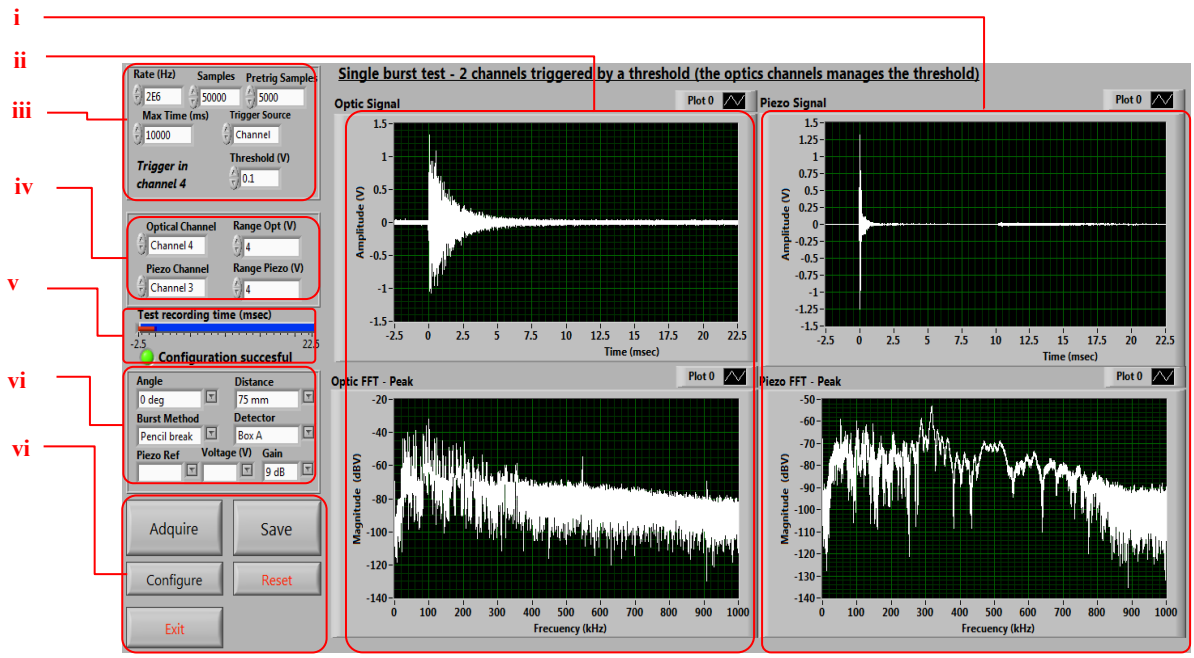


**Figure 36 Sub-application for simultaneous acquisition from the FOAES and from one benchmark sensor. (i) Graphical representation of the results on time and frequency domain for the FOAES. (ii) Graphical representation of the results on time and frequency domain for the benchmark sensor. (iii) DAQ channel selection for the signal acquisition, acquisition rate, time-out, and trigger channel. (iv) Voltage interval to be digitalised, coupling, acquisition length and acquisition pre-trigger. (v) Graphical representation of the acquisition and status of the DAQ. (vi) Parameters of the acquisition to be stored in the file. (vii) Control buttons.**

## Sensor noise characterisation

The noise or signals generated by the FOAES when illuminated by each of the lasers in the absence of acoustic excitation were recorded.

The sensors were secured on the centre of the testing plate (when not embedded) by the use of a thin layer of coupling agent. The sensor was illuminated by one of the lasers, and its output connected to the Box A. The Box A was powered by an AE2A amplifier, which applied further amplification to the signal before sending it to the DAS. The DAS was configured to acquire at an acquisition rate of 2 MSamples/s over duration of 1.25 s. The trigger level was set at 0 V, which effectively meant the immediate triggering of the acquisition as soon as the system was armed (by pressing the button "Acquire" in the user interface as it can be seen in Figure 35 (iv). After the acquisition was completed, the software plotted automatically the

data in time and frequency domain by performing the FFT so that the user can save it or repeat the measurement if something was suspected to be erroneous. These tests were performed to detect and discard sensors with a low SNR prior starting the proper characterisation tests.

Sensor response against discrete excitation sources

Hsu-Nielsen source and AE piezoelectric sensors working as emitters were placed at 75 mm away from the centre of the FOAES and moved along the circumference every 45°, as detailed in Figure 29. The DAS was configured at 2 MSamples/s, a pre-trigger of 2.5 ms, and a total acquisition length of 25 ms. The trigger level was set just above the measured noise level calculated in the previous step (to avoid the acquisition to be triggered by the noise generated by the sensor).

The Hsu-Nielsen source bursts were performed consistently with the breaking of the lead tip of the mechanical pencil aligned with the centre of the sensor. For the emitters, they were connected to the signal generator and manually triggered to launch a unique burst of 10 sinuses of peak to peak amplitude of ±10 V. The selected frequencies for the sinuses were the sensors' resonance frequencies: 300 kHz and 500 kHz in the case of the R30α and R50α respectively.

The data for both excitation sources were collected using the customised software described in Figure 35 or Figure 36, depending on the FOAES was surface mounted (just the FOAES being characterised) or embedded (FOAES and a benchmark sensor simultaneous characterisation). The results were represented on the screen in time and frequency domain by performing a FFT, and if successful was saved by pressing the "Save" button.

The sensor was illuminated by one of the lasers, and its output connected to the Box A. When simultaneous characterisation of the FOAES and the benchmark AE piezoelectric sensors was carried out, the AE sensor was connected via a 2/4/6 pre-amplifier procured from Mistras, USA to another AE2A amplifier. The AE2A amplifiers were used not just for powering the Box A and the preamplifiers, but to add further amplification to the signals before sending them to the DAS. A schematic diagram of the overall setup is shown in Figure 37. The tests were repeated over a circle with a radius of 75 mm from the sensor's centre by shifting the position by 45° at every step as shown in Figure 28.

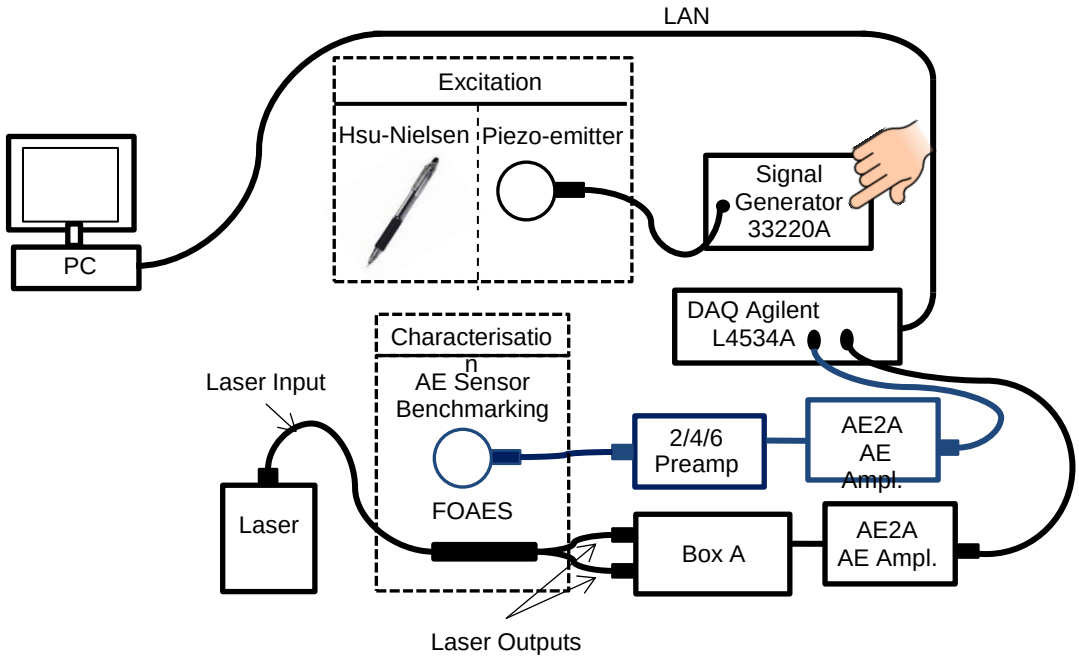


**Figure 37 Detail of the setup for characterising the sensor by a discrete AE signal. The sources were a Hsu-Nielsen for broadband signals, or piezo-emitters launching a burst of sinuses for mono-frequency signals. The signal generator was manually triggered. Regarding to the signals collected by the DAQ, the schema shows in blue colour the option for simultaneous acquisition of the FOAES and a benchmark sensor. When the sensor was surface mounted and thus just the FOAES was characterised, this blue part of the schema disappeared.**

### 3.5.4 FOAES frequency sweep characterisation

The frequency sweep characterisation tests were designed to obtain a direct comparison between each FOAES and the benchmark AE piezoelectric sensors, when continuous sinuses at the same frequency were used as excitation source. The frequency was changed in steps or swept in order to cover the full bandwidth of Box A (100 kHz to 500 kHz).

Developed software

Custom-built LabVIEW® software was commissioned to enable the automatic control of the tests, minimising the time required to operate the signal generator, trigger the system, perform the analysis and save the data. The software had a configuration menu for the DAQ where the relevant parameters for the automatic acquisition were easily introduced, such as: (i) physical channel for the FOAES and for the benchmark AE sensor; (ii) acquisition rate; (iii) voltage range; and (iv) pre-trigger and total samples. For these tests, an acquisition rate of 2 MSamples/s with a signal of length 50 ms (without pre-trigger) was used as standard.

The software enabled to control the signal generator to generate continuously sinus waves at the programmed frequency and amplitude on the testing plates or panels. Each testing point (voltage and frequency) started with a stabilisation time of 0.5 s until performing the acquisition. After finishing the 0.5 s interval the software acquired one or two channels (FOAES alone, or simultaneous FOAES and benchmark AE piezoelectric sensor), switching then the signal generator off for a further 0.5 s. The latter dead-time was found experimentally to be enough to dissipate the ultrasonic waves travelling in the plate to a level that no destructive or constructive interferences or residual harmonics were found when starting the next measurement. In a parallel loop, the software converted the obtained signal in the frequency domain by running an FFT and calculated the frequency and amplitude of the

recorded main harmonic (normally a single peak). The raw data together with peak amplitude and frequency were then stored in the file. The main screen and main functional areas are explained in Figure 38.

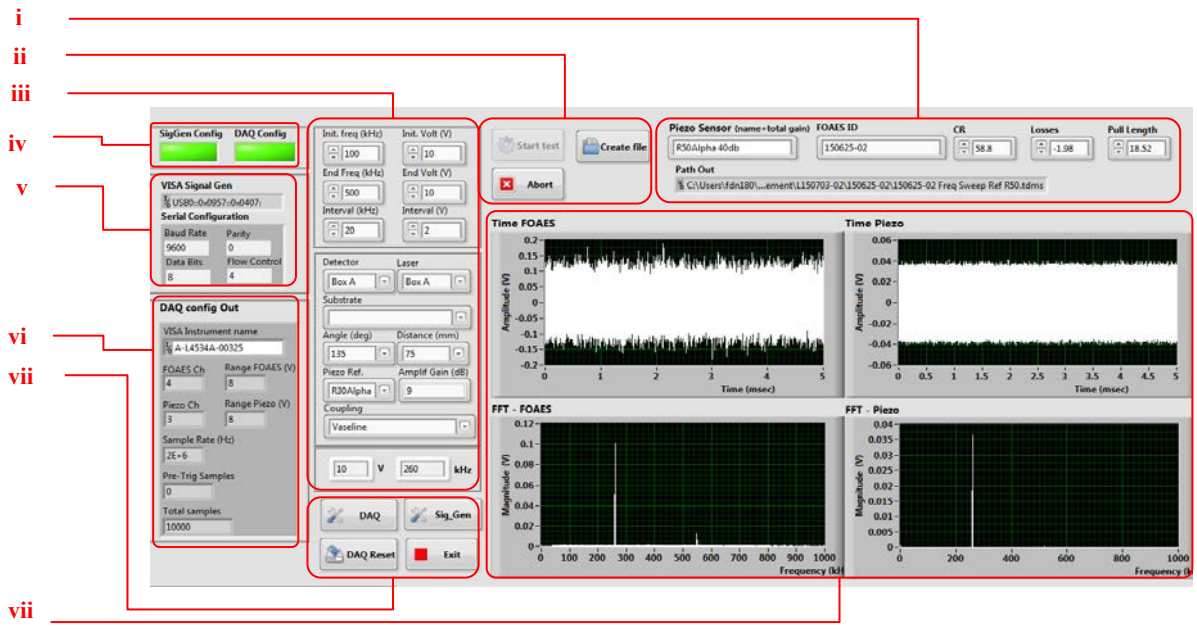


**Figure 38 Frequency sweep test main screen. (i) Sensors details to be stored in the file, and path were the file is being stored. (ii) Controls for starting a tests, create a new file or abort the tes. (iii) Pull-down menus for configuring initial, steps and final frequencies and voltages. (iv) Status of the signal generator and DAQ. (v) Actual configuration of the signal generator. (vi) Actual configuration of the DAQ. (vii) Controls to reconfigure or reset the signal generator and DAQ. (viii) Graphical information of the test, in time and frequency domain.**

## FOAES frequency sweep test

As before, while the embedded FOAES was tested simultaneously with a benchmark AE piezoelectric sensor, the surface mounted sensors were tested independently. A schematic diagram of the setup is shown in Figure 39 where both possibilities are illustrated. Box A and the benchmark AE piezoelectric sensor (if simultaneous characterisation was employed) were connected to one AE2A amplifier each (the AE sensor via a 2/4/6 preamplifier). The outputs

were connected to different channels of the DAS. The piezo-emitter exciting the setup was driven by a signal generator controlled by the same PC controlling the DAS. The usual configuration was to sweep frequencies ranging from 100 kHz to 500 kHz in intervals of 20 kHz, and with amplitudes in the signal generator from 2 to 10 V. This enabled the carrying out of 100 different combinations of frequency and amplitude per excitation point. The tests were repeated every 45° at 75 mm from the sensor's centre, as detailed in Figure 28.

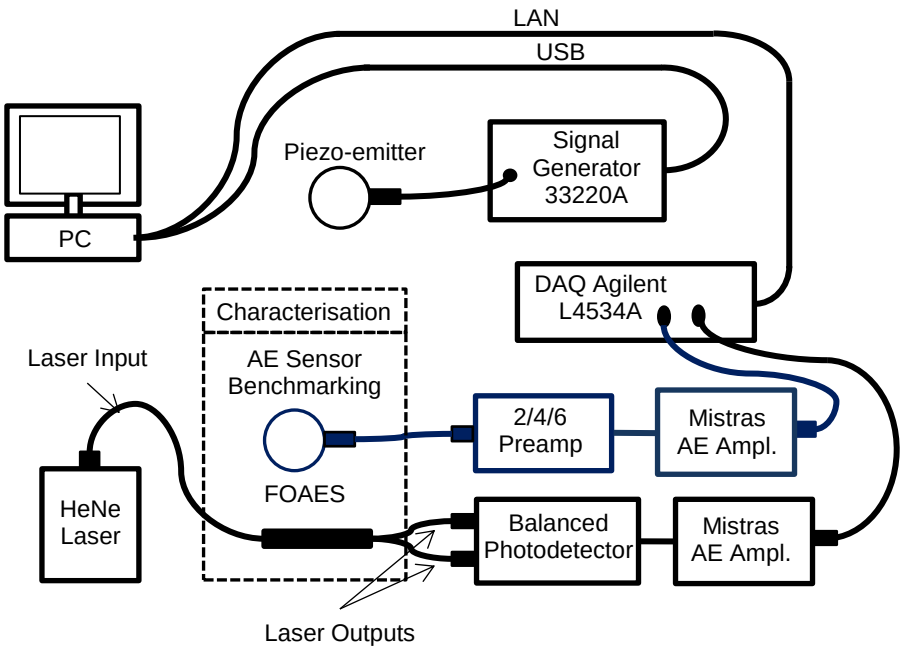


**Figure 39 Detail of the setup for the frequency sweep test. The piezo-emitter is driven by a signal generator which is automatically setup and trigger by the control PC. The same PC controls the acquisition of the DAQ. The DAQ can have two inputs from two different AE2A amplifiers. The Box A was always connected in the PC, whereas the blue blocks representing the benchmark AE sensor and its associated hardware were only connected when the FOAES was embedded and thus, simultaneous characterisation was performed.**

### 3.5.5 Summary of the characterisation tests

A summary of the different tests, including details about the trigger, pre-trigger, acquisition time, AE excitation source or repetition are shown in Table 4.

**Table 4 Summary of the different parameter used during the characterisation tests.**

| Experiment | Trigger | Pre-Trigger | Acquisition Time | AE Excitation | Repetitions |
|---|---|---|---|---|---|
| Noise characterisation | Manual | 0 msec | 1500 msec | None | 1 repetition |
| Discrete excitation sources | Channel | 2.5 msec | 25 msec | Hsu-Nielsen and piezo-emitters | Every 45° at 75 mm from the sensor's centre |
| Frequency sweep test | Automatic | 0 msec | 5 msec | Piezo-Emitters | |

Acquisition rate for all the experiments: 2 MSamples/second

## 3.6 Comparison of embedded FOAES with AE benchmark sensors by tensile testing

The last experiments consisted of the comparison between the benchmark AE piezoelectric sensors with embedded FOAES during tensile testing using a universal testing machine Instron 5507 (Instron, USA).

### 3.6.1 Samples preparation

Samples were prepared from previously characterised embedded FOAES. The longitudinal area of the panel containing the FOAES was cut at both sides of the sensor using an angular cutting tool, extracting strips of approximately 27 mm width and 300 mm length. The strips were polished on sides, reducing the width to 25 mm and ensuring that the FOAES was perfectly aligned at 12.5 mm of both edges. End-tabs made by aluminium of 25x60x2mm were bonded at both extremes of the testing strip by the use of the epoxy adhesive Araldite

procured from Huntsman Corporation, USA, for three minutes. A strain gauge FLA5-11 procured from Tokyo Sokki Kenkyujo Co Ltd., Japan, with a gauge length of 5mm was attached on the testing strip at one side of the centre of the FOAES to monitor the sustained strain during the tensile test. The strain gauge was secured on the testing strip by the CN adhesive also procured from Tokyo Sokki Kenkyujo Co Ltd., Japan, and was interrogated in a quarter-bridge configuration by a NI 9219 multipurpose data acquisition card procured from National Instruments, USA, via custom-written LabVIEW® software.

For comparison purposes, a fully characterised FOAES packaged in a capillary was surface mounted on a strip of composite of $(0/90)_4$ configuration. The sensor was coupled onto the surface by Araldite for 3 minutes, placing the benchmark sensors and strain gauge all together on the opposite face. Figure 40 shows an image of the samples ready for being tested, a detail of the strain gauge, and schematics of the position of all the elements for the embedded and surface mounted FOAES.

Finally, to understand the quantitative effect on the mechanical properties of laminates with and without embedded FOAES, three reference samples of a laminate $(90/0)_8$ were prepared from a spare untouched panel. These laminates were instrumented just with the benchmark AE R30α and R50α piezoelectric sensors, positioning them in the same face and as close as possible to the longitudinal middle point.

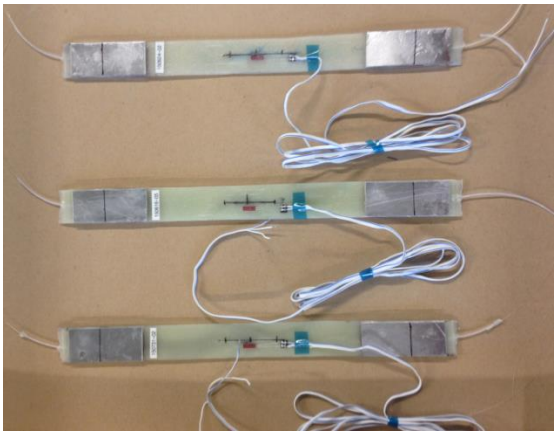

(i)

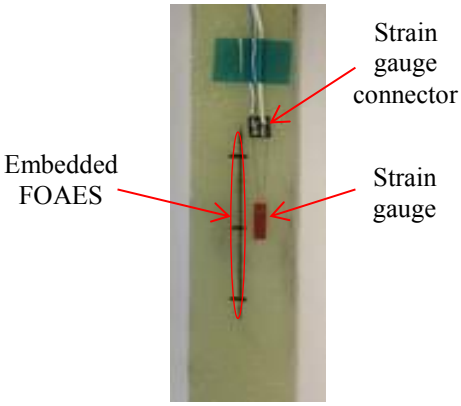


(ii)

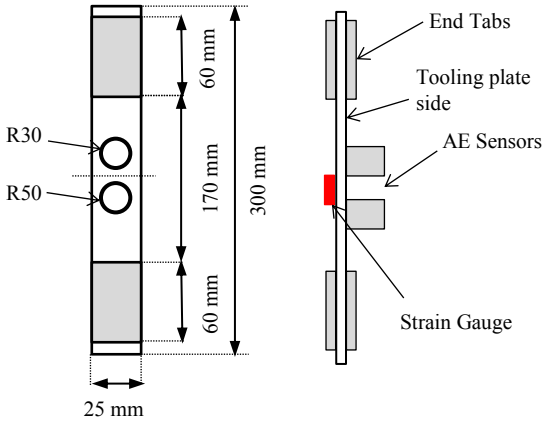


(iii)

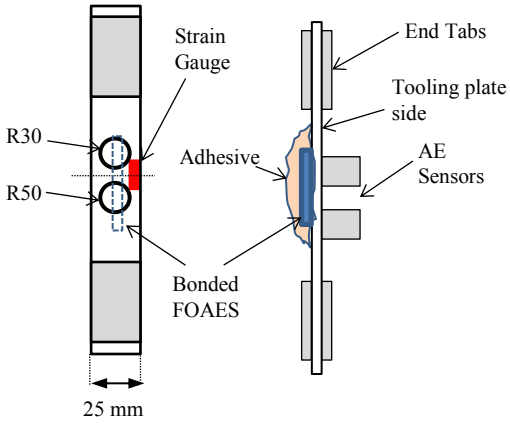


(iv)

**Figure 40 Details of the samples prepared for the tensile test. Figure 40 (i) shows three sensors prepared for the test. Figure 40 (ii) shows the position of the FOAES and of the strain gauge. Figure 40 (iii) gives a schematic of the relative position and dimensions of all the elements. Figure 40 (iv) shows the position of all the elements for the surface mounted FOAES.**

### 3.6.2 Test setup

The universal testing machine was equipped with a load cell of 100 kN and wedge-action grips. Analogue outputs were extracted from the tensile machine via BNC cables with scales from 0 to 10 V. These outputs were correlated with the load and displacement of the machine representing ranges from 0 to 100 kN and from 0 to 50 mm respectively. The linear speed configured during the tests was 2 mm/min.

The two benchmark piezoelectric AE sensors were connected to pre-amplifiers 2/4/6, and the embedded FOAES to the Box A. The FOAES was illuminated by the HeNe laser. The three outputs were subsequently connected into a commercial 4-channel AE PCI-2 acquisition system procured from Mistras, USA. This 4-channel PCI-2 system had the same phantom power supply for powering the two pre-amplifiers and the Box A as the aforementioned AE2A amplifiers. The signal collected from the PCI-2 card together with the parametric signals from the tensile machine (voltage and displacement) were acquired and saved in real time by the windows-based AE software AEwin® developed by Mistras, USA. The data from the strain gauge was synchronised, logged and stored in another computer placed next to the AE system.

The configuration of the acquisition of the PCI-2 system was carried out by setting up several parameters including: (i) amplification; (ii) frequency and anti-aliasing filtering; (iii) acquisition rate; (iv) signals filtering attending to different criteria as threshold, energy, PDT, HDT, HLT and maximum hit duration; and (v) other features such as classification or clustering which were not used.

The acquisition rate was set to 2 MSamples/s for the three channels, with bandpass filter from 100 to 500 kHz. To minimise the acquisition of signals not related to damage occurring into the composite laminate during the tensile tests, the threshold level or minimum amplitude of the AE events was experimentally calculated to be 50 dB in the case of the benchmarking sensors and 60 dB for the FOAES. Finally and with regards to the wave filters, a configuration suitable for high-dumping metallic materials (to be known as AEwin 1) was experimentally found to work well when acquiring AE signatures from the FOAES. The reason for this was the longer time required for the FOAES to get damped and excited when compared with conventional piezoelectric sensors, and thus, longer PDT and HDT were

required [50]. A second configuration recommended for composites and non-metallic material was tested as well for comparison purposes [50] (to be known as AEwin 2). A table comparing both configurations is shown in Table 5.

**Table 5 Description of the configurations AEwin 1 and AEwin 2.**

| | System Configurations | |
|---|---|---|
| **Parameter** | **AEwin 1** | **AEwin 2** |
| Laser- FOAES | HeNe | |
| Bandpass filter | 100/500 kHz | |
| Acquisition Rate | 2 MSamples/Channel | |
| Threshold level | - R30α and R50α: 50 dB<br>- FOAES: 60 dB | |
| PDT (μsec) | 300 | 20 |
| HDT (μsec) | 600 | 200 |
| HLT (μsec) | 1200 | 300 |

The input and output of the FOAES were joined to FC/PC patch cables by the fusion splicer. The sample was then secured in the jaws of the tensile machine taking special care not to trap or break the optical fibres of the FOAES. The optical fibres were connected to the laser and Box A (input and outputs respectively). Coupling agent was then applied, and the benchmark piezoelectric sensors secured using duct tape. Finally, the cable of the strain gauge was connected to one channel of the acquisition card. The photographs in Figure 41 show the experimental setup.

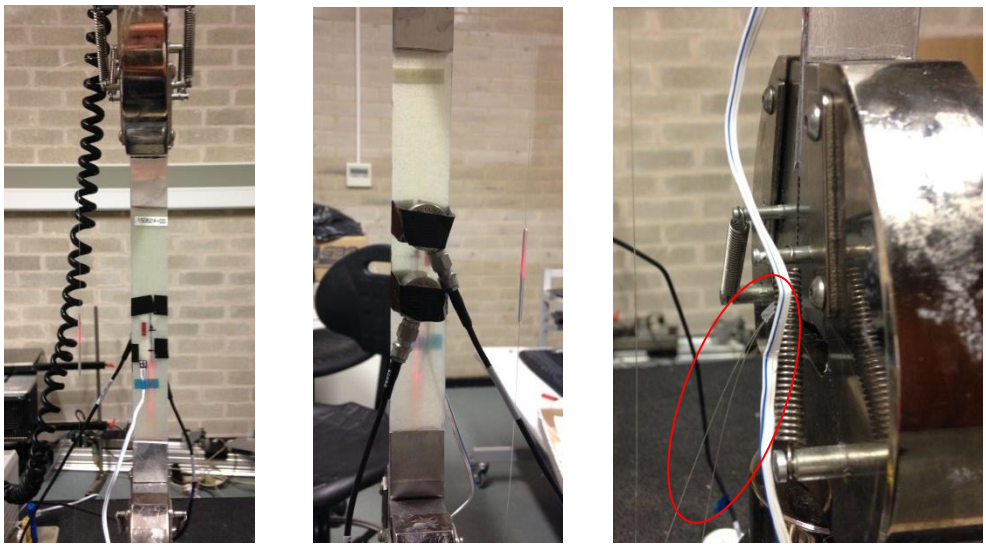

(i) (ii) (ii)

**Figure 41 Pictures of the setup. Figure 41 (i) shows some light bleeding out from the embedded FOAES and the strain gauge. Figure 41 (ii) illustrate how the benchmark sensors R30α and R50α were secured. Figure 41 (iii) shows the optical fibres coming out from the universal testing machine's jaws.**

When the entire system was correctly connected, mechanical pencil lead tip breaks were performed to ensure that all the sensors were coupled correctly and acquired AE signals. If successful, a first test was run from 0 to 0.3% strain using the configuration AEwin 2. The system was then returned to the original position and the configuration changed to AEwin 1. Then, pencil breaks and a second tensile test to breaking load was performed. In the case of the control samples without FOAES, just the pencil breaks and tensile test to breaking load were performed using the configuration AEwin 2. The test details are summarised in Table 6.

**Table 6 Detail of the test performed**

| | **Samples with FOAES** | | **Samples without FOAES** |
|---|---|---|---|
| Pencil Breaks? | Yes | Yes | Yes |
| Configuration | AEwin 2 | AEwin 1 | AEwin 2 |
| Test Performed | Strain test up to 0.3% | Strain test to breaking load | Strain test to breaking load |

# CHAPTER 4

## Sensors Manufacturing and Packaging

# 4 Sensors Manufacturing and Packaging

## 4.1 Introduction

The different parameters which were found to influence the performance of the FOAES during the manufacturing process are discussed. Several configurations changing the aforementioned parameters were set to understand the relationship between the different manufacturing variables and the properties of the produced FOAES. A region of interest was defined to classify the sensors with respect to the obtained losses and coupling ratio. Five different configurations used for producing FOAES within the region of interest were defined. FOAES manufactured under the different five configurations were Type-I packaged (bonded on-glass) and acoustically pre-assessed. This enabled the selection of the manufacturing parameters of the most responsive sensor to carry on with the next stages of the project (Type-II packaging and embedding). Finally, the methodology and the hardware commissioned for precisely positioned the sensor over a glass rectangle (packaging Type-I) and for inserting the FOAES into a glass capillary (packaging Type-II) will be in-depth described.

## 4.2 Sensor Manufacturing

The manufacturing process required two different classes of parameters to be considered; firstly the physical properties of the optical fibres and their physical preparation before manufacturing, and secondly the manufacturing parameters employed during the operation of the customised commercial FBT rig. The main objective of this part of the project was to understand the relationship between these two sets of parameters for producing the FOAES.

Due to the sensor being intensity-based, the first stage in the manufacturing was to narrow down the configurations capable of consistently producing sensors with losses lower than -2 dB and coupling rate between 40 and 60%. These limits were obtained experimentally, as sensors with losses higher that this value made the SNR produced by the interrogation units too low for being acceptable to be used in sensing applications. With respect to the coupling rate and due to the differential nature of the interrogation unit, a very unbalanced FOAES made the optical power of one of the inputs of the detector very small and nearly not distinguishable from the background noise decreasing the overall sensitivity.

### 4.2.1 Manufacturing variables

The output variables from the manufacturing process were defined as: (i) excess losses, (ii) coupling rate, (iii) tapered length and subsequently diameter of the tapered region, and (iv) repeatability or how consistent were the results when the inputs of the process were kept constant.

With respect to the inputs, the following parameters were controlled: (i) fibre type and stripped length; (ii) timers controlling the pre-drawing, pre-heating and post-elongation; (iii) torch size; (iv) torch relative height to the fibres plane; (v) torch initial distance to the fibres (initial distance to the heat source); (vi) torch movement speed; (vii) $H_2$ flow rate; (vii) puller-to-puller initial distance; and (viii) pulling speed.

In addition, several strippers and cleaning methods were tested. The results were assessed first in a JEOL 6060 Scanning Electron Microscope (SEM) and later validated visually by the presence of burn signs or incandescent dots during the manufacturing process (these meant that the fibres were not completely clean and some thermoplastic was burning, creating

inclusions and degrading the overall performance of the fibres as explained in the literature review). Some micrographs showing the results are included in Figure 42.

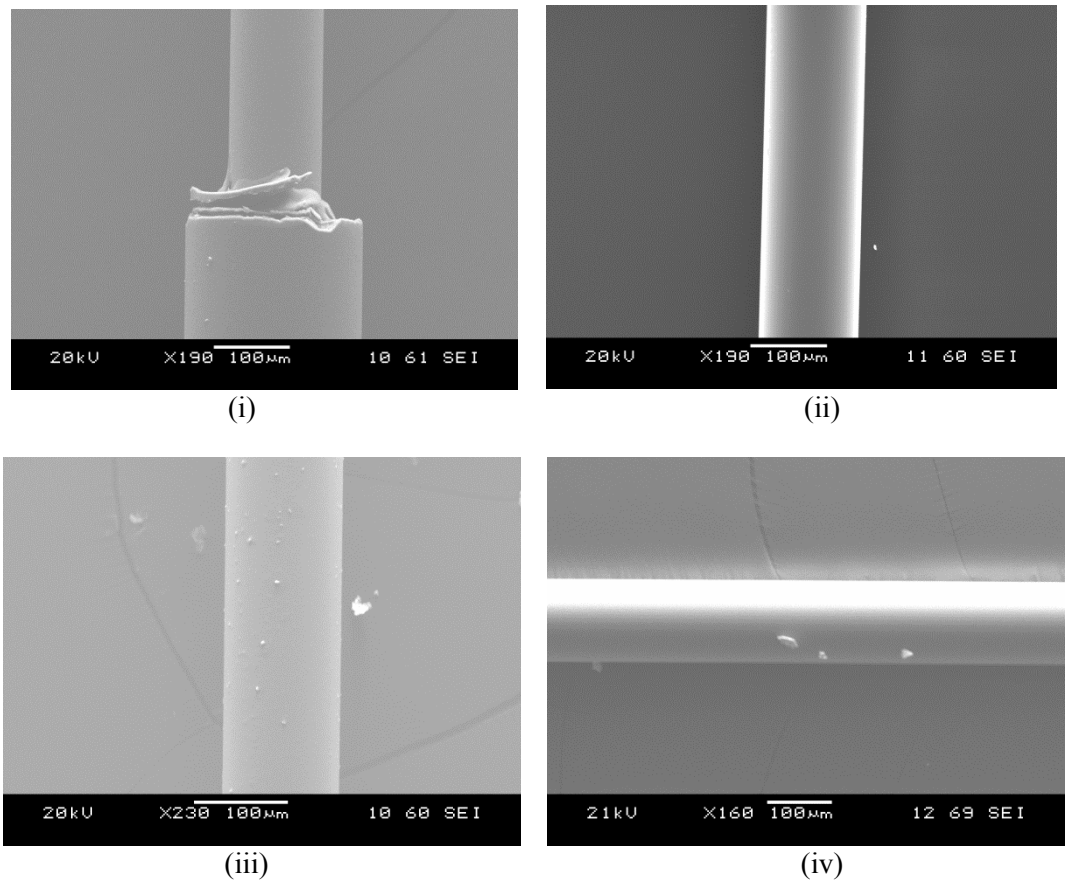


**Figure 42 SEM inspection of several optical fibres stripping methods;(i) and (ii) shows a good stripping process without any relevant thermoplastic residues; (iii) and (iv) shows two section of optical fibres containing several residues.**

The best results were obtained by using a Miller FO 103-D-250 optical stripper followed by two acetone-impregnated lint-free tissues, one isopropanol-impregnated lint-free tissue and one last dry lint-free tissue. In addition, to avoid contamination during the manipulation gloves were used during the whole process.

The optimal pulling speeds were found to be correlated with the hydrogen flow rate by a very tight margin. Once the hydrogen flow rate was set, the speed had to be adjusted in such a way that the amount of heat introduced was in equilibrium with the energy absorbed by the

process. Thus, the temperature was kept as close as possible to the melting point. Higher speeds created flawed and very brittle tapered region, which normally broke during the manufacturing process. Lower speeds on the other hand introduced too much heat in the process and the tapered region started to flow by gravity, ending up with a non-straight and high loss sensor.

The pre-draw and pre-heating were adjusted in the same way. For a defined torch and hydrogen flow rate these parameters were adjusted to avoid fracture or melting at the beginning of the process. This was visually controlled by observing the tapered region and monitoring power drops in the input power, as shown in Figure 43.

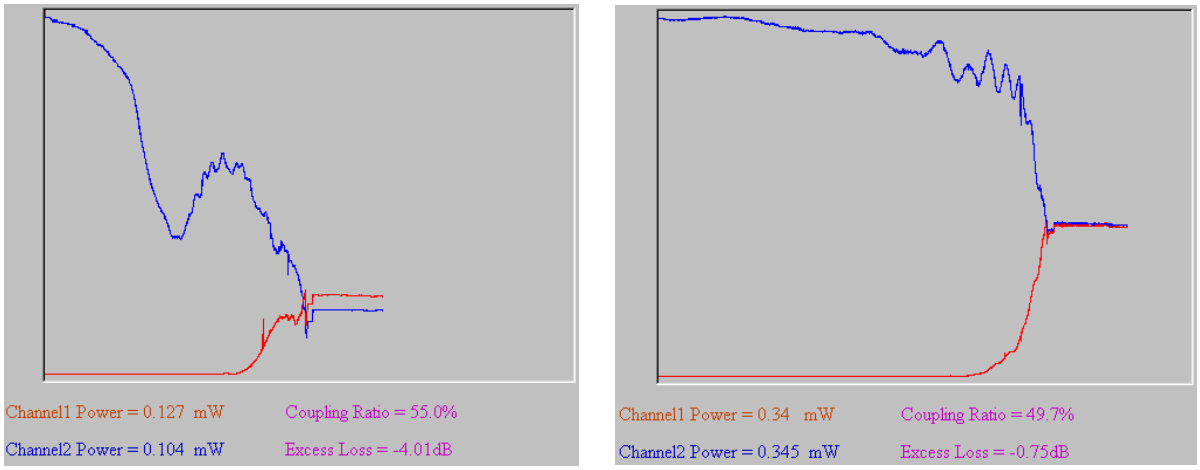


(i) (ii)

**Figure 43 Detail of two tapering process as obtained from the control computer; (i) shows a coupling process where the power decreased from the beginning, due to an incorrect setup; (ii) shows a correct process with a very steady input energy which dropped just when the power transmission started (low losses).**

The fibres knot-to-knot distance, defined as the length where the optical fibres are suffering lateral force enabling the mutually fusion process, was found to be related with the stripped length and the puller's initial distance. The size of the flame had to be contained well inside the knots to avoid melting them and thus, stopping the lateral force and subsequently breaking the sensor. It was experimentally found that an initial puller's distance of 50 mm with a 40

mm stripping length on the optical fibres developed knot-to-knot distances from 14 to 17 mm, which worked fine with the majority of the setups. These parameters were then fixed to the aforementioned values to reduce the number of variables.

The inputs were modified in a progressive manner to understand the changes in the outputs. The results of the first 292 sensors organised as coupling ratio VS losses is represented in Figure 44.

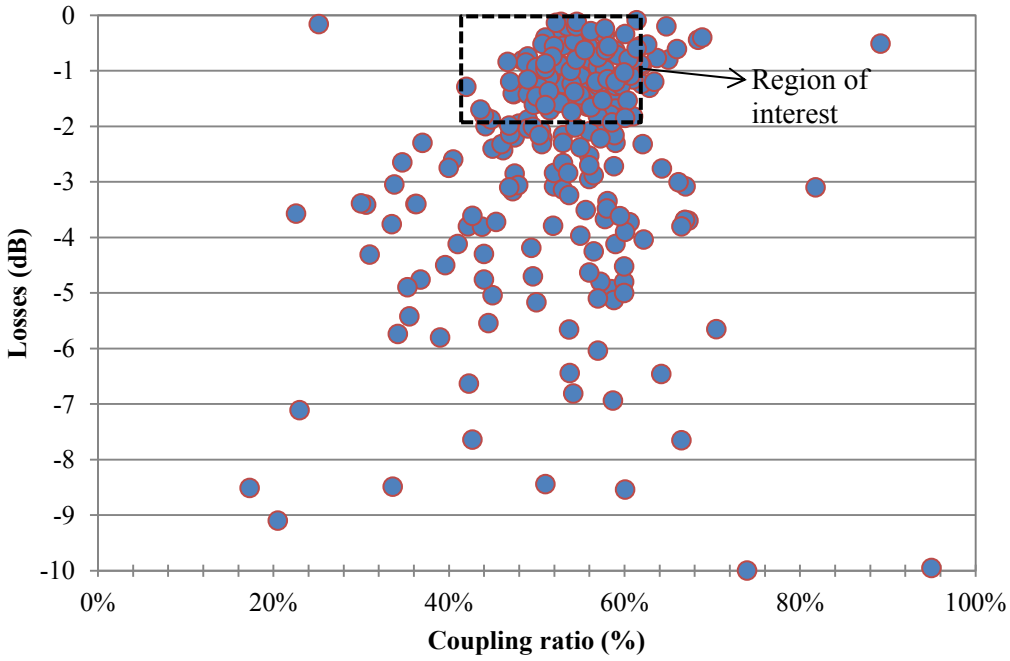


**Figure 44 Detail of the first 292 manufactured sensors, represented by their coupling rate and loses. In the graph, the area where the sensors presented the defined properties has been signalled.**

It was experimentally found that some configurations were resulting in sensors manufactured within the desired region of interest. However, the repeatability of configurations providing "good" couplers were found to depend on the optical fibre used as row material as indicated in Figure 45. Optical fibres with higher numerical aperture and tighter tolerances in this parameter were found to produce sensors exhibiting lower losses. A numerical comparison between the results obtained with the SM630HP (tighter tolerances in the variability of the

numerical aperture) and SM600 (higher tolerances in the numerical aperture) is given in Table 7 and Figure 46.

**Table 7 Average and Standard Deviation of the losses and coupling rate obtained when sensors were manufactured by SM630HP and SM600.**

| | Losses (dB) | | Coupling ratio (%) | |
|---|---|---|---|---|
| | **Average** | **Standard Deviation** | **Average** | **Standard Deviation** |
| **SM630HP** | -1.10 | 0.89 | 55.69 | 7.42 |
| **SM600** | -3.50 | 2.76 | 51.06 | 11.41 |

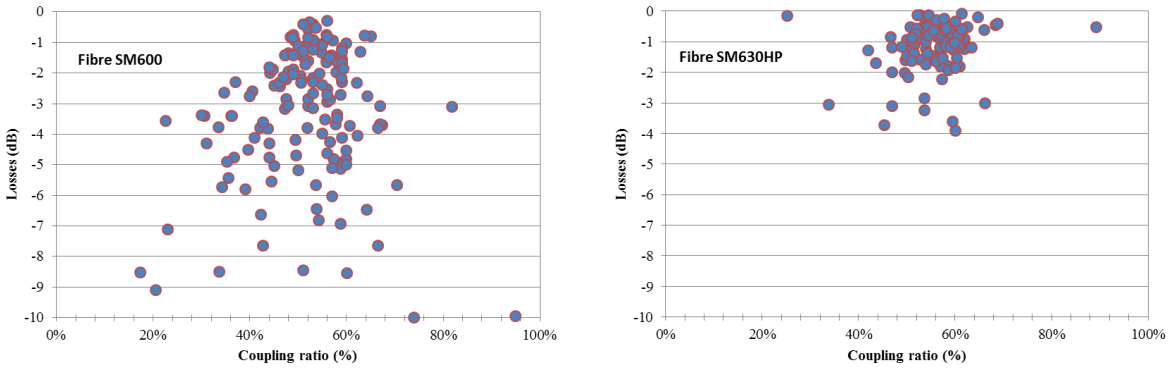


(i) (ii)

**Figure 45 Representation of the sensors depending on the optical fibre used as row material; (i) shows the more scatter characteristics obtained with the SM600 while (ii) represent the more clustered characteristics obtained by the SM630HP.**

For the configurations providing consistently sensors inside of the defined region of interest, the geometrical characteristics of the tapered section was also inspected and measured. Because the sensor response was based in the coupling of external perturbations into the tapered length, repeatability on the geometrical characteristics for sensors with the same manufacturing setup was desired to ensure same sensor acoustic response. The sensor's geometry was simulated to that of the hourglass shape as shown in Figure 47, and the parameters L, Ø, $\alpha 1$ and $\alpha 2$ were measured with an optical microscope at a magnification of

20X as detailed in Figure 47. The adopted criteria was to define Ø as waist or minimum diameter found in the tapered region, L as tapered length or the distance to the lateral points at both sides of the centre where the diameter increases by 1.5 times the waist diameter, and exit angles $\alpha_1$ and $\alpha_2$ as the angles at the left and right respectively of "L".

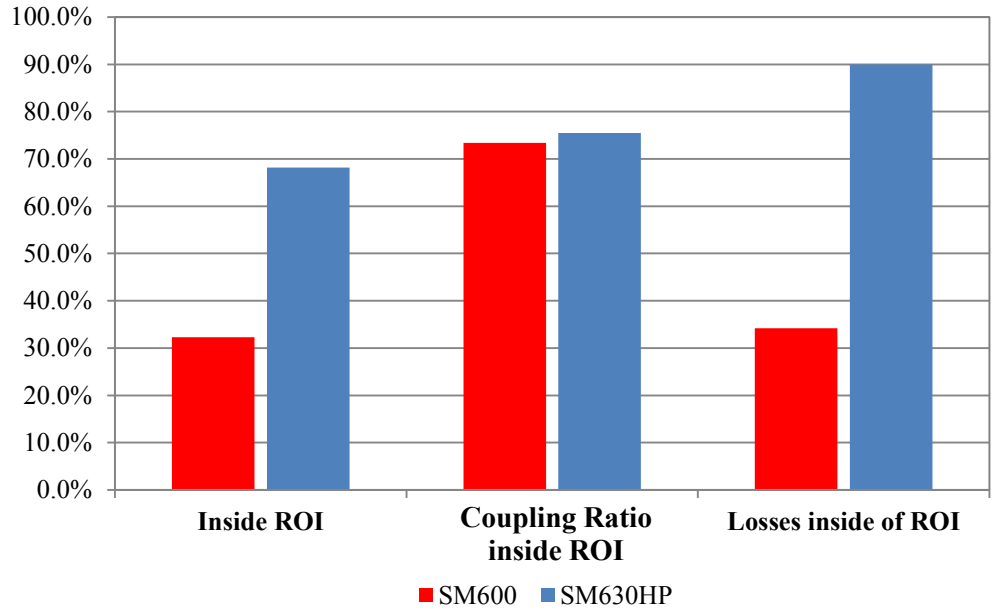


**Figure 46 Percentage of sensors manufactured by the SM630HP and SM600 which were successfully located inside of the region of interest (ROI), shown as the first data series. In addition, the percentages of sensors within the correct coupling ratio from 40 to 60% and with losses below-2dB are shown as second and third data series respectively.**

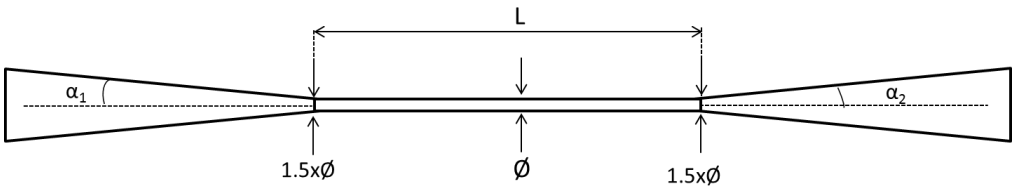


(i)

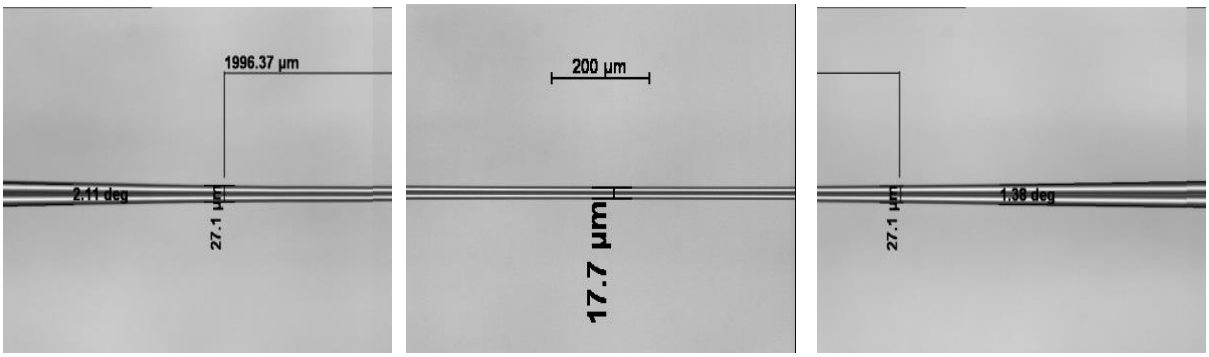


(ii) (iii) (iv)

**Figure 47 Geometrical simplification of the sensor's tapered length; (i) schematic of the defined parameters of the tapered length; (ii) to (iv) show the measurements of a real sensor.**

A representation of the parameters stated above is presented in Figure 48. A clear relationship was found between waist diameter and tapered length with the manufacturing parameters pulling speed, pulled length and torch size. This can be explained as the increase in the length was achieved by "extracting" material from the volume below the torch. Therefore, the longer the tapered length the biggest the decrease in diameter, and the wider the flame, the bigger the volume of material available for the tapering process. However, there was some degree of geometrical variability from sensor to sensor when the same setup was applied. In addition, the sensor was found to be non-symmetric or not "mirror image", presenting different exit angles at left and right sides. These variabilities were found even in sensors using the same manufacturing parameters and setup. This was speculated to be mainly related to the lack of brushing movement in the torch.

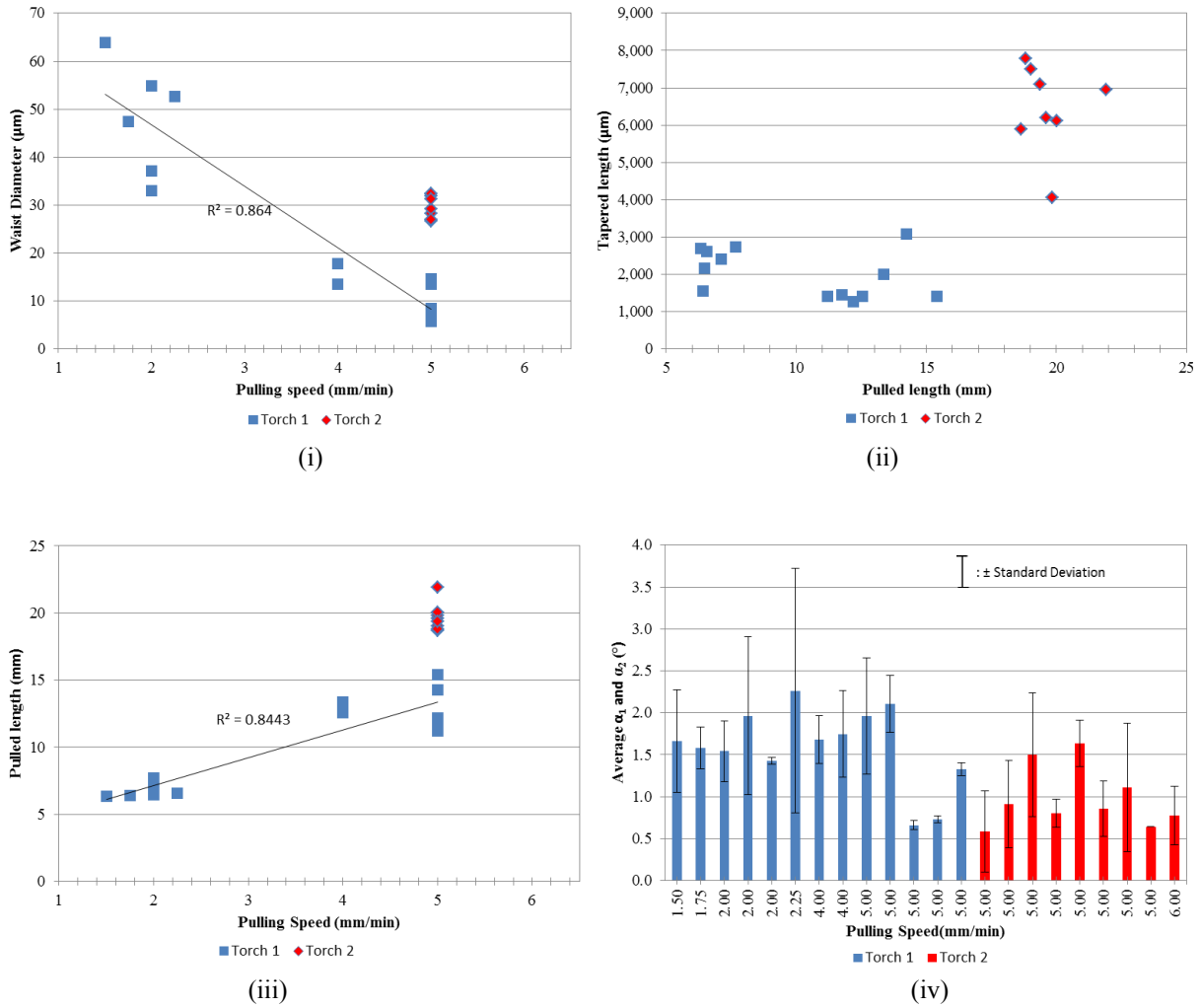


**Figure 48 Graphical representation of the measured parameters of the sensors (sensor's waist, tapered length and lateral angles α1 and α2). Figure 48 (i), (ii) and (iii) show the relationship between the obtained waist diameter and tapered length with the manufacturing variables pulling speed and pulled length (speed and distance traversed by the pulling stations during the manufacturing process of each sensor) and torch size. Figure 48 (iv) represent the average of each sensor's exit angles α1 and α2 together with the respective standard deviation; an smaller standard deviation meant higher symmetry in the sensor geometrical characteristics.**

The extensive experimentation enabled the definition of five configurations which consistently produced sensors within the defined region of interest, as are described in Table 8. The rest of the manufacturing parameters were found to be the same for the five configurations and are summarised in Table 9.

**Table 8 Variable parameters of the five acoustically tested configurations.**

| Configuration | Torch | Speed | H2 (sccm) |
|---|---|---|---|
| **1** | **1** | **4** | **150** |
| **2** | **1** | **5** | **165** |
| **3** | **2** | **5** | **210** |
| **4** | **2** | **5** | **220** |
| **5** | **2** | **6** | **220** |

**Table 9 Fixed manufacturing values of the acoustically tested sensors for all the configurations detailed below.**

| Parameter | Value |
|---|---|
| Fibre reference | SM630HP |
| Pre-drawn (mm) | 0 |
| Pre-heating (ms) | 2,500 |
| Elongation (mm) | 100 |
| Post-elongation (ms) | 100 |
| Torch Height (mm) | 6.5 |
| Torch Speed (mm/min) | 1200 |
| Puller-To-Puller distance (mm) | 50 |
| Stripped length (mm) | 40 |

### 4.2.2 Sensor's acoustic assessment

As previously discussed, five configuration producing sensors under the region of interest were selected. A total of 33 sensors were acoustically assessed on an aluminium plate of 500x500x3mm. The excitation methodology discussed in the point 3.5 was applied: frequency sweep of sinuses (100 to 500 kHz every 20 kHz) to characterise the frequency response. For simplification purposes as the goal of these tests was to find the sensors with the higher overall response, it was decided to test just with the Box A laser.

Due to the fact that the sensors were surface mounted, it was not possible to perform a direct or parallel comparison with the R30α and R50α (it was physically impossible to place both

sensors in the same central point). Therefore, two sensors R30α and R50α were characterised using the described methodology of sweeping frequency but just at angle 0°. These sensors were set up as discussed in Chapter 3, setting up a total amplification of 49 dB.

Frequency Sweep Test

In order to facilitate the interpretation of the data, each configuration was represented by averaging the response of all its sensors at each direction in two different graphs: one graph showing the response when excited by the R30α, and a second graph when excited by the R50α.

The results from "Configuration 1" to "Configuration 5" are given from Figure 49 to Figure 53 respectively. The results of one R30α and one R50α are shown in Figure 54.

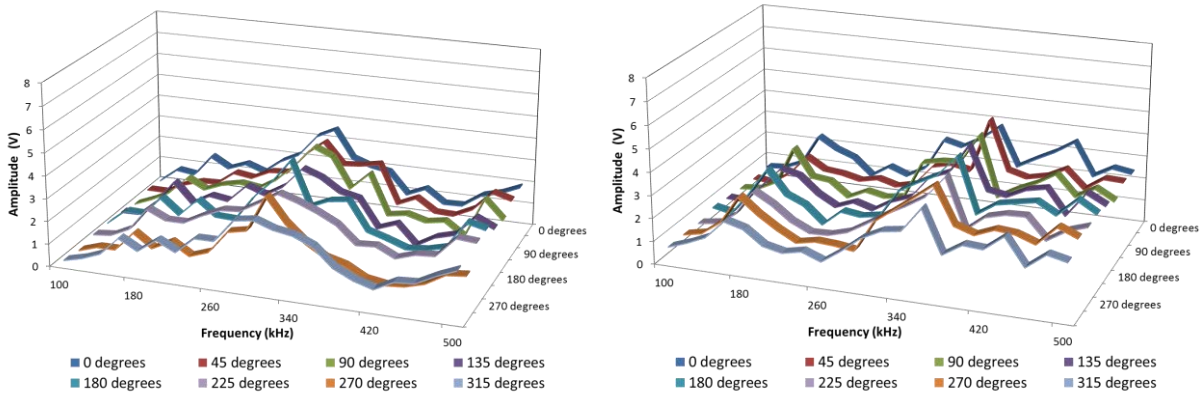


(i) (ii)

**Figure 49 Response of the "configuration 1" sensors when the piezo-emitters R30α (i) and R350α (ii) were used as excitation source.**

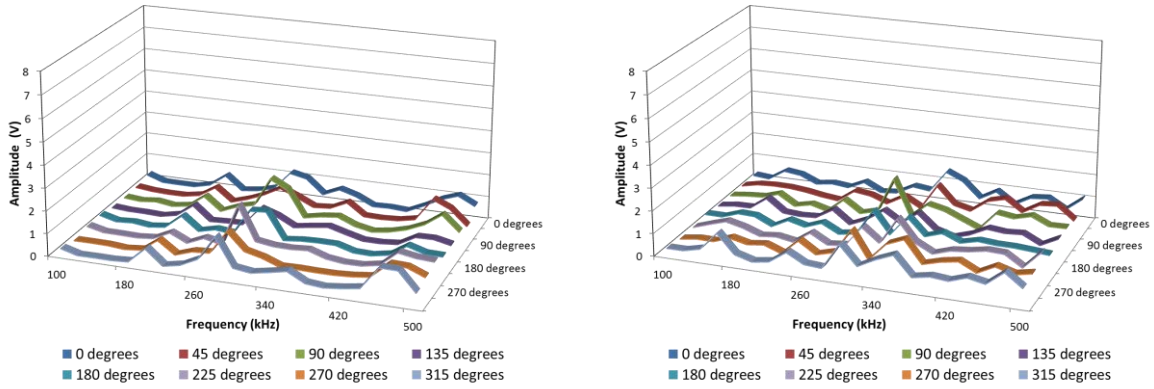


(i) (ii)

**Figure 50 Response of the "configuration 2" sensors against the piezo-emitter R30α (i) and R350α (ii).**

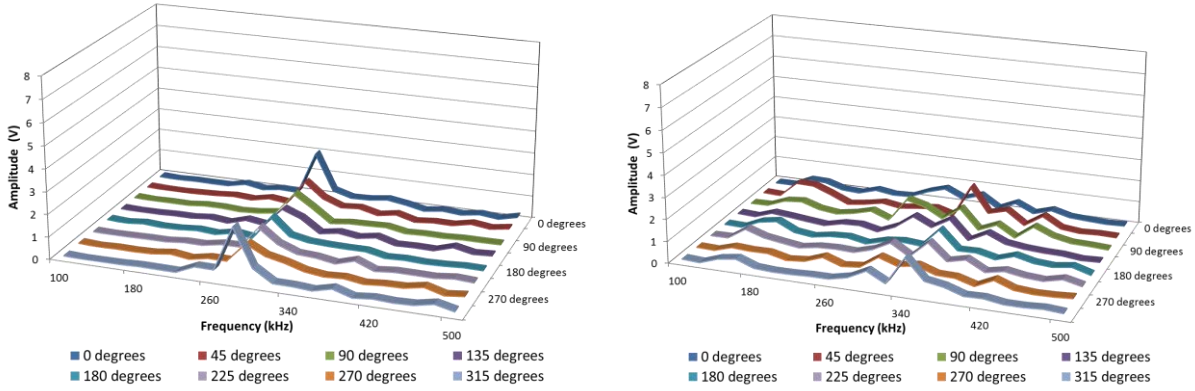


(i) (ii)

**Figure 51 Response of the "configuration 3" sensors when the piezo-emitters R30α (i) and R350α (ii) were used as excitation source.**

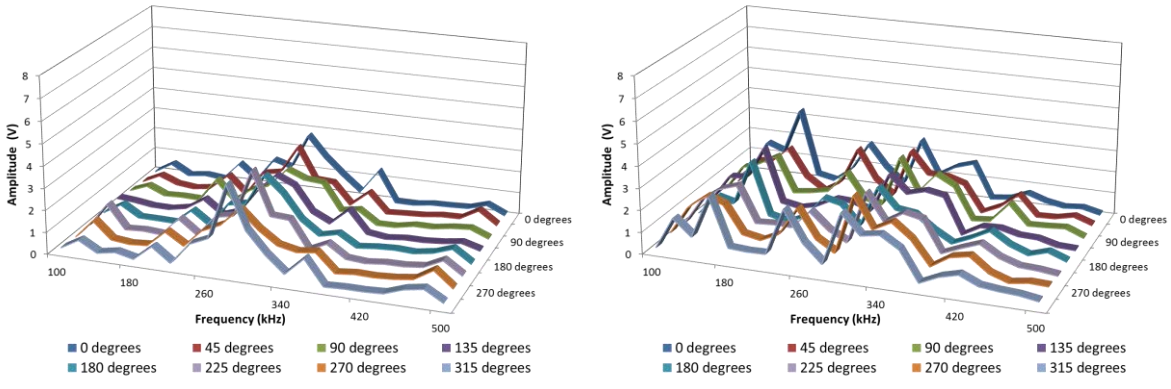


(i) (ii)

**Figure 52 Response of the "configuration 4" sensors when the piezo-emitters R30α (i) and R350α (ii) were used as excitation source.**

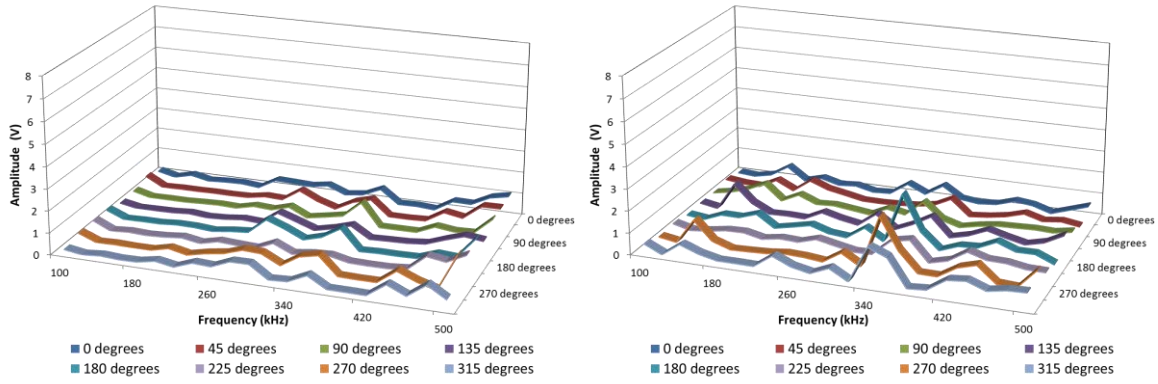


(i) (ii)

**Figure 53 Response of the "configuration 5" sensors when the piezo-emitters R30α (i) and R350α (ii) were used as excitation source.**

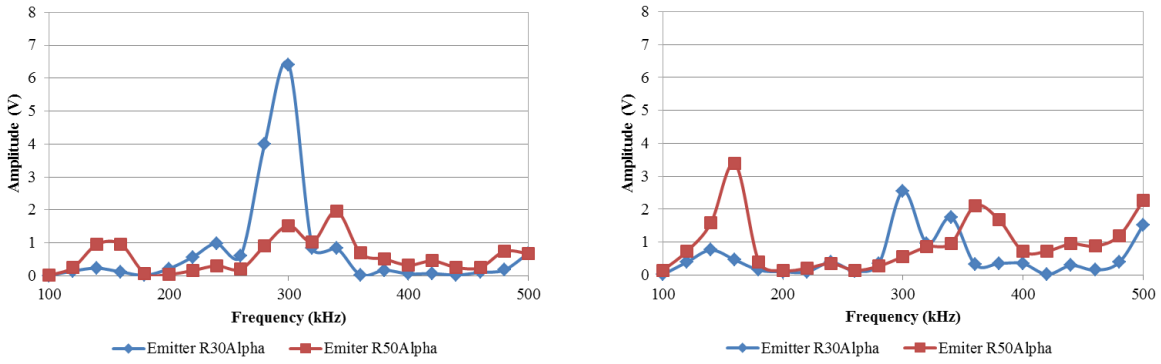


(i) (ii)

**Figure 54 Response of the piezoelectric sensors R30α and R50α performing as sensors against the piezo-emitter R30α and R350α at 0°. Figure 54 (i) shows the response of the R30α, while Figure 54 (ii) shows the response of the R50α.**

It was found that some configuration 2, 3 and 5 produced a very poor response when compared with Configuration 1 and 4. When the response of Configuration 1 and 4 were compared, despite the fact that Configuration 1 was showing a slightly better performance, the standard deviation or variability from sensor to sensor was nearly double that of Configuration 4. In practice, this meant that some sensors of Configuration 1 were nearly flat while others were presenting a very high response as shown in Figure 55. The reasons behind this high variability of Configuration 1 were not well understood. Therefore, it was decided that Configuration 4 presented the better characteristics for carrying on with the next stages of the project (the best response and lower variability from sensor to sensor).

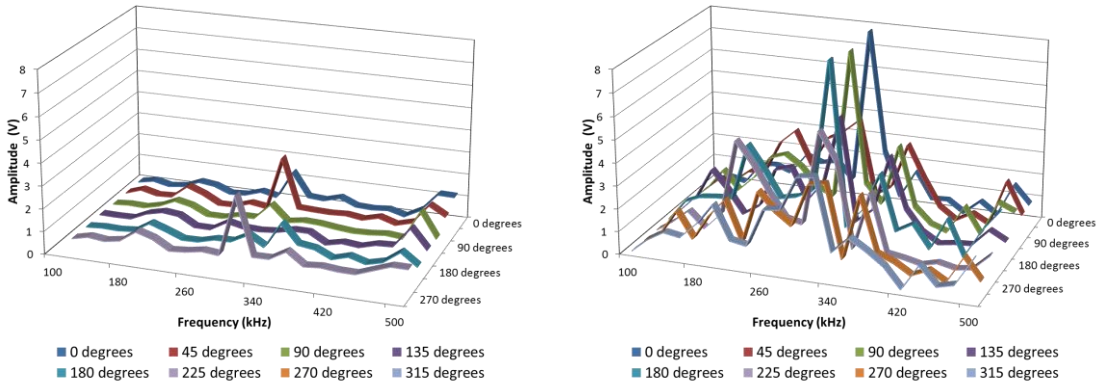


(i) (ii)

**Figure 55 Response of two "Configuration 1" sensors under the excitation of the R30α. The sensor on the left (i) presented a very poor response while the one on the right (ii) was nearly saturating the output at 300 kHz.**

With regards to the fidelity or frequencies where the main harmonic was located as the sensors were excited by pure sinusoidal signals, all 5 configurations were found to reproduce with extremely high accuracy the frequency of the emitter. In the case of the Configuration 4, the average frequency of all the sensors and the standard deviation are shown in Figure 56.

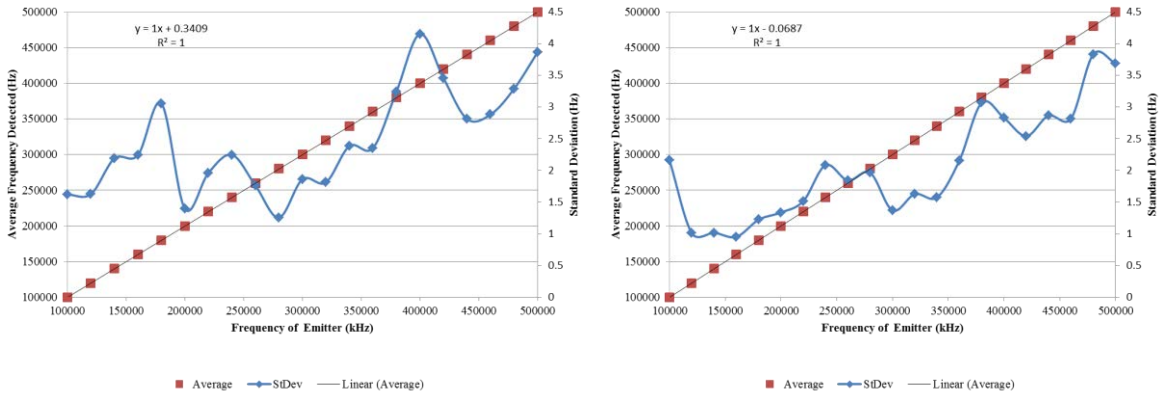


(i) (ii)

**Figure 56 Detail of the fidelity of the sensors under Configuration 4. Figure 56 (i) shows the data when a R30α is used as emitter, while Figure 56 (ii) shows the same information when a R50α is used as emitter The data has been averaged by frequency, being each point the average of all the sensors at all the tested direction (0 to 315°). The standard deviation has been superimposed with the scale in a secondary axis. It has to be noted that the linear fitting of the averages have an $R^2$ of 1, and that the standard deviations are below 4.5 Hz.**

### 4.2.3 Configuration selection

After all the analysis was performed and as stated in the previous section, Configuration 4 was found to be the best candidate for progressing to the next stage of the project. The sensors produced under this configuration were consistently inside of the region of interest presenting the best compromise between response and repeatability under the excitation of both piezo-emitters. However and as it was noticed before, this variability from sensor to sensor when comparing the amplitudes at the same frequencies still was noticeable, as showed in Figure 57. It was speculated that this difference was boosted by the non-geometrical reproducibility which was inherent to this manufacturing process (FBT without brushing movement).

All the configurations were found to present excellent fidelity matching the frequencies of the emitter at all the frequency ranges.

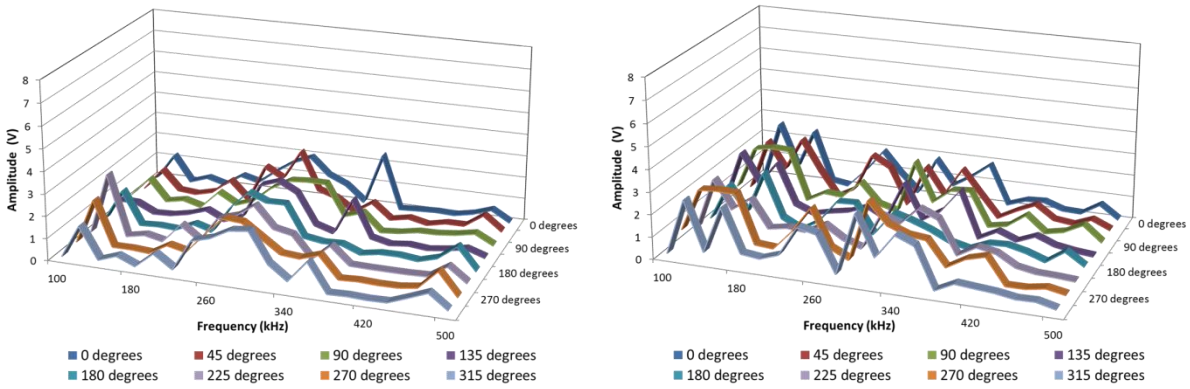


**Figure 57 Standard deviation of the average response of "Configuration 4" sensors. Graph on the left (i) shows standard deviation of average response when excited by piezo emitter R30α while the graph on the rigth (ii) shows the same information when excited by piezo emitter R50α.**

## 4.3 Sensor packaging

One of the objectives of the project was to ensure that a robust packaging methodology was developed, and that the manufactured sensors could be introduced into the packaging with a high survival ratio. The packaging process consisted of the introduction of the tapered section of two fused optical fibres of diameter 250 microns each into a glass capillary of internal diameter of 700 microns, where the cross sectional area in the narrower point was below 100 microns and thus highly fragile. The process had to be done without: (i) contact or abrasion during the traversing process; (ii) without detaching the optical fibres from the pullers of the FBT machine to avoid bending and thus, a breakage of the sensor; and (iii) creating constrains during the manufacturing process.

### 4.3.1 Hardware description

To overcome all the objectives detailed above the FBT machine was accommodated, levelled and secured over a composite core breadboard damping surface. A bespoke platform using as many off-the-self components as possible was designed and constructed. This bespoke platform was lying over the working plane of the FBT machine, secured by two vertical custom machined parts to the breadboard damping surface. Different perspectives of the platform before and after the assembly are shown as Figure 58.

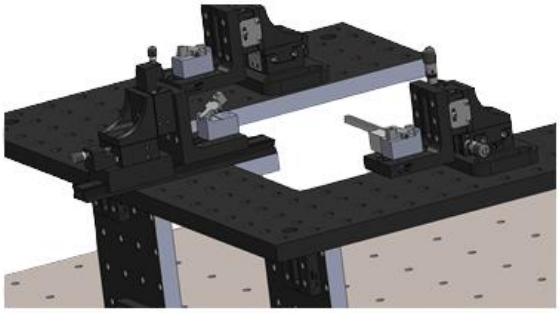

(i)

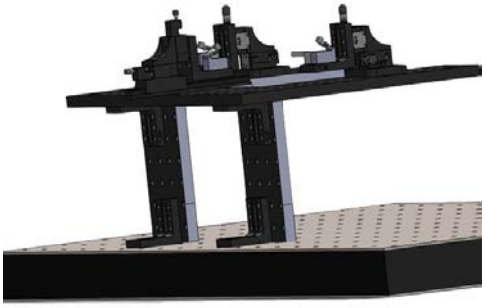

(ii)

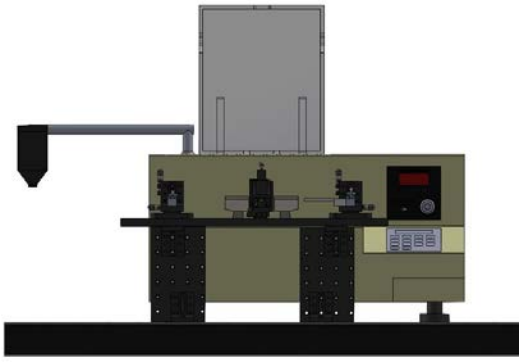

(iii)

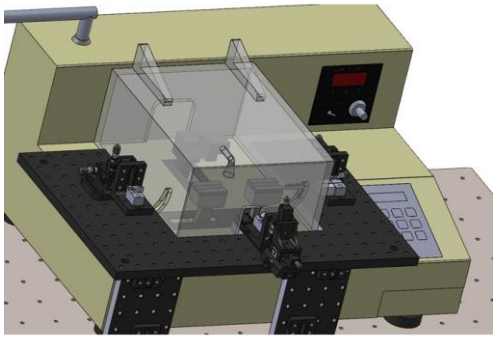

(iv)

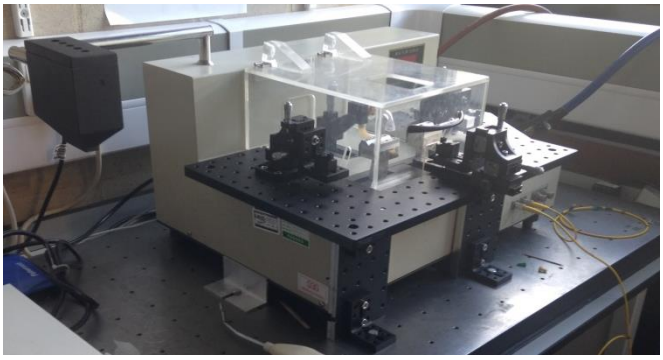

(v)

**Figure 58 Perspectives of the packaging platform. Figure 58 (i) and (ii) show the platform attached over the damping surface via two vertical aluminium custom parts and optical quality angular. Figure 58 (iii) and (iv) shows a frontal and a rotated isometric perspective respectively. Figure 58 (v) shows a real picture of the setup.**

As Figure 58 demonstrates, the machined of the custom platform enabled the FBT machine to operate without any changes, allowing the cover to be deployed or release. Two three-axis translation stages equipped with micrometres were attached onto the custom platform at both sides of the machine pullers. Two fibre clamps designed for single fibres of 250 microns of diameter were modified by re-machining the V-grooves making them suitable to accommodate two fibres. Then, the clamps were attached to the three-axis translation stages via optical quality aluminium angular profiles. A third two-axis translation stage was attached on the middle, between both machine pullers. This third translation stage was equipped with another machined clamp modified to accommodate the external diameter of the glass capillary

of 870 microns. The translation stage was deployed and retrieved from below the tapered region of the sensor via an optical dovetail rail.

The machined platform was then levelled parallel to the FBT drawing plane in such a way that the V-groove of the three-axis translation stages were aligned horizontally with the V-grooves of the FBT machine pullers. Finally, a custom machined aluminium part used as sliding fixture was attached to the right hand side three-axis translation stage, as shown in Figure 59 (vi). This sliding fixture was responsible to hold the capillary during the manufacturing process and until the packaging process was started. The dimensions and position of the slider were calculated to enable the cover to be deployed/withdraw without any contact. A schematic of the translation stages, sliding platform and clamps with the cover deployed is shown as Figure 59. A photo of the setup is given as Figure 60.

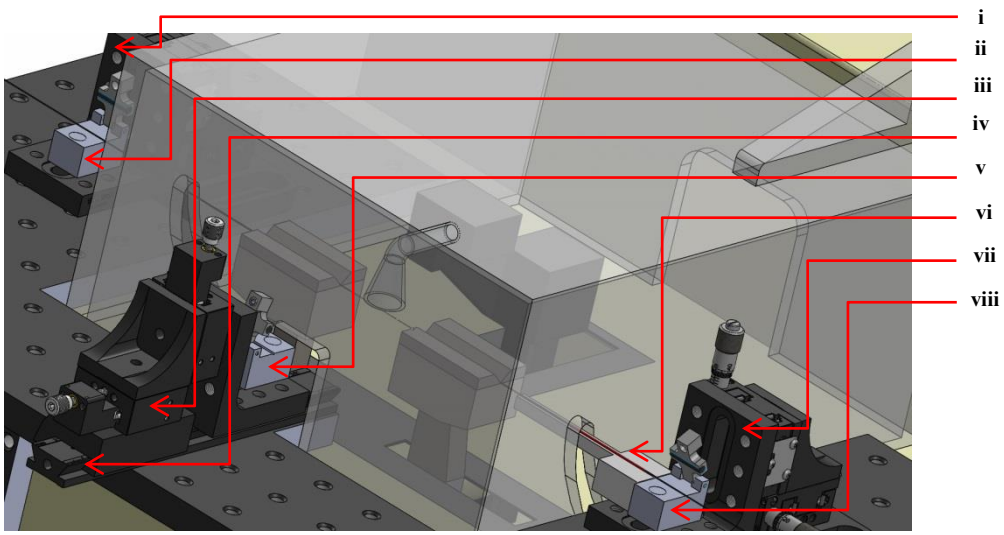


**Figure 59 Description of the custom platform. (i) Angular profile and left three-axis translation stage. (ii) Left modified clamp to accommodate 2 fibres. (iii) Two-axis translation stage. (iv) Dovetail slider position/release the packaging clamp under the manufactured sensor. (v) Central modified clamp for the 870 microns external diameter of the glass capillary. (vi) Sliding fixture, with the capillary accommodated onto the custom V-Groove. (vii) Angular profile for attaching the right modified clamp to the right three-axis translation stage. (viii) Right modified clamp to accommodate 2 fibres.**

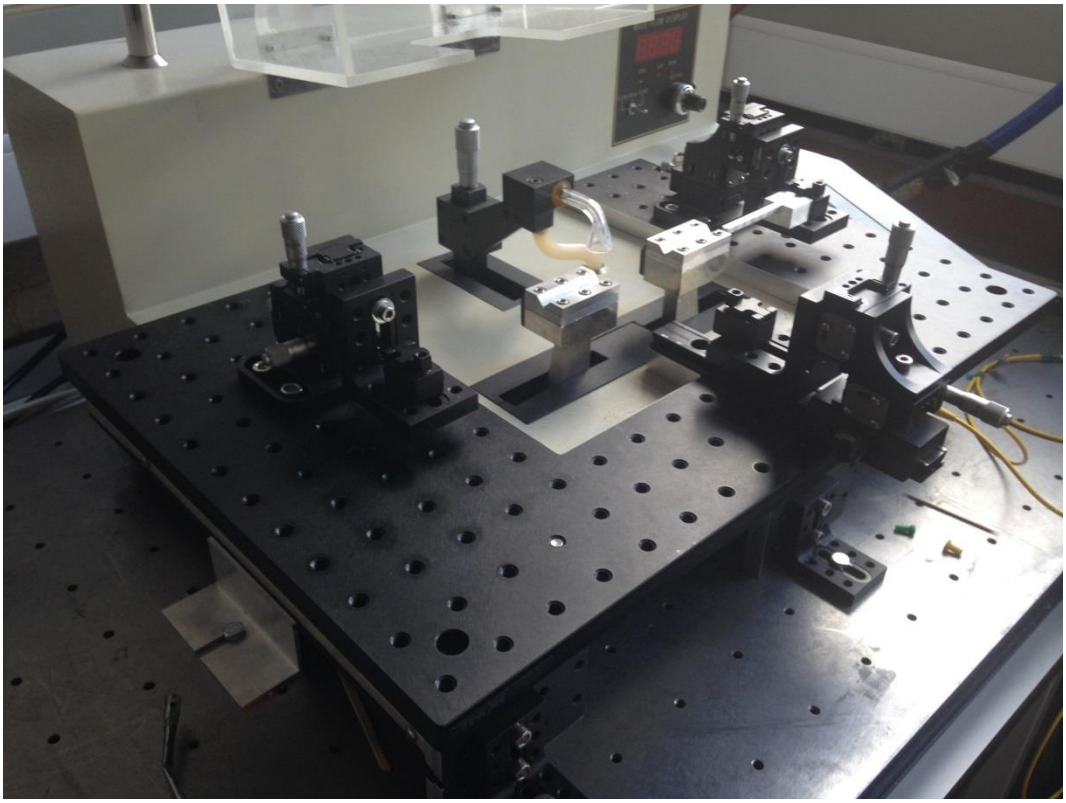

**Figure 60 Picture of the setup after being installed on the FBT machine.**

### 4.3.2 Packaging process step-by-step

The process started, as discussed in the previous chapter, with the optical fibres preparation. A central length of 40 mm of each fibre was stripped and appropriately cleaned. One of the fibres was inserted through the capillary and patch cables finishing in FC/PC connectors joined at both ends. The fibre was accommodated in the vacuum-pullers the FBT machine and the capillary traversed until resting on the sliding fixture on the right side known as detector side. The connector on the detector's side was attached to one port of the FBT machine's optical detector, and the connector at the other end of the optical fibre was connected to the laser.

The second optical fibre was joined to a third patch cable and connected to the second port of the FBT machine's optical detector; its unconnected extreme was traversed through the capillary until making both stripped lengths coincident. The fibres were then twisted two times and centred between the vacuum pullers, and the vacuum turned on securing the setup. A schematic of this starting position is shown in Figure 61.

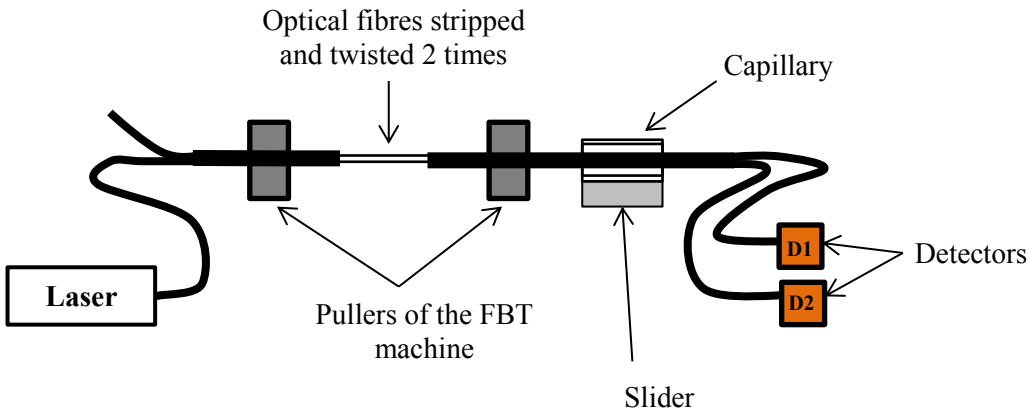


**Figure 61 Detail of the steps for the fibres preparation before staring the sensor manufacturing.**

The detectors were calibrated following the standard procedure for this machine, the hydrogen ignited and the cover deployed. The sensor was then manufactured with the desired configuration. As soon as the manufacturing process was completed, the hydrogen flow was cut to extinguish the hydrogen flame. After this point, the packaging process started by positioning the fibres in the V-grooves installed in the translation stages at either sides of the FBT machine's pullers (Figure 59 (ii) and (viii)), locking them in position. The translation stages were then adjusted to apply enough tension to make the fibres visually straight. The vacuum was then released, with the sensor and fibres held just by the clamps as shown in Figure 62.

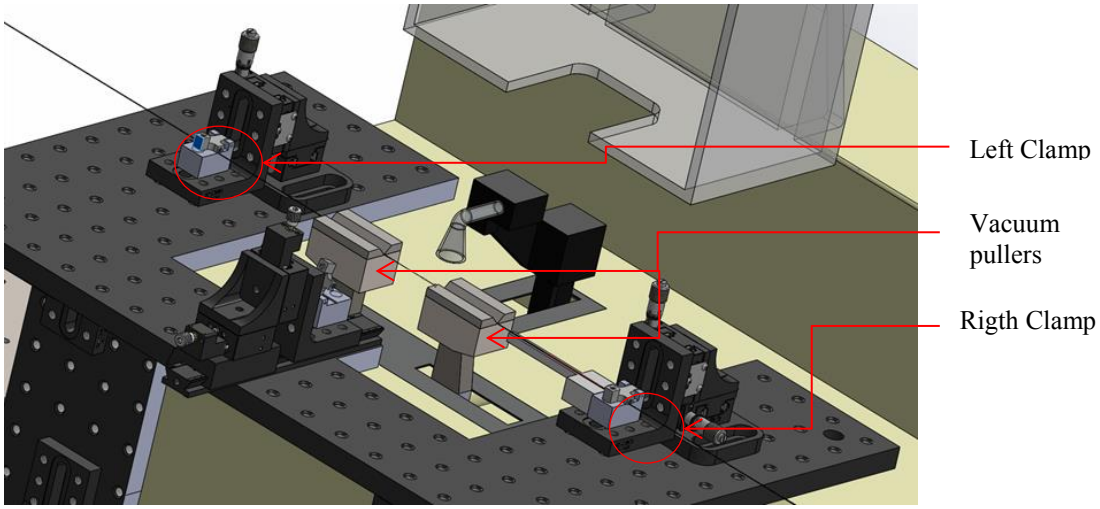


**Figure 62 Detail of the sensor hold by the fibre clamps located on the translation stages at either sides of the vacuum pullers.**

At that moment, the sensor was free to be lifted 750 microns actuating simultaneously the micrometers controlling the height of both left and right translation stages. After finishing the lifting of the sensor, the V-grooves of the slider and the left vacuum puller were aligned, so that the capillary could be traversed being always contained in a V-groove, and thus, avoiding the contact with the fibres. A detail of this alignment and traversing movement of the capillary is shown in Figure 63.

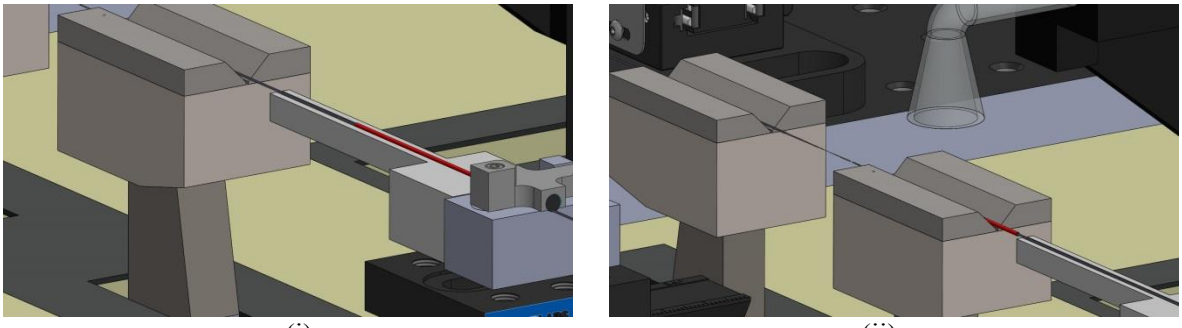

(i) (ii)

**Figure 63 Detail of the alignment of the V-grooves of the slider and vacuum puller, and of the traversing movement of the capillary. Figure 63 (i) shows the position of the capillary before starting the traversing movement. Figure 63 (ii) shows the capillary after being traversed to the V-groove of the first puller.**

Finally, the V-groove of the central translation stage is positioned underneath the tapered region of the sensor and lifted to the appropriate position and aligned with the V-grooves of the vacuum pullers. In this moment, the capillary could be traversed up to its final position covering the tapered region of the sensor, as shown in Figure 64. The position of the capillary was centred and then secured by releasing the clamp.

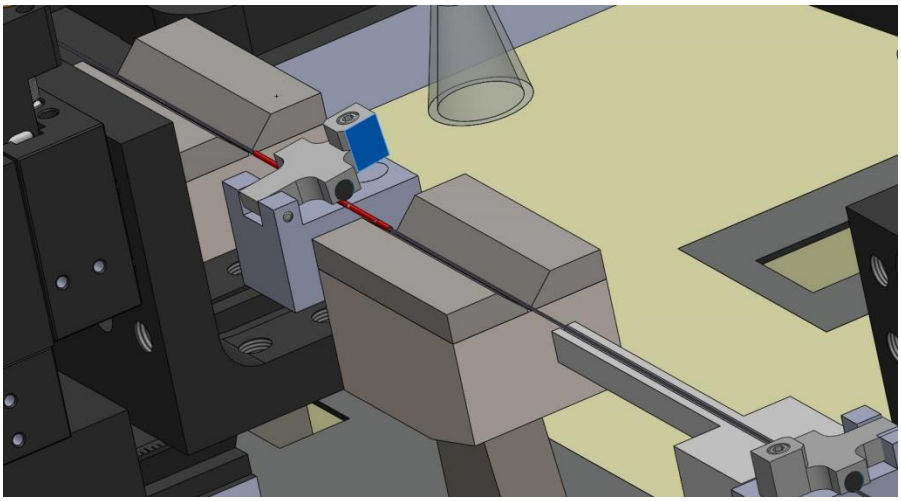

**Figure 64 Illustration of the capillary in its final position, and locked by the fibre clamp during the curing of the UV adhesive.**

The UV adhesive was a then applied at both sides of the capillary and cured by the application of the built-in UV light. Once cured, the sensor was completed and robust enough for being manipulated. The clamps of the three translation stages were retrieved and the sensor removed.

If the packaged used was Type-I the process was much simpler as capillary was not inserted, and therefore the sensor was manufacturing as a normal coupler. After finishing the manufacturing the packaging glass rectangular piece was positioned over the central

translation stage and secured using the fibre clamp. Once clamped, it was moved into position below the tapered region and lifted to the appropriate position. The UV adhesive was applied and then cured using the built-in UV light. After this point the sensor was finished, and was ready to be removed. In this type of packaging the tapered region was unprotected (bonded on the glass surface), so special care was taken during their storage or manipulation to avoid damaging them.

## 4.4 Chapter summary

The resulting outcome of several manufacturing configurations applied to two different optical fibres was investigated. Five different configurations were selected as producing sensors within the optimal region of interest, producing sensors with SNR high enough to be successfully interrogated during subsequent experiments. The five configurations were assessed by exciting the sensors at different directions, and in discrete frequencies from 100 to 500 KHz every 20 kHz. The configuration with the best overall performances was selected for the next steps of the research.

The developed novel packaging process was in-depth explained. It enabled the insertion of the FOAES in a glass capillary, without friction or mutual contact. The commissioned custom hardware was designed to perform the process without any modification in the FBT machine, and without creating any constrains in the manufacturing process.

# CHAPTER 5

# Sensors Characterisation and Embedding

# 5 Sensors Characterisation and Embedding

## 5.1 Introduction

In the previous chapter sensors were manufactured under different manufacturing configurations. The experimental manufactured sensors were subsequently tested and assessed. The configuration resulting in the best performance was selected for carrying out forward the next step of this research project which focused on the characterisation of in-capillary packaged sensors mounted on the surface of the test piece and embedded in laminates of different architectures.

This chapter discusses the developed process for embedding the FOAES, the different curing cycles and processes applied for manufacturing the laminates, and the final characterisation of the FOAES, before being embedded on a reference composite plate, and after being surface-mounted on a panel.

A comparison between the response before and after being embedding has been carried out for embedded and surface-bonded sensors. Surface-bonded sensors were tested as an alternative process to embedding. The directionality of the FOAES was quantified using statistical parameters. Finally, the linearity and fidelity of all the previously tested sensors were assessed.

Although all tests were repeated with both lasers (HeNe and Box A), just the data from the HeNe are used for the detailed analysis. The reason for this is the higher SNR permitted by the HeNe when compared with the Box A laser, which enabled the extraction of richer frequency spectra despite having less nominal power.

## 5.2 Process developed for embedding the FOAES into composite panels

A roll of unidirectional glass-fibre prepreg was brought from the storage temperature conditions of -18°C at which it was kept to ambient temperature. The prepreg was kept into a sealed polyethylene bag to avoid moisture ingression. Squares of 300x300 $mm^2$ were then cut and stored in a sealed bag until being laid up on the laminate. The cut prepegs were protected by two different liners, paper on one side and plastic on the other. Due to the reinforcement being unidirectional and thus unsupported, the liner plastic was first removed to ensure that the unidirectional geometry of the prepreg was not distorted (the paper liner did not deform). The prepreg was then applied onto the laminate in the appropriate orientation with the help of a specially designed metallic frame with the exposed face of the prepreg facing down. The 90° angle of the frame enabled the precise 0° or 90° relative orientation of the different plies of the laminate. Pressure was then applied onto the paper liner with the help of a roller to compact this new layer and to extract the air. The paper liner was then removed and if required, a perforated release film was then laid over the prepreg applying further pressure with the same roller to eliminate any remaining air bubbles.

When half of the layers were applied, the FOAES were symmetrically positioned onto the prepreg. It was made certain that the capillary and the interrogation optical fibres were perfectly aligned with the unidirectional reinforcement of both top and bottom layers, as detailed in Figure 65. The centre of the capillary, where each FOAES was embedded was at 150 ± 5 mm from the edges of the laminate. When more than one FOAES were embedded, the rule of 150 ± 5 mm only applied longitudinally. The transverse of FOAES to FOAES distance was distributed equally (i.e. distance from the edge of the laminate to the first FOAES was the same with that from FOAES to FOAES). The interrogation of the optical fibres was protected at both extremes of the laminate by using PTFE tubing, which acted as sleeves. In this way it

was possible to avoid having the sharp edges cutting or damaging the fibres during the demoulding process and subsequent manipulation required by the characterisation process. Finally, a gentle pressure was applied on the FOAES, optical fibres and PTFE sleeves to integrate them within the reinforcement prior to applying the rest of the layers in order to complete the lamination process.

The pressure application during the lamination of subsequent layers after embedding the FOAES was limited due to the presence of the glass capillary and the inherent risk of brittle fracture when rolling the roller over it. Consequently, it was decided to set an area of 5 mm at both sides of the capillary, where manual pressure was not applied. Therefore the compaction and consolidation of this area was performed with the use of the autoclave during the de-bulking and/or curing cycle. When the panels where finished, they were sandwiched between the release film and vacuum bagged using standard practices as illustrated in Figure 67.

After the first batch of panels were manufactured, it was found that resin bleeding out from the prepegs during the curing cycle spread along the interrogation optical fibres of the FOAES. The resin bleed out and its spreading along the interrogation optical fibres caused them to be effectively embedded in a cured epoxy resin lamina, resulting in their fracture when demoulding. To avoid this undesirable phenomenon, a sealing process was developed to stop the flow of the bleeding resin and prevent contact with the interrogation optical fibres, as shown in Figure 66.

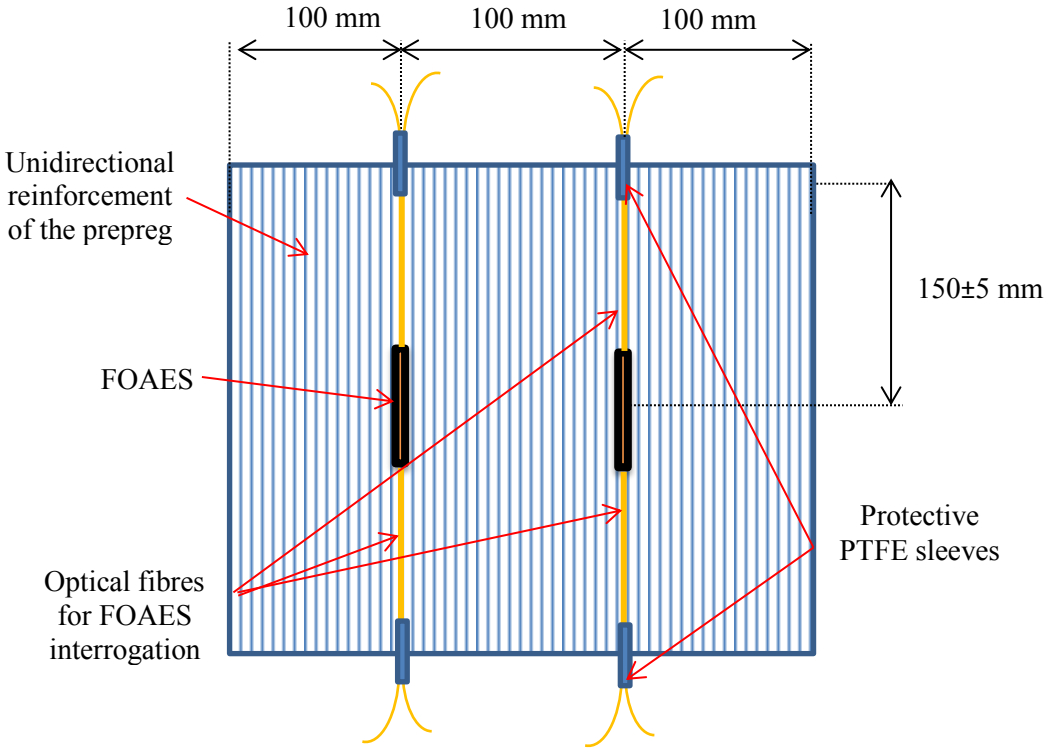


**Figure 65 Schematic of the positioning of the prepegs, two FOAES and their interrogation optical fibres and the protective PTFE sleeves.**

A silicone sealant was applied longitudinally between the top and bottom release films to set a barrier between the laminate and interrogation optical fibres. From further experiments performed it was found that the resin was able to travel through the interior of the protection sleeves of PTFE. Therefore, additional sealing was applied at the end of all the protection sleeves prior to curing the laminates. This type of complete sealing process was found to be robust enough to enable the embedding and posterior demoulding of the panels without any further complications arising with respect to the condition of the interrogation optical fibres.

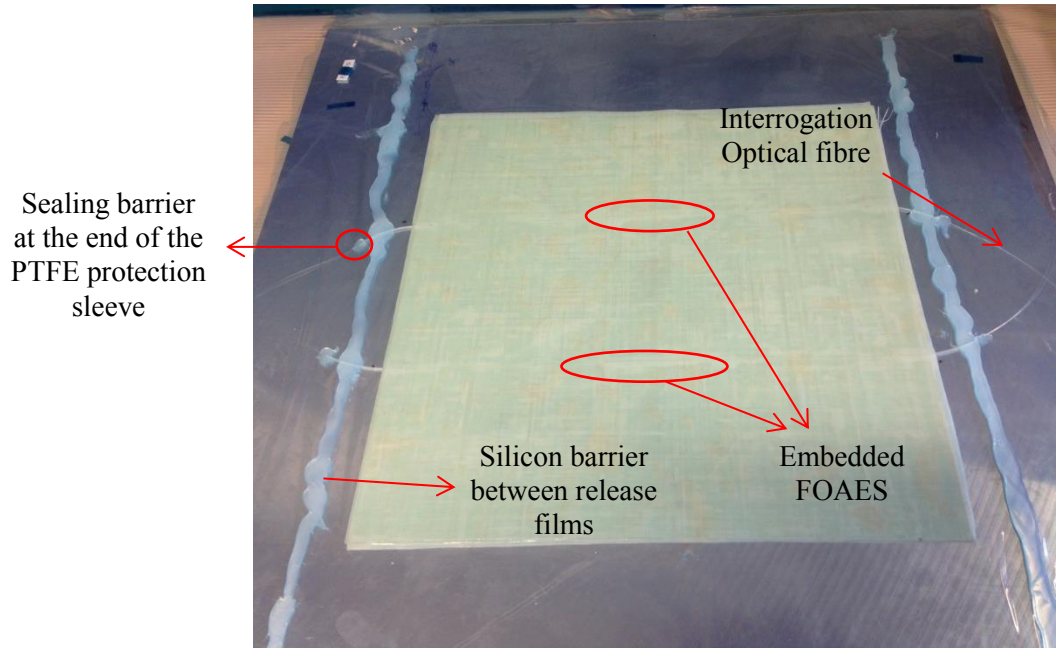


**Figure 66 Detail of the sealing process developed to stop the resin bleeding out from the prepegs to get in contact with the interrogation optical fibres. A silicione barrier was applyied between the top and bottom release films. Additional sealing barriers were applied at the ends of the PTFE tubing or protective sleeve.**

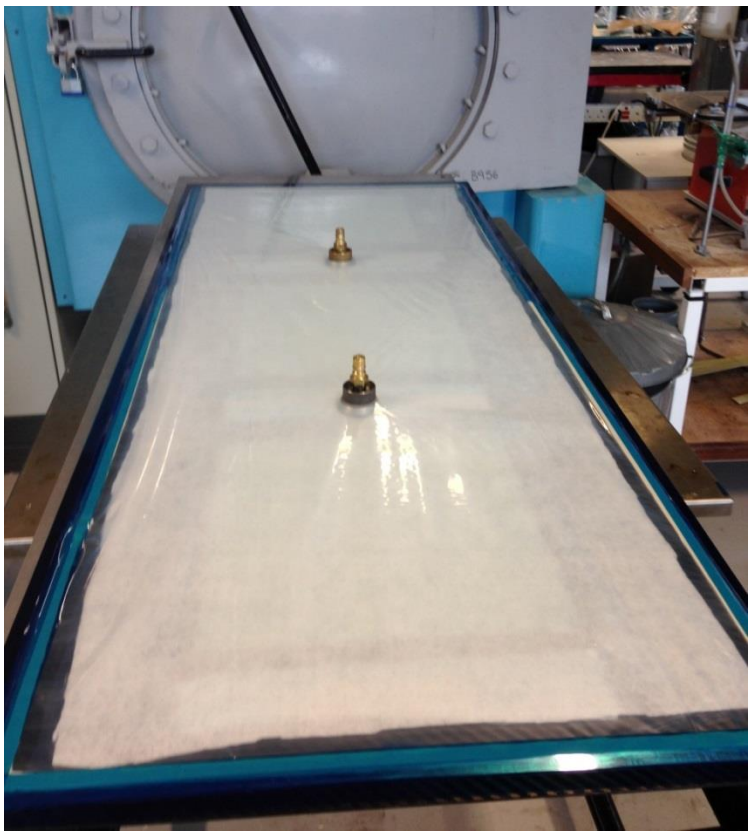

**Figure 67 Panels ready to be cured after being vacuum bagged following standard procedures.**

## 5.3 Laminates manufacturing processes

Several laminates were manufactured during this project using unidirectional glass-fibre/epoxy prepegs at different orientations. As described before, this material was found to be extremely difficult to manipulate and to compact when several layers were laid. This effect was even more noticeable when the sensors were embedded and consequently mechanical pressure could not be applied at the proximity of the capillary. Therefore air removal, compaction and FOAES integration within the laminate had to be achieved during the manufacturing process.

Different curing cycles were tested as follows, to introduce more severe conditions to the sensors in a controlled manner: (i) Cycle A, with application of vacuum only; (ii) Cycle B, with application of pressure only; and (iii) Cycle C with application of both pressure and vacuum. The aim was to ensure that Cycle C could be applied by studying first the effects of vacuum or pressure in the FOAES survivability. For all cycles, curing of the laminate was carried out at a temperature of 80°C. The applied dwell time was adjusted at 90 minutes at a temperature of 40°C to de-bulk and compact the laminate. The dwell temperature was selected from the datasheet of the prepreg, being as high as possible to decrease the viscosity of the resin but also low enough to minimise the cross linking of the resin system. An additional de-bulking step was added before the curing of the last batch of laminates, to improve even more the consolidation and reduce the amount of trapped air. The details summarising the different laminates, number of plies and orientation, curing cycle and other relevant information are shown in Table 10. Detail of the curing process and added de-bulk cycle are as also shown in Figure 68.

**Table 10 Laminates manufactured, detailing number of plies, orientation, and further details.**

| Laminate Id | Plies | Configuration | Lay-Up | De-bulk | Autoclave Process | FOAES Embedded |
|---|---|---|---|---|---|---|
| L150512-01 | 4 | (0)4 | 0-0-0-0 | No | A | 3 |
| L150519-01 | 4 | (0)4 | 0-0-0-0 | No | B | 1 |
| L150519-02 | 4 | (0)4 | 0-0-0-0 | No | B | 2 |
| L150519-03 | 4 | (0)4 | 0-0-0-0 | No | B | 0 |
| L150703-01 | 4 | (0)4 | 0-0-0-0 | No | B | 2 |
| L150703-02 | 4 | (0)4 | 0-0-0-0 | No | B | 2 |
| L150717-01 | 4 | (0)4 | 0-0-0-0 | No | B | 2 |
| L150717-02 | 8 | (0)8 | 0-0-0-0-0-0-0-0 | No | C | 1 |
| L150717-03 | 4 | (0/90)2 | 90-0-0-90 | No | C | 2 |
| L150722-01 | 4 | (0/90)2 | 90-0-0-90 | No | C | 2 |
| L150722-02 | 4 | (0/90)2 | 90-0-0-90 | No | C | 2 |
| L150805-01 | 8 | (0/90)4 | 90-0-90-0-0-90-0-90 | Yes | C | 2 |
| L150805-02 | 8 | (0/90)4 | 90-0-90-0-0-90-0-90 | Yes | C | 2 |

It was found that the 100% of the embedded FOAES survived after being co-cured in the laminate using the preliminary cycles A or B. These results enabled the embedment of new sensors using the more demanding and desired cycle C, which combined vacuum and pressure at the same time. Again, all the embedded FOAES survived to the autoclave process. Thus, the FOAES was assessed to be resistant enough to withstand an industrial autoclave process based on Cycle C.

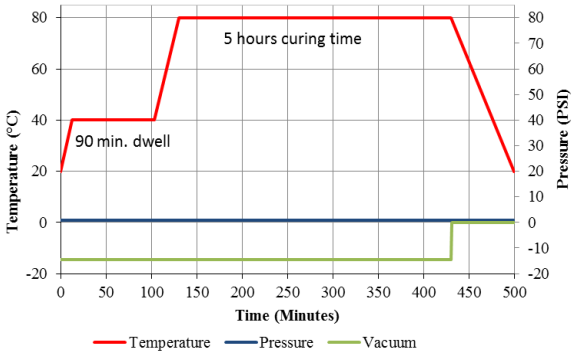


(i)

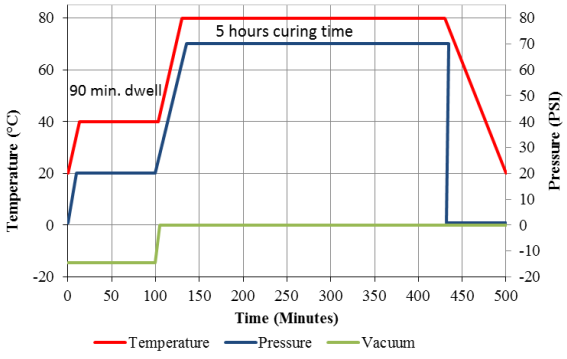


(ii)

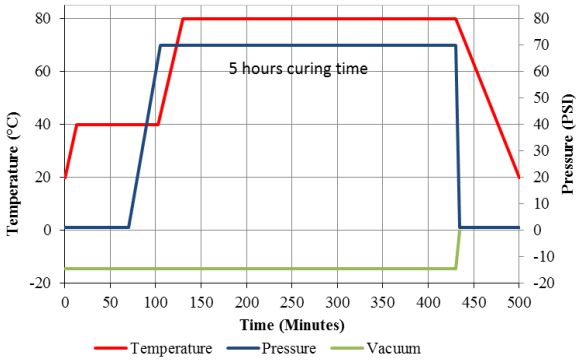


(iii)

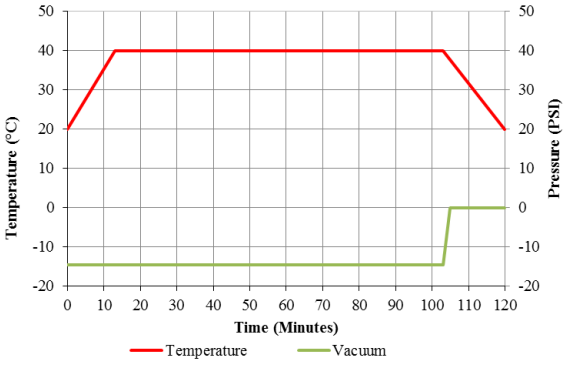


(iv)

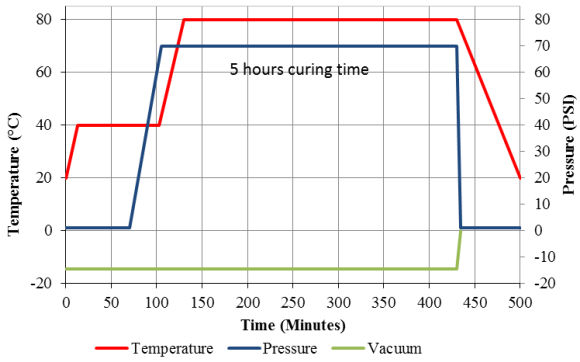


(iii)

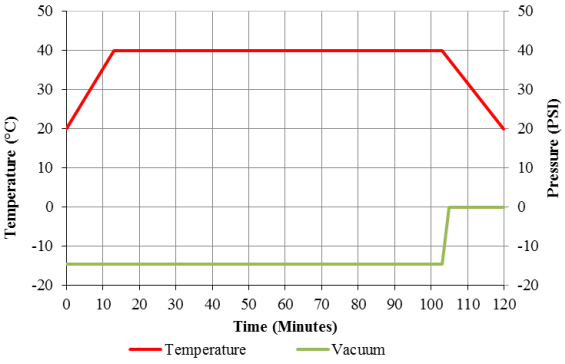


(iv)

**Figure 68 Detail of the different curing cycles. Figure 68 (i) to (iii) show the evolution of the vacuum, pressure and temperature during the three applied cures from cycles A to cycle C. Figure 68 (iv) describes the de-bulking cycle.**


**Figure 69 Detail of the two FOAES embedded into the laminate L150519-02 (red ellipses).**

## 5.4 FOAES: on-surface and embedded acoustic characterisation

The effect of the embedding in the acoustic response was investigated. Sensors manufactured under the optimum conditions selected in Chapter 4 were manufactured and packaged in glass capillaries. A unidirectional four layer composite panel (L150519-03) was manufactured without any embedded sensor to be used for the surface-mounting characterisation experiments. As detailed in section 3.5, a circle with a radius of 75 mm was drawn at the centre of the plate on the tooling or flat side and the excitation points marked every 45°. The FOAES were coupled to the plate parallel to the panel's reinforcement using vaseline as coupling agent as shown in Figure 70.

The sensors were then characterised using discrete frequency sweeping, following the methodology described in section 3.5.4. Due to the FOAES being mounted on the surface of

the test piece, it was not possible to test simultaneously with the benchmarking piezoelectric sensors R30α and R50α (the FOAES was mounted on the central position of the characterisation circle). All tests were repeated with both lasers HeNe and Box A.

A total of 23 from the previously surface-mounted characterised FOAES were selected and embedded in 13 different laminates, as detailed in Table 10. Once embedded, the successfully demoulded 16 sensors unaffected by the previously reported bleeding of the resin from the prepegs were selected for the same discrete frequency sweep characterisation as for the surface-mounted testing. The centre and exact position of the capillary of the embedded FOAES were located with the help of a lamp projecting light through the laminate. Circles of 75 mm were drawn with the centres coincident with the middle point of each FOAES. For each circle, the line containing the 0° and 180° excitation points was drawn collinear with the capillary of the FOAES. The rest of the excitation points at every 45° were later located and marked. The FOAES were then simultaneously characterised in successive experiments with both HeNe and Box A lasers, first with the R30α and later with R50α piezoelectric sensors used as reference.

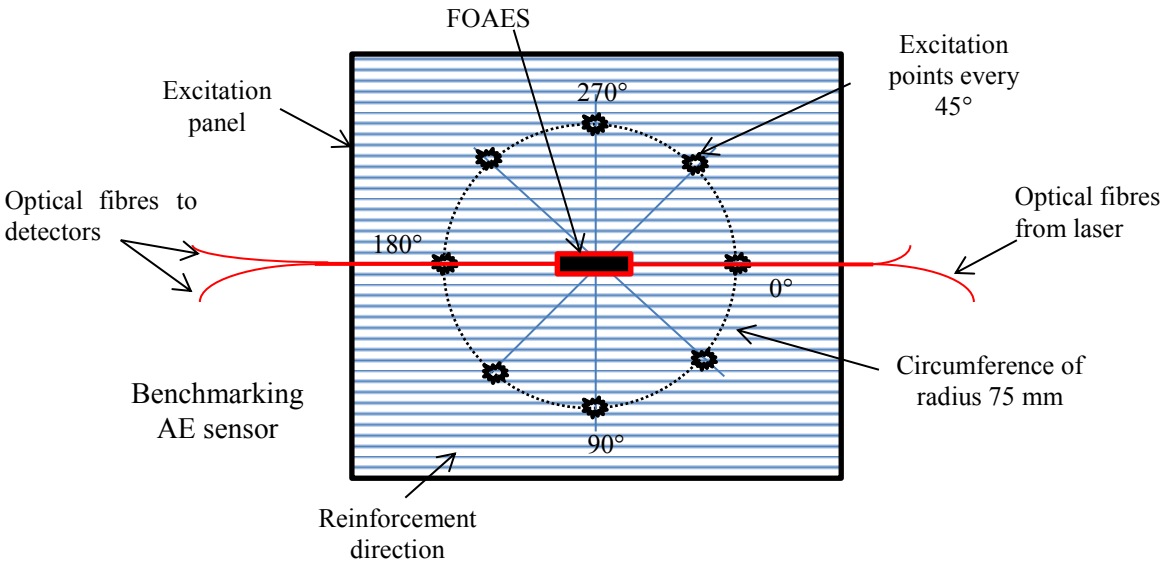


**Figure 70 Schematic of the on-surface setup to characterise the FOAES.**

The results for twelve of on-surface and embedded sensors are given in Figure 71 to Figure 82. The results of the remainder four sensors were omitted due to the data of the surface-mounting characterisation being found to be corrupt. Therefore, for those latter set of four sensors it was not possible to compare the change of the responses between the surface-mounted and embedded conditions.

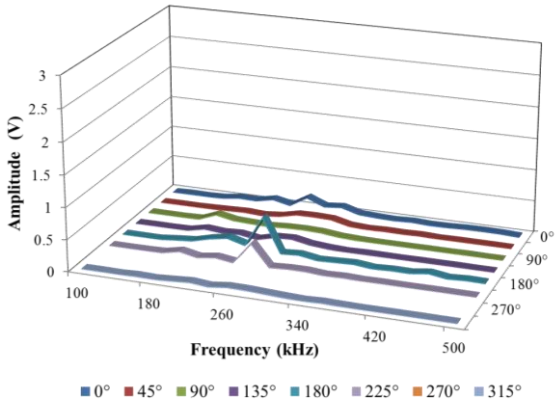


(i)

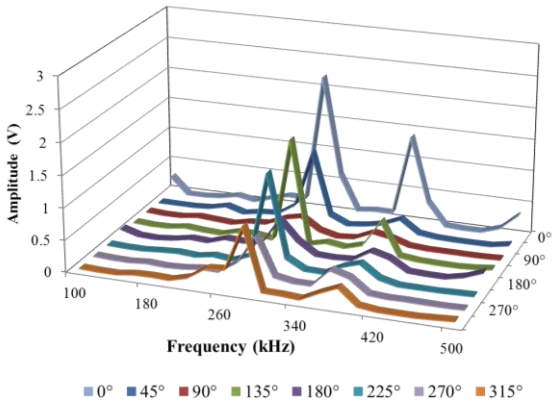


(ii)

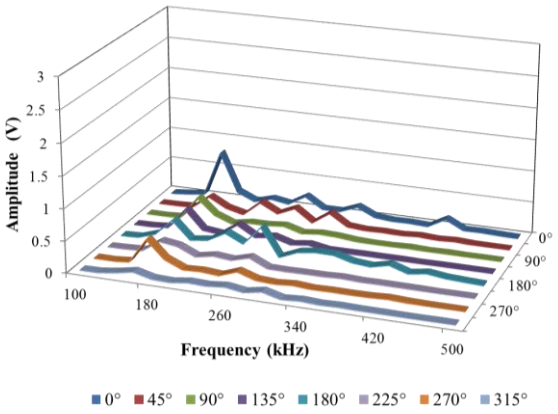


(iii)

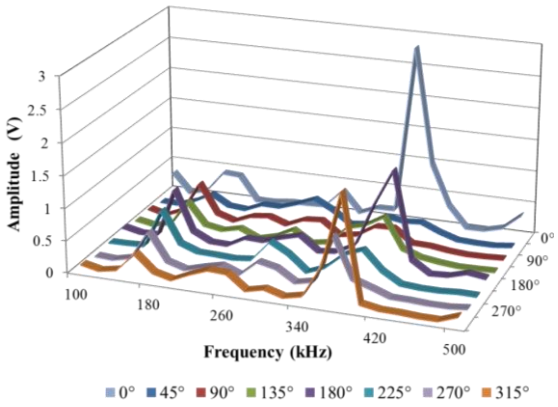


(iv)

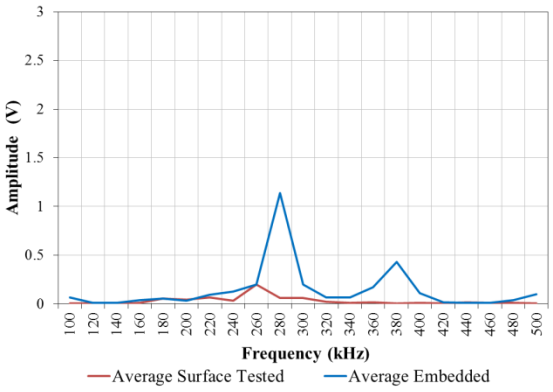


(v)

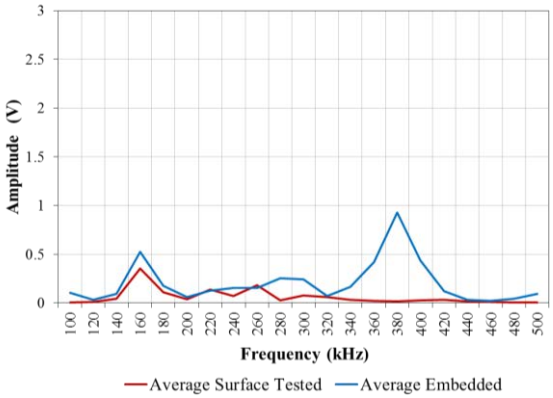


(vi)

**Figure 71 Characterisation of the sensor 150625-03, on-surface and embedded in a $(0)_4$ laminate by the use of the HeNe laser. Figure 71 (i) and (ii) show the frequency response for the on-surface and embedded characterisation tests respectively, using a R30α as emitter. Figure 71 (iii) and (iv) show the same information when a R50α was used as emitter. Figure 71 (v) and (vi) show summarised information averaging the response at the different directions when R30α and R50α were used as emitters respectively.**

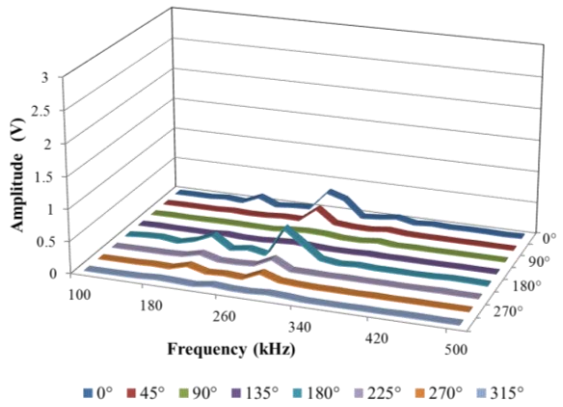


(i)

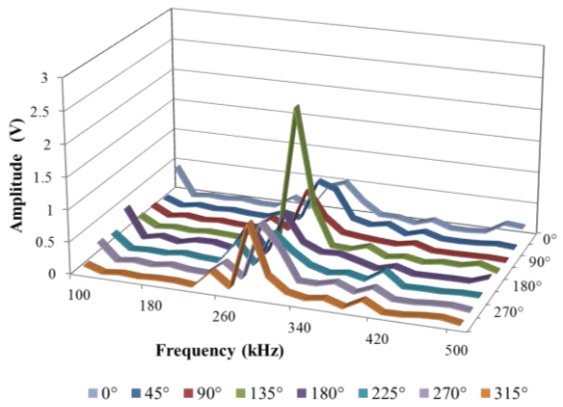


(ii)

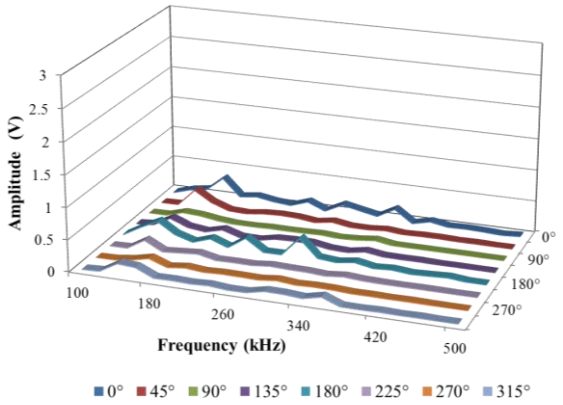


(iii)

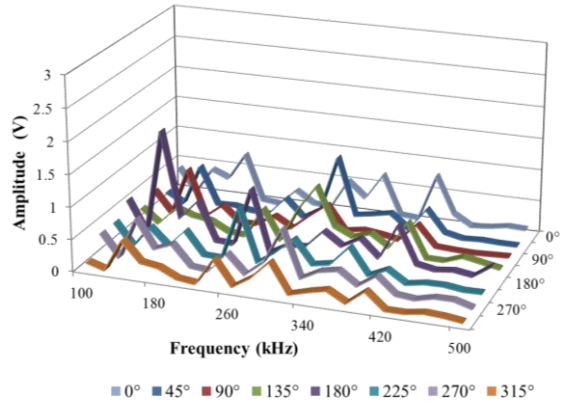


(iv)

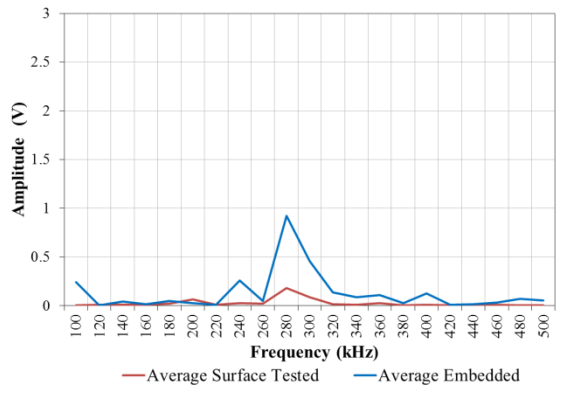


(v)

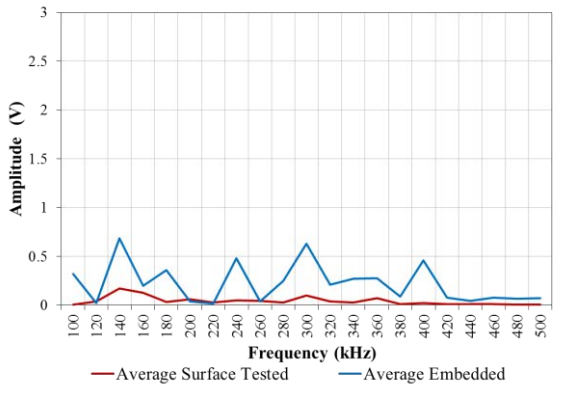


(vi)

**Figure 72 Characterisation of the sensor 150624-06, on-surface and embedded in a $(0)_4$ laminate by the use of the HeNe laser. Figure 72 (i) and (ii) show the frequency response for the on-surface and embedded characterisation tests respectively, using a R30α as emitter. Figure 72 (iii) and (iv) show the same information when a R50α was used as emitter. Figure 72 (v) and (vi) show summarised information averaging the response at the different directions when R30α and R50α were used as emitters respectively.**

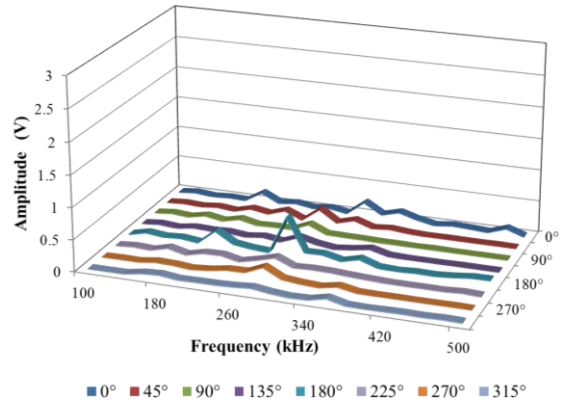


(i)

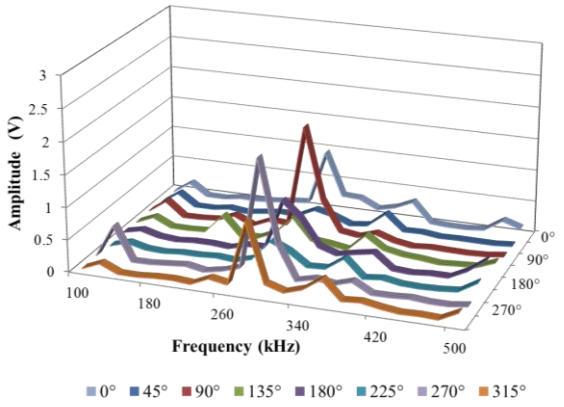


(ii)

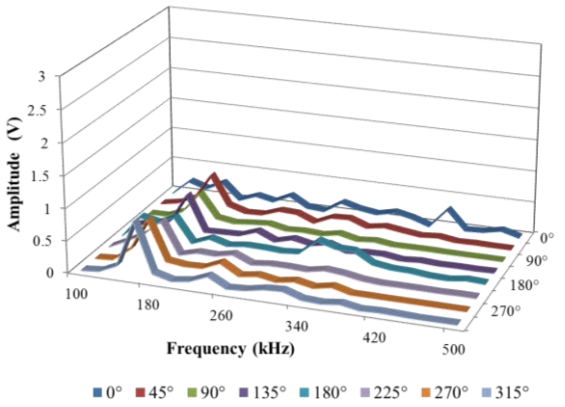


(iii)

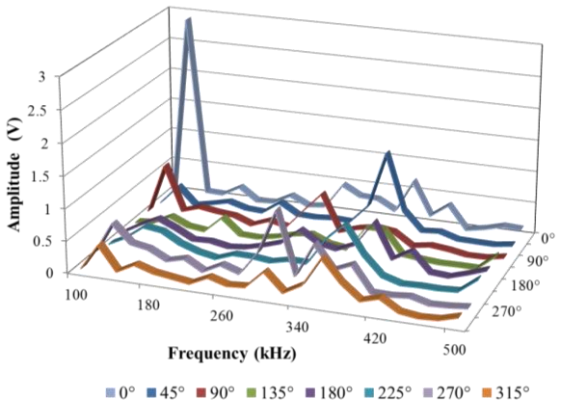


(iv)

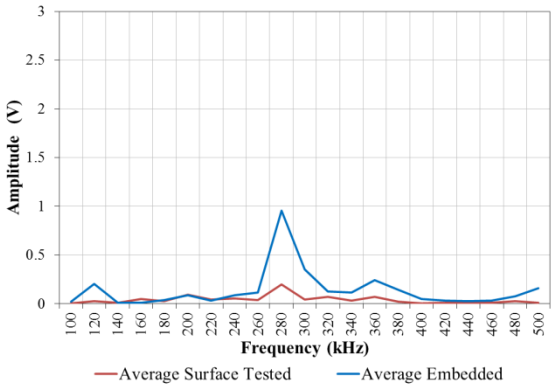


(v)

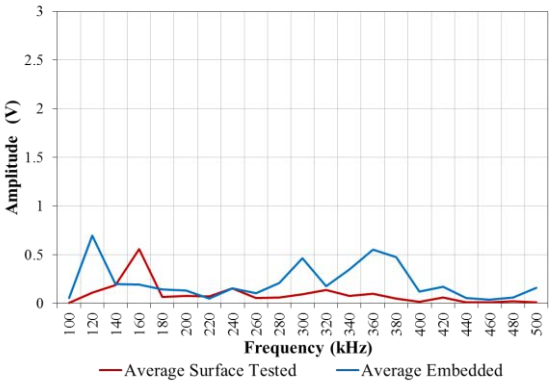


(vi)

**Figure 73 Characterisation of the sensor 150625-02, on-surface and embedded in a $(0)_4$ laminate by the use of the HeNe laser. Figure 73 (i) and (ii) show the frequency response for the on-surface and embedded characterisation tests respectively, using a R30α as emitter. Figure 73 (iii) and (iv) show the same information when a R50α was used as emitter. Figure 73 (v) and (vi) show summarised information averaging the response at the different directions when R30α and R50α were used as emitters respectively.**

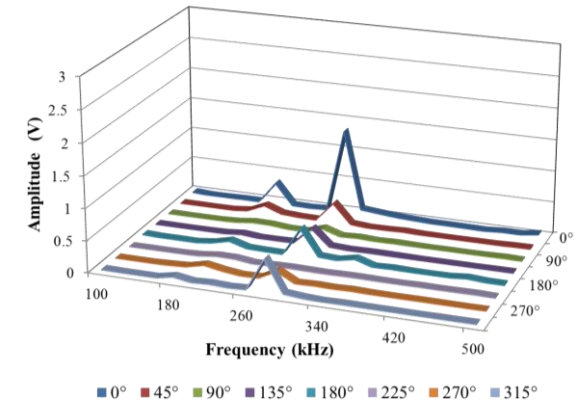


(i)

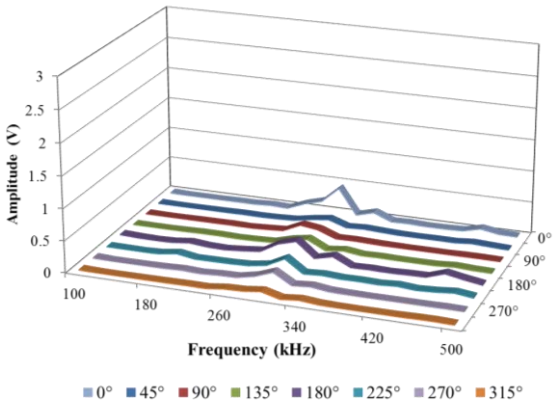


(ii)

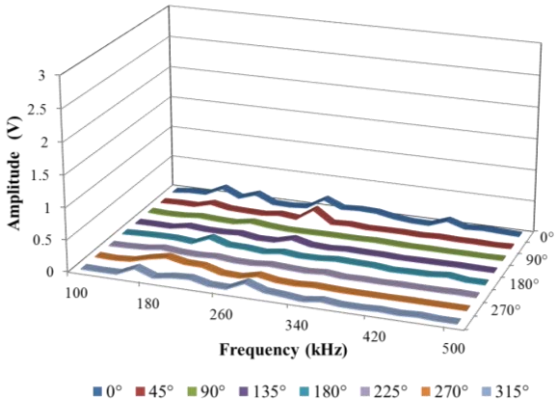


(iii)

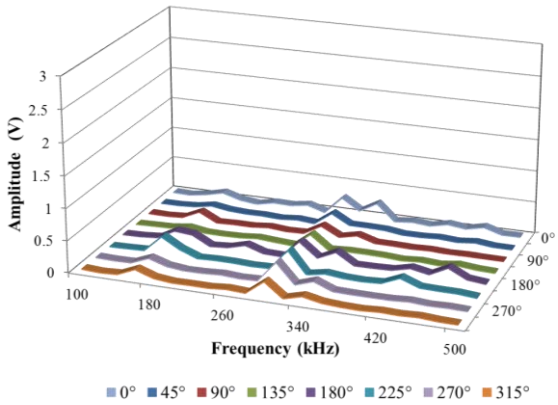


(iv)

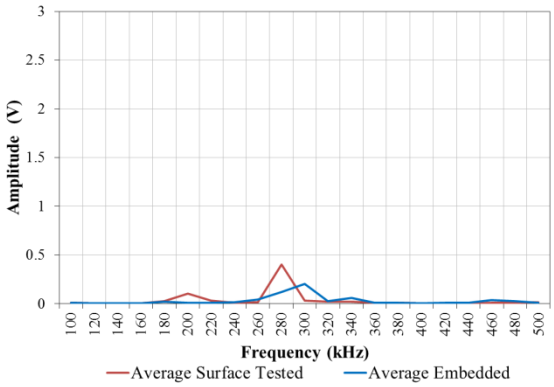


(v)

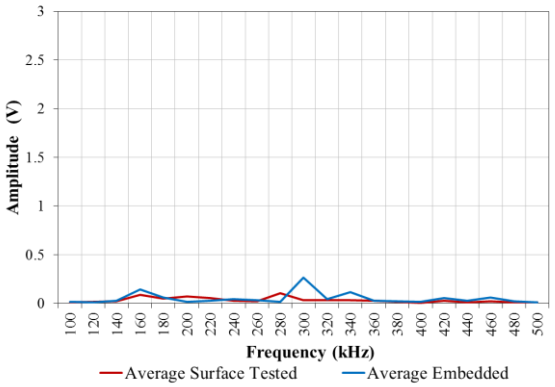


(vi)

**Figure 74 Characterisation of the sensor 150616-04, on-surface and embedded in a $(0)_4$ laminate by the use of the HeNe laser. Figure 74 (i) and (ii) show the frequency response for the on-surface and embedded characterisation tests respectively, using a R30α as emitter. Figure 74 (iii) and (iv) show the same information when a R50α was used as emitter. Figure 74 (v) and (vi) show summarised information averaging the response at the different directions when R30α and R50α were used as emitters respectively.**

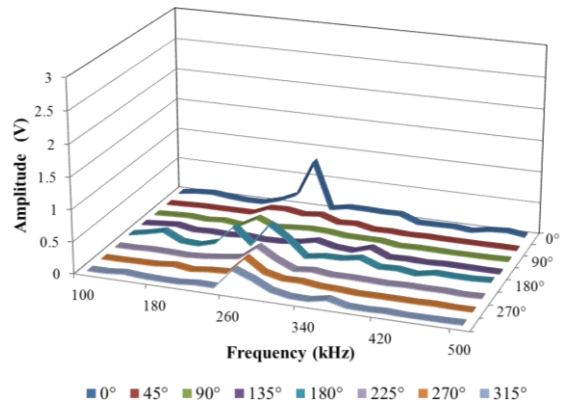


(i)

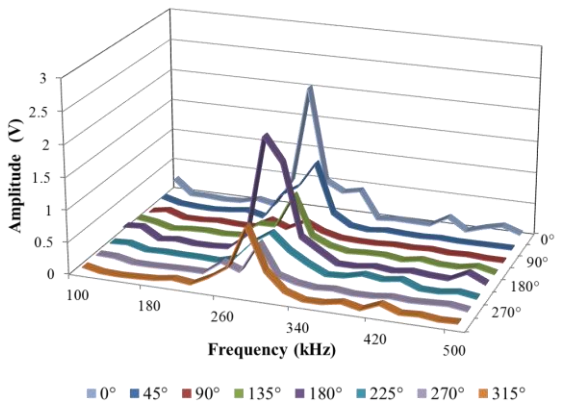


(ii)

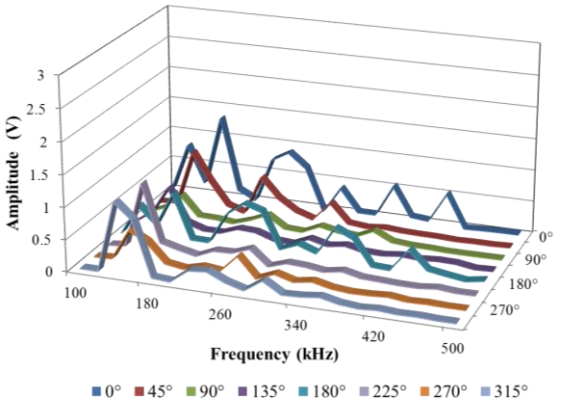


(iii)

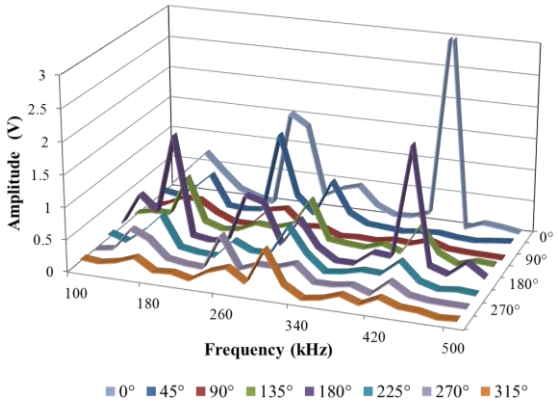


(iv)

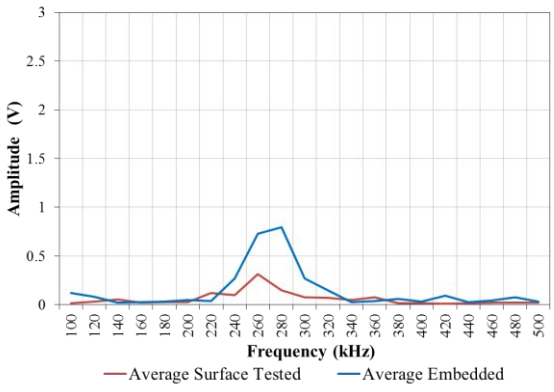


(v)

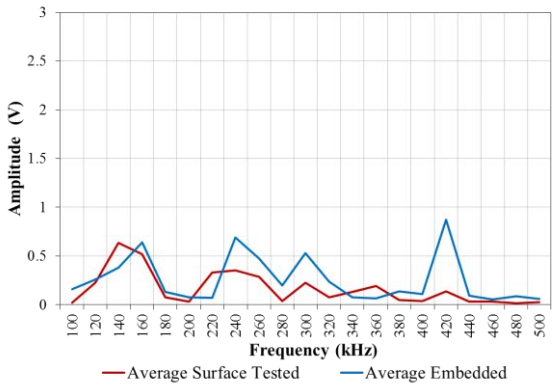


(vi)

**Figure 75 Characterisation of the sensor150624-02, on-surface and embedded in a $(0)_4$ laminate by the use of the HeNe laser. Figure 75 (i) and (ii) show the frequency response for the on-surface and embedded characterisation tests respectively, using a R30α as emitter. Figure 75 (iii) and (iv) show the same information when a R50α was used as emitter. Figure 75 (v) and (vi) show summarised information averaging the response at the different directions when R30α and R50α were used as emitters respectively.**

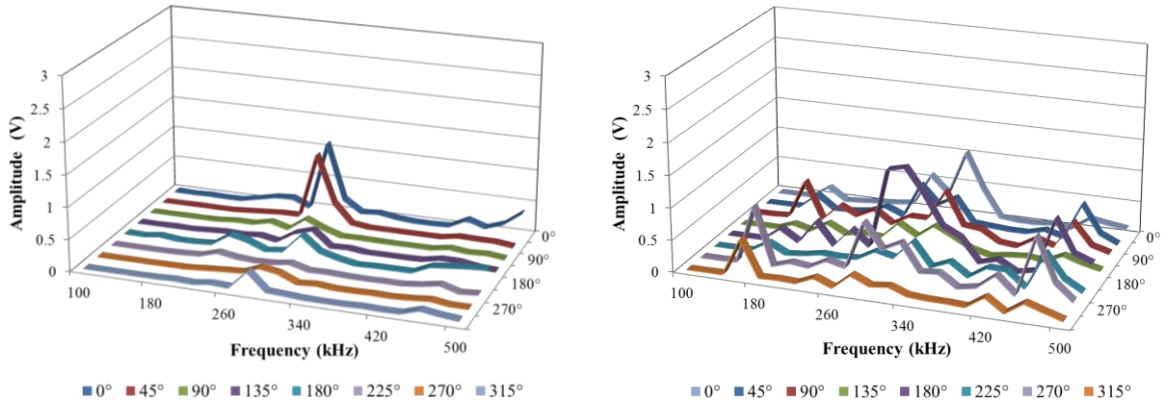


(i) (ii)

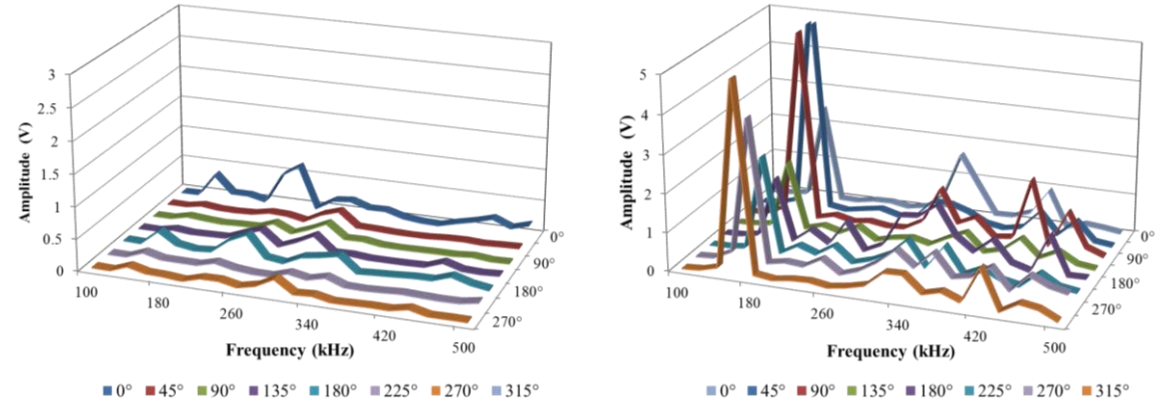


(iii) (iv)

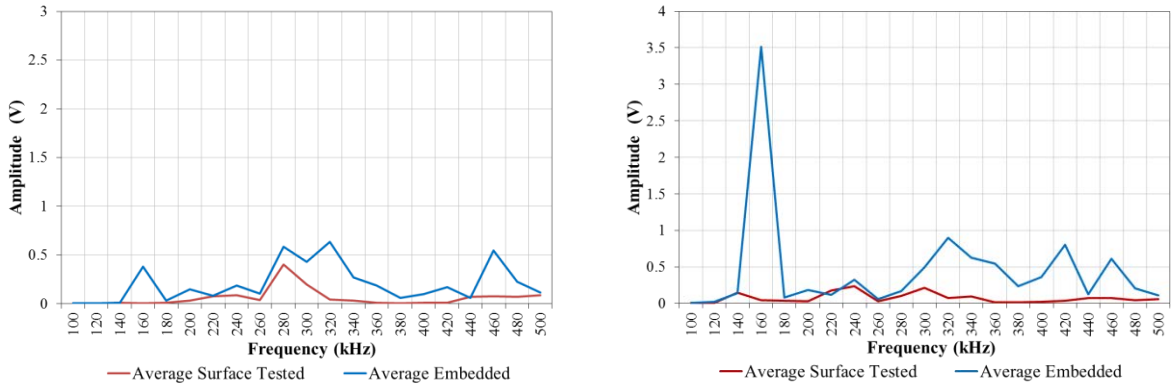


(v) (vi)

**Figure 76 Characterisation of the sensor 150616-02, on-surface and embedded in a $(0/90)_2$ laminate by the use of the HeNe laser. Figure 76 (i) and (ii) show the frequency response for the on-surface and embedded characterisation tests respectively, using a R30α as emitter. Figure 76 (iii) and (iv) show the same information when a R50α was used as emitter. Figure 76 (v) and (vi) show summarised information averaging the response at the different directions when R30α and R50α were used as emitters respectively.**

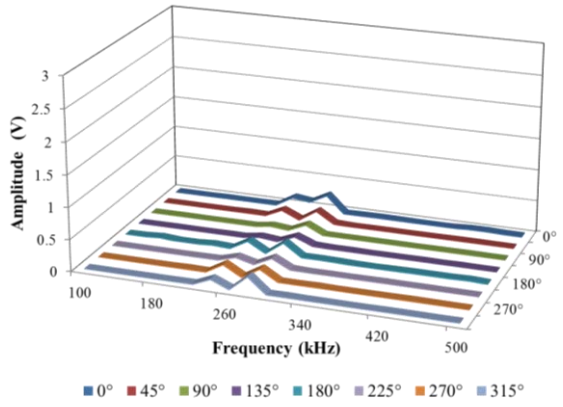


(i)

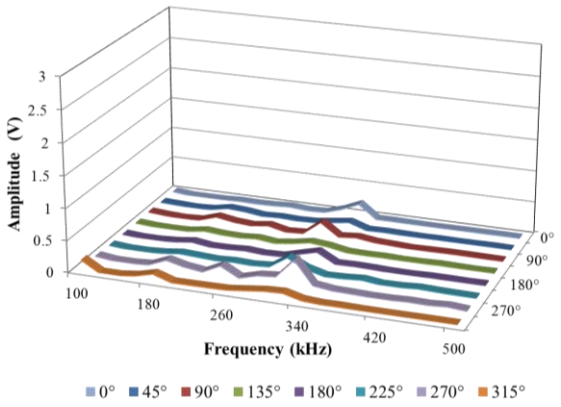


(ii)

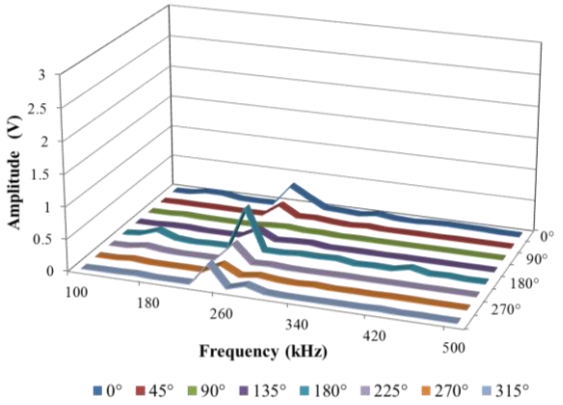


(iii)

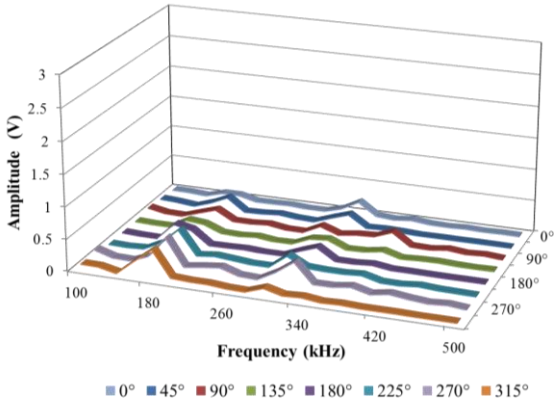


(iv)

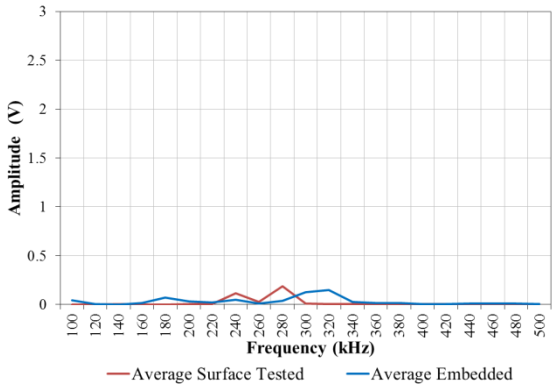


(v)

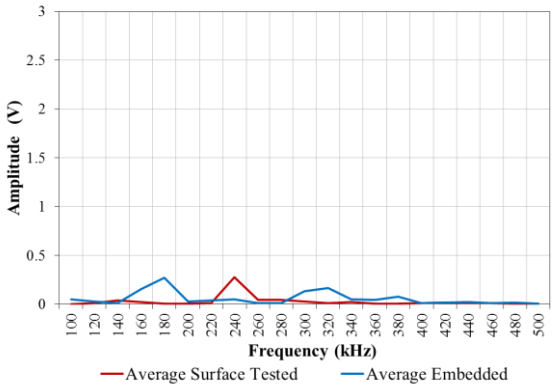


(vi)

**Figure 77 Characterisation of the sensor 150616-03, on-surface and embedded in a $(0/90)_2$ laminate by the use of the HeNe laser. Figure 77 (i) and (ii) show the frequency response for the on-surface and embedded characterisation tests respectively, using a R30α as emitter. Figure 77 (iii) and (iv) show the same information when a R50α was used as emitter. Figure 77 (v) and (vi) show summarised information averaging the response at the different directions when R30α and R50α were used as emitters respectively.**

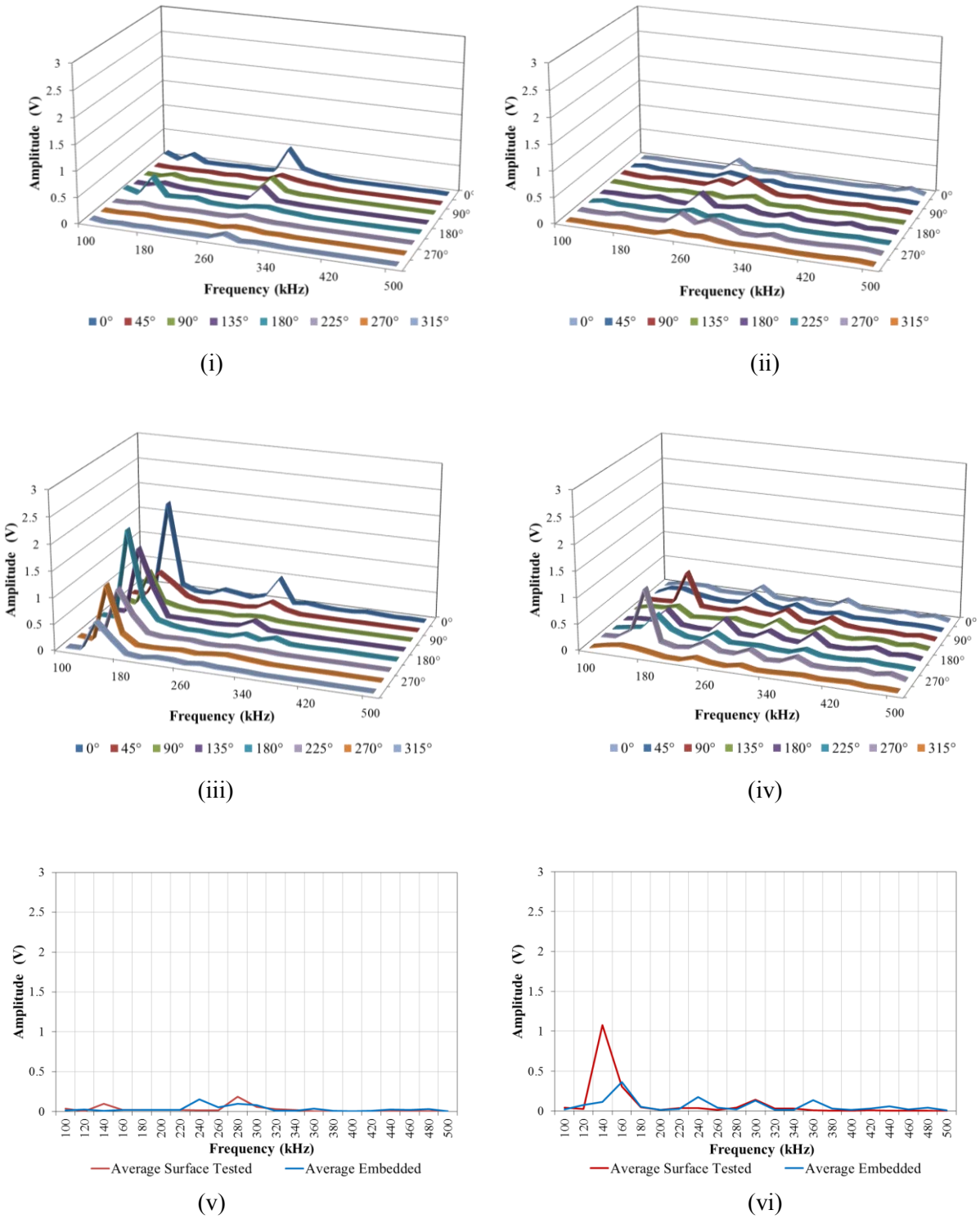


**Figure 78 Characterisation of the sensor 150624-03, on-surface and embedded in a $(0/90)_2$ laminate by the use of the HeNe laser. Figure 78 (i) and (ii) show the frequency response for the on-surface and embedded characterisation tests respectively, using a R30α as emitter. Figure 78 (iii) and (iv) show the same information when a R50α was used as emitter. Figure 78 (v) and (vi) show summarised information averaging the response at the different directions when R30α and R50α were used as emitters respectively.**

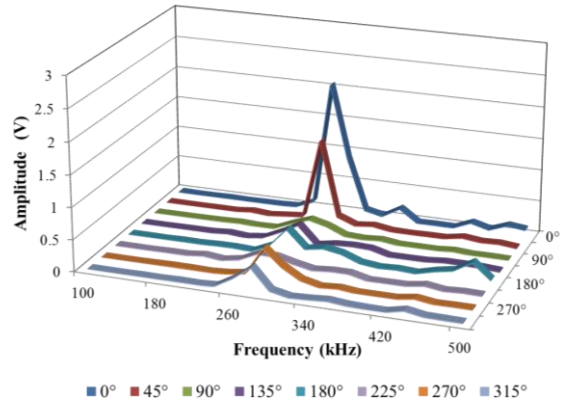


(i)

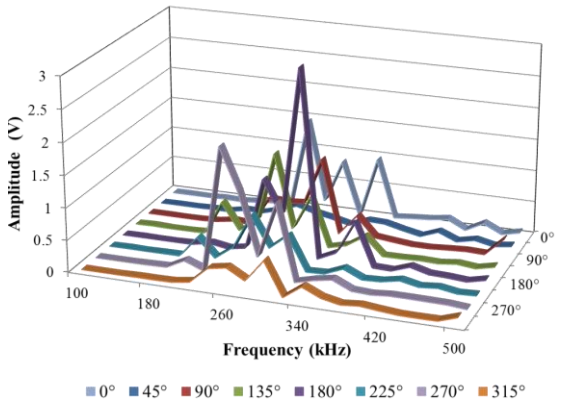


(ii)

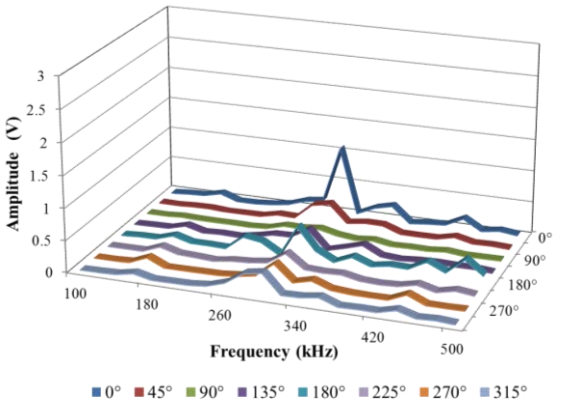


(iii)

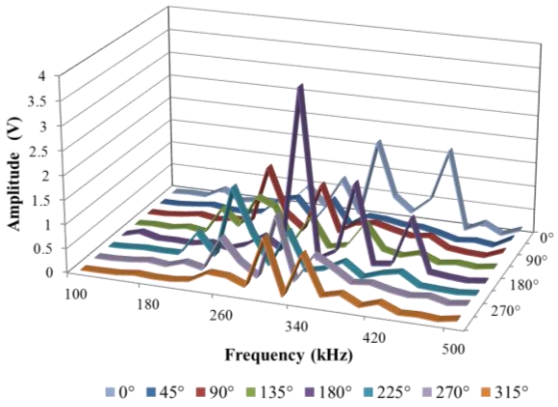


(iv)

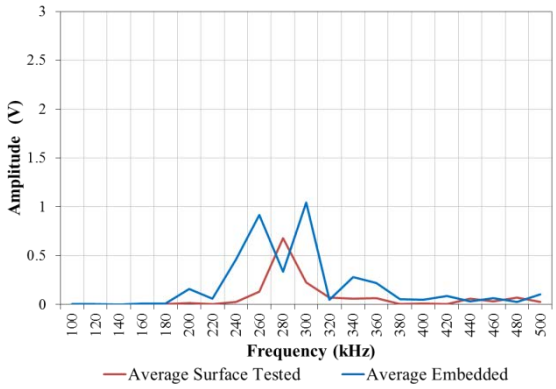


(v)

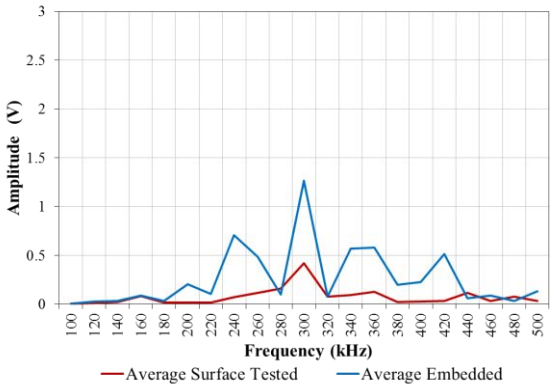


(vi)

**Figure 79 Characterisation of the sensor 150625-04, on-surface and embedded in a $(0/90)_2$ laminate by the use of the HeNe laser. Figure 79 (i) and (ii) show the frequency response for the on-surface and embedded characterisation tests respectively, using a R30α as emitter. Figure 79 (iii) and (iv) show the same information when a R50α was used as emitter. Figure 79 (v) and (vi) show summarised information averaging the response at the different directions when R30α and R50α were used as emitters respectively.**

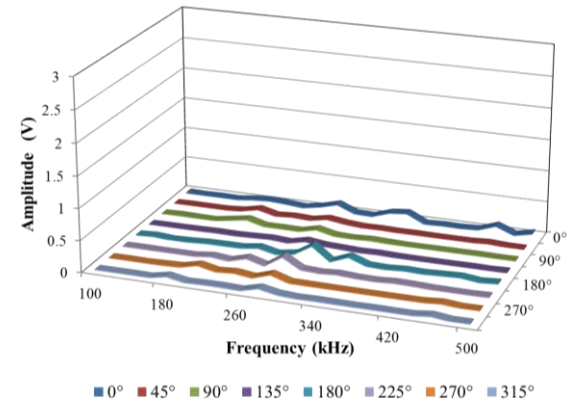


(i)

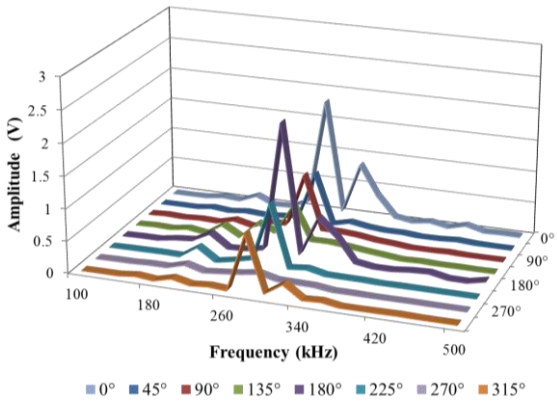


(ii)

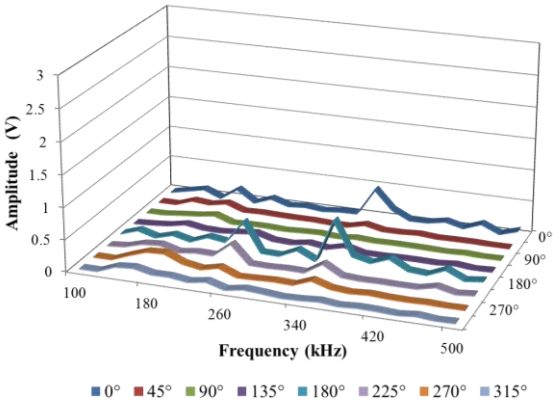


(iii)

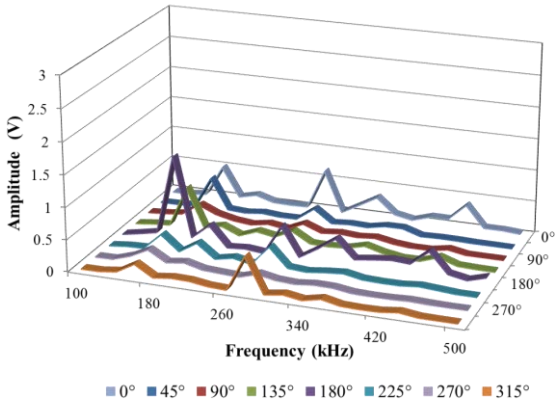


(iv)

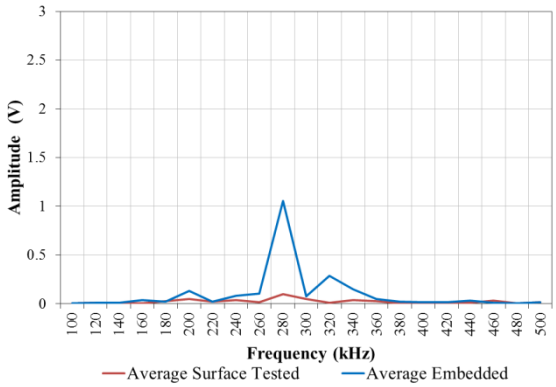


(v)

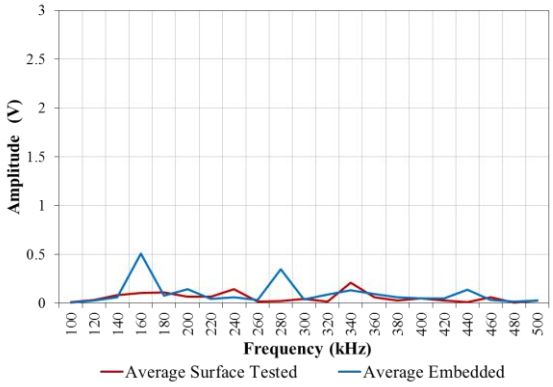


(vi)

**Figure 80 Characterisation of the sensor 150616-05, on-surface and embedded in a $(0)_8$ laminate by the use of the HeNe laser. Figure 80 (i) and (ii) show the frequency response for the on-surface and embedded characterisation tests respectively, using a R30α as emitter. Figure 80 (iii) and (iv) show the same information when a R50α was used as emitter. Figure 80 (v) and (vi) show summarised information averaging the response at the different directions when R30α and R50α were used as emitters respectively.**

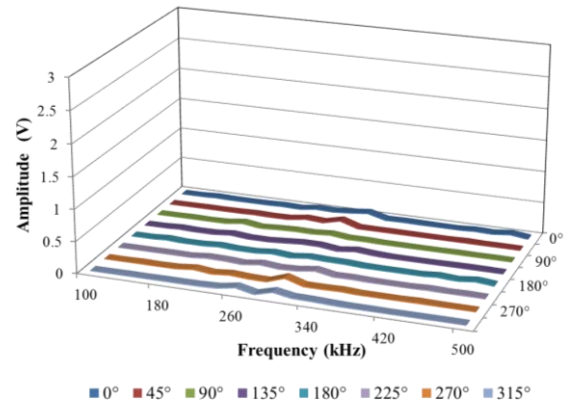


(i)

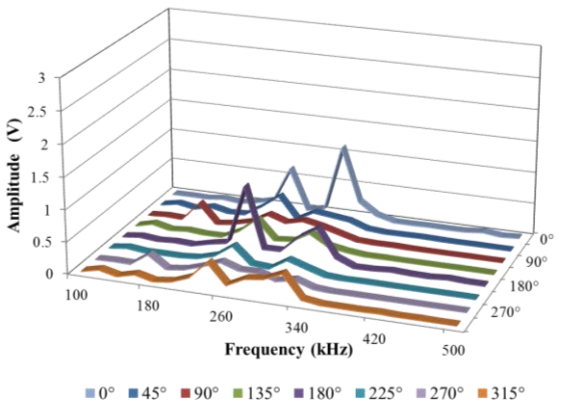


(ii)

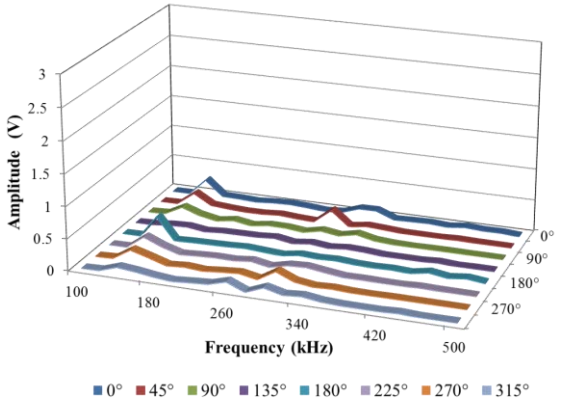


(iii)

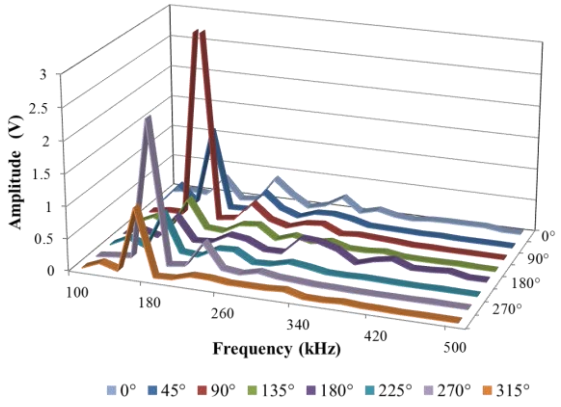


(iv)

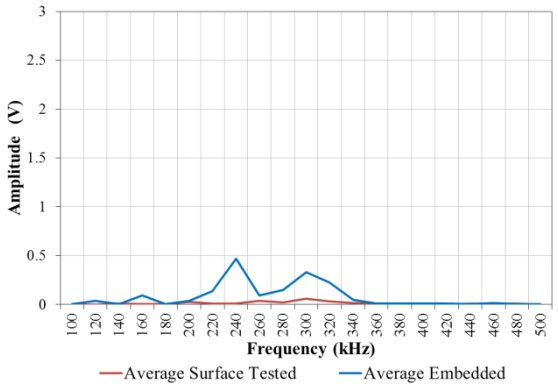


(v)

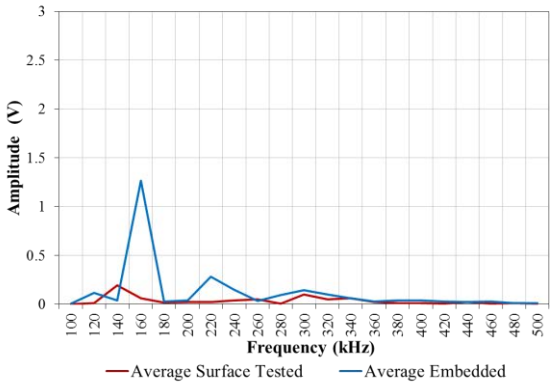


(vi)

**Figure 81 Characterisation of the sensor 150624-04 on-surface and embedded in a $(0)_8$ laminate by the use of the HeNe laser. Figure 81 (i) and (ii) show the frequency response for the on-surface and embedded characterisation tests respectively, using a R30α as emitter. Figure 81 (iii) and (iv) show the same information when a R50α was used as emitter. Figure 81 (v) and (vi) show summarised information averaging the response at the different directions when R30α and R50α were used as emitters respectively.**

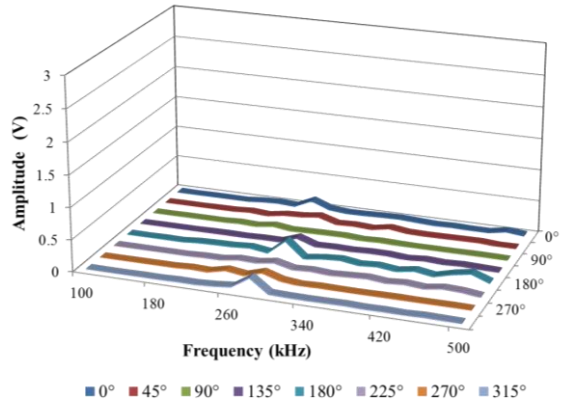


(i)

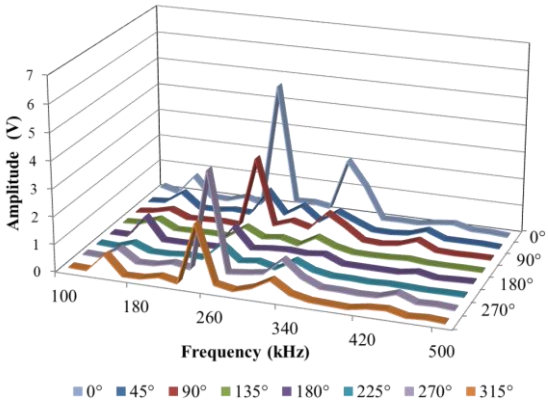


(ii)

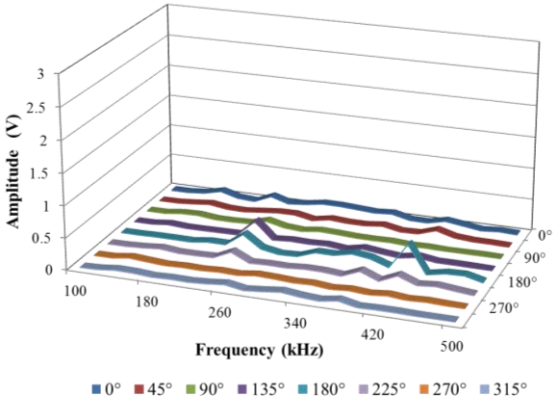


(iii)

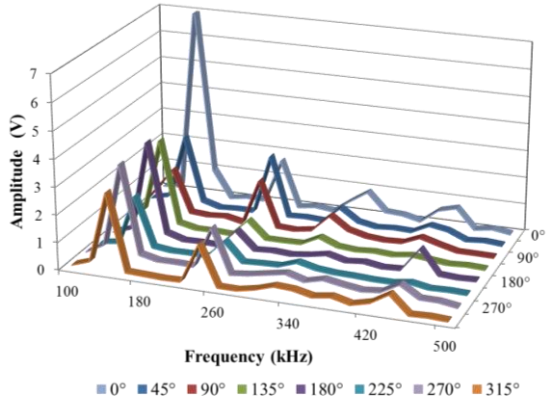


(iv)

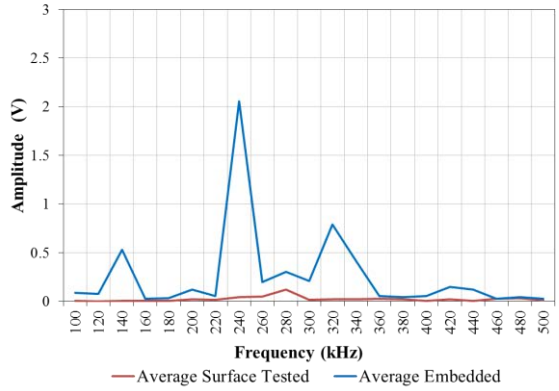


(v)

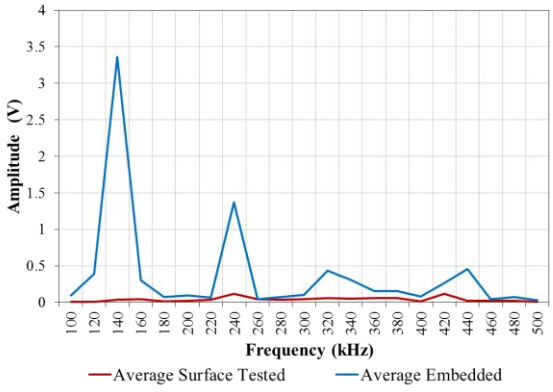


(vi)

**Figure 82 Characterisation of the sensor 150731-02, on-surface and embedded in a $(0/90)_4$ laminate by the use of the HeNe laser. Figure 82 (i) and (ii) show the frequency response for the on-surface and embedded characterisation tests respectively, using a R30α as emitter. Figure 82 (iii) and (iv) show the same information when a R50α was used as emitter. Figure 82 (v) and (vi) show summarised information averaging the response at the different directions when R30α and R50α were used as emitters respectively.**

As it can be seen from the results obtained, the general effect of the embedding was the dramatic increase in the amplitude of the recorded signals when compared with the response of the surface-mounted testing conditions. In addition, the capability of the sensor for collecting higher frequencies (the ones with highest decay with increasing distance from the source) or bandwidth was generally improved as well, especially when the R50α was used as the piezo-emitter. The resonance of the R50α also lies at higher frequencies.

On the other hand, three of the sensors (Figure 74, Figure 77 and Figure 78) exhibited no improvement and even some deterioration of their response was observable when embedded. It was speculated that some resin could have got into the capillary during the curing of the laminate, causing degradation of the overall properties of these sensors as a result.

Finally, there is a general trend for the sensors embedded in unidirectional laminates to exhibit higher response to the directions aligned with the laminate's reinforcement – 0°± 45° and 180° ± 45°.

## 5.5 Surface bonding of the FOAES

One of the main problems when embedding the FOAES is the relative large diameter of the interrogation optical fibres and capillary when compared with the reinforcement glass fibres. A last experiment was performed to understand if the bonding on the surface has a similar effect than the embedding, increasing the response by improving the coupling.

Two of the sensors previously characterised on the composite reference plate were bonded on a bi-directional $(0/90)_8$ laminate, using Araldite 3 minutes and with an identical layout as described in Figure 65. The sensors were then characterised using the methodologies described in section 3.5, firstly by using successively the R30α and the R50α as piezo-

emitters on the same face where the FOAES were surface-bonded, and secondly reversing the plate and exciting the laminate on the opposite face where the FOAES was bonded. When testing on the same face where the FOAES was bonded, the simultaneous characterisation with a conventional AE sensor was not possible due to the FOAES being bonded on the centre.

The results of the tests performed on the same face (excitation on the same face where the FOAES were bonded) are shown in Figure 83 and Figure 84. The results for the tests with the excitation on the opposite face where the FOAES were bonded are shown in Figure 85 and Figure 86.

As it can be seen, when the excitation was carried out on the same face where the FOAES was bonded, a stronger response, higher than that observed for the embedded condition, was observed. Nonetheless, when the excitation was performed in the opposite face where the FOAES was bonded, the increase in the response when compared with surface-mounting characterisation was much more moderate in comparison with that observed in the embedded condition. In addition and in contrast to what was observed with the embedded sensors, there were no improvements in the frequency ranges or bandwidths of the FOAES.

It was speculated that the differences in the amplitude when the excitation was performed on opposite faces of the panel were related to the through-thickness attenuation of the signal since FRPCs have highly anisotropic microstructure resulting in a strong attenuation effect. Furthermore, the nature of the adhesive can add some damping effect which can influence the propagation of higher frequencies. A substance with closer matching acoustic impedance than the epoxy of the prepreg would possibly result in better performance.

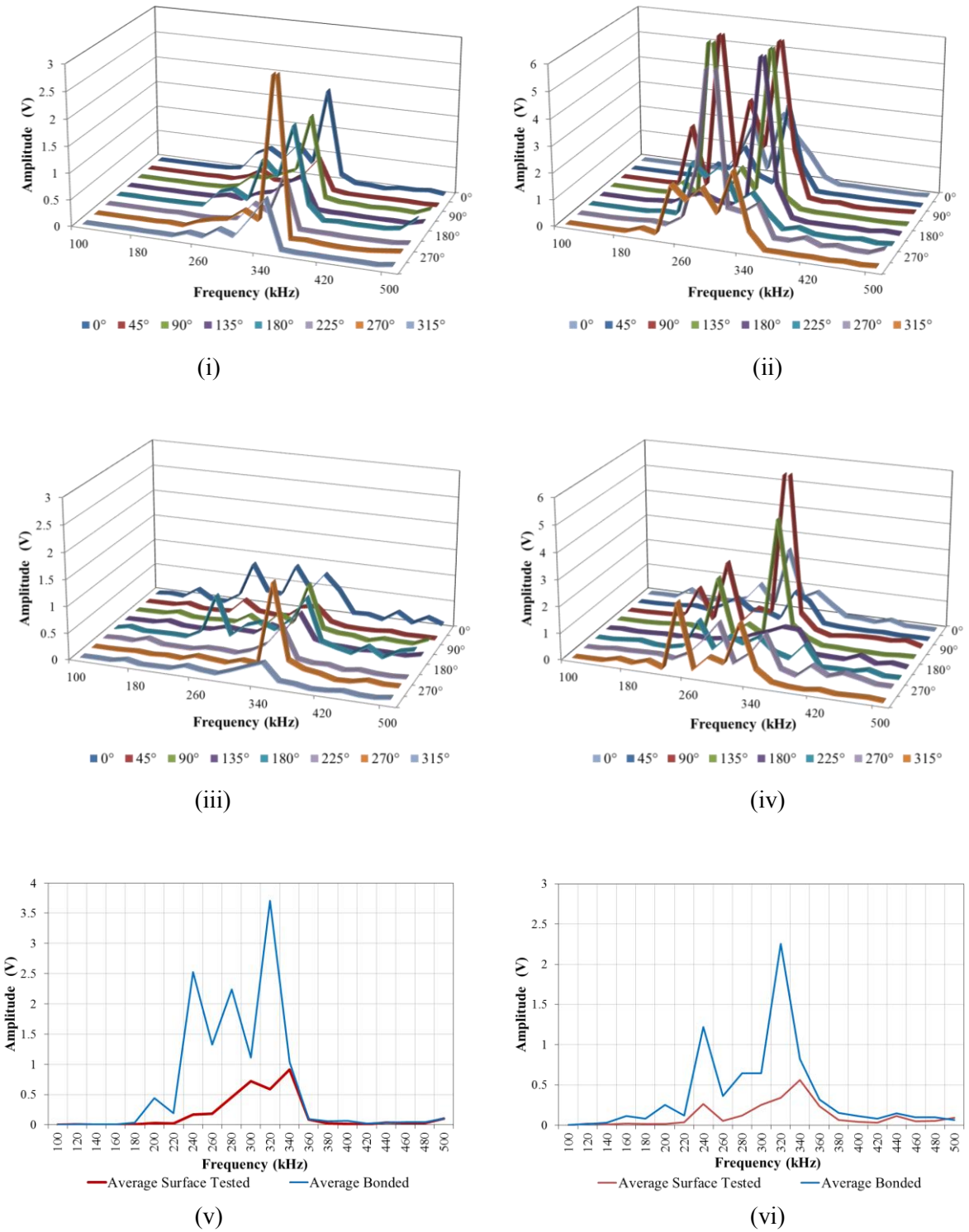


**Figure 83 Characterisation of the sensor 150722-02, on-surface and bonded in a $(0/90)_4$ laminate by the use of the HeNe laser. The excitation was performed on the same face where the FOAES was bonded. Figure 83 (i) and (ii) show the frequency response for the on-surface and bonded characterisation tests respectively, using a R30α as emitter. Figure 83 (iii) and (iv) show the same information when a R50α was used as emitter. Figure 83 (v) and (vi) show summarised information averaging the response at the different directions when R30α and R50α were used as emitters respectively.**

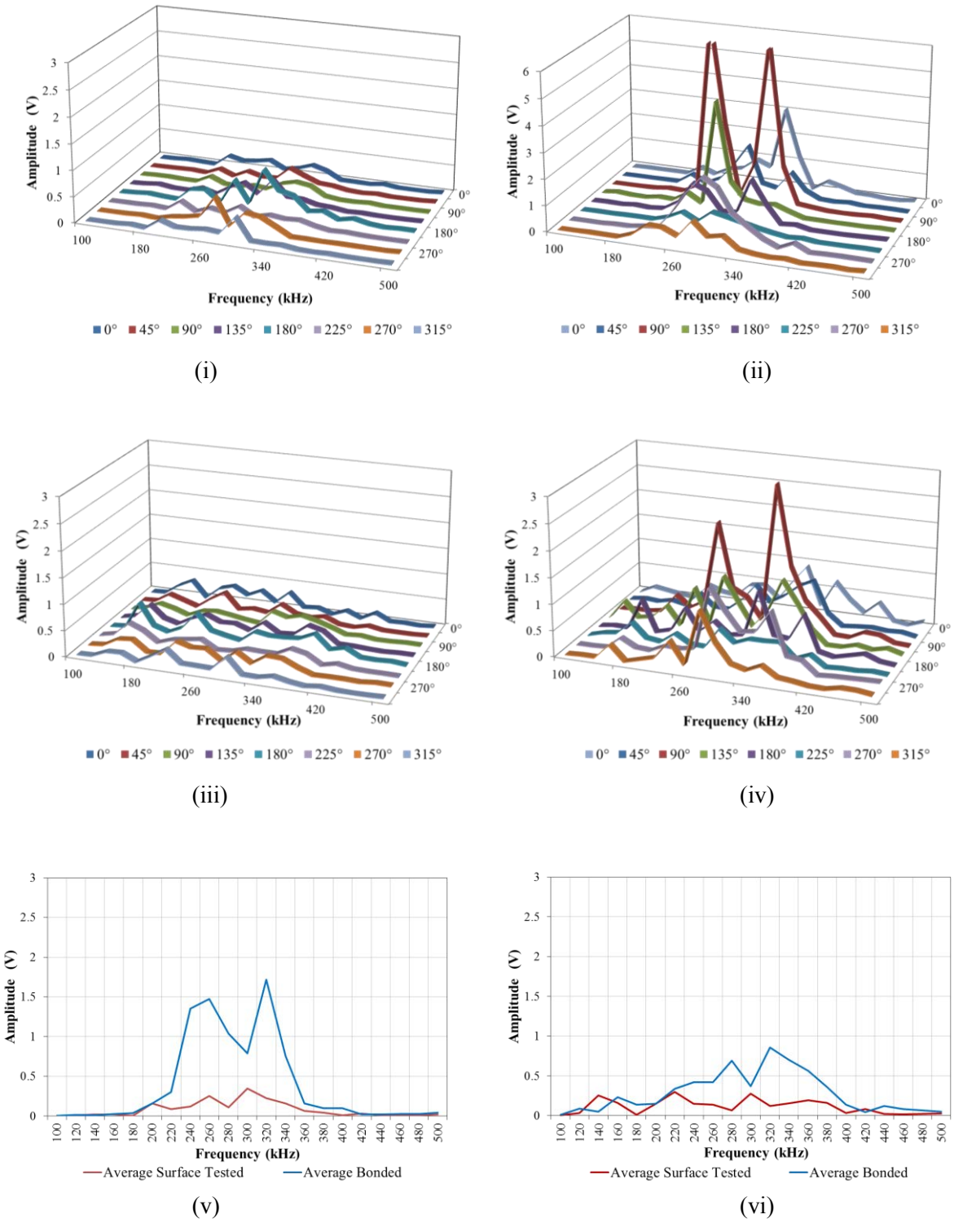


**Figure 84 Characterisation of the sensor 150722-03, on-surface and bonded in a $(0/90)_4$ laminate by the use of the HeNe laser. The excitation was performed on the same face where the FOAES was bonded. Figure 84 (i) and (ii) show the frequency response for the on-surface and bonded characterisation tests respectively, using a R30α as emitter. Figure 84 (iii) and (iv) show the same information when a R50α was used as emitter. Figure 84 (v) and (vi) show summarised information averaging the response at the different directions when R30α and R50α were used as emitters respectively.**

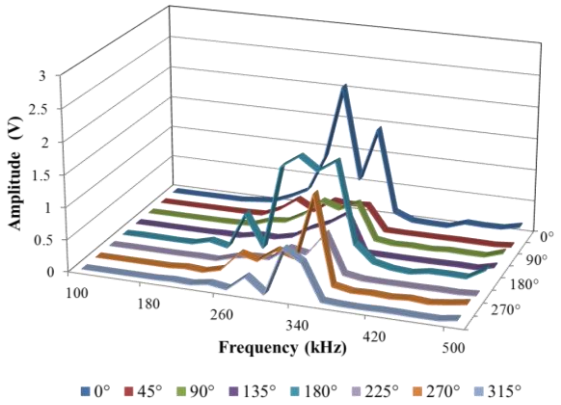


(i)

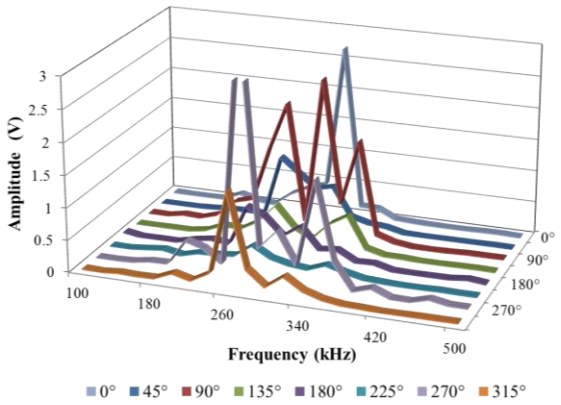


(ii)

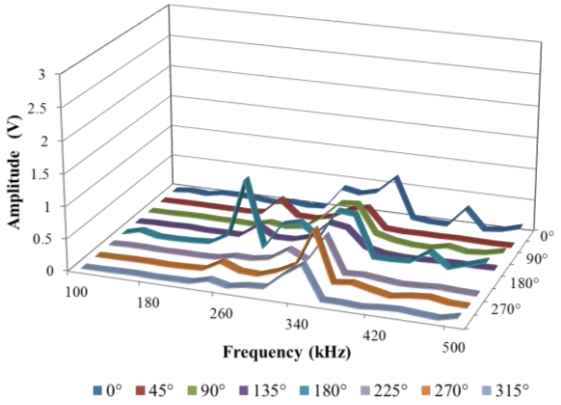


(iii)

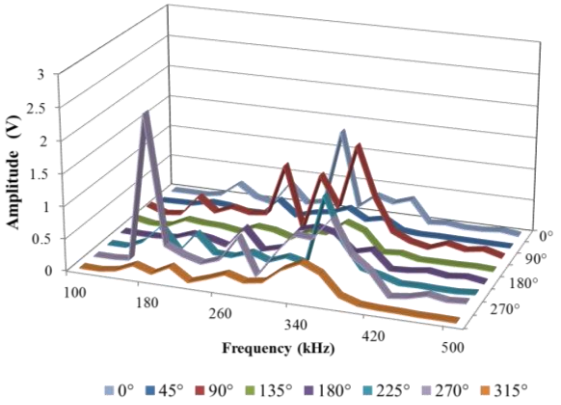


(iv)

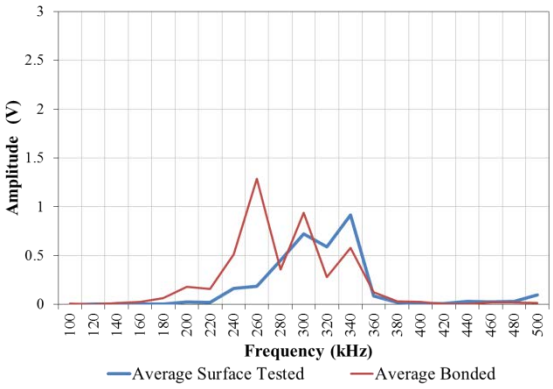


(v)

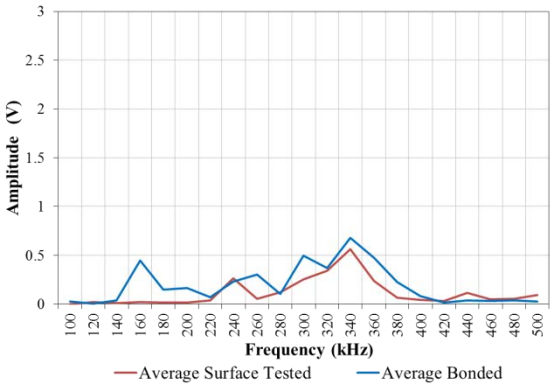


(vi)

**Figure 85 Characterisation of the sensor 150722-02, on-surface and bonded on a $(0/90)_4$ laminate by the use of the HeNe laser. The excitation was performed on the opposite face where the FOAES was bonded. Figure 85 (i) and (ii) show the frequency response for the on-surface and bonded characterisation tests respectively, using a R30α as emitter. Figure 85 (iii) and (iv) show the same information when a R50α was used as emitter. Figure 85 (v) and (vi) show summarised information averaging the response at the different directions when R30α and R50α were used as emitters respectively.**

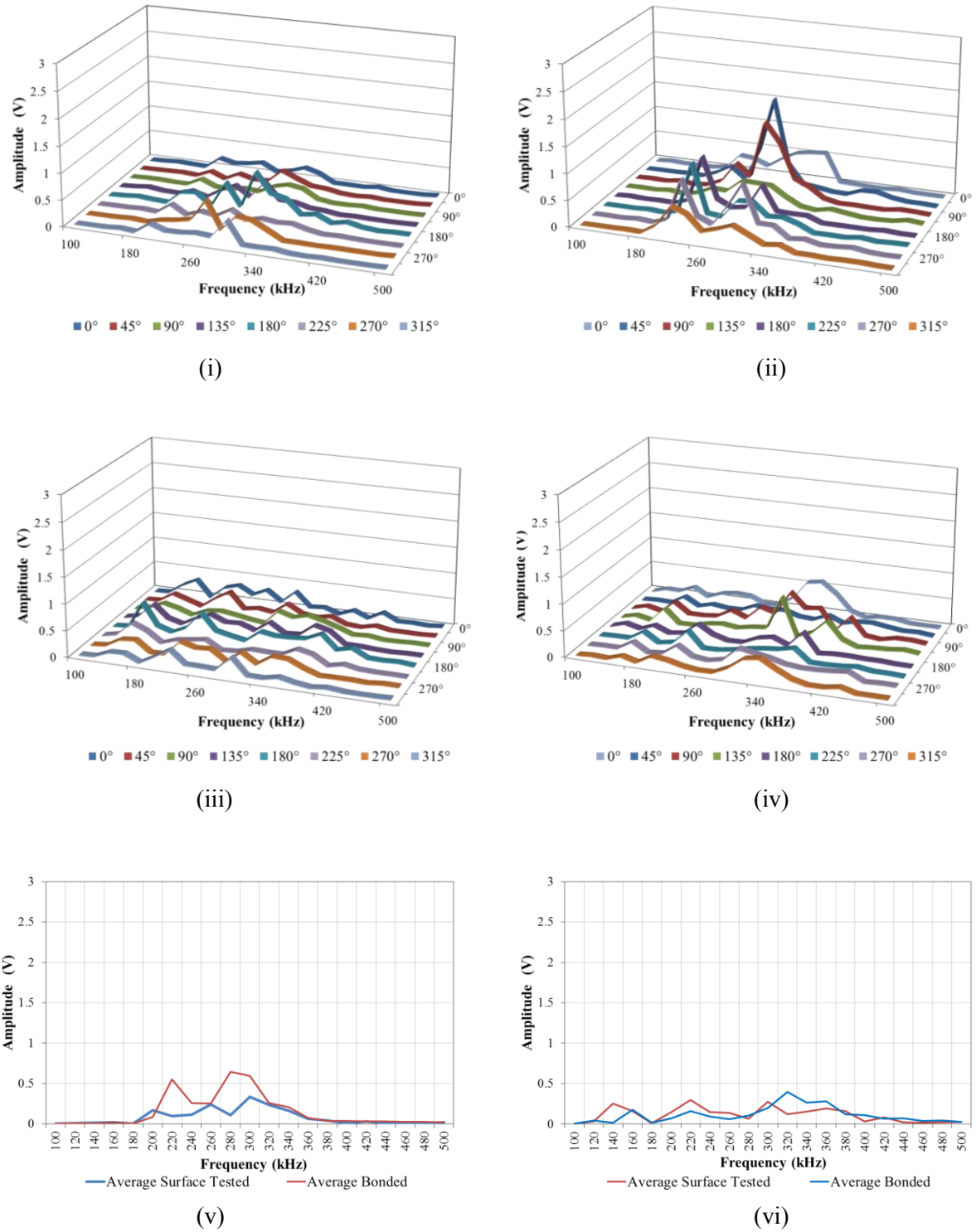


**Figure 86 Characterisation of the sensor 150722-03, on-surface and bonded on a $(0/90)_4$ laminate by the use of the HeNe laser. The excitation was performed on the opposite face where the FOAES was bonded. Figure 85 (i) and (ii) show the frequency response for the on-surface and bonded characterisation tests respectively, using a R30α as emitter. Figure 85 (iii) and (iv) show the same information when a R50α was used as emitter. Figure 85 (v) and (vi) show summarised information averaging the response at the different directions when R30α and R50α were used as emitters respectively.**

## 5.6 Directionality of the FOAES

The data discussed in the previous sections of this chapter have shown that all the FOAES were detecting signals of different amplitudes when similar stimuli were applied at different angles. This phenomenon is called directionality and is normally related to the highly anisotropic nature of the response of the FOAES combined with the anisotropic acoustic properties of FRPC materials where the acoustic waves are propagating along the fibres which act as waveguides.

In order to establish a qualitative assessment of the FOAESs directionality, a comparison with the simultaneously characterised benchmarking piezoelectric sensors R30α and R50α was performed. The R30α and R50α piezoelectric sensors have a specified maximum directionality of ±1.5 dB [197, 198], so by comparing the standard deviation at each frequency expressed as percentage of the average would enable the assessment of each FOAES as having lower, similar or higher directionality. For understanding better if the embedding of the FOAES improved or worsened the directionality, the standard deviation of the data collected from the surface-mounted configuration testing was expressed in the same way (percentage over the average for each frequency) for each FOAES.

The results for the characterised FOAES (twelve embedded and two bonded) are shown in Figure 87 to Figure 100.

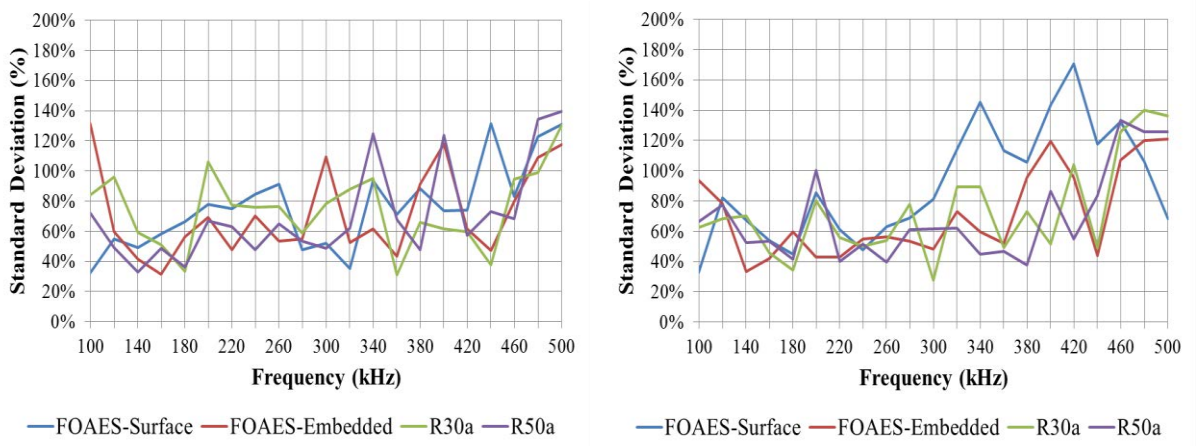


(i) (ii)

**Figure 87 Directionality of the sensor 150625-03 (on-surface and embedded on a $(0)_4$ laminate) expressed as the standard deviation in percentage over the amplitude of the peaks. The comparative data of the references R30α and R50α when embedded are added for comparison purposes. Figure 87 (i) and (ii) show the data when additional R30α and a R50α were used as emitters respectively.**

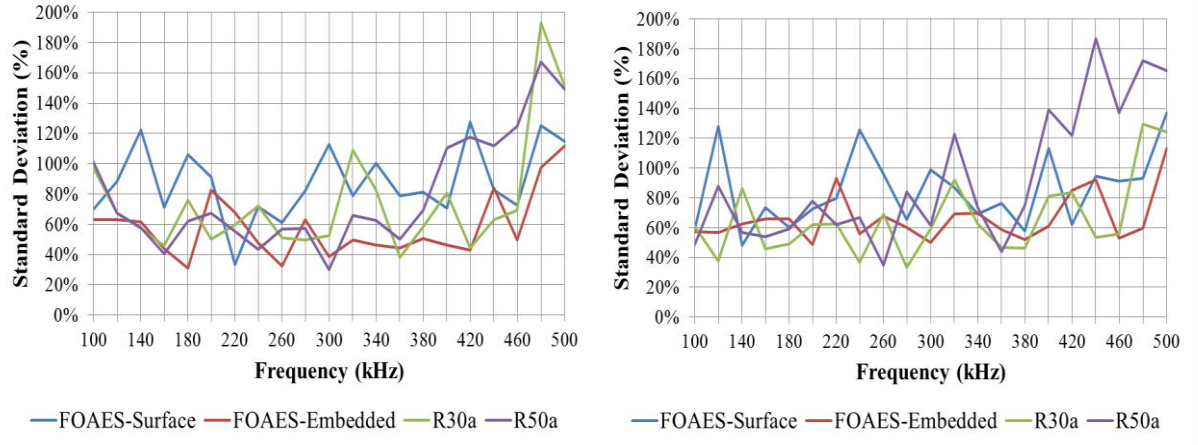


(i) (ii)

**Figure 88 Directionality of the sensor 150624-06 (on-surface and embedded on a $(0)_4$ laminate) expressed as the standard deviation in percentage over the amplitude of the peaks. The comparative data of the references R30α and R50α when embedded are added for comparison purposes. Figure 88 (i) and (ii) show the data when additional R30α and a R50α were used as emitters respectively.**

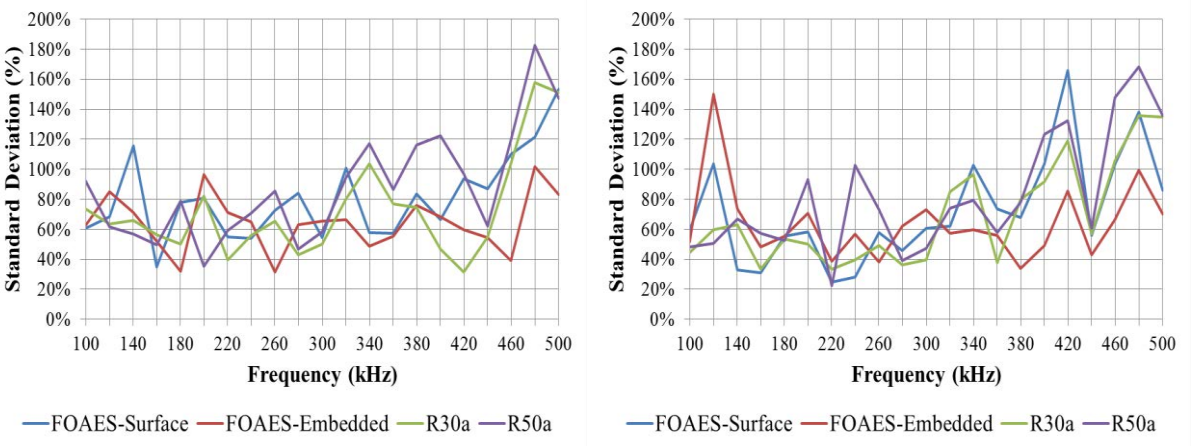


(i) (ii)

**Figure 89 Directionality of the sensor 150625-02 (on-surface and embedded on a $(0)_4$ laminate) expressed as the standard deviation in percentage over the amplitude of the peaks. The comparative data of the references R30α and R50α when embedded are added for comparison purposes. Figure 89 (i) and (ii) show the data when additional R30α and a R50α were used as emitters respectively.**

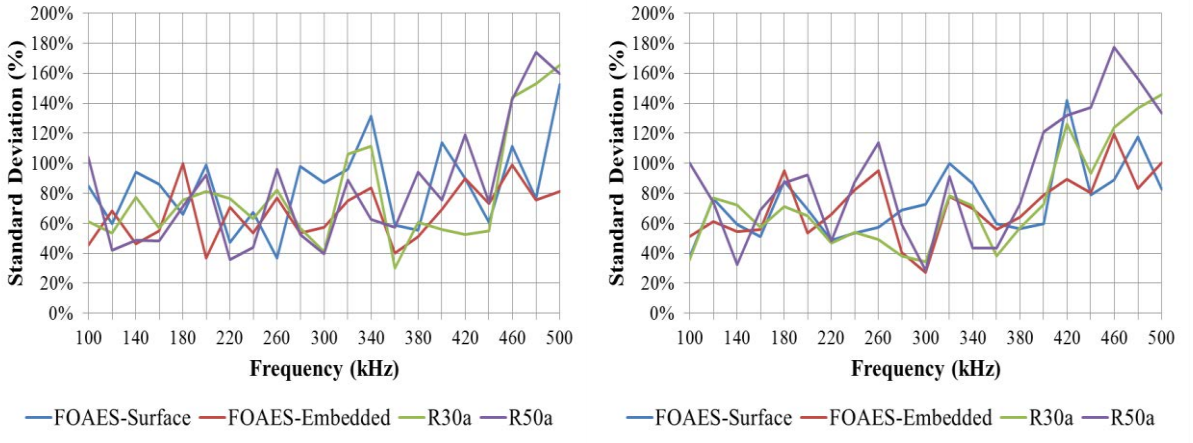


(i) (ii)

**Figure 90 Directionality of the sensor 150616-04 (on-surface and embedded on a $(0)_4$ laminate) expressed as the standard deviation in percentage over the amplitude of the peaks. The comparative data of the references R30α and R50α when embedded are added for comparison purposes. Figure 90 (i) and (ii) show the data when additional R30α and a R50α were used as emitters respectively.**

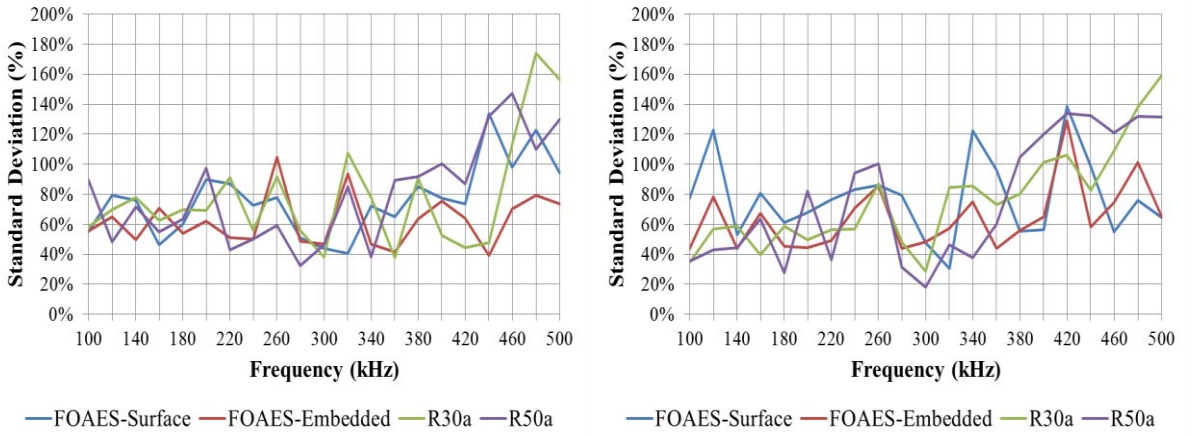


**Figure 91 Directionality of the sensor 150624-02 (on-surface and embedded on a $(0)_4$ laminate) expressed as the standard deviation in percentage over the amplitude of the peaks. The comparative data of the references R30α and R50α when embedded are added for comparison purposes. Figure 91 (i) and (ii) show the data when additional R30α and a R50α were used as emitters respectively.**

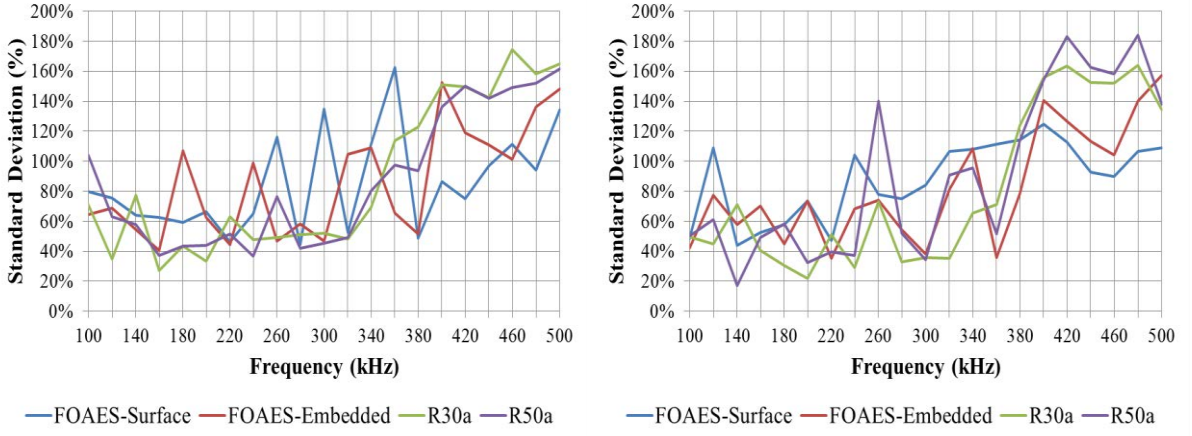


**Figure 92 Directionality of the sensor 150616-05 (on-surface and embedded on a $(0)_8$ laminate) expressed as the standard deviation in percentage over the amplitude of the peaks. The comparative data of the references R30α and R50α when embedded are added for comparison purposes. Figure 92 (i) and (ii) show the data when additional R30α and a R50α were used as emitters respectively.**

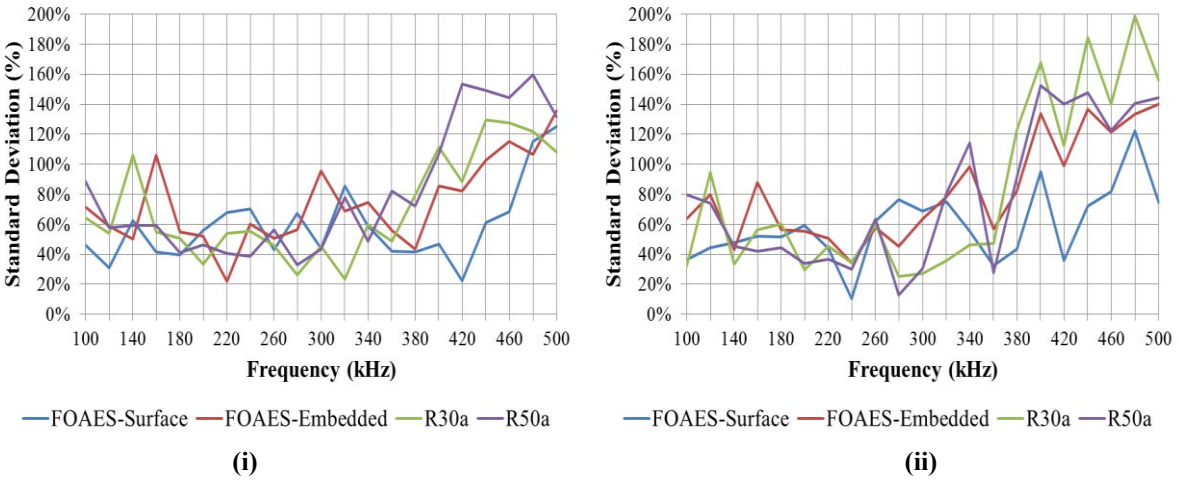


**Figure 93 Directionality of the sensor 150624-04 (on-surface and embedded on a $(0)_8$ laminate) expressed as the standard deviation in percentage over the amplitude of the peaks. The comparative data of the references R30α and R50α when embedded are added for comparison purposes. Figure 93 (i) and (ii) show the data when additional R30α and a R50α were used as emitters respectively.**

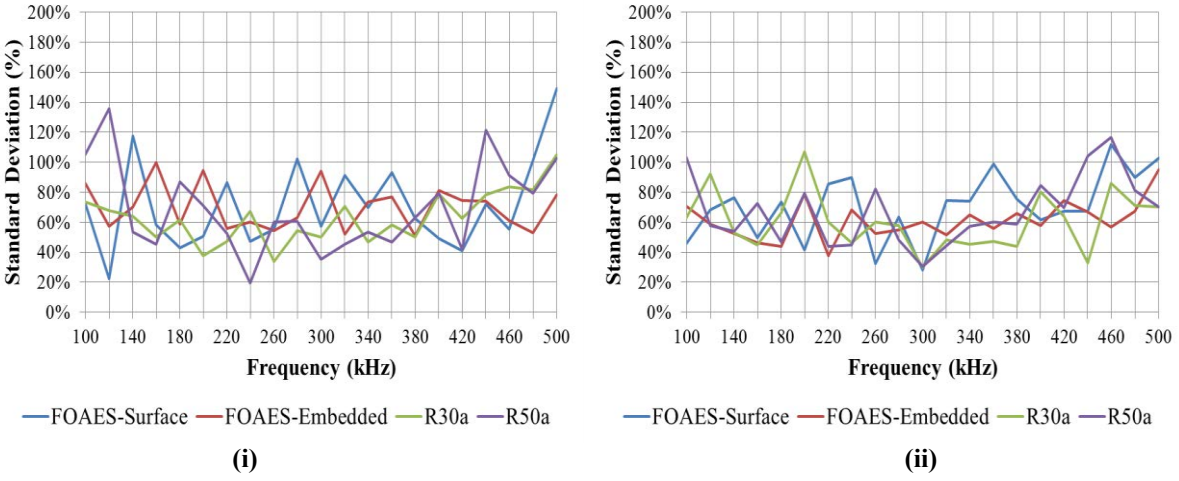


**Figure 94 Directionality of the sensor 150616-02 (on-surface and embedded on a $(0/90)_2$ laminate) expressed as the standard deviation in percentage over the amplitude of the peaks. The comparative data of the references R30α and R50α when embedded are added for comparison purposes. Figure 94 (i) and (ii) show the data when additional R30α and a R50α were used as emitters respectively.**

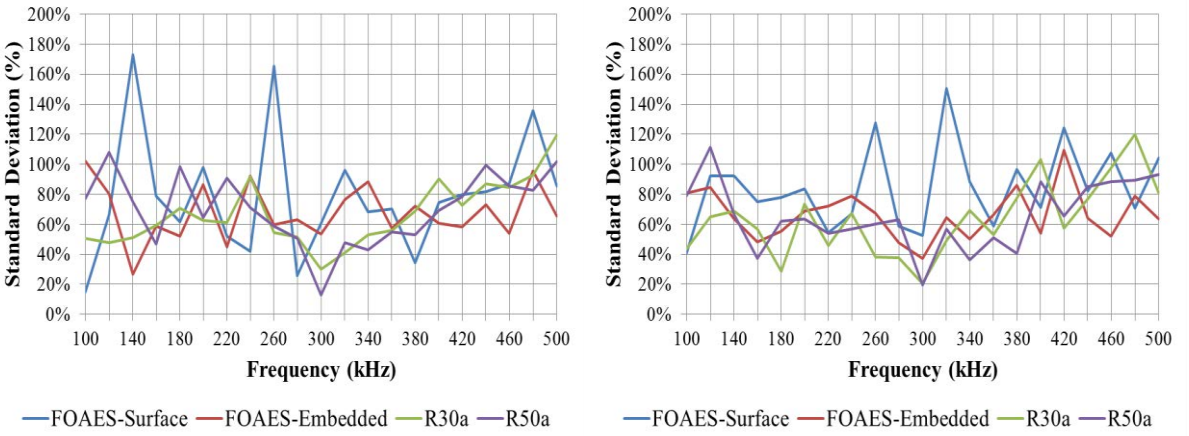


(i) (ii)

**Figure 95 Directionality of the sensor 150616-03 (on-surface and embedded on a $(0/90)_2$ laminate) expressed as the standard deviation in percentage over the amplitude of the peaks. The comparative data of the references R30α and R50α when embedded are added for comparison purposes. Figure 95 (i) and (ii) show the data when additional R30α and a R50α were used as emitters respectively.**

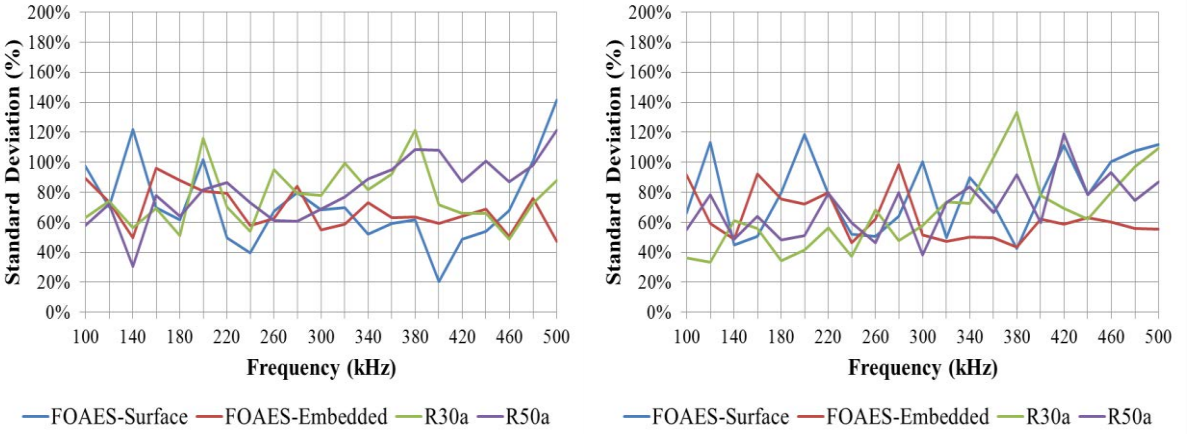


(i) (ii)

**Figure 96 Directionality of the sensor 150624-03 (on-surface and embedded on a $(0/90)_2$ laminate) expressed as the standard deviation in percentage over the amplitude of the peaks. The comparative data of the references R30α and R50α when embedded are added for comparison purposes. Figure 96 (i) and (ii) show the data when additional R30α and a R50α were used as emitters respectively.**

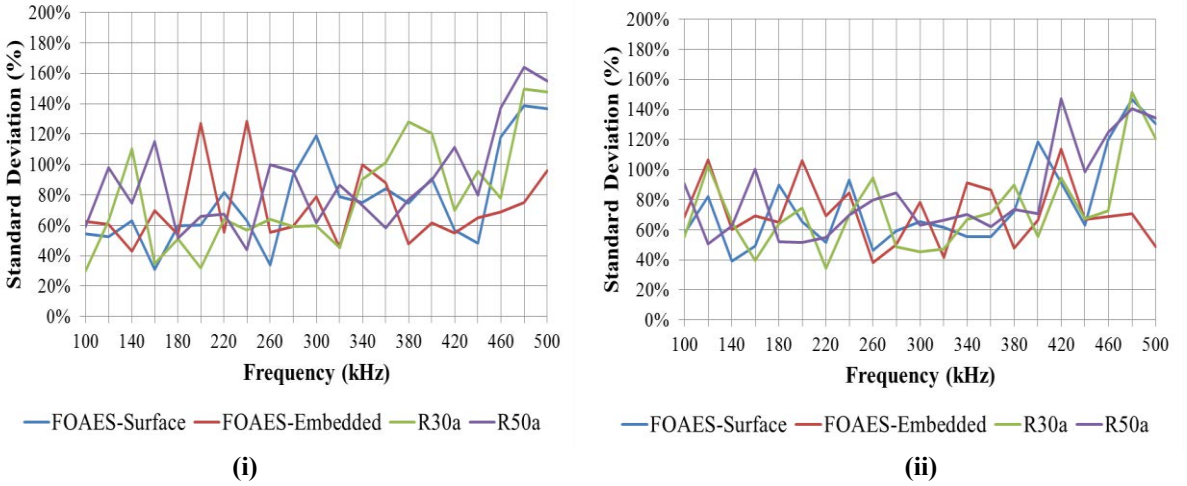


(i) (ii)

**Figure 97 Directionality of the sensor 150625-04 (on-surface and embedded on a (0/90)2 laminate) expressed as the standard deviation in percentage over the amplitude of the peaks. The comparative data of the references R30α and R50α when embedded are added for comparison purposes.**

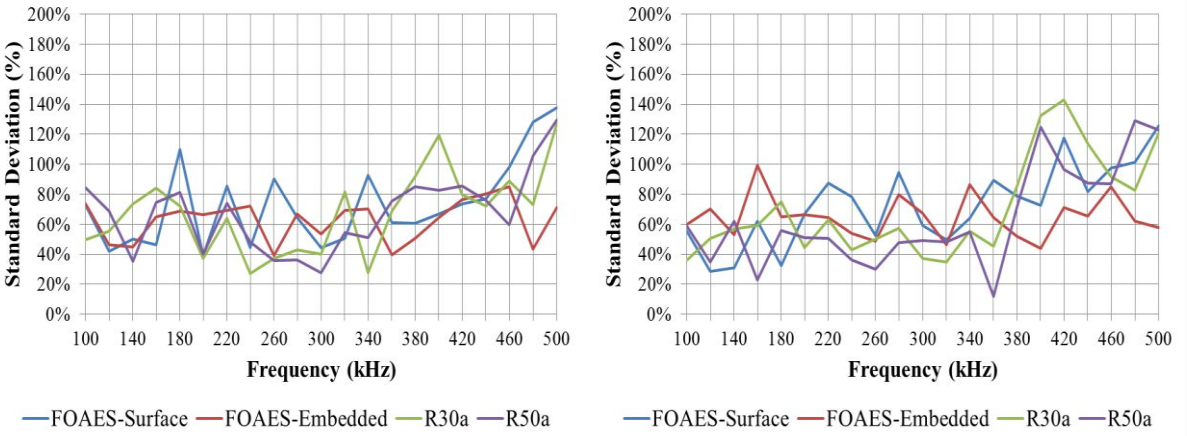


(i) (ii)

**Figure 98 Directionality of the sensor 150731-02 (on-surface and embedded on a (0/90)4 laminate) expressed as the standard deviation in percentage over the amplitude of the peaks. The comparative data of the references R30α and R50α when embedded are added for comparison purposes. Figure 98(i) and (ii) show the data when additional R30α and a R50α were used as emitters respectively.**

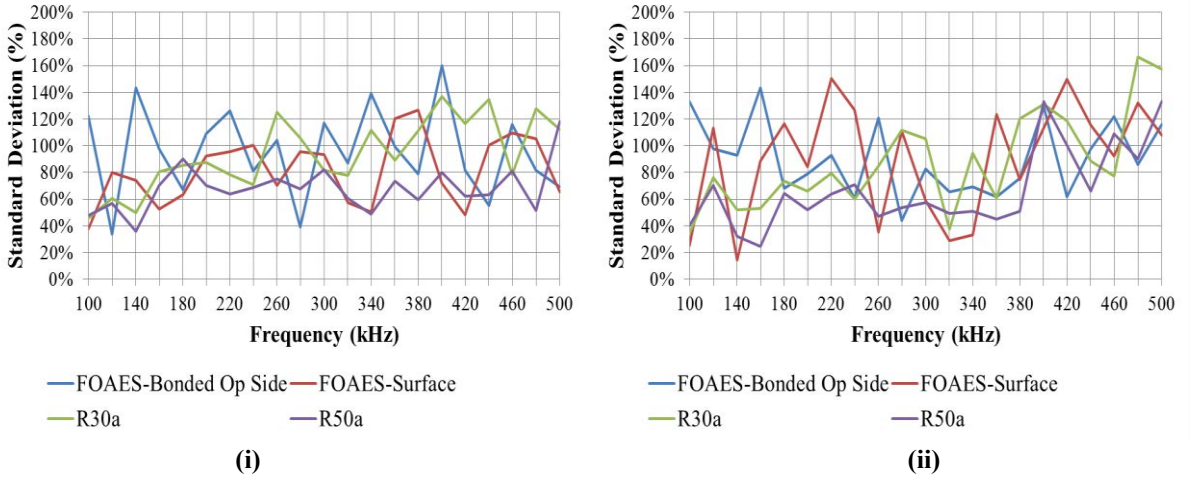


**Figure 99 Directionality of the sensor 150722-02 (on-surface and bonded on a $(0/90)_4$ laminate) expressed as the standard deviation in percentage over the amplitude of the peaks. For comparison purposes the emitter was located at the opposite side where the FOAES was bonded (to enable the use of the comparison AE commercial sensors). Figure 99 (i) and (ii) show the data when a R30α and a R50α were used as emitters respectively.**

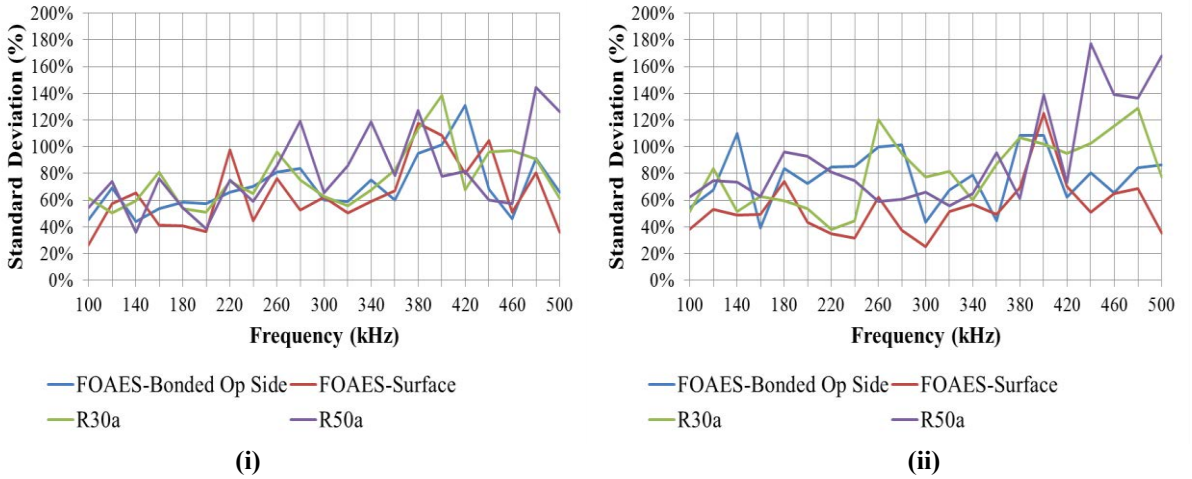


**Figure 100 Directionality of the sensor 150722-03 (on-surface and bonded on a $(0/90)_4$ laminate) expressed as the standard deviation in percentage over the amplitude of the peaks. For comparison purposes the emitter was located at the opposite side where the FOAES was bonded (to enable the use of the comparison AE commercial sensors). Figure 100 (i) and (ii) show the data when a R30α and a R50α were used as emitters respectively**

As it is clearly evident, the FOAES showed a comparable directionality with that of the benchmarking piezoelectric R30α and R50α sensors. In some frequencies and in some laminates the directionality was even observed to be slightly smaller. Just the sensor150616-03 (Figure 95) exhibited some peaks much higher than the overall trend presented by the commercial benchmark piezoelectric sensors. Similar conclusion can be drawn when analysing the effects in directionality of the embedding or bonding process. No particular trend was identified and therefore this parameter does not seem to be affected by the coupling media (Vaseline, embedment or bonding).

It should be considered that the variability of the response with the excitation angle or directionality is not a direct measurement of the directionality of the sensor (both FOAES and benchmarking piezoelectric sensors) but a combination of directionality of the sensor and anisotropy of the transmission media (material). However, the comparison with sensors of known directionality gives a qualitative idea of the assimilated behaviour of the novel optical sensors. An in-depth analysis of the directionality would require hardware and resources not available in this project.

## 5.7 Linearity and Fidelity of the FOAES

The linearity represents the increase in the amplitude of the signals detected by the FOAES as the excitation amplitude from the source was increased. To enable the evaluation of linearity of the FOAES, frequency sweep tests were repeated at different excitation amplitudes. The emitter used to produce the excitation (reference) signals was powered using continuous sinuses at different amplitudes via the signal generator (from – 2 V to +10 V with intervals of 2 V). The amplitude of the main harmonics detected was used to correlate them with changes in the amplitude of the excitation source using FFT spectral analysis.

It was consistently found that the amplitude of the FOAES response increased linearly with the linear changes of the excitation source as shown in Figure 101. This is especially important when studying real acoustic signatures, where a significant part of the analysis and filtering is based in amplitude or energy of the collected signals.

With respect to the fidelity (i.e. how accurately is the sensor picking up the frequencies of the acoustic signatures) the behaviour of the FOAES had been found to be consistently excellent. The performed experiments enabled the excitation of the plate with a dominant frequency. The comparison between the frequencies observed after the analysis of the data collected with the excitation frequency allowed the assessment of the fidelity. To carry out a global assessment, the average and standard deviation at each frequency for all the embedded FOAES was calculated and the data plotted. As it can be clearly seen from Figure 102, the FOAES exhibit a linear trend in all the collected frequencies with a negligible standard deviation. Similar results were obtained for both different piezo-emitters used in the experiments - R30$\alpha$ and R50$\alpha$. This effectively suggests that the FOAES are able to reliably detect and quantify the frequency of acoustic events.

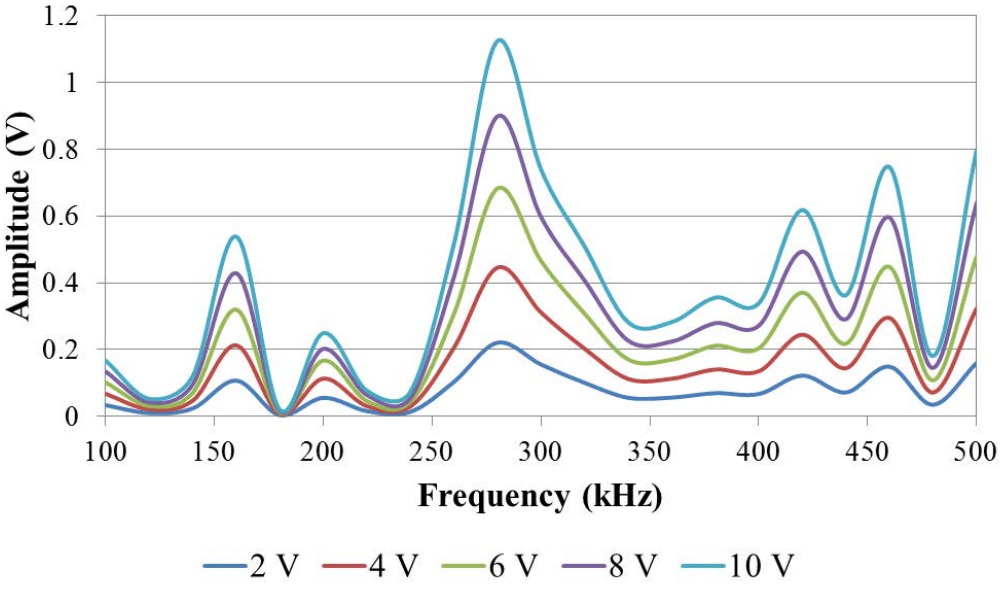


**Figure 101 Response of the sensor 150326-02 when excited with an R30α using continuous sinuses at 5 different amplitudes: 2V, 4V, 6V, 8V and 10V. This graph was extracted powering the FOAES with the HeNe laser and placing the emitter at the 0 degrees position.**

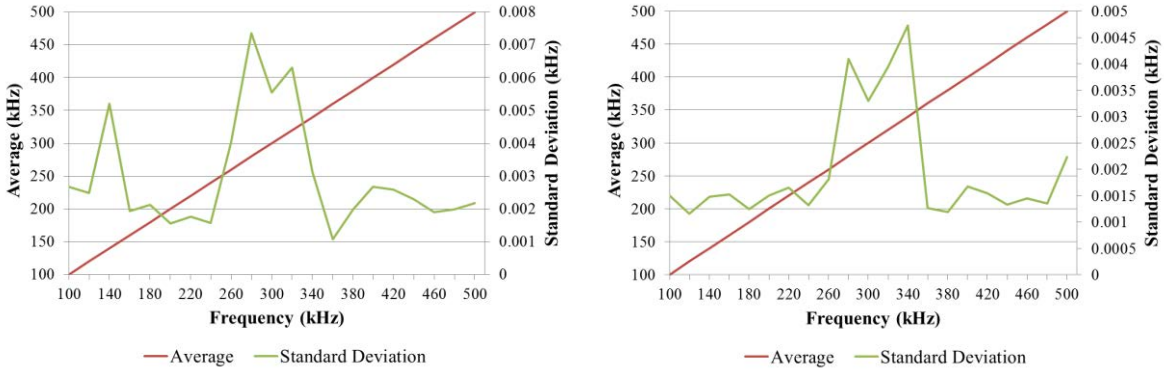


(i) (ii)

**Figure 102 Average and standard deviation per each frequency for all the embedded sensors. Figure 102 (i) shows the data when a R30α was used as emitter. Figure 102 (ii) shows the data when a R50α was used as emitter.**

## 5.8 Chapter Summary

Several FOAES were embedded in different configuration of glass fibre-epoxy panels manufactured by unidirectional prepegs. The FOAES was demonstrated to be able to withstand an industrial autoclave cycle as described in Figure 68 (iv). However, a sealing process was found to be necessary to avoid the resin bleeding out to encapsulate the optical fibres.

The FOAES were characterised by discrete frequency sweep before and after embedding, and their results compared. There were observed an overall improvement in the bandwidths and amplitudes. However, some sensors experienced a decrease in the acoustic properties after embedding. Resin ingression into the capillary was speculated as the potential reason.

The directionality of the embedded FOAES and surface characterised conventional piezoelectric PZT AE sensors (R30α and R50α) was assessed as similar. In addition, the FOAES were found to exhibit a linear response and excellent fidelity. This was potentially a consequence of the physical configuration of the sensor – double cantilevered optical fibre. The optical fibre will vibrate with the same frequency of the excitation source, and the amplitude of the oscillation will be related to the energy or amplitude of the aforementioned excitation. The oscillation will be translated into proportional opposite variations of the transmitted power to both optical power outputs. This phenomenon will increase in the frequencies where the sensor is more resonant or close to its natural frequencies, and will be reduced or even cancelled where the frequencies are above the damping limit.

# CHAPTER 6

## Comparison of embedded FOAES with surface-mounted piezo-electric AE sensors

# 6 Comparison of embedded FOAES with surface-mounted piezo-electric AE sensors

## 6.1 Introduction

The last stage of the project was the direct comparison of the performance of the embedded FOAES characterised in the previous chapter with the performance of the surface-mounted commercial piezoelectric AE sensors. Longitudinal strips of 25 mm width containing each embedded FOAES in the centre were marked on the laminates. Special care was taken for the marking lines to be parallel to the FOAES, as detailed in Figure 103. The strips were then cut with a 75 mm diameter electro-deposited diamond circular blade, keeping at least a couple of millimetres of clearance from the red lines.

The edges of the cut strips were finally polished in a flat belt grinder by a P320 aluminium oxide sanding belt. The flat surface of the equipment enabled the possibility of achieving flat edges parallel to the FOAES. The process for each strip was considered finished when the flat edges exactly matched the marked red line were achieved.

This overall process of cutting off strips was found to have a high ratio of sensor mortality, due to the high degree of vibration and especially by breaking the optical fibres coming out from the laminates at both extremes of the FOAES.

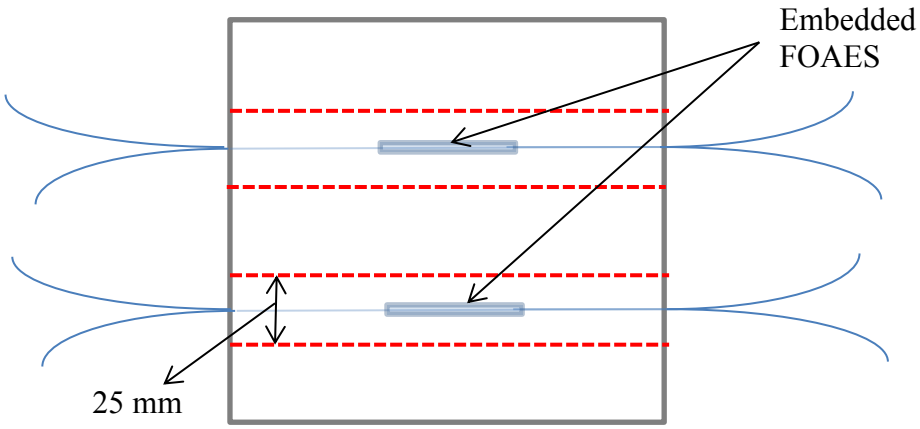


**Figure 103 Detail of strips marked on the laminate where the FOAES were embedded.**

The surviving strips were appropriately cleaned, and both extremes at both sides were gently sanded with a P500 sand paper and cleaned with Acetone. Aluminium end-tabs were then bonded to the strips with fast curing epoxy Araldite®, as described in Chapter 3.

The tooling side of the strip was used to install the benchmarking piezoelectric AE sensors, as described in Figure 40. The R30α and R50α piezoelectric sensors were coupled to the surface using a Vaseline layer and secured with duct tape. To ensure that the strain suffered by the FOAES was successfully monitored, a strain gauge FLA5-11 was bonded following the standard process recommended by the manufacturer on opposite side of the strip (non-flat). Due to slight protuberance created by the embedded FOAES, the strain gauges were applied at one side of the centre of the FOAES. A detail of one FOAES ready for the test is shown in Figure 104.

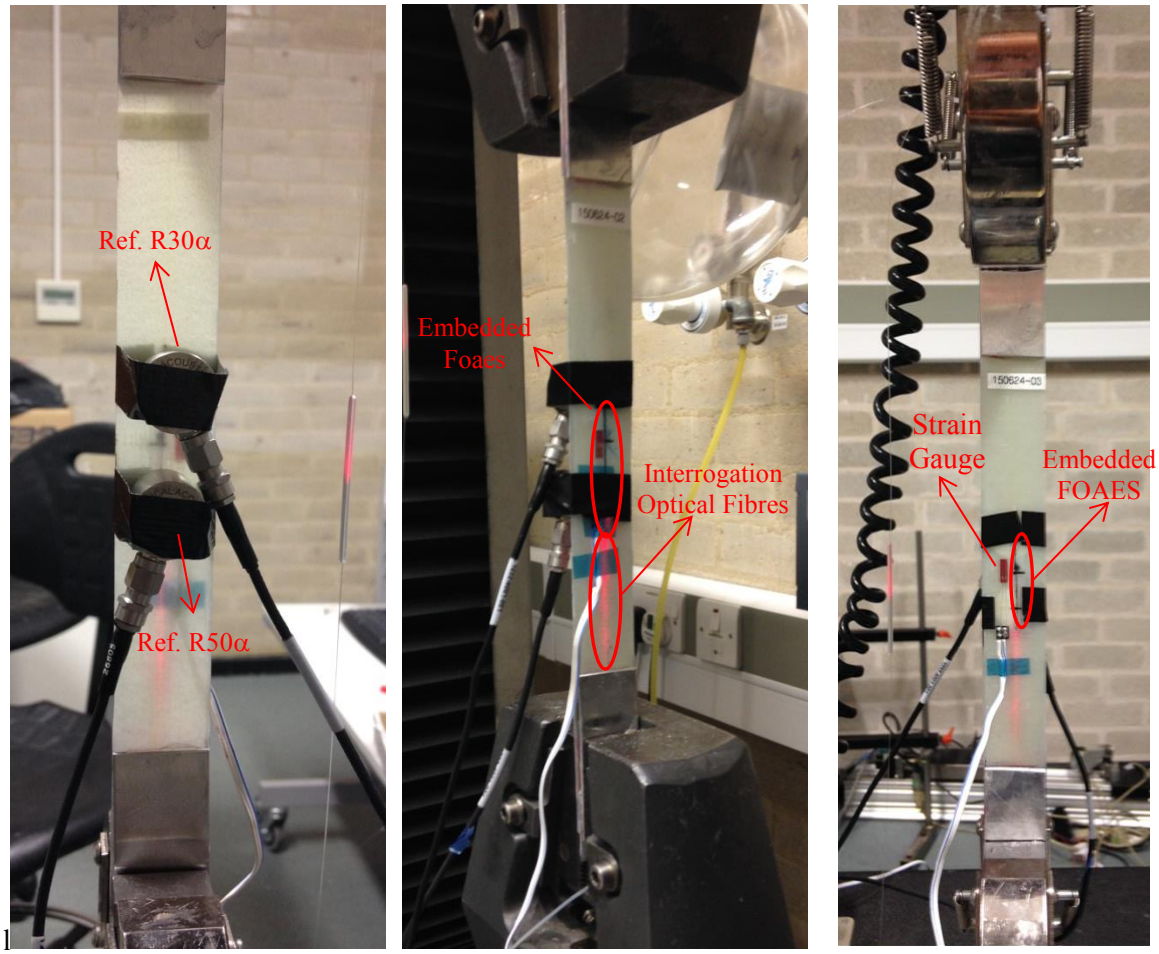


**Figure 104 FOAES prepared for being characterised in parallel with the two reference conventional AE sensors; (i) detail of the R30α and R50α attached to the testing strip by cloth tape; (ii) full setup with the FOAES, reference sensors and strain gauges visible; and (iii) strain gauge and FOAES.**

The strain and displacement of the test were recorded as parametric values in the AE system by the use of the analogue outputs of the tensile machine. This enabled the synchronisation of the AE equipment with the tensile machine. In the case of the strain gauge monitoring system, the strain was synchronised with the displacement of the tensile machine by matching the time "0 s" when the strain in the strain gauge and displacement in the tensile machine started to increase.

Finally the samples were tested until final failure, and the strain and acoustic signatures recorded. A picture of one of the strips containing the FOAES after being tested is shown in Figure 105.

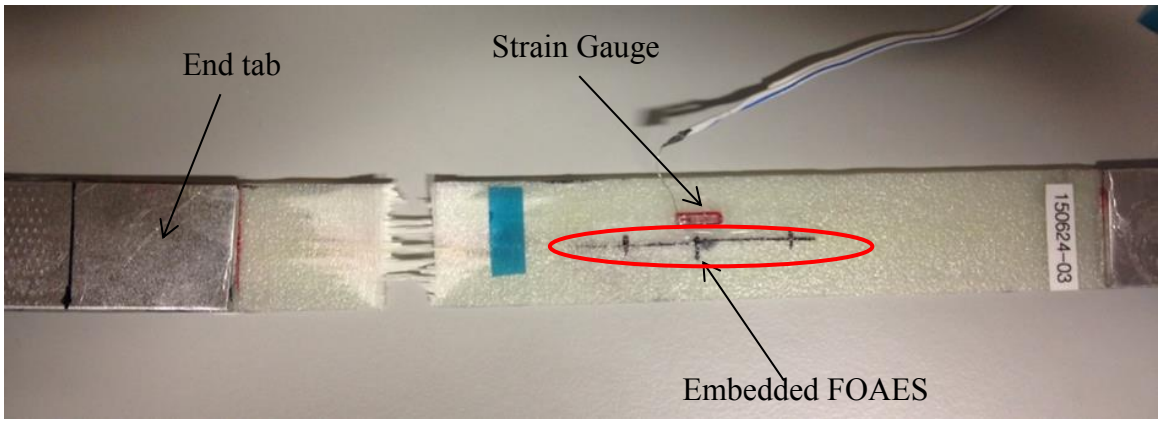


**Figure 105 Picture of one strip containing the FOAES after being tested.**

As described in Chapter 3, two different configurations were tested: one named as Configuration 1 specially designed for high-dumping metal, and a second configuration named as Configuration 2 used in composites with commercial AE sensors. Their differences were mainly longer PDT, HDT and HLT in Configuration 1 than in Configuration 2 (see Table 5).

Configuration 2 was tested initially for a reduced assessment of the laminate and embedded FOAES, by separating the jaws at 2mm/min until having different levels of strain monitored using a strain gauge attached onto the laminate. The tests were carried out progressively up to 0.1%, 0.2% and 0.3% of strain, collecting a new set of pencil breaks at all these points to understand if the strain was changing the performance of the FOAES. After collecting the signals from last pencil break tests at 0.3% strain, the laminates were brought back to 0% strain and the configuration of the AE hardware changed to Configuration 1. At that point, the

laminates were subjected to a full strain-stress test up to rupture at the same test speed of 2 mm/min.

Configuration 2 was found not to be suitable for the FOAES due to the damping characteristics. While the R30α and R50α piezoelectric sensors had enough time for detecting the AE signals and returning to the relaxed state, the signal in the FOAES was still decaying while the acquisition software closed some of the acoustic events. In the same way, Configuration 1 was found to be suitable when working with the FOAES but sometimes it created several hits in the commercial AE sensors to be picked up as a single event. In addition, despite of having a lot of acoustic activity happening during the pre-test up to 0.3% of strain (possibly due to matrix cracking) using the Configuration 2, it was found that the activity drastically disappeared in this strain interval when subsequently testing up to final failure using Configuration 1. Due to this reasons, it was decided after testing a few sensors not to perform the pre-test up to 0.3%. Testing directly to final failure using just Configuration 1 was elected instead. Examples of the unwanted effects generated by both Configuration 1 and Configuration 2 are shown in Figure 106.

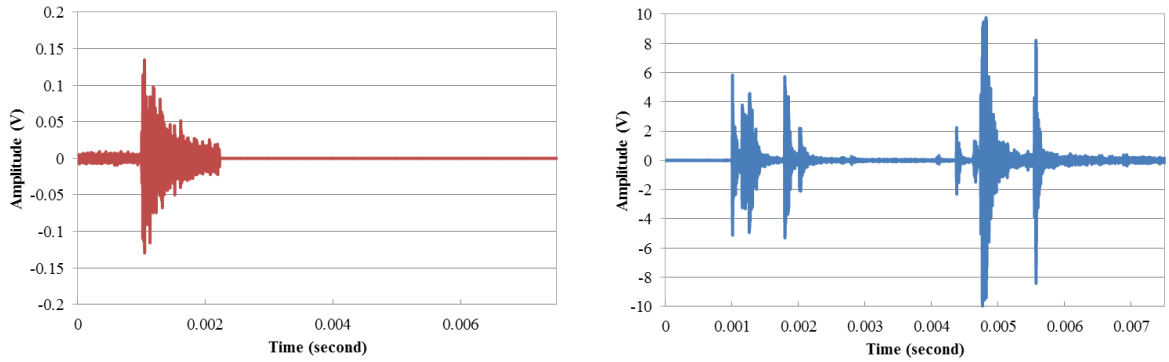


**Figure 106 Example of the unwanted effects of both configurations in the FOAES and in the conventional AE sensors. (i) Uncompleted signal collected by the FOAES when Configuration 2 was applied; and (ii) multiple hit collected by the R50α when Configuration 1 was selected.**

## 6.2 Direct comparison between FOAES and benchmark sensors

The data of each test was organised to show the cumulative number of hits per sensor type and the cumulative "Absolute Energy" of the hits, as shown in Figure 107 to Figure 112. With respect to the "Absolute Energy", the data are calculated for digitised signals as described by Equation (21) where $\Delta t$ is the sample width in seconds, $R$ is the resistance in Ohms, $V_i(t)$ is the sample amplitude in Volts, and the summation is carried out over the total length of the signal in seconds [49].

$$E = \left(\frac{\Delta t}{R}\right) \cdot \sum_i V_i^2\,(t) \qquad \textbf{(21)}$$

For the Mistras AE system this process is automatically performed, and the absolute energy can be converted in units of $10^{-21}$ Joules by multiplying the values by 9.31x10-4.

As it can be appreciated in the different figures, the FOAES is able to replicate and pick up the acoustic activity in a similar way that the conventional AE sensors when the appropriate configuration was set. The FOAES was able to track the degradation of the plates, showing the same trend that the conventional sensors. The FOAES showed as well very rich power spectra, but the correlation of the different failure modes with the FOAES was out of the scope of this project.

However, it should be noted that there were clear differences in the number of hits detected by the FOAES and the benchmarking sensors, and thus in the cumulative energy. These differences made necessary the use a secondary axis to represent the information of FOAES, and hence to have a good visual comparison. The causes for the FOAES to collect lower

number of events than the benchmark sensors were attributed to the laser system used in the experiments, and to the relatively low SNR of the interrogation system when compared to system of the piezoelectric AE sensors. The HeNe used to excite the FOAES was relatively very low power for the overall SNR of the system and had not polarisation control. This involved that just the higher energy events were able to create a signal strong enough to be above the system noise, being the low energy events detected by the benchmark sensors unnoticed by the FOAES. In addition, being the FOAES sensitive to changes in the polarisation of the light used for its interrogation, the changes in the polarisation state in the laser induced a higher system noise and thus, contributed to an even lower SNR of the system.

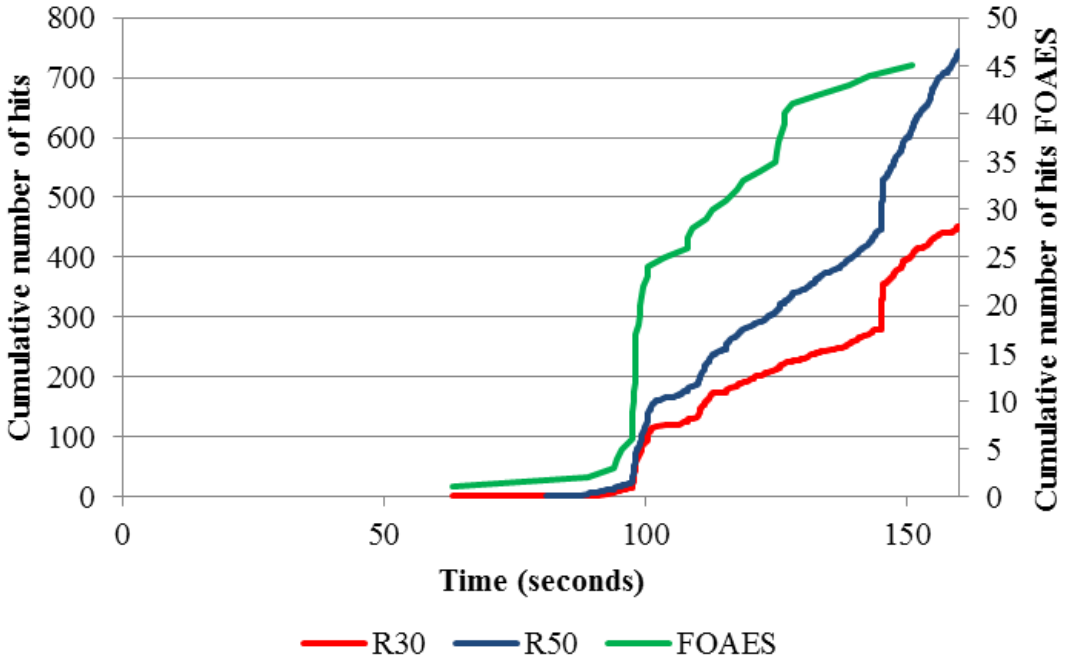


(i)

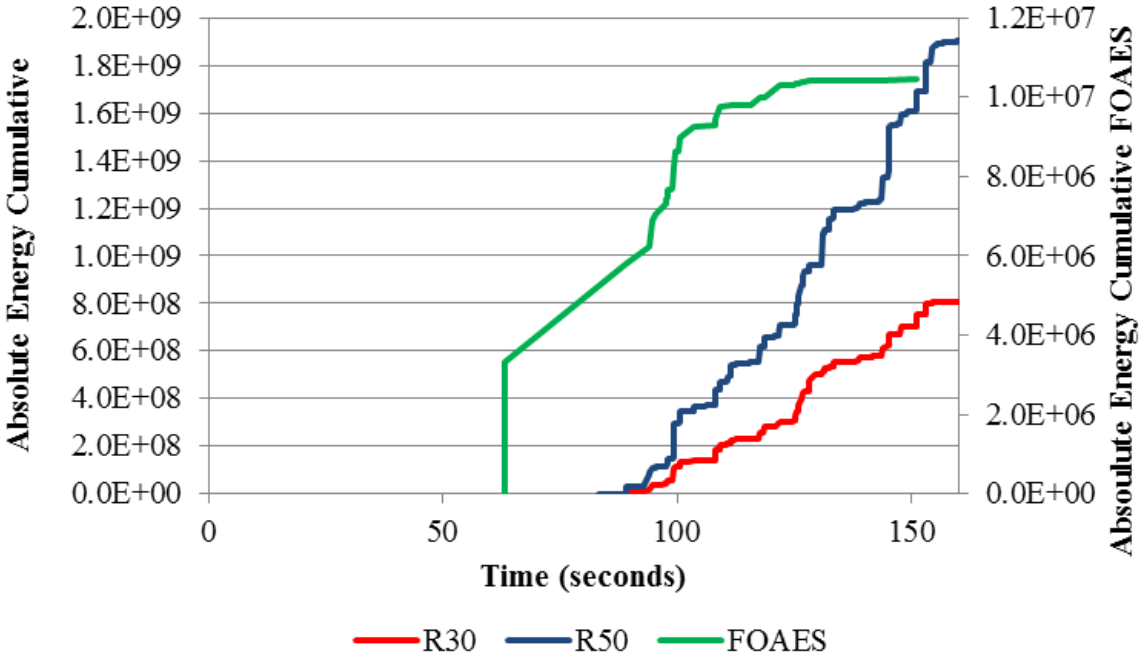


(ii)

**Figure 107 Cumulative number hits and cumulative Absolute Energy for the sensor 150616-05, shown respectively as Figure 107 (i) and (ii). In both graphs the data for the FOAES is attached as a secondary Y-axis, to enhance the visual comparison with the benchmarking sensors R30α and R50α.**

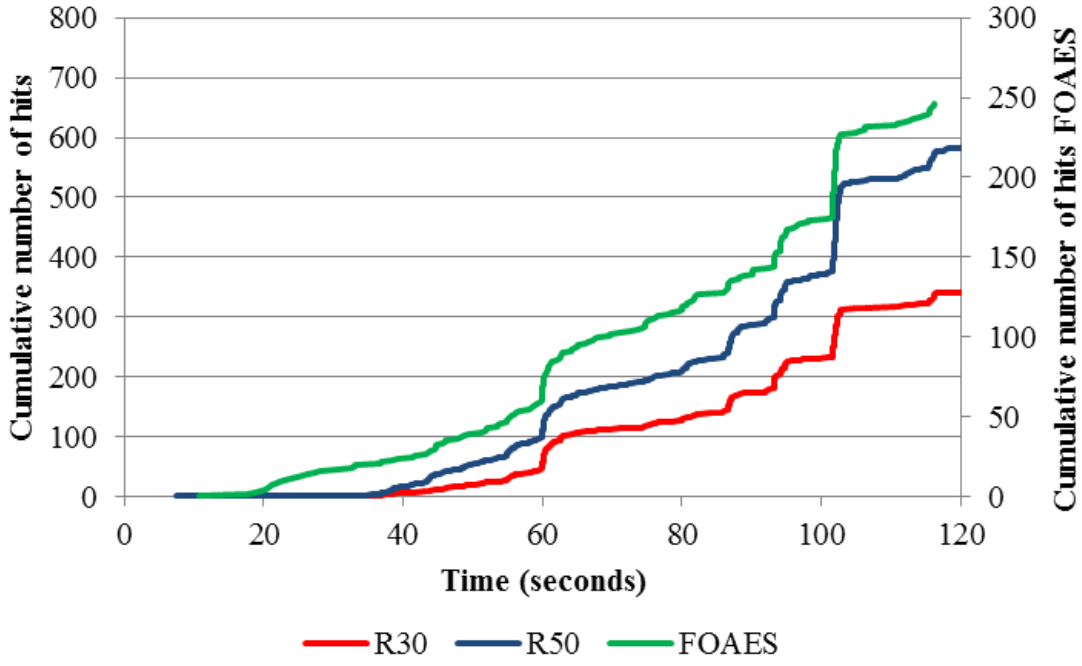


(i)

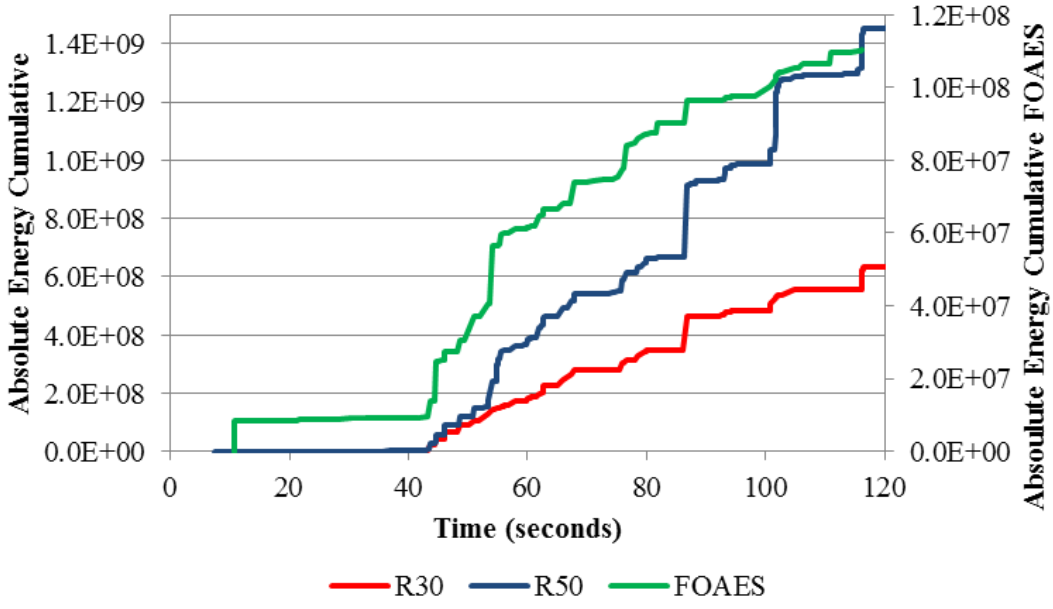


(ii)

**Figure 108 Cumulative number hits and cumulative Absolute Energy for the sensor 150624-02, shown respectively as Figure 108 (i) and (ii). In both graphs the data for the FOAES is attached as a secondary Y-axis, to enhance the visual comparison with the benchmarking sensors R30α and R50α.**

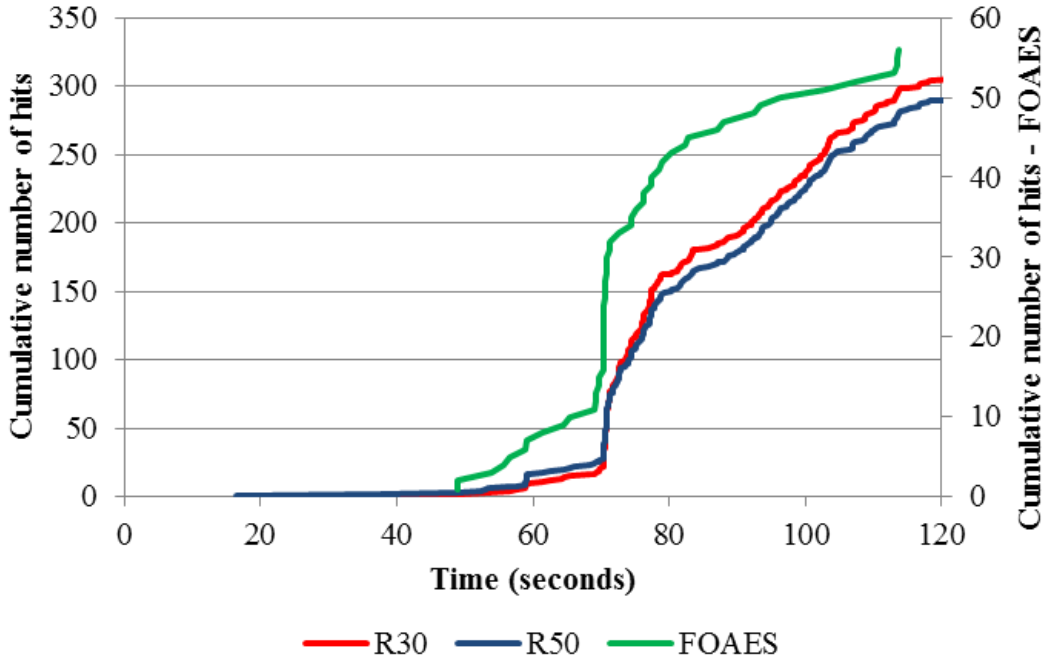


(i)

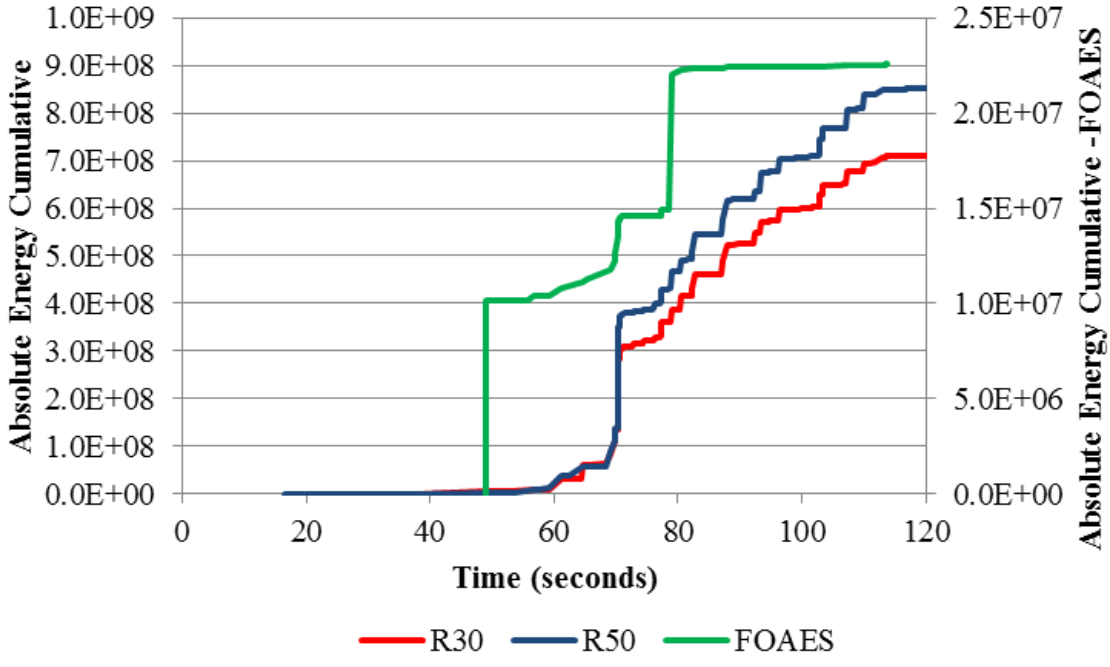


(ii)

**Figure 109 Cumulative number hits and cumulative Absolute Energy for the sensor 150624-04, shown respectively as Figure 109 (i) and (ii). In both graphs the data for the FOAES is attached as a secondary Y-axis, to enhance the visual comparison with the benchmarking sensors R30α and R50α.**

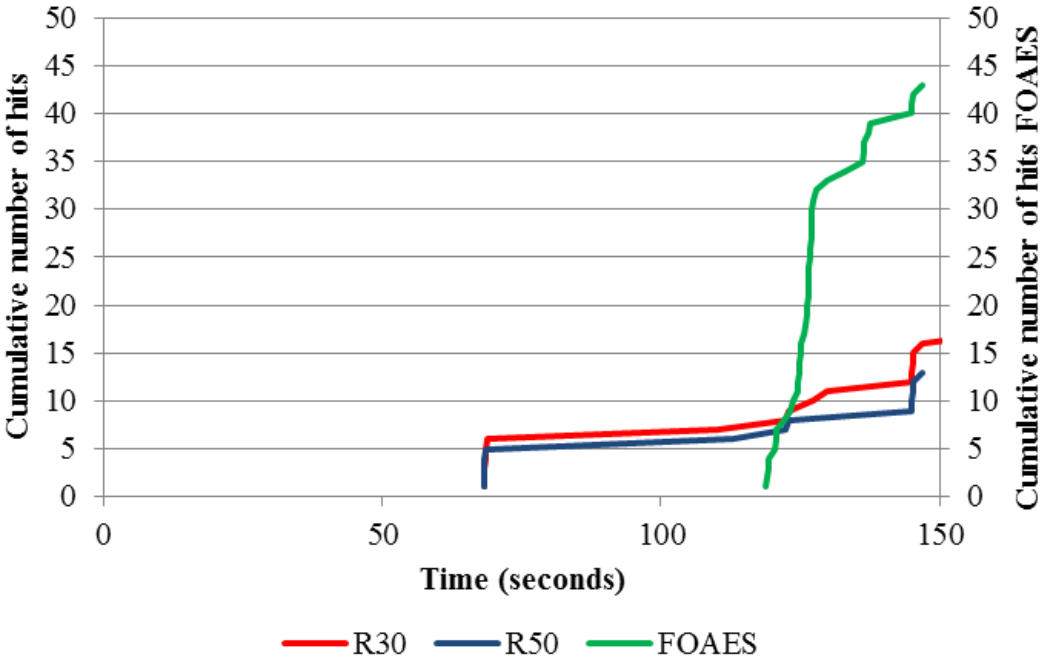


(i)

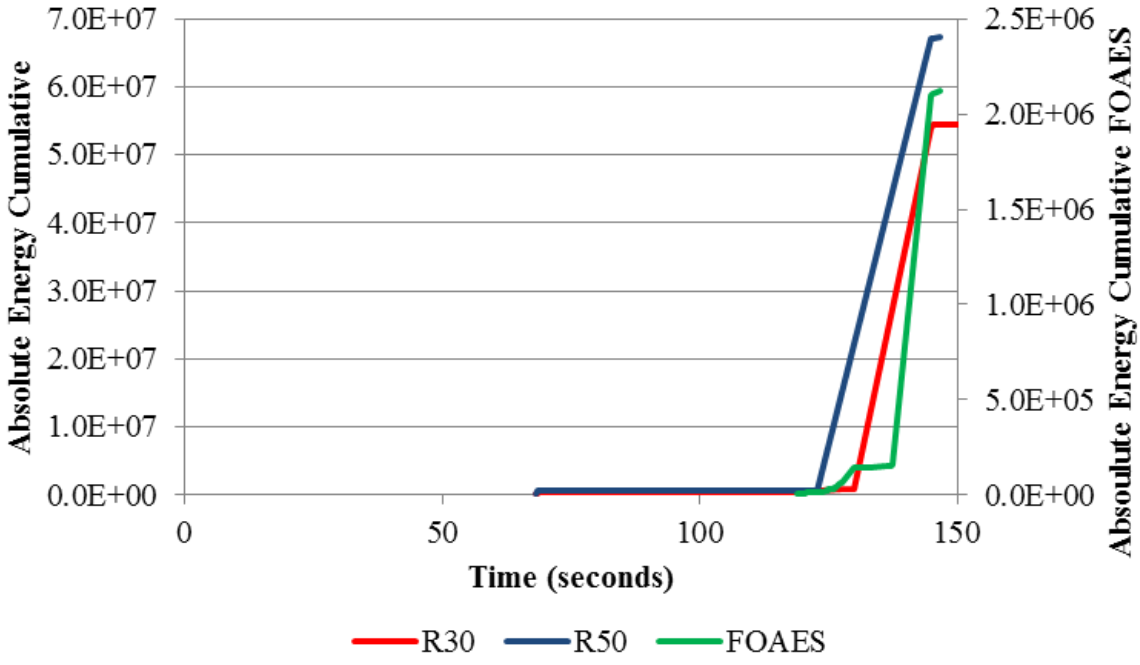


(ii)

**Figure 110 Cumulative number hits and cumulative Absolute Energy for the sensor 150625-03, shown respectively as Figure 109 (i) and (ii). In both graphs the data for the FOAES is attached as a secondary Y-axis, to enhance the visual comparison with the benchmarking sensors R30α and R50α.**

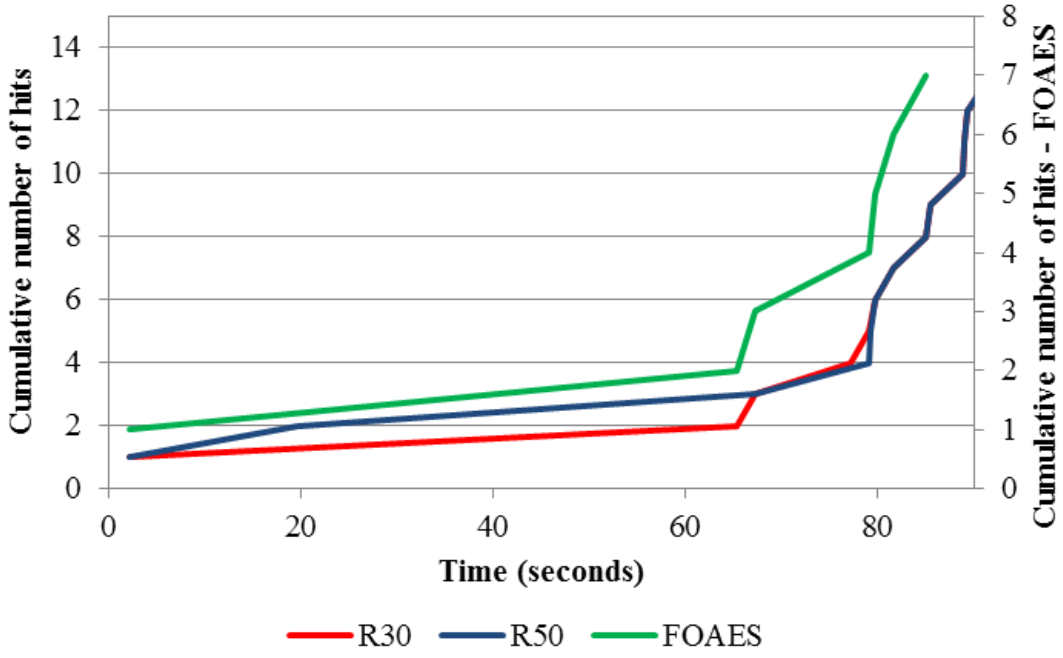


(i)

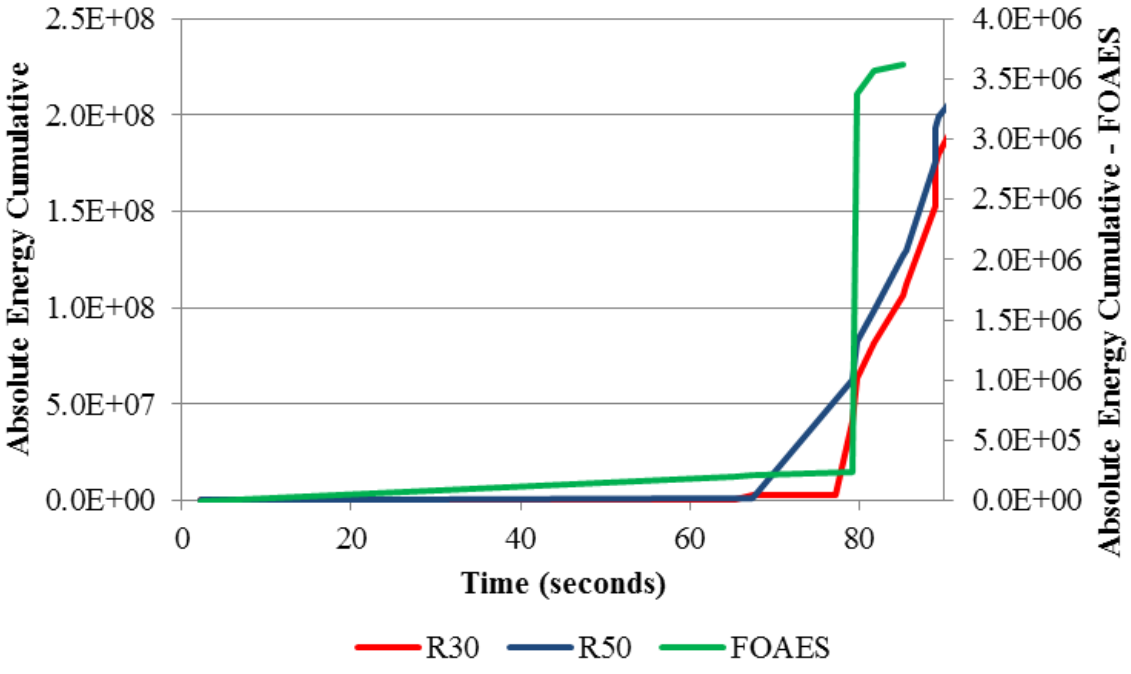


(ii)

**Figure 111 Cumulative number hits and cumulative Absolute Energy for the sensor 150625-04, shown respectively as Figure 111 (i) and (ii). In both graphs the data for the FOAES is attached as a secondary Y-axis, to enhance the visual comparison with the benchmarking sensors R30α and R50α.**

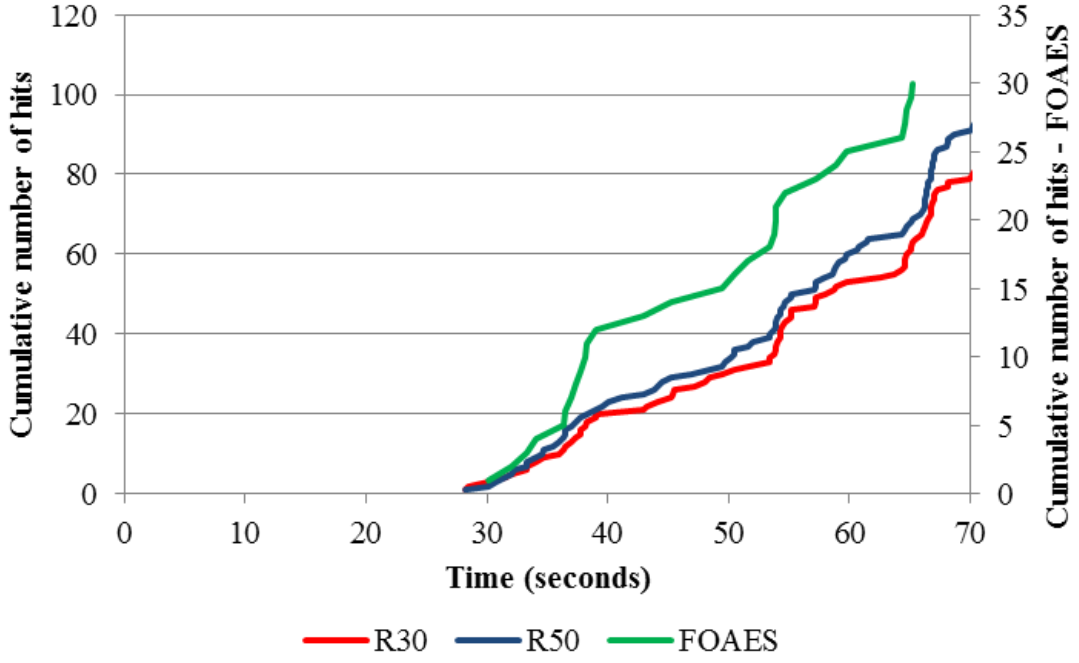


(i)

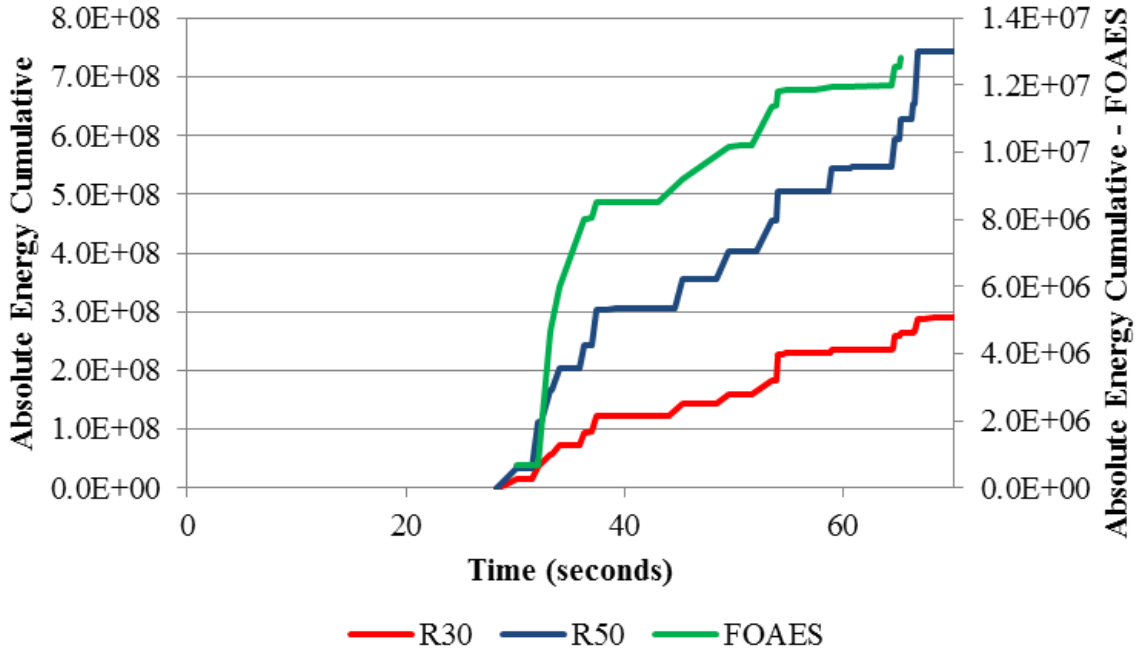


(ii)

**Figure 112 Cumulative number hits and cumulative Absolute Energy for the sensor 150722-03, shown respectively as Figure 112 (i) and (ii). In both graphs the data for the FOAES is attached as a secondary Y-axis, to enhance the visual comparison with the benchmarking sensors R30α and R50α.**

## 6.3 Survivability of the FOAES under increasing strain

The main purpose of the use of the strain gauge was as explained before, to monitor the precise strain applied at the area where the centre of the FOAES was located. Due to the tapered geometry and having the FOAES the minimum cross-section at this location, this is where strain was expected to be the highest. The strain at the time where the last hit was received from the FOAES in the AE system was considered as the failure or fracture strain of the sensor. The data of the different sensors is shown in Figure 113.

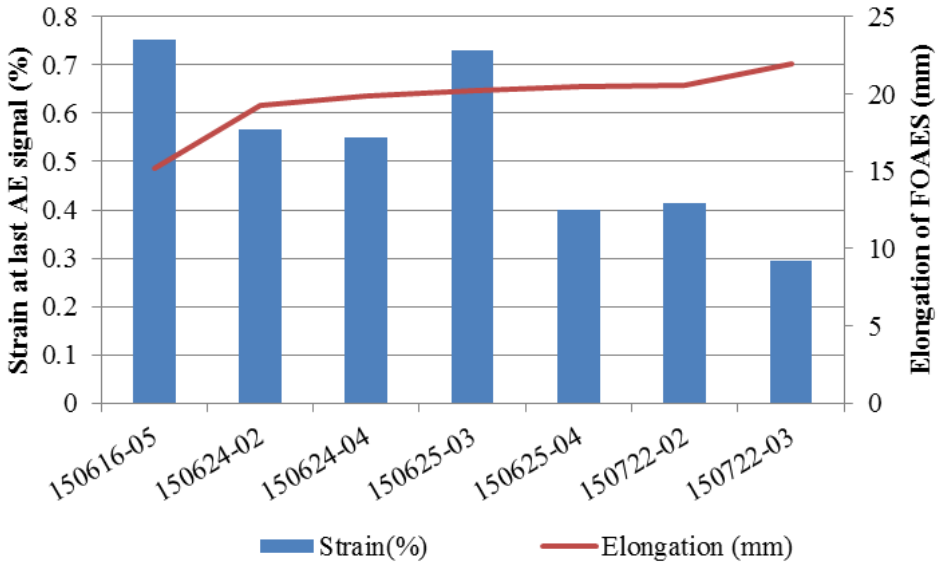


**Figure 113 Strain at which the last acoustic signature was received from each FOAES, and elongation of the FOAES during the manufacturing process (secondary Y axis).**

As expected by the non-regular geometrical characteristics obtained during the manufacturing process, different levels of strain have been monitored when the last acoustic signature was received. It can be appreciated that there were correlation between drawing length or elongation during the manufacturing of the FOAES (longer drawing length will have a direct impact in the diameter of the tapering region) and the minimum strain withstood by the

FOAES until stopping working. Longer sensors with potentially smaller diameter in the tapered length were broken at lower strains.

The assumption of longer sensors produces shorter diameter in the tapered length can be demonstrated by the use of the data of the non-packaging sensors showed in the Chapter 4. The statistical correlation factor (Pearson product moment correlation) between the waist diameter and drawing length for FOAES calculated with the same torch and material than the embedded ones was calculated and showed in Table 11. This parameter, which ranges from -1 to 1, indicates the strength of the relationship between two variables; 0 indicates not correlation while ±1 indicates positive/negative perfect correlation [199, 200]. It is generally accepted that a correlation factor higher in absolute value than 0.5 as in our situation is the reflexion of a strong relationship between the variables [199]. The negative sign of -0.59 indicates an inverse relationship which perfectly matches with the experimental data obtained; i.e. longer drawing lengths produce smaller waist diameters.

**Table 11 Statistical Correlation (Pearson product moment correlation) between the waist diameter and drawing length for FOAES calculated with the same between waist diameter and manufacturing drawing length.**

| Sensor | Waist (µm) | Drawing Length (mm) |
|---|---|---|
| 150225-01 | 31.82 | 19.6 |
| 150226-01 | 32.34 | 19.02 |
| 150227-01 | 26.56 | 21.91 |
| 150326-01 | 32.32 | 19.84 |
| 150326-02 | 28.15 | 18.66 |
| 150331-01 | 29.19 | 18.82 |
| 150331-02 | 31.29 | 20.02 |
| 150401-01 | 27.01 | 19.38 |
| 150319-01 | 19.81 | 21.51 |

| Correlation Factor | -0.59 |
|---|---|

This relationship can be used for approximately calculating individual brackets of strain that the FOAES can withstand, inferred from the drawn distance measured during the manufacturing process.

## 6.4 Embedding VS surface bonded FOAES

One of the main drawbacks or concerns when embedding a sensor is the well-known subsequent distortion at the microscale level of the laminate. This causes abnormal load distribution and unexpected stress concentration areas/volumes which can end up with the premature or unforeseen fracture of a composite material. To investigate the suitability of the surface bonded FOAES, the sensor 150722-02 was attached on the surface using the fast curing epoxy Araldite®. Due to space limitations the R30α and R50α piezoelectric sensors were placed both at opposite side of the strain gauge to avoid any damage in the strain gauge wiring (the opposite face was fully used to bond the FOAES on the surface). The results are shown in Figure 114, where similar result as the embedded sensors were obtained.

The two benchmark piezoelectric sensors and the FOAES experienced a similar trend for cumulative hits and for cumulative absolute energy. It can be seen in Figure 114 (i) that at 35, 40, 48, 52 and 72 seconds there are changes in the rate of the cumulative hits are detected. Figure 114 (ii) which represents the absolute cumulative energy shows similar behaviour: times of 35, 40, 48, 64, 68 and 72 seconds show a sudden increase of the energy collected by the sensors. While the increase of the absolute energy at times of 35, 40, 48 and 72 seconds can be related to the increase of the cumulative hits contributing to the total absolute energy, the times of 64 and 68 seconds can be related mainly to higher energy events due to reinforcement fibres cracking.

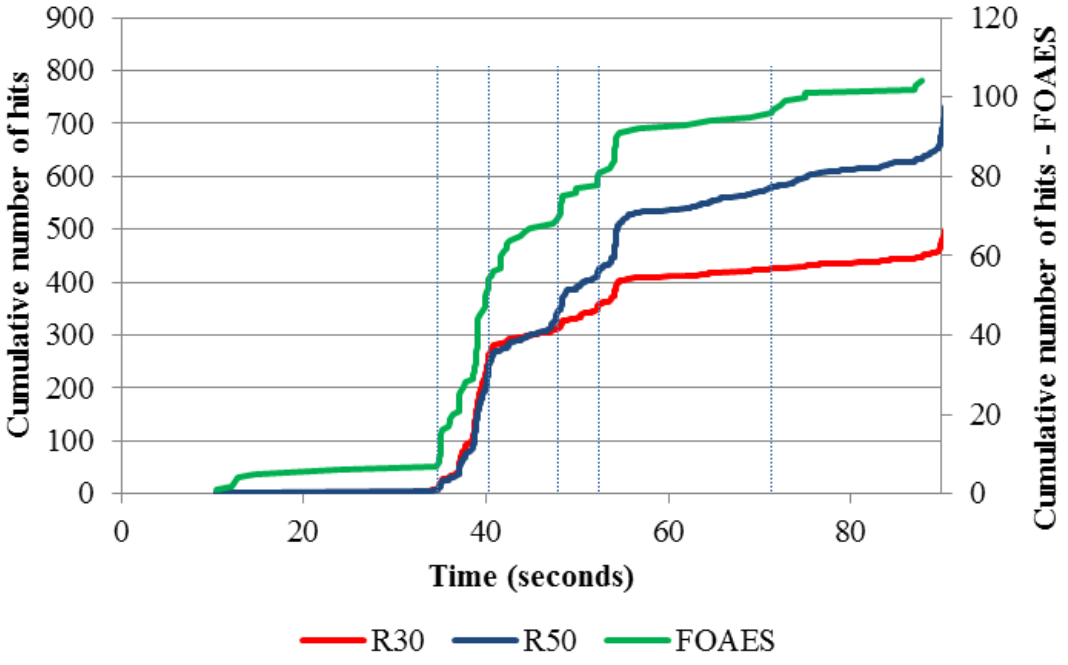


(i)

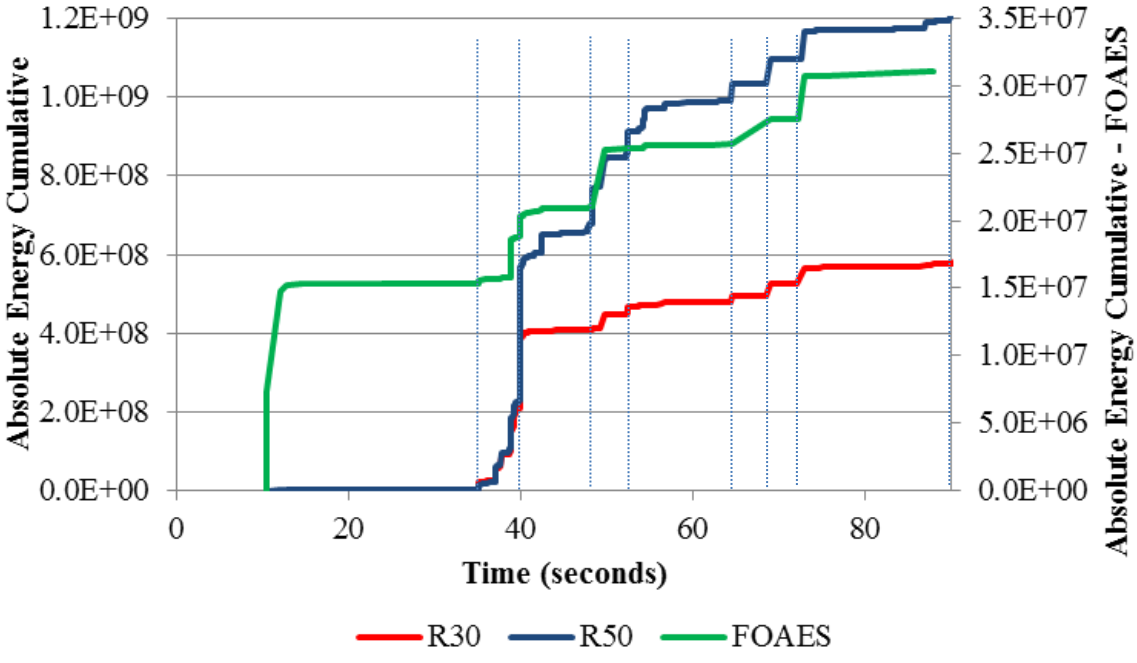


(ii)

**Figure 114 Cumulative number hits and cumulative Absolute Energy for the sensor 150722-02, shown respectively as Figure 114 (i) and (ii). In both graphs the data for the FOAES is attached as a secondary Y-axis, to enhance the visual comparison with the benchmarking sensors R30α and R50α.**

Even though just one experiment was performed for understanding the effects of surface bonding with a theoretically less effective coupling between the sensor and the surface, the results showed a very promising alternative. The FOAES can be applied on surface by the use of an adhesive layer or even by wet lamination of the same reinforcement used on the composite panel. This will enable the instrumentation of existing structures as well as an easy replacement of the AE sensors if required. In addition, no distortion will be introduced into the laminates, reducing the time and simplifying the processes required to embed the FOAES.

## 6.5 Pencil Breaks: Influence of the strain in the response of FOAES

As previously explained, pencil breaks or Hsu-Nielsen excitation were applied to the laminates under test at different strains levels to understand if changes in the FOAES response occurred. The pencil breaks was used for 3 embedded FOAES and one surface bonded FOAES. The tests were repeated using Configuration 2 at 0%, 0.1%, 0.2% and 0.3% strain measured by the strain gauge. The descriptors of the signal such as duration, absolute energy, counts, counts to peak and rise time were compared for the different FOAES. To ensure that any detected trends were not caused by differences in the Hsu Nielsen energy releasement, the benchmark conventional AE sensors were analysed in parallel.

While rise time and counts to peak did not show any particular trend while the strain of the plate was increased for any of the embedded or surface bonded FOAES, there were clear changes in the counts and duration of the embedded FOAES. It is speculated that these two parameters may be reduced due to a higher stiffness of the sensor under strain and thus, an increase of the damping. In addition, both the energy and the amplitude suffered a very steady decrease with the strain. With respect to the surface bonded FAOES it looked less affected by the strain than the embedded sensor, possibly by the partial dissipation of the strain across the

bonding line. The graphs for the different signal descriptors for the embedded FOAES are shown in Figure 115 to Figure 117. The same information for the surface bonded FOAES is shown in Figure 118.

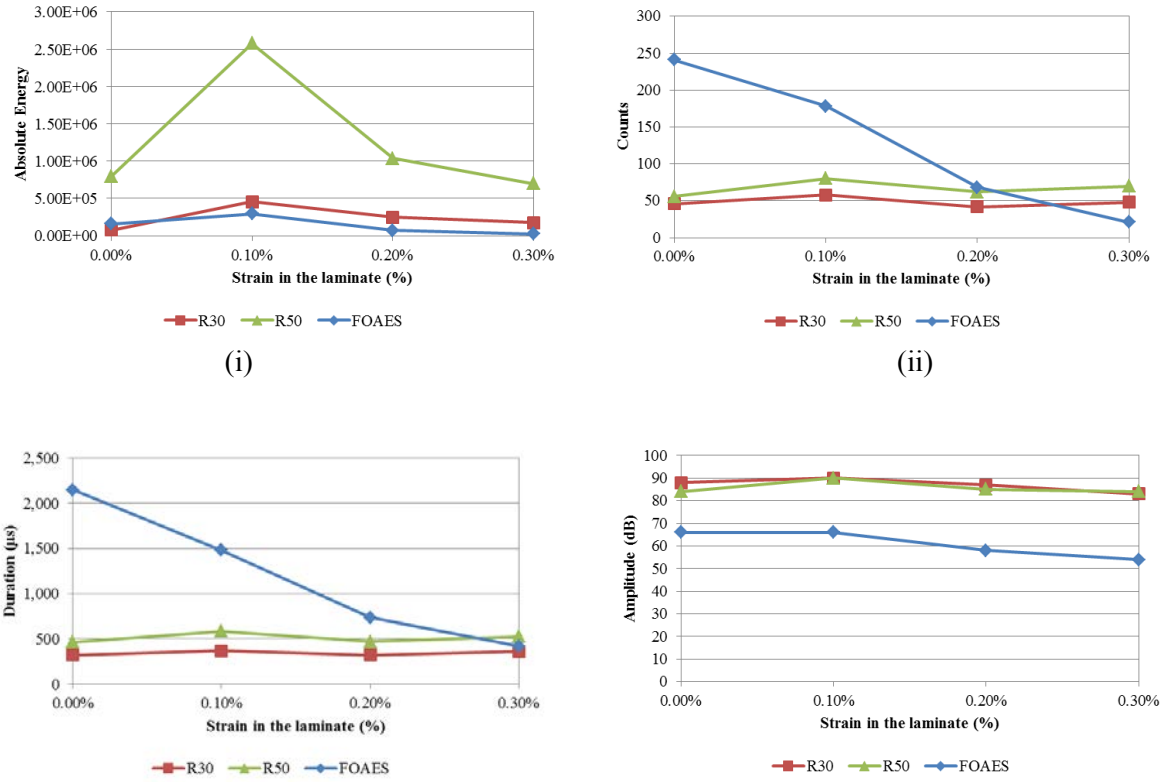


**Figure 115 Representation of some of the pencil breaks descriptors at different levels of strain for the embedded FOAES 150616-05. The pencil breaks were simultaneously acquired by the FOAES and the benchmark sensors R30α and R50α. Figure 115 (i) to (iv) represent absolute energy, counts, duration and amplitude respectively.**

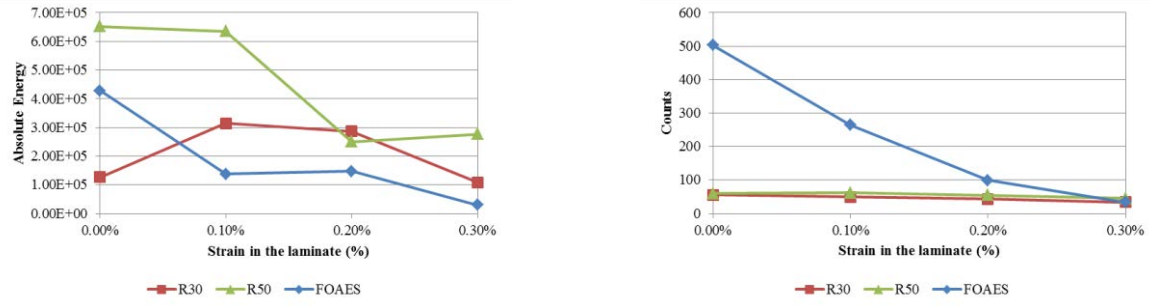

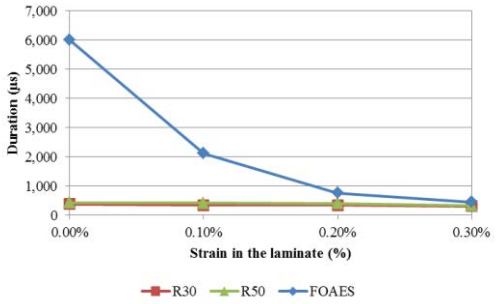


(iii)

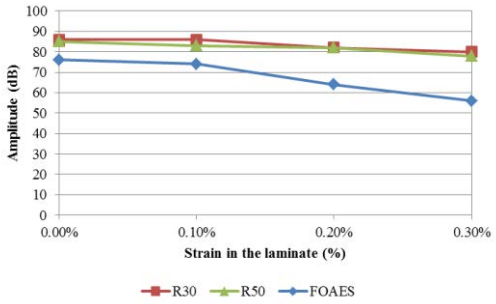


(iv)

**Figure 116 Representation of some of the pencil breaks descriptors at different levels of strain for the embedded FOAES 150624-02. The pencil breaks were simultaneously acquired by the FOAES and the benchmark sensors R30α and R50α. Figure 116 (i) to (iv) represent absolute energy, counts, duration and amplitude respectively.**

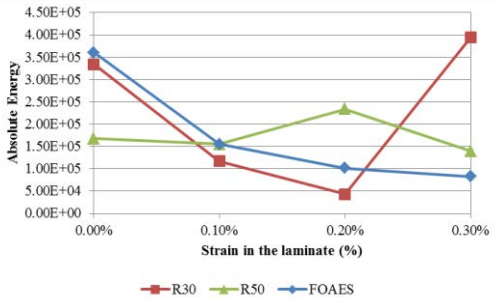


(i)

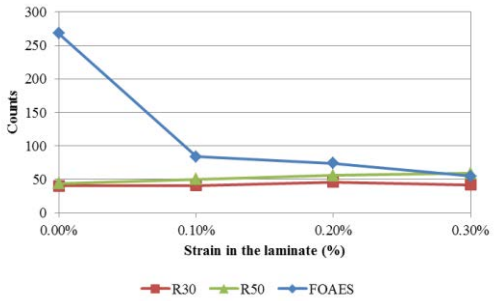


(ii)

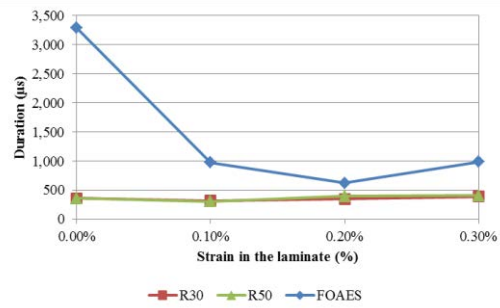


(iii)

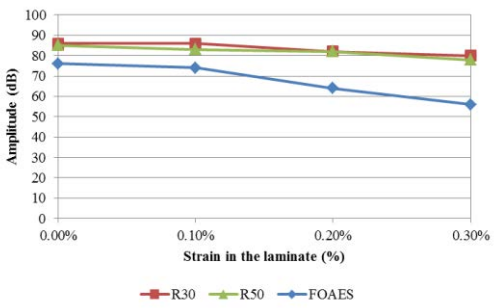


(iv)

**Figure 117 Representation of some of the pencil breaks descriptors at different levels of strain for the embedded FOAES 150722-03. The pencil breaks were simultaneously acquired by the FOAES and the benchmark sensors R30α and R50α. Figure 117(i) to (iv) represent absolute energy, counts, duration and amplitude respectively.**

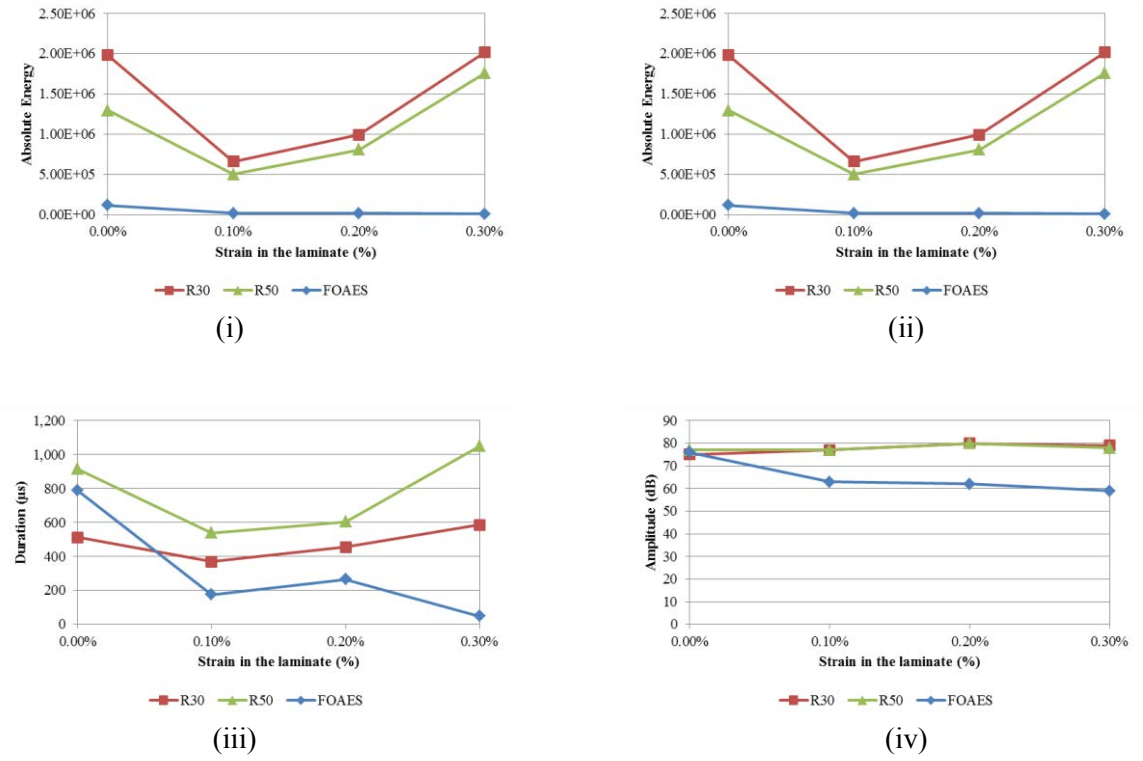


**Figure 118 Representation of some of the pencil breaks descriptors at different levels of strain for the surface mounted FOAES 150722-02. The pencil breaks were simultaneously acquired by the FOAES and the benchmark sensors R30α and R50α. Figure 118 (i) to (iv) represent absolute energy, counts, duration and amplitude respectively.**

## 6.6 Chapter summary

A direct comparison between embedded FOAES and benchmarking PZT AE sensors was performed during tensile testing. Portions of the plates containing the FOAES were cut, polished and end-tabbed. A strain gauge was bonded at the centre of the embedded FOAES to monitor the strain in that area. A surface bonded FOAES was tested too, to assess the influence of a theoretically less effective coupling.

The FOAES required longer time than conventional piezoelectric PZT sensors to return to the relaxed position after being excited. This is an unwanted effect which made necessary the use

of a configuration with longer PDT, HDT and HLT. Reducing the active length of the sensor may reduce this effect but at the expense of the sensitivity of the sensor potentially.

The FOAES showed a similar trend in cumulative hits and cumulative energy, but recorded fewer events than the PZT sensors. It was speculated that this different was created by the much lower SNR of the optical interrogation system when compared with the commercial PZT sensors.

Finally, the FOAES showed sensitivity to strain; when the laminate where the FOAES was embedded was elongated from 0.1 to 0.3%, the total counts and duration of the signals changed. In addition, correlation was found between manufacturing drawn length and minimum strain at breakage.

# CHAPTER 7

## Conclusions and future work

# 7 Conclusions and future work

## 7.1 Conclusions

### 7.1.1 FOAES manufacturing

The fabrication of the FOAES was studied in depth by progressively changing the different manufacturing variables and assessing their effect. The importance of using fibres with high and consistent numerical aperture was stated. An appropriate stripping process was developed, which was able to remove the thermoplastic coating in its entirety. It was found experimentally that sensors with losses lower than 2 dB and coupling ratio from 40 to 60% provided a much higher SNR. Therefore, several configurations producing consistently sensors within the stated limits were identified. Further acoustic characterisation narrowed down the manufacturing configuration to the optimal one. This was selected to produce the sensors for the rest of the study.

A novel methodology for embedding the FOAES in glass capillaries in a repeatable, consistent and reliable manner was designed, commissioned and tested. It is composed mainly from off-the-self part, and can be adapted to any existing FBT equipment.

The geometrical characteristics of the produced FOAES were investigated. It was found that the sensors were not symmetrical, and that there were notable differences between FOAES produced by the same manufacturing configuration. This is an unwanted characteristic of the applied FBT process. It was speculated that the lack of brushing movement of the torch was creating a non-uniform temperature in the fusing volume, and therefore creating a non-symmetrical geometry.

The surface characterisation of the FOAES showed differences in the frequency response for sensors with identical manufacturing parameters. On the other hand, all sensors exhibited excellent fidelity. This can be related to different geometrical characteristics from sensor-to-sensor introduced by the applied FBT process, and to the double cantilever configuration of the sensor. While the sensor will vibrate with identical frequency to the perturbation and therefore will replicate them very accurately, the amplitude of the oscillation will depend on the resonance frequencies of the sensor. Such resonance frequencies will have a strong dependency of the geometry of the sensor.

### 7.1.2 Sensor embedding

A preliminary study on the influence of the autoclave curing cycle in the survivability of the FOAES was performed. It was demonstrated that the developed packaging technique can withstand an industrial autoclave process as detailed in Figure 67 (iv).

A comparison between capillary packaged FOAES before and after embedding was performed. A general increase of the response including a higher bandwidth was obtained. This was potentially due to the better coupling than when tested on surface. On the other hand, bonded FOAES experienced the same increase in the response but not improvements in the bandwidth. It was speculated that the applied adhesive was partly damping the highest frequencies, so potentially this could be resolved with a stiffer adhesive. However, few sensors showed decay in performance after embedding. It was suspected that resin of the laminate may penetrated in the capillary changing the behaviour of the sensor.

The directionality of the embedded sensors was assessed by simultaneous comparison with commercial piezoelectric PZT sensors R30α and R50α (both below 1.5 dB). Both the FOAES and commercial piezoelectric PZT exhibited similar directionality. This means that despite the

irregular geometry of the FOAES, when packaged using two different adhesives at both sides of the capillary (one very rigid, and one medium-soft) the directionality is under the normal specification of other commercial AE sensors.

Finally, the FOAES showed linear response. This effectively meant that the amplitude of the spectrum was dependant on the amplitude of the source. This is a very important feature, as in AE signal analysis it is possible to use the energy or properties related to the amplitude of the signals to characterise/categorise the collected acoustic events. A non-linear sensor will add complexity to the analysis of the signals.

### 7.1.3 Comparison of embedded FOAES with surface-mounted piezo-electric AE sensors

Simultaneous tensile tests were performed using embedded FOAES and the same commercial PZT AE sensors. The events collected from the FOAES showed a very rich frequency spectrum, aligned with the ones acquired simultaneously by the PZT AE sensors.

On the other hand, the FOAES collected fewer events than the PZE AE sensors. This was attributed to the low power of the laser combined with its unpolarised nature, which made the low energy events undetectable to the FOAES-based system.

The trend in cumulative hits and energy showed correlation between the FOAES and piezoelectric PZT AE sensors. This meant that the FOAES was able to monitor the structural health of the tested samples as the different damage mechanisms evolved (matrix, interface or reinforcement failure). Furthermore, a bonded FOAES performed identically well. This was a very important outcome because one the main hurdles when embedding sensors in composites is the distortion introduced in the laminate. A bonded or laminated FOAES will avoid the necessity of the embedment while will add all the advantages of the FOS.

The FOAES required much more time than the PZT sensors to return to the relaxed state after picking up a signal. This damping behaviour was an undesired issue. In order to avoid cutting the signals acquired by the FOAES, the AE acquisition system was configured with much longer PDT, HDT and HLT. This phenomenon could be reduced by the use of a very soft adhesive in one of the extremes of the capillary. Unfortunately, it was not possible to include this investigation in this research work.

Finally, the embedded FOAES was found to be sensitive to the strain. The AE signals were shorter and with less counts according the strain was increased. In addition, correlation between manufacturing draw length and minimum strain at failure was identified. Effectively, this finding means that future FOAES should be designed in such a way that the sensor's waist diameter is inversely proportional to the expected strain in the structure.

## 7.2 Future work

The present work has stated the difficulties in producing consistent FOAES using a conventional FBT process. The lack of geometrical repeatability means that a big population of sensors is required to conclude the effects of the manufacturing parameters in the sensor response. Therefore, producing the FOAES using other techniques such as polishing or brushing FBT will be highly recommended. The suitability of modifying a fusion splicer to produce the FOAES will be another alternative worth of being investigated; this will enable the localised melting via electric discharges with the highly accurate pulling movement from the motorised translation stages.

The characterisation of the sensor would require a broadband emitter, with an even frequency response along the band under investigation. This will simplify the characterisation providing

a more meaningful data, as the reference will excite will very similar amplitude all the frequencies in the band of interest.

With regards with the embedding, further work should be carried out in order to increase understanding with respect to the influence of the bonding as a potential alternative to embedding. The influence of the stiffness or modulus of the adhesive in the sensor response, as well as attaching the sensor via wet lamination onto the panels should be considered.

The effect of the undamped nature of the FOAES will need further work, in order to bring the sensor to the relaxed state once the acoustic perturbation has finished. This will be achievable by using a very soft adhesive in one side of the capillary and/or by modifying the geometrical characteristics of the sensor. Also reducing the active length of the sensor may contribute in addressing this issue.

Finally, further work should be carried out to improve the interrogation system. The effect of a polarised laser together with higher power should be investigated to understand the minimum requirements to pick up low energy events during AE test. It would be advisable to commission an off-the-self balanced amplified photodetector to interrogate the sensor; this will reduce uncertainties about the performances of the custom made system used in this project.

# References


1. Cuadra, J., Prashanth, A.V., Hazeli, K., Bartoli,I., and Kontsos, A. (2013) *Damage quantification in polymer composites using a hybrid NDT approach.* **Composites Science and Technology**, 83(0): p. 11-21.

2. Nair, A. and Cai, C.S. (2010) *Acoustic emission monitoring of bridges: Review and case studies.* **Engineering structures**, 32(6): p. 1704-1714.

3. Scott, I.G. and Scala, C.M. (1982) *A review of non-destructive testing of composite materials.* **NDT International**, 15(2): p. 75-86.

4. Hellier, C. (2001) *Acoustic Emission Testing*, in *Handbook of non-destructive evaluation*. McGraw-Hill Porfessional. p. 603.

5. Zheng, G.T., Buckley, M.A., Kister, G., and Fernando, G.F. (2001) *Blind deconvolution of acoustic emission signals for damage identification in composites.* **AIAA**, 39(6): p. 1198-1205.

6. Narisawa, I., Oba, H. (1984) *An evaluation of acoustic emission from fibre-reinforced composites.* **Journal of Materials Science**, 19: p. 1777-1786.

7. Godin, N., Huguet, S., and Gaertner, R. (2005) *Integration of the Kohonen's self-organising map and k-means algorithm for the segmentation of the AE data collected during tensile tests on cross-ply composites.* **NDT & E International**, 38(4): p. 299-309.

8. Godin, N., Huguet, S., Gaertner, R., and Salmon, L. (2004) *Clustering of acoustic emission signals collected during tensile tests on unidirectional glass/polyester composite using supervised and unsupervised classifiers.* **NDT & E International**, 37(4): p. 253-264.

9. Holford, K., Pullin, M. and Pullin, R. (2007) *Current practice and applications of acoustic emission*, in **Experimental Analysis of Nano and Engineering Materials and Structures**, Springer. p. 927-928.

10. Muravin, B.. *Acoustic Emission Portal at Muravin.com*, Cited 2013 from http://www.muravin.com/.

11. Grosse, C. and Ohtsu, M. (2008) *Acoustic Emission Testing - Basics for research and Applications in Civil Engineering*, Springer Berlin Heidelberg.

12. Di Sante, R. (2015) *Fibre optic sensors for structural health monitoring of aircraft composite structures: recent advances and applications.* **Sensors**, 15(8): p. 18666-18713.

13. Verstrynge, E., Pfeiffer, H. and Wevers, M. (2014) *A novel technique for acoustic emission monitoring in civil structures with global fiber optic sensors.* **Smart Materials and Structures**, 23(6): p. 065022.

14. Wild, G. and Hinckley, S. (2008) *Acousto-Ultrasonic Optical Fiber Sensors: Overview and State-of-the-Art.* **Sensors Journal, IEEE**, 8(7): p. 1184-1193.

15. Vaara, P., Leinonen, J. (2012) *Technology Survey on NDT of Carbon-fiber Composites.* **Publications of Kemi-Tornio University of Applied Sciences. Serie B**. Reports 8/2012.

16. Kapadia, A.. *Non Destructive Testing of Composite Materials*, TWI.

17. Takeda, S., Aoki Y., Ishikawa T., Takeda N., and Kikukawa H. (2007) *Structural health monitoring of composite wing structure during durability test.* **Composite Structures**, 79(1): p. 133-139.

18. Fernando, G.F. (2005) *Fibre optic sensor systems for monitoring composite structures.* **Reinforced Plastics**, 49(11): p. 41-49.

19. Mazumdar, S.K. (2002) *Introduction and raw materials for part fabrication*, in **Composites manufacturing: materials, product and process engineering**, CRC Press.

20. Pitkethly, M.J. and Doble, J.B. (1990) *Characterizing the fibre/matrix interface of carbon fibre-reinforced composites using a single fibre pull-out test.* **Composites**, 21(5): p. 389-395.

21. Jang-Kyo,K and Sham, M-L. (2000) *Impact and delamination failure of woven-fabric composites.* **Composites Science and Technology**, 2000. 60(5): p. 745-761.

22. Soutis, C. and Curtis P.T. (1996) *Prediction of the post-impact compressive strength of CFRP laminated composites.* **Composites Science and Technology**, 56(6): p. 677-684.

23. Ladeveze, P. and LeDantec, E. (1992) *Damage modelling of the elementary ply for laminated composites.* **Composites Science and Technology**, 43(3): p. 257-267.

24. Vavrik, D., Jakubek, J., Jandejsek, I., Krejci, F., Kumpova, I., and Zemlicka, J. (2015) *Visualization of delamination in composite materials utilizing advanced X-ray imaging techniques.* **Journal of Instrumentation**, 10(04): p. C04012.

25. Krumm, M., Sauerwein, C., Hämmerle, V., Oster, R., Diewel, B., Sindel, M., and Audi, A.G. (2012) *Capabilities and Application of Specialized Computed Tomography Methods for the Determination of Characteristic Material Properties of Fiber Composite Components*. **Conference on Industrial Computed Tomography,** Wels, Austria.

26. Crupi, V., Epasto, G., and Guglielmino, E. (2011) *Computed Tomography analysis of damage in composites subjected to impact loading.* **Frattura ed Integrità Strutturale**, (17): p. 32.

27. Kinney , K., Ray, H., Klann, T., and Raju, B. (1999) *Fast neutron radiography for composite materials evaluation and testing.* **Nuclear Instruments and Methods in Physics Research Section A: Accelerators, Spectrometers, Detectors and Associated Equipment**, 422(1–3): p. 929-932.

28. Balaskó, M., Veres, I., Molnár, Gy, Balaskó, Zs, and Sváb, E. (2004) *Composite structure of helicopter rotor blades studied by neutron- and X-ray radiography.* **Physica B: Condensed Matter**, 350(1–3): p. 107-109.

29. Diamanti, K. and Soutis C. (2010) *Structural health monitoring techniques for aircraft composite structures.* **Progress in Aerospace Sciences**, 46(8): p. 342-352.

30. Imielińska, K., Castaings, M., Wojtyra, R., Haras, J., Le Clezio, E. and Hosten, B. (2004) *Air-coupled ultrasonic C-scan technique in impact response testing of carbon fibre and hybrid: glass, carbon and Kevlar/epoxy composites.* **Journal of Materials Processing Technology**, 157–158: p. 513-522.

31. Hopkins, D., Neau, G. and Le Ber, L. (2011) *Advanced phased-array technologies for ultrasonic inspection of complex composite parts*. **Smart materials, structures & NDT in aerospace conference**.

32. Habermehl, J., Lamarre, A. and Olympus NDT (2008) *Ultrasonic phased array tools for composite inspection during maintenance and manufacturing*.**17th World conference on nondestructive testing**, Shanghai, China.

33. Drinkwater, B.W. and Wilcox, P.D. (206) *Ultrasonic arrays for non-destructive evaluation: A review.* **NDT & E Internationa**l, 39(7): p. 525-541.

34. Toubal, L., Karama M., and Lorrain, B. (2006) *Damage evolution and infrared thermography in woven composite laminates under fatigue loading.* **International Journal of Fatigue**, 28(12): p. 1867-1872.

35. Dattoma, V., Marcuccio, R., Pappalettere, C., and Smith, G. M. (2001) *Thermographic investigation of sandwich structure made of composite material.* **NDT & E International**, 34(8): p. 515-520.

36. Aggelis, D.G., Barkoula, N.M., Matikas, T.E. and Paipetis, A.S. (2012) *Acoustic structural health monitoring of composite materials : Damage identification and evaluation in cross ply laminates using acoustic emission and ultrasonics.* **Composites Science and Technology**, 72(10): p. 1127-1133.

37. Arumugam, V.R., Shankar, N., Sridhar, B.T.N., and Stanley, A.J. (2010) *Ultimate Strength Prediction of Carbon/Epoxy Tensile Specimens from Acoustic Emission Data.* **Journal of Materials Science & Technology**, 26(8): p. 725-729.

38. Haselbach, W. and Lauke, B. (2003) *Acoustic emission of debonding between fibre and matrix to evaluate local adhesion.* **Composites Science and Technology**, 63(15): p. 2155-2162.

39. Okoroafor, E.U. and Hill, R., (1994) *Relating acoustic emission signal parameters to the strength of fibres used in the manufacture of polymeric composites.* **Ultrasonics**, 33(2).

40. Read, I., Foote, P. and Murray, S. (2002) *Optical fibre acoustic emission sensor for damage detection in carbon fibre composite structures.* **Measurement Science and Technology**,1 3(1): p. N5.

41. R'Mili, M., Moevus, M., and Godin, N. (2008) *Statistical fracture of E-glass fibres using a bundle tensile test and acoustic emission monitoring.* **Composites Science and Technology**, 68(7-8): p. 1800-1808.

42. Zheng, S.X., McBride, R., Barton, J.S., Jones, J.D.C., Hale, K.F. and Jones, B.E. (1992) *Intrinsic optical fibre sensor for monitoring acoustic emission.* **Sensors and Actuators**, 31(1–3): p. 110-114.

43. Ono, K. and Gallego, A. (2012) *Research and Applications of AE on Advanced Composites.* **Journal of Acoustic Emission**, 30: 180-229.

44. WenXiao, P., DaKai, L., and Dongsheng, L. (2006) *Optical fiber sensor layer embedded in smart composite material and structure.* **Smart Materials and Structures**, 15(5): p. 1231.

45. Baranov, V.M., Kudryavtsev, E.M., Sarychev, G.A. and Schavelin, V.M. (2011) *Acoustic Emission in Friction*. **Tribology**, (Vol. 53). Elsevier.

46. Wevers, M., Van Dijck, G., Desadeleer, W., Winkelmans, M. and Van Den Abeeele, K. (2004) *Acoustic emission for on-line monitoring of damage in various application fields.* **Proceedings EWGAE**, **DGZfP**, 22: p. 253-263.

47. De Oliveira, R. and Marques, A. T. (2008) *Health monitoring of FRP using acoustic emission and artificial neural networks.* **Computers & Structures**, 86(3-5): p. 367-373.

48. Rongsheng, C., Bradshaw, T., Burns, J.,Cole, P., Jarman, P., Pedder, D.,Theobald, R. and Fernando, G.F. (2006) *Linear location of acoustic emission using a pair of novel fibre optic sensors.* **Measurement Science and Technology**, 17(8): p. 2313.

49. Beattie, A.G, (2013) *Acoustic Emission Non-Destructive Testing of Structures using Source Location Techniques.* **Sandia National Laboratories**, Livemore, California.

50. Physical Acoustics Corporation, (2004) *AEwin SOFTWARE Rev 2*, Princeton Jct., New Jersey, USA.

51. White, G. (1995) *Introduction to machine vibration*. **DLI Engineering Corp**.

52. National Instrument (2004) *Aliasing and Sampling at Frequencies Above the Nyquist Frequency*. White Paper from www.ni.com.

53. Yilmazer, P., Amini, A. and Papaelias, M. (2012) *The structural health condition monitoring of rail steel using acoustic emission techniques*. **Proceedings 51st Annual Conference NDT**, pp. 1-12.

54. Han, Z., Luo, H., Sun, C., Li, J., Papaelias, M. and Davis, C. (2014) *Acoustic emission study of fatigue crack propagation in extruded AZ31 magnesium alloy.* **Materials Science and Engineering**, 597: p. 270-278.

55. Mayorkinos, P., Amini, A., Huang, Z., Vallely, P., Cardoso Dias, D. and Kerkyras, S. (2016) *Online condition monitoring of rolling stock wheels and axle bearings.* **Proceedings of the Institution of Mechanical Engineers, Part F: Journal of Rail and Rapid Transit**, 230(3): p. 709-723.

56. Nunez Laodeno, R., Hideo, N. and Kenichi, Y. (2008) *Characterization of AE Signals Generated by Gas Leak on Pipe with Artificial Defect at Different Wall Thickness.* **Material Transactions**, 49(10): p. 2341 to 2346.

57. Ennaceur, C., Laksimi, A., Hervé, C. and Cherfaoui, M. (2006) *Monitoring crack growth in pressure vessel steels by the acoustic emission technique and the method of potential difference.* **International Journal of Pressure Vessels and Piping**, 83(3): p. 197-204.

58. Ozevin, D. and Harding, J. (2012) *Novel leak localization in pressurized pipeline networks using acoustic emission and geometric connectivity.* **International Journal of Pressure Vessels and Piping**, 92(0): p. 63-69.

59. Cole, P.T. and Watson, J.R. (2006) *Acoustic emission for corrosion detection*. **Advanced Materials Research**, Trans Tech Publ.

60. Denga, J., Xiaob, H., Huo, W., Luo, M., May, R., Wang, A. and Liu, Y. (2000) *Optical fiber sensor-based detection of partial discharges in power transformers.* ***Optics & Laser Technology,*** *3*3.5: 305-311.

61. Zargari, A. and Blackburn, T.R. (1998) *Acoustic detection of partial discharges using non-intrusive optical fibre sensors.* **Proceedings of the 1998 IEEE 6th International Conference, Conduction and Breakdown in Solid Dielectrics**, pp. 573-576. IEEE.

62. Rabiei, M. and Modarres, M. (2013) *Quantitative methods for structural health management using in situ acoustic emission monitoring.* **International Journal of Fatigue**, 49(0): p. 81-89.

63. Kim, I., Lee, H. and Kim, J. (2005) *Impact Damage Detection in Composite Laminates Using PVDF and PZT Sensor Signals.* **Journal of Intelligent Material Systems and Structures**, 16(11-12): p. 1007-1013.

64. Scholey, J., Wilcox P.D., Wisnom, M.R. and Friswell, M.I. (2010) *Quantitative experimental measurements of matrix cracking and delamination using acoustic emission.* **Composites Part A: Applied Science and Manufacturing**, 41(5): p. 612-623.

65. Hellmann, S. (2010) *Analysis and optimisation of a novel fibre optic acoustic emission sensor system*. **Master Disertation**, University of Birmingham - Hochschule Mannheim.

66. Quispitupa, A, Shafiq, B., Just, F. and Serrano, D. (2004) *Acoustic emission based tensile characteristics of sandwich composites.* **Composites Part B: Engineering**, 35(6): p. 563-571.

67. Laksimi, A., Benmedakhene, S., and Bounouas, L. (1999) *Monitoring acoustic emission during tensile loading of thermoplastic composites materials*. **Proceeding of ICCM,** vol. 12.

68. Stepanova, L.N., Lebedev E.Y., Kareev, A.E., Chaplygin, V.N. and Katarushkin, S. A. (2004) *Use of the acoustic emission method in detecting the fracture process in specimens made of composite materials.* **Russian Journal of Nondestructive Testing**, 40(7): p. 455-461.

69. Awerbuch, J., Leone, F. A., Ozevin, D. and Tan T. (2016) *On the applicability of acoustic emission to identify modes of damage in full-scale composite fuselage structures.* **Journal of Composite Materials**, 50(4): p. 447-469.

70. Godin, N., Huguet, S. and Gaertner, R. (2006) *Influence of hydrolytic ageing on the acoustic emission signatures of damage mechanisms occurring during tensile tests on a polyester composite: Application of a Kohonen's map.* **Composite Structures**, 72(1): p. 79-85.

71. Hamstad, M.A. and Moore, R.L. (1986) *Acoustic Emission from Single and Multiple Kevlar 49 Filament Breaks.* **Journal of Composite Materials**, 20(1): p. 46-66.

72. Chi, Z., Chou, T. and Shen, G. (1984) *Determination of single fibre strength distribution from fibre bundle testings.* **Journal of materials science**, 19(10): p. 3319-3324.

73. Jihan, S., Siddiqui, A.M. and Sweet, M.A.S. (1997) *Fracture strength of E-glass fibre strands using acoustic emission.* **NDT & E International**, 30(6): p. 383-388.

74. Hill, R. and Okoroafor, E.U. (1995) *Weibull statistics of fibre bundle failure using mechanical and acoustic emission testing: the influence of interfibre friction.* **Composites**, 26(10): p. 699-705.

75. Ni, Q. and Iwamoto, M. (2002) *Wavelet transform of acoustic emission signals in failure of model composites.* **Engineering Fracture Mechanics**,. 69(6): p. 717-728.

76. De Groot, P.J, Wijnen, P.A.M, and Janssen, R.B.F. (1995) *Real-time frequency determination of acoustic emission for different fracture mechanisms in carbon/epoxy composites.* **Composites Science and Technology**, 55(4): p. 405-412.

77. Ramirez-Jimenez, C.R., Papadakis, N., Reynolds, N., Gan, T.H., Purnell, P. and Pharaoh, M. (2004) *Identification of failure modes in glass/polypropylene composites by means of the primary frequency content of the acoustic emission event.* **Composites Science and Technology**, 64(12): p. 1819-1827.

78. Bohse, J. (2000) *Acoustic emission characteristics of micro-failure processes in polymer blends and composites.* **Composites Science and Technology**, 60(8): p. 1213-1226.

79. Giordano, M., Calabro, A., Esposito, C., Salucci, C. and Nicolais, L. (1999) *Analysis of acoustic emission signals resulting from fiber breakage in single fiber composites.* **Polymer Composites**, 20(6): p. 758-770.

80. Kangas, J. and Kohonen, T. (1996) *Developments and applications of the self-organizing map and related algorithms.* **Mathematics and Computers in Simulation**, 41(1-2): p. 3-12.

81. Likas, A., Vlassis, N. and Verbeek. J.J. (2003) *The global k-means clustering algorithm.* **Pattern recognition**, 36(2): p. 451-461.

82. Ng, M.K. (2000) *A note on constrained k-means algorithms.* **Pattern recognition**, 33(3): p. 515-519.

83. Kostopoulos, V., Loutas, T. and Dassios, K. (2007) *Fracture behavior and damage mechanisms identification of SiC/glass ceramic composites using AE monitoring.* **Composites Science and Technology**, 67(7-8): p. 1740-1746.

84. Crivelli, D., Guagliano, M. and Monici, A. (2014) *Development of an artificial neural network processing technique for the analysis of damage evolution in pultruded composites with acoustic emission.* **Composites Part B: Engineering**, 56(0): p. 948-959.

85. Gutkin, R, Green, C.J., Vangrattanachai, S., Pinho, S.T., Robinson, P. and Curtis, P.T. (2011) *On acoustic emission for failure investigation in CFRP: Pattern recognition and peak frequency analyses.* **Mechanical Systems and Signal Processing**, 25(4): p. 1393-1407.

86. Qi, G., Barhorst, A., Hashemi, J. and Kamala, G. (1997) *Discrete wavelet decomposition of acoustic emission signals from carbon-fiber-reinforced composites.* **Composites Science and Technology**, 57(4): p. 389-403.

87. Qi, G. (2000) *Wavelet-based AE characterization of composite materials.* **NDT & E International**, 33(3): p. 133-144.

88. Marec, A., Thomas, J.H. and El Guerjouma, R. (2008) *Damage characterization of polymer-based composite materials: Multivariable analysis and wavelet transform for clustering acoustic emission data.* **Mechanical Systems and Signal Processing**, 22(6): p. 1441-1464.

89. Surgeon, M. and Wevers, M. (1999) *One sensor linear location of acoustic emission events using plate wave theories.* **Materials Science and Engineering**, 265(1–2): p. 254-261.

90. Aljets, D., Chong, A., Wilcox, S. and Holford, K. (2010) *Acoustic emission source location in plate-like structures using a closely arranged triangular sensor array.* **Journal of Acoustic Emission**, 28: p. 85-98.

91. Eaton, M.J., Pullin, R. and Holford, K.M. (2012) *Acoustic emission source location in composite materials using Delta T Mapping.* **Composites Part A: Applied Science and Manufacturing**, 43(6): p. 856-863.

92. Jingpin, J., Bin, W. and Cunfu, H. (2008) *Acoustic emission source location methods using mode and frequency analysis.* **Structural Control and Health Monitoring**, 15(4): p. 642-651.

93. Chen, R., Fernando, G.F., Butler, T. and Badcock, R.A. (2004) *A novel ultrasound fibre optic sensor based on a fused-tapered optical fibre coupler.* **Measurement Science and Technology**, 15(8): p. 1490.

94. Fu, T., Fan, J. M., Wang, C.T., Liu, Y. and Leng, J. S. (2008) *A novel multifunctional optical fiber sensor based on FBG and fiber optic coupler*. **Proceeding SPIE**, vol. 6933, pp. 693317-9.

95. Bin, M., Qingmei, S., Hongliang, C. and Xiaoyang, H. (2007) *Experimental Study of Coupling Fibre-optic Vibration Sensor*. **Automation and Logistics, 2007 IEEE International Conference,** pp. 1331-1335.

96. Zhou, G. and Sim, L.M. (2002) *Damage detection and assessment in fibre-reinforced composite structures with embedded fibre optic sensors-review.* **Smart Materials and Structures**, 11(6): p. 925.

97. Burns, J.M. (2011) *Development and characterisation of a fibre-optic acoustic emission sensor*. **PhD Thesis**, School of Metallurgy and Materials, College of Engineering & Physical Sciences, University of Birmingham.

98. Fu, T., Liu, Y., Li, Q. and Leng, J. (2009) *Fiber optic acoustic emission sensor and its applications in the structural health monitoring of CFRP materials.* **Optics and Lasers in Engineering**, 47(10): p. 1056-1062.

99. Liu, K., Ferguson, S.M. and Measures, R.M. (1990) *Fiber-optic interferometric sensor for the detection of acoustic emission within composite materials.* **Optics Letters**,15(22): p. 1255-1257.

100. Matsuo, T., Cho, H. and Takemoto, M. (2006) *Optical fiber acoustic emission system for monitoring molten salt attack.* **Science and Technology of Advanced Materials**, 7(1): p. 104-110.

101. Li, Y., Wang ,X. and Bao, X. (2011) *Sensitive acoustic vibration sensor using single-mode fiber tapers.* **Applied Optics**, 50(13): p. 1873-1878.

102. Zhao, J., Shi, Y., Shan, N. and Yuan, X. (2008) *Stabilized fiber-optic extrinsic Fabry–Perot sensor system for acoustic emission measurement.* **Optics & Laser Technology**, 40(6): p. 874-880.

103. Rice, T., Gifford. D., Childers, B., Cooper, K. and Furrow, K. (2003) *Fiber optic distributed strain, acoustic emission, and moisture detection sensors for health maintenance in aircraft testing applications.* **Proceedings IEEE Systems Readiness Technology Conference**, Autotestcon 2003.

104. Perez, I.M., Cui, H. and Udd, E. (2001) *Acoustic emission detection using fiber Bragg gratings.* **Naval Air Warfare Center Aircraft Div Patuxent River**, MD.

105. Kister, G., Wang, L. Ralph, B. and Fernando, G. F. (2003) *Self-sensing E-glass fibres.* **Optical Materials**, 21(4): p. 713-727.

106. Lee, D.C., Lee, J. J., Kwon, I.B. and Seo, D.C.( 2001) *Monitoring of fatigue damage of composite structures by using embedded intensity-based optical fiber sensors.* **Smart Materials and Structures**,10(2): p. 285.

107. Badcock, R.A. and Fernando, G.F. (1995) *An intensity-based optical fibre sensor for fatigue damage detection in advanced fibre-reinforced composites.* **Smart Materials and Structures**, 4(4): p. 223.

108. Su, L. and Elliott, S.R.(2010) *All-fiber microcantilever sensor monitored by a low-cost fiber-to-tip structure with subnanometer resolution.* **Optics Letters**, 35(8): p. 1212-1214.

109. Culshaw, B. (2005) *The optical fibre Sagnac interferometer: an overview of its principles and applications*. **Measurement Science and Technology**, 17.1 (2005): R1.

110. Giurgiutiu, V. (2016) *Chapter 7 - Fiber-Optic Sensors*, in *Structural Health Monitoring of Aerospace Composites*. **Academic Press: Oxford.** p. 249-296.

111. Giurgiutiu, V. (2016) *Chapter 9 - Impact and Acoustic Emission Monitoring for Aerospace Composites SHM*, in *Structural Health Monitoring of Aerospace Composites*. **Academic Press: Oxford.** p. 317-394.

112. Lee, B.H., Kim, Y.H., Park, K.S., Eom, J. B., Jin, K.M., Rho, B.S. and Choi, H.Y. (2012) *Interferometric Fiber Optic Sensors.* **Sensors**, 12(3): p. 2467.

113. Teixeira, J.G.V., Leite, I.T, . Silva, S. and Frazão, O. (2014) *Advanced fiber-optic acoustic sensors.* **Photonic Sensors**, 4(3): p. 198-208.

114. Cole, J. H., Kirkendall, C., Dandridge, A., Cogdell, G. and Giallorenzi T.G. (2004) *Twenty-five years of interferometric fiber optic acoustic sensors at the Naval Research Laboratory*. **Washington Academy of Sciences.**

115. Baillie, P.W.R. (1999) *Application of Acoustic Emission Sensing for the Non-Destructive Evaluation of Advanced Composite Materials*. **Brunel Centre of Manufacturing Metrology**, Brunel University.

116. Chapman, M. (2002) *Heterodyne and homodyne interferometry*. **White Paper**, from www.renishaw.com

117. RP Photonics (2016) *Optical Heterodyne Detection*. **RP Photonics Encyclopedia**.

118. Watson, T., Tayag, J. and Collins, R. (2012) *Digital Demodulation of Interferometric Signals*. **Modern Metrology Concerns**. L. Cocco, Editor p. 317-332.

119. Bucaro, J., Dardy, H.D. and Carome, E.F. (1997) *Optical fibre acoustic sensor.* **Applied Optics**, 16 (7): p. 1761-2.

120. Baillie, P.W.R., Hale, K.F., Fernando, G.F. and Jones, B.E. (1995) *Optical fibre sensing of acoustic emission in fibre reinforced composites*. **Proc. Conf. Sensors and their Applications VII**,. Dublin: A.T. Augousti.

121. Pierce, S., Philp, W. R. Gachagan, A., McNab, A., Hayward, G. and Culshaw, B. (1996) *Surface- bonded and embedded optical fibres as ultrasonic sensors.* **Applied Optics**, 35(25): p. 5191-5197.

122. Her, S. and Yang, C. (2012) *Dynamic Strain Measured by Mach-Zehnder Interferometric Optical Fiber Sensors.* **Sensors**, 12(3): p. 3314.

123. Brown, D.A., Cameron, C.B., Keolian, R.M., Gardner, D.L. and Garrett, S.L. (1991) *A symmetric 3x3 coupler based demodulator for fiber optic interferometric sensors.* **In Proceeding SPIE 1991**, Dec 1 (Vol. 1584, pp. 328-335).

124. Kwon, I.B., Kim, C.G. and Hong, C.S. (1998) *Simultaneous sensing of the strain and points of failure in composite beams with an embedded fiber optic Michelson sensor.* **Composites Science and Technology**, 57(12): p. 1639-1651.

125. Changsen, S., Yujin, L. and Ansari, F. (2004) *Serially multiplexed dual-point fiber-optic acoustic emission sensor.* **Journal of Lightwave Technology**, 22(2): p. 487-493.

126. Zhang, T., Pang, F., Liu, H., Cheng, J., Lv, L., Zhang, X., Chen, N. and Wang, T. (2016) *A Fiber-Optic Sensor for Acoustic Emission Detection in a High Voltage Cable System.* **Sensors** (Basel, Switzerland), 16(12): p. 2026.

127. Matsuo, T., Yokoi, N., Cho, H. and Takemoto, M. (2007) *Michelson-Type Optical Fiber Laser Interferometer for Cylinder Wave Monitoring.* **Material Transactions**, 48(6): p. 1208-1214.

128. Gang, T. Hu, M., Qiao, X., Li, J., Shao, Z., Tong, R. and Rong, Q. (2017) *Fiber-optic Michelson interferometer fixed in a tilted tube for direction-dependent ultrasonic detection.* **Optics and Lasers in Engineering**, 88: p. 60-64.

129. Lee, C. E., Alcoz, J. J., Yeh, Y., Gibler, W. N., Atkins, R. A. and Taylor, H. F. (1992) *Optical fiber Fabry-Perot sensors for smart structures.* **Smart Materials and Structures**, 1(2): p. 123.

130. Dae-Hyun, K., Bon-Yong, K., Chun-Gon, K. and Chang-Sun, H. (2004) *Damage detection of composite structures using a stabilized extrinsic Fabry–Perot interferometric sensor system.* **Smart Materials and Structures**, 13(3): p. 593.

131. Machavaram, V.R. (2006) *Micro-machining Techniques for the Fabrication of Fibre Fabry-Perot Sensors*. **Engineering Systems Department**, Cranfield University.

132. Dorighi, J. F., Krishnaswamy, S. and Achenbach, J. D. (1995) *Stabilization of an embedded fiber optic Fabry-Perot sensor for ultrasound detection.* **IEEE Transactions on Ultrasonics, Ferroelectrics, and Frequency Control**, 42(5): p. 820-824.

133. Kashyap, R. (2010) *Chapter 10 - Principles of Optical Fiber Grating Sensors*, in *Fiber Bragg Gratings (Second Edition)*, R. Kashyap, Editor **Academic Press: Boston**. p. 441-502.

134. Kersey, A., Davis, M.A., Patrick, H.J., Leblanc, M.K., Koo, P., Askins, C.G., Putnam, M.A. and Friebele, E.J. (1997) *Fiber grating sensors.* **Journal of Lightwave Technology**, 15(8): p. 1442-1463.

135. Ajoy, G., Thyagarajan, K. (1998) *An Introduction to Fiber Optics*. **Cambridge University Press**.

136. Hill, K.O., Malo, B., Bilodeau, F., Johnson, D.C. and Albert, J. (1993) *Bragg gratings fabricated in monomode photosensitive optical fiber by UV exposure through a phase mask.* **Applied Physics Letters**, 62(10): p. 1035-1037.

137. Meltz, G., Morey, W.W. and Glenn, W.H. (1989) *Formation of Bragg gratings in optical fibers by a transverse holographic method.* **Optics Letters**, 14(15): p. 823-825.

138. Lee, B. (2003) *Review of the present status of optical fiber sensors.* **Optical Fiber Technology**, 9(2): p. 57-79.

139. Hiroshi, T., Nobuyuki, T., Kei, U. and Junji, T. (2004) *Impact damage detection in CFRP using fiber Bragg gratings.* **Smart Materials and Structures**, 13(4): p. 719.

140. Betz, D.C., Thursby, G., Culshaw, B., and Wieslaw J.S. (2003) *Acousto-ultrasonic sensing using fiber Bragg gratings.* **Smart Materials and Structures**, 12(1): p. 122.

141. Betz, D.C., Thursby, G., Culshaw, B. and Wieslaw, J.S. (2006) *Identification of structural damage using multifunctional Bragg grating sensors: I. Theory and implementation.* **Smart Materials and Structures**, 15(5): p. 1305.

142. Betz, D.C., Thursby, G., Culshaw, B. and Wieslaw, J.S. (2007) *Structural Damage Location with Fiber Bragg Grating Rosettes and Lamb Waves.* **Structural Health Monitoring**, 6(4): p. 299-308.

143. Wu, Q. and Okabe, Y. (2012) *High-sensitivity ultrasonic phase-shifted fiber Bragg grating balanced sensing system.* **Optics Express,** 20(27): p. 28353-28362.

144. Wu, Q. and Okabe, Y. (2012) *Ultrasonic sensor employing two cascaded phase-shifted fiber Bragg gratings suitable for multiplexing.* **Optics Letters**, 37(16): p. 3336-3338.

145. Wu, Q., Yu, F., Okabe, Y. and Kobayashi, S. (2015) *Application of a novel optical fiber sensor to detection of acoustic emissions by various damages in CFRP laminates.* **Smart Materials and Structures**, 24(1): p. 015011.

146. Okabe, Y., Yashiro, S., Kosaka, T. and Takeda N. (2000) *Detection of transverse cracks in CFRP composites using embedded fiber Bragg grating sensors.* **Smart Materials and Structures**, 9(6): p. 832.

147. Okabe, Y., Mizutani, T., Yashiro, S. and Takeda, N. (2002) *Detection of microscopic damages in composite laminates.* **Composites Science and Technology**, 62(7–8): p. 951-958.

148. Takeda, N., Okabe, Y., Kuwahara, J., Kojima, S. and Ogisu, T. (2005) *Development of smart composite structures with small-diameter fiber Bragg grating sensors for damage detection: Quantitative evaluation of delamination length in CFRP laminates using Lamb wave sensing.* **Composites Science and Technology**, 65(15–16): p. 2575-2587.

149. Okabe, Y., Kuwahara, J., Natori, K., Takeda N., Ogisu, T., Kojima, S. and Komatsuzaki, S. (2007) *Evaluation of debonding progress in composite bonded structures using ultrasonic waves received in fiber Bragg grating sensors.* **Smart Materials and Structures**, 16(4): p. 1370.

150. Mendoza, E., Prohaska, J., Kempen, C., Esterkin, Y., Sun, S. and Krishnaswamy, S. (2012) *Distributed Fiber Optic Acoustic Emission Sensor (FAESenseTM): System for Condition Based Maintenance of Advanced Structures*. ***6th European Workshop on Structural Health Monitoring***, Dresden, Germany.

151. Pouet, B.F., Ing, R.K., Krishnaswamy, S. and Royer, D. (1996) *Heterodyne interferometer with two-wave mixing in photorefractive crystals for ultrasound detection on rough surfaces.* **Applied Physics Letters**, 69(25): p. 3782-3784.

152. Guemes, J.A. and Menéndez, J.M. (2002) *Response of Bragg grating fiber-optic sensors when embedded in composite laminates.* **Composites Science and Technology**, 62(7–8): p. 959-966.

153. Botsis, J., Humbert, L., Colpo, F. and Giaccari, P. (2005) *Embedded fiber Bragg grating sensor for internal strain measurements in polymeric materials.* **Optics and Lasers in Engineering**, 43(3–5): p. 491-510.

154. Fan, Y. and Kahrizi, M. (2006) *Characterization of a FBG strain gage array embedded in composite structure.* **Sensors and Actuators**, 121(2): p. 297-305.

155. Ling, H., Lau, K., Cheng, L. and Jin, W. (2006) *Viability of using an embedded FBG sensor in a composite structure for dynamic strain measurement.* **Measurement**, 39(4): p. 328-334.

156. de Oliveira, R., Ramos, C.A. and Marques, A.T. (2008) *Health monitoring of composite structures by embedded FBG and interferometric Fabry–Pérot sensors.* **Computers & Structures**, 86(3–5): p. 340-346.

157. Lam, P., Lau, K., Ling, H., Su, Z. and Tam, H. (2009) *Acousto-ultrasonic sensing for delaminated GFRP composites using an embedded FBG sensor.* **Optics and Lasers in Engineering**,. 47(10): p. 1049-1055.

158. Frieden, J., Cugnoni, J., Botsis, J., Gmür, T. and Ćorić, D. (2010) *High-speed internal strain measurements in composite structures under dynamic load using embedded FBG sensors.* **Composite Structures**, 92(8): p. 1905-1912.

159. Birks, T.A. and Li, Y.W. (1992) *The shape of fiber tapers.* **Journal of Lightwave Technology**, 10(4): p. 432-438.

160. Ghatak, A.K., Thyagarajan, K. (1989) *Optical Electronics*. Cambridge University Press.

161. Eisenmann, M. and Weidel, E. (1988) *Single-mode fused biconical couplers for wavelength division multiplexing with channel spacing between 100 nd 300 nm.* **Journal of Lightwave Technology**, 6(1): p. 113-119.

162. Thyagarajan, K. and Ghatak, A. (2007) *Fiber Optic Essentials*. Willey Survival Guides in Engineering: John Willey & Sons, Inc.

163. Senior, J.M. (1992) *Optical Fiber Communications: Principles and Practice*. Second Edition 1992: Prentice Hall.

164. Sheem, S.K. and Giallorenzi, T.G. (1979) *Single-mode fiber-optical power divider: encapsulated etching technique.* **Optics Letters**, 4(1): p. 29-31.

165. Liao, F.J. and Boyd, J. T. (1981) *Single-mode fiber coupler.* **Applied Optics**, 20(15): p. 2731-2734.

166. Sylvester, W.R. and McKeeman, J.C. (1990) *Automation of fiber optic polished coupler fabrication*. **Southeastcon '90. Proceedings, IEEE**.

167. Bergh, R.A. and Shaw, H.J. (1985) *Method of manufacturing a fiber optic directional coupler*. **U.S. Patent No. 4,536,058**, 20 Aug. 1985

168. Bilodeau, F., Faucher, S., Hill, K.O. and Johnson D.C. (1990) *Fabrication technique for low-loss fused taper directional couplers and pressure sensor produced thereby*. **U.S. Patent No. 4,895,423**, 23 Jan. 1990

169. Black, R.J., Lacroix, S., Gonthier, F. and Love, J.D. (1991) *Tapered single-mode fibres and devices. II. Experimental and theoretical quantification.* **IEE Proceedings J-Optoelectronics**, 1991 Oct;138(5):355-64**.**

170. Boucouvalas, A.C. and Georgiou, G. (1986) *Tapering of single-mode optical fibres.* **IEE Proceedings J (Optoelectronics)**, 133(6): p. 385-392.

171. Cryan, C.V. and Hussey, C.D. (1992) *Fused polished singlemode fibre couplers.* **Electronics Letters**, 28(2): p. 204-205.

172. Cryan, C.V., Donnchadha, M.O., Lonergan, J. M. and Hussey, C.D. (1992) *Fused polished polarisation-maintaining fibre couplers.* **Electronics Letters**, 28(9): p. 857-858.

173. Varghese, S. (2008) *Fabrication and characterisation of all fiber components for optical access networks*. **International school of photonics**, Cochin Universitiy of Science and Technology.

174. Kawasaki, B., Kawachi, M., Hill, K. and Johnson, D. (1983) *A single mode fiber coupler with variable coupling ratio.* **Lightwave Technology Journal**, 1(1): p. 176-178.

175. Bilodeau, F., Hill, K.O., Johnson, D.C. and Faucher, S. (1987) *Compact, low-loss, fused biconical taper couplers: overcoupled operation and antisymmetric supermode cutoff.* **Optics Letters**, 12(8): p. 634-636.

176. Bilodeau, F., Hill, K.O., Faucher, S. and Johnson, D.C. (1988) *Low-loss highly overcoupled fused couplers: fabrication and sensitivity to external pressure.* **Journal of Lightwave Technology**, 6(10): p. 1476-1482.

177. Chaudhuri, P.R., Pal, B.P. and Shenoy, M.R. (2000) *Understanding coupling mechanism in fused fiber coupler-based components: role of core and cladding modes*. **International Conference on Fiber Optics and Photonics**, Allied Publishers.

178. Chaudhuri, P.R., Pal, B.P. and Shenoy, M.R. (2000) *Modelling of fused 2x2 all-fibre coupler components.* **Proceedings of the National Symposium on Advances of Microwave and Lightwave Technology**, University of Delhi, p. 26-29.

179. Marcuse, D. (1973) *Coupled Mode Theory of Round Optical Fibers.* **Bell System Technical Journa**l, 52(6): p. 817-842.

180. Marcuse, D. (1971) *The coupling of degenerate modes in two parallel dielectric waveguides.* **Bell System Technical Journa**l, 50: p. 1791-1816.

181. Snyder, A.W. (1972) *Coupled-Mode Theory for Optical Fibers.* **The Journal of the Optical Society of America**, 62(11): p. 1267-1277.

182. Haus, H. and Huang, W.P. *Coupled-mode theory.* **Proceedings of the IEEE**, 79(10): p. 1505-1518.

183. Payne, F.P., Hussey, C.D. and Yataki, M.S. (1985) *Modelling fused single-mode-fibre couplers.* **Electronics Letters**, 21(11): p. 461-462.

184. Sheem, S.K., Taylor, H.F., Moeller, R.P. and Burns, W.K. (1981) *Propagation characteristics of single-mode evanescent field couplers.* **Applied Optics**, 1981. 20(6): p. 1056-1059.

185. Chang, H., Lin, T.and Wu, T. (1995) *Accurate coupling coefficients for fiber couplers with weakly fused cross sections.* **Applied Optics**, 34(27): p. 6168-6171.

186. Payne, F. P., Hussey, C. D. and Yataki, M. S. (1985) *Polarisation analysis of strongly fused and weakly fused tapered couplers.* **Electronics Letters**, 21(13): p. 561-563.

187. Ravets, S., Hoffman, J. E., Orozco, L. A., Rolston, S. L., Beadie, G. and Fatemi, F.K. (2013) *A low-loss photonic silica nanofiber for higher-order modes.* **Optics Express**, 21(15): p. 18325-18335.

188. Yataki, M.S. (1988) *Fused taper single mode fibre couplers*. **PhD Thesis,** University of Southampton.

189. Chiang, K.S. (1997) *Effects of cores in fused tapered single-mode fiber couplers.* **Optics Letters**, 12(6): p. 431-433.

190. Lacroix, S., Gonthier, F. and Bures, J. (1994) *Modeling of symmetric 2 × 2 fused-fiber couplers.* **Applied Optics**, 33(36): p. 8361-8369.

191. Kumar, A., Thyagarajan, K. and Ghatak, A.K. (1983) *Analysis of rectangular-core dielectric waveguides: an accurate perturbation approach.* **Optics Letters**, 8(1): p. 63-65.

192. Thorlabs. *2x2 Single Mode Fused Fiber Optic Couplers*. Cited 2014 from: http://www.thorlabs.de/newgrouppage9.cfm?objectgroup_id=374.

193. Sheem, S. K. and J. H. Cole, *Acoustic sensitivity of single-mode optical power dividers.* Opt. Lett., 1979. 4(10): p. 322-324.

194. Doyle, C., Chen, R., Liu, T., Zheng, G. and Fernando, G.F. (2002) *Fiber optic acoustic emission sensor based on a fused tapered coupler*. **Proceeing SPIE**, Vol. 4694.

195. Chao, L., Li, P., Song, G., Ze-xin, K., Jiang, S. and Jun-fang, Y. (2011) *A second-order approximation coupling model of fused biconical tapered fiber coupler*. **International Conference on Advanced Infocom Technology 2011 (ICAIT 2011)**.

196. Jian, X. and Bin, M. (2008) *Study of fiber-optic coupler's strain characteristic based on variational theory*. **IEEE International Conference Automation and Logistics (ICAL 2008)**.

197. Mistras, *R30α Sensor (2010)*. Cited 2015 from: http://www.physicalacoustics.com/content/literature/sensors/Model_R30a.pdf

198. Mistras, *R50α Sensor (2011)*. Cited 2015 from: http://www.physicalacoustics.com/content/literature/sensors/Model_R50a.pdf

199. Kubiak, T.M. Benbow, D.W. (2010) *The Certified Six Sigma Black Belt Handbook*. 2nd Edition.

200. Minitab. *Pearson product moment correlation*. Cited 2017 14th January from: http://support.minitab.com/en-us/minitab/17/topic-library/modeling-statistics/regression-and-correlation/correlation-and-covariance/basics-of-correlation-and-covariance/.